UNIVERSITY OF Southampton

University of Southampton Research Repository

Copyright © and Moral Rights for this thesis and, where applicable, any accompanying data are retained by the author and/or other copyright owners. A copy can be downloaded for personal non-commercial research or study, without prior permission or charge. This thesis and the accompanying data cannot be reproduced or quoted extensively from without first obtaining permission in writing from the copyright holder/s. The content of the thesis and accompanying research data (where applicable) must not be changed in any way or sold commercially in any format or medium without the formal permission of the copyright holder/s.

When referring to this thesis and any accompanying data, full bibliographic details must be given, e.g.

Thesis: Author (Year of Submission) "Full thesis title", University of Southampton, name of the University Faculty or School or Department, PhD Thesis, pagination.

Data: Author (Year) Title. URI [dataset]

http://eprints.soton.ac.uk

University of Southampton

FACULTY OF ENGINEERING AND PHYSICAL SCIENCES

Engineering Sciences Unit

EXTENDING FATIGUE LIFE OF INDUSTRIAL LOW-PRESSURE FV566 TURBINE BLADES: EFFICACY OF A LIFETIME EXTENSION STRATEGY TO EXTEND SERVICE LIFE

DOI: 10.5258/SOTON/T0044

by

BENJAMIN MICHAEL DAVID CUNNINGHAM

ORCID ID: 0000-0002-2604-4242

THESIS FOR THE DEGREE OF DOCTOR OF PHILOSOPHY

April 2022

University of Southampton

Abstract

FACULTY OF ENGINEERING AND PHYSICAL SCIENCES

Engineering Sciences Unit

Thesis for the degree of Doctor of Philosophy

EXTENDING FATIGUE LIFE OF LOW-PRESSURE FV566 TURBINE BLADES: EFFICACY OF A LIFETIME EXTENSION STRATEGY TO EXTEND SERVICE LIFE

by

Benjamin Michael David Cunningham

The fir-tree-root-fillets of turbine blades are prone to fatigue cracking on the notch surfaces and pose a potential risk of fatigue failure before expected service life due to increasing exposure to start-stop fatigue loading conditions. Turbine systems are additionally subjected to 10 % over-speed testing annually. Turbine blades are being replaced at high cost due to the serious safety risk in the case of catastrophic failure. The efficacy of a proposed lifetime-extension strategy involving grinding out existing cracks, identifiable via non-destructive testing (thus changing the notch geometry), followed by T0 shot peening and the effect of additional overload cycles was investigated.

FV566 martensitic stainless-steel material extracted from ex-service turbine blades was tested and the characteristic baseline material microstructure, mechanical properties and fatigue behaviour examined. Single edge notch bend and U-notch specimens (with industry representative geometries) were subjected to 3-point bending fatigue loading in the low cycle fatigue regime. A finite element model of the test specimens with elastic-plastic material modelling was developed to calculate required loads and stress and strain distributions in the notch field with various U-notch geometries. The effects of industry representative ‘as-received’ and polished notch surface conditions on the crack initiation behaviour was investigated. The effect of relatively small industry representative overloads up to 150 % of the maximum baseload every 150 baseload cycles were compared with constant amplitude loading and the effect on initiation behaviour and crack growth rates examined. Various U-notch geometries expected after grinding out existing cracks were fatigue tested at different strain ranges to establish the influence of notch geometry on fatigue behaviour. T0 industrial representative shot peening was applied to U-notched specimens and the residual stress profiles obtained via XRD. The effect shot peening on fatigue behaviour was investigated for various loading conditions (including overload) and notch geometries. A lifetime prediction method was developed which was capable of accounting for the application of the proposed lifetime extension strategy and was compared with experimental testing.

Early crack initiation was observed in the as-received notch surface condition due to the presence of corrosion pits. A polished surface condition increased the number of cycles to crack initiation. The presence of an overload 110 % or less of the maximum baseload every

150 baseload cycles did not affect fatigue life. An overload of 150 % retarded both long and short crack growth rates, attributed to compressive residual stress ahead of the crack tip, resulting in an overall increase in fatigue life. Additionally, a compressive residual stress induced in the notch field increased the number of cycles to crack initiation, improving fatigue life overall. Shot peening damaged the notch surface causing pre-existing cracks and early crack initiation. However, the compressive residual stress field from shot peening significantly retarded short crack growth and increased overall fatigue life. After 1.2 % total strain range the lifetime extension benefit from shot peening was diminished. Notch geometry was not found to have a notable difference on fatigue life when tested at identical strain ranges. The lifetime extension strategy was found to increase the overall life of U-notch samples assuming the strain range remained constant throughout the test. The lifetime prediction model was able to predict the number of cycles to failure for a sample subjected to the lifetime extension strategy and offer a lifetime prediction that accounts for a likely increase in strain range after changing the notch geometry.

The service life of turbine blades may be improved by adopting the lifetime extension strategy. Finite Element modelling of actual turbine blade geometry with industry relevant loading conditions is required to establish the increase in strain range expected from grinding out existing cracks in-situ. Further experimentation is then required to apply the method developed in this thesis to actual turbine blade geometry prior to incorporating the lifetime extension strategy as a maintenance procedure.

Table of Contents

Table of Tables

Table of Figures

Table of Figures

Table of Figures

Table of Figures

Research Thesis: Declaration of Authorship

Print name:	Benjamin Michael David Cunningham
Title of thesis:	EXTENDING FATIGUE LIFE OF LOW-PRESSURE FV566 TURBINE BLADES: EFFICACY OF A LIFETIME EXTENSION STRATEGY TO EXTEND SERVICE LIFE

I declare that this thesis and the work presented in it are my own and has been generated by me as the result of my own original research.

I confirm that:

- This work was done wholly or mainly while in candidature for a research degree at this University;
- Where any part of this thesis has previously been submitted for a degree or any other qualification at this University or any other institution, this has been clearly stated;
- Where I have consulted the published work of others, this is always clearly attributed;
- Where I have quoted from the work of others, the source is always given. With the exception of such quotations, this thesis is entirely my own work;
- I have acknowledged all main sources of help;
- Where the thesis is based on work done by myself jointly with others, I have made clear exactly what was done by others and what I have contributed myself;
- Parts of this work have been published as:

B. M. D. Cunningham, A. Evangelou, C. You, A. Morris, J. Wise P. A. S. Reed, A. Hamilton ‘Fatigue crack initiation and growth behaviour in a notch with periodic overloads in the low-cycle fatigue regime of FV566 ex-service steam turbine blade material’. Fatigue Fract Eng Mater Struct. 2021. https://doi.org/10.1111/ffe.13617

Signature: Date: 21/04/2022

Acknowledgements

I have had to face many challenges throughout my years, made all the more difficult because of a stammer and Asperger's syndrome. While many people supported me in what I wanted to do, not everyone believed in me. One family member thought I would be better off just working in MacDonald's and one 'expert' on autism thought that a nice job in a quiet library is probably where I would end up. Somehow, despite the odds, my resolve has remained undiminished, and I have managed to achieve the seemingly improbable, I am a Doctor of Engineering. A PhD can feel like a lonely place at times, but it is only upon reflection that one can really appreciate how collaborative research really is. There are so many people that I would like to thank, for whom without their guidance, support and contribution, my PhD would not have been possible.

I would firstly like to thank the two best supervisors I could have imagined having, my main supervisor Professor Philippa Reed and my second supervisor Dr Andrew Hamilton for all the time they spent showing me how to be a researcher and without whom, I would not have completed this work. I would also like to thank Dr Andy Morris Chief Mechanical Engineer at EDF energy for funding this PhD (EPSRC grant number EP/N509747/1), maintaining an industrial focus, and providing the testing material, and James Wise at Frazer-Nash Consultancy for sample preparation and help with additional testing. Associate Professor Chao You from Nanjing University and former Southampton University student who helped me get to grips with ABAQUS and carried out some modelling work for me. A big thankyou to Mitchell Leering from Coventry University for help with residual stress measurements, I know a lot of work went into that! Angelos Evangelou who carried out some of the initial testing and analysis on the overloads project. Kittikorn Konlam for helping me carry out some of my tests for his Masters Degree. Although I did not meet them properly in person, I would like to thank Katherine Soady and Binyan He whose theses were a constant source of inspiration, and Southdown Materials Testing Ltd for analysing the chemical constituents of my material.

Next I would like to thank that staff at the University of Southampton. Sue Berger and Katherine Day for ongoing help with administration problems. Geoff Howell, Aga Knyter, Heather Porter and Deepak Kumar for help with material preparation prior to testing and analysis. Andrew Robinson for help and useful discussions with material and fatigue testing. Shuncai Wang for helping me with the scanning electron microscope Tim Woolman and Laurence Dwyer at the Engineering Design and Manufacturing Centre and F&M Engineering for help with designing and manufacturing my testing rig. Sandwell UK Ltd for shot peening my samples, and Brian Mellor for being such an influential person and asking me difficult questions in my preliminary vivas.

B.M.D. Cunningham
There are many people both past and present from the offices of the material research department I would like to thank for their friendship and support. Mike Giles for mentoring me at the beginning of my PhD and teaching me about beer and Metal music, Angelos Evangelou for helping me get up to speed with training and helping me with my first few tests. Somsubhro Chaudhuri for being the most entertaining person ever, giving me the opportunity to see Belgium and showing me that poo can be interesting (to a limited degree). Alex Marek for teaching that life is possibly better in Poland. Andreu Laborda for showing me that you can start work at 2pm. Alvaro Sanchez for teaching me about the difficulties of aluminium and how much better steel is to polish. Kim Donghyuk for teaching me about Asian and Korean culture. Ara Khodavirdi for being a good friend and helpful partner. Diego Martinez de Luca for making me glad I am not working on Instron 1. Anqi Liang for giving me the opportunity to experience a Chinese wedding. Yuan Guo Tan for showing me how to look busy by playing League of Legends (aka LOL). Talha for giving me opportunity to practice answering difficult questions and Kieran Ball for showing that it is somehow possible to do a PhD while living with a family miles away. Marie Salome Duval Chaneac for sharing some wonderful times together. Luis Pena for helping me with the art of polishing, games of chess and wonderful discussions about interesting things. Charlie Burson-Thomas for being one of the nicest people I know. To the new starters Joseph Doyle, Yeajin Lee and Ellis Hill, I wish you all the best in your PhD journey.

Lastly, I would like to thank my family. In particular my Nan, Mum, Tony and Dad who have lived through my PhD with me and supported me all the way, and my Nanny and Grandad who are smiling down from above.

I will never forget the experience that was the Gin and Anime club, the unresolvable fights about which strategy was best in age of empires, the quirky presentations during the donut meetings and assigning soul dogs to so many of you. It has been a privilege to be part of such a varied community, I have learnt so much about different cultures and countries, more than enough to confirm what I already know, that we are all human.

Definitions and Abbreviations

a	The depth of a semi-elliptical crack
a_f	Final crack length
a_g	Crack length at start of grow out
a/c	Ratio between crack depth and half projected surface crack length for semi-elliptical cracks
AFM	Atomic Force Microscopy
b	Fatigue strength exponent
B	Sample breadth
B_w	Finite width correction factor
BEI	Backscattered Electron Image
BL	Baseload
c	Fatigue ductility exponent
$c_{Project}$	Half the total projected length of a semi-elliptical surface crack
C	Paris-law constant
CA	Constant Amplitude
Con	Conservative
CC	Crack Coalescence
CCGT	Combined Cycle Gas Turbine
CM	Coffin-Manson
CRS	Compressive Residual Stress
CSA	Cross Sectional Area
CT	Compact Tension (specimen)
d	Out-of-plane distance
d	Distance between crystallographic planes
d_x	Projected out-of-plane distance
dc/dN	Projected surface crack growth per cycle
DCPD	Direct Current Potential Drop
DCM	DCPD Crack Growth Monitor

E	Young's modulus
EBSD	Electron Backscatter Diffraction
EDX / EDS	Energy Dispersive X-ray Spectroscopy
EPFM	Elastic Plastic Fracture Mechanics
EXP	Experiment
F	Total maximum force
FE (M)	Finite element (modelling)
FEA	Finite Element Analysis
FEG SEM	Field Emission Gun Scanning Electron Microscope
FNC	Frazer-Nash Consultancy
FV	Firth Vickers
FWHM	Full Width Half Maximum
G	Ground (or as-received) surface condition
$\mathcal{G}$	Energy release rate (LEFM)
H	Monotonic strength coefficient
H_0	Macro-hardness
HP	High Pressure (turbine blades)
HRC	Hardness Rockwell C
HV	Hardness in Vickers Hardness
IP	Intermediate Pressure (turbine blades)
k_t	Stress concentration factor
K_I	Stress intensity factor (mode I – tensile opening)
K_{Eff}	Effective stress intensity factor
K_{op} / K_{cl}	Stress intensity factor required to induce crack opening
K_{max}	Maximum stress intensity factor
K_{min}	Minimum stress intensity factor
$K_{Surface}$	Stress intensity factor for semi-elliptical short cracks
$K_{Threshold}$	Threshold stress intensity factor
J	Energy release rate (EPFM)
L	Sample length

LC	Long Crack
LCF / HCF	Low Cycle Fatigue / High Cycle Fatigue
LE	Lifetime Extension (strategy)
LEFM	Linear Elastic Fracture Mechanics
LP	Low Pressure (turbine blades)
$M_{f(0)}$	Front face correction factor
m	Paris-law constant (exponent)
n	Strain hardening exponent
n	Integer multiple of wavelength
N	Number of cycles
N_{BL}	Number of baseload cycles per overload sequence
N_c	Number of cycles to crack initiation
N_f	Number of cycles to failure
N_{fOL}	Estimated number of cycles to failure including overloads
$N_{f\Delta\varepsilon BL}$	Total cycles to failure at CA baseload strain range
$N_{f\Delta\varepsilon OL}$	Total cycles to failure at overload strain range
N_{OL}	Number of overload cycles per overload sequence
NDT	Non-Destructive Testing
NF	Notch Field
OEM	Original Equipment Manufacturer
OL	Overload
OLR	Overload Ratio
OM	Optical Microscopy
P_{max}	Maximum load during baseload cycle
P_{min}	Minimum load during baseload cycle
P_{OL}	Maximum load during overload cycle
P	Polished (surface condition)
PBB	Plain Bend Bar
PM	Palmgren-Miner
PSB	Persistent Slip Band

R	Resistance
R-ratio	Ratio between minimum and maximum load
R_a	Arithmetical mean vertical deviation of the assessed roughness line profile from the mean line
r_p	Radius of the plastic zone
S	Nominal or far field stress
SC	Short Crack
SEI	Secondary Electron Image
SEN(B)	Single Edge Notch (Bend)
SP	Shot Peen
SWT	Smith-Watson-Topper
S_t	Top roller span
S_b	Bottom roller span (for 4-point bending)
TA	Tensile Axis
TWI	The Welding Institute
T	Traction Vector (J-integral)
U	Ratio between ΔK_{eff} and ΔK used to quantify plastic closure
UTS	Ultimate Tensile Strength
V	Voltage
W	Specimen total depth (not including notch)
w_s	Surface Energy
X	Potential difference across crack
XFEM	Extended Finite Element Method
XRD	X-ray Diffraction
Y	Geometry correction factor
δ_t (CTOD)	Crack Tip Opening Displacement
Δ	Range
ε'_f	Fatigue ductility coefficient
ε_{11} / ε_{xx}	Strain along tensile axis
ε_a	Strain amplitude

Definitions and Abbreviations

ε_e	Elastic strain
ε_p	Plastic strain
ε_t	Total strain
Γ	J-integral contour path
λ	Wavelength of X-ray
ϑ	Angle of X-ray penetration
μ	Shear modulus
ρ	Notch radius
σ_a	Stress amplitude
σ_b	Pure bending stress at the notch surface
σ'_f	Fatigue strength coefficient
σ_{11} / σ_{xx}	Stress in the longitudinal direction
σ_{max}	Maximum stress
σ_y	Yield strength
ν	Poisson's ratio

Chapter 1: Introduction

1.1 Background

1.1.1 Power Generation

Electricity is the lifeblood of modern society, improving the comforts of life from heating and lighting, to enabling rapid development of large cities. There are two main methods of generating electricity, namely from renewable resources such as wind power or non-renewable sources such as fossil fuels or natural gas. The Combined Cycle Gas Turbine plant (CCGT) is one example of a non-renewable energy generation method involving the use of natural gas. West Burton B is one of three CCGT units in England that produces a maximum power output between 1305 MW and 1332 MW, enough to power a city the size of Sheffield.

A typical CCGT operation cycle is shown in Figure 1-1. Electrical energy is produced by converting chemical and thermal energy into kinetic energy. Natural gas and air are compressed at high pressures resulting in thermal energy. This heats a boiler which in turn produces steam. The steam is superheated and expanded through a steam turbine causing the turbine to rotate. Both the gas and steam turbines rotate a shaft that contains magnetic couples producing electricity. The gas turbine area (red in Figure 1-1) is the same for all CCGTs and contains the blades that are of interest for this study. A typical turbine consists of High Pressure (HP), Intermediate Pressure (IP) and Low Pressure (LP) turbine blades. During operation, a rotational frequency of 3000 cycles per minute can be experienced.

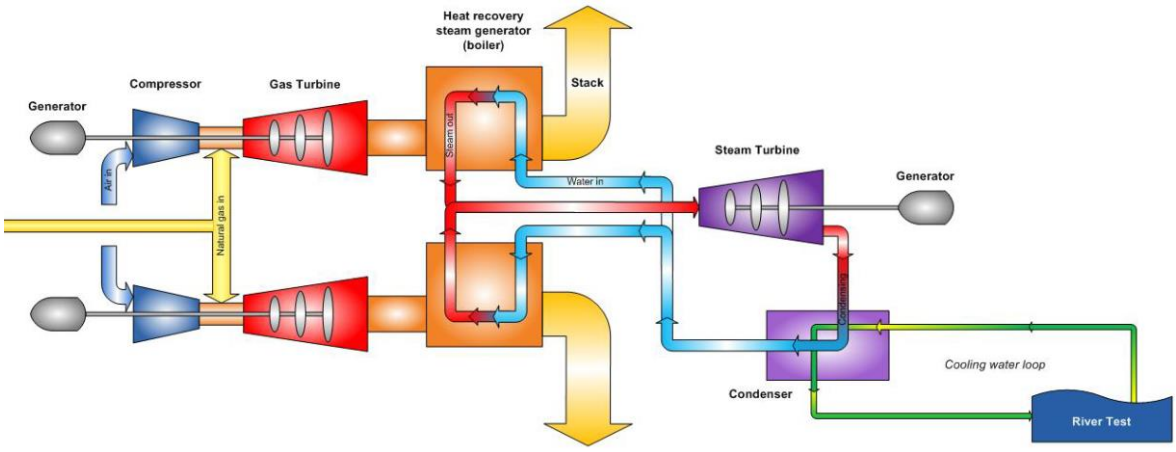

Figure 1-1: A schematic for a typical example of a CCGT power plant at Marchwood [1]. Note that other CCGT plants such as West Burton B may have a different layout.

1.1.2 Turbine blades

Steam turbine blades are typically made from 11-15 % Cr martensitic stainless-steel materials to meet the requirements needed to sustain adequate performance within their harsh working environments as outlined in Table 1-1.

Requirement in design and service	**Material Property**
High static strength	Minimum of 700 MPa
Long-term strength	Creep rupture strength > 100 000 h Creep rupture elongation > 10 %
Toughness	High fracture toughness values and after long-term aging.
Fatigue strength	Low Cycle Fatigue (LCF) High Cycle Fatigue (HCF)
Crack tolerance	Creep crack growth behaviour Fatigue crack growth behaviour
Oxidation resistance	Oxidation behaviour
Erosion resistance	Erosion behaviour
Good weldability	Lower carbon content
Low cost	Lower than Austenitic stainless steel and Ni-base alloy with ease of fabrication

Table 1-1: Material property requirements for high temperature HP, IP and LP steam turbine blades [2].

Turbine blades are typically forged; regions of intricate geometry such as fir-tree-root-fillets are machined where assembly is required. The turbine blade is assembled with the turbine rotor at the base of the blade with a fir-tree-root-fillet design (Figure 1-2 A). Grooves in the shape of a fir-tree allow the blade to be slotted onto the shaft. Female threads from the turbine rotor (known as rotor disc head steeples) can be seen in Figure 1-2 B) [3]. This PhD will focus on testing from material extracted from an Alstom English Electric turbine blade unit such as the one shown in Figure 1-3.

Areas of high stress concentration such as the fir-tree-root-fillets can be shot peened for the purposes of enhanced fatigue resistance. A typical shot peening process applied to turbine blades is MI230R 13A 200 % (known as ‘T0’). High impact shot is fired which deforms material in a localised area. A dimpled surface is observed after shot peening indicating plastic deformation has occurred. A compressive residual stress field is formed along with

strain hardening that enhances fatigue resistance. More information regarding shot peening will be discussed in Chapter 2.3.

A B

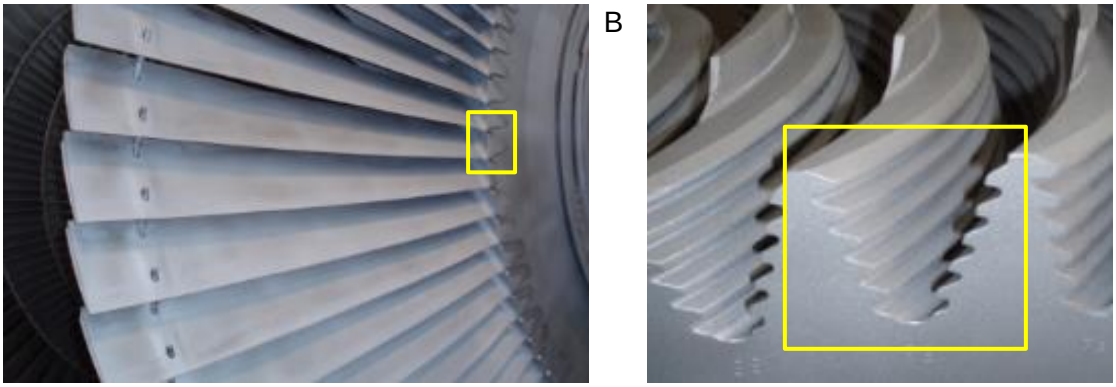

Figure 1-2: A) LD66 Turbine blades as fitted into the rotor disc head steeples. B) A close up view of the fir-tree-root-fixings [4].

Figure 1-3: An image of the Alstom English Electric turbine unit at West Burton A [4].

1.1.3 Turbine blade maintenance

Safety critical parts such as turbine blades must be routinely inspected to ensure safe operating conditions. Electricity cannot easily be stored for later use and must usually be generated on demand. Turbine units are therefore subjected to start-up and shut-down procedures (start-stop cycles), as required to meet fluctuating demand. The large centripetal acceleration experienced by the blades during operation followed by shut down induces excessive cyclic stress at localised stress concentration areas such the at the fir-tree-root fillets. The stress experienced by the blades is high enough to exceed the yield strength of the material and subject these fatigue prone areas to low cyclic fatigue conditions (less than 100 000 cycles to failure). During maintenance, the blades will be removed, and non-destructive testing carried out to inspect and monitor any defects such as cracks within the fir-tree-root-fillets. A typical inspection of the turbine blades lasts for 12 weeks whereby no electricity will be produced during this time.

1.2 11 – 15 % Cr tempered martensitic stainless steel

Tempered martensitic stainless steels containing between 11–15 % Cr, are suitable materials for turbine blade applications due to their high strength and corrosion resistance. These materials typically contain slight variations in additional alloying elements such as Cr, Mo and V alloys to achieve particular material property requirements. The chemical composition and heat treatment of the materials directly affects their mechanical properties and fatigue behaviour. The material and mechanical properties of three martensitic stainless steels are compared in Chapter 3. Therefore, the remainder of Chapter 1 will discuss how tempered martensite is formed and how variations in additional alloying elements and formation processes can impact the fatigue behaviour and life.

Low pressure turbine blades generally experience lower temperatures (approximately 250 °C) than their high pressure counterparts (approximately 570 °C) [5]. Therefore, while creep resistance is a key consideration for material selection for high pressure turbine blades, creep fatigue is less impactful for low pressure turbine blades. The material properties of 11–15 % Cr stainless steels can be affected by temperatures in the region of 300 °C [6] and as such may impact fatigue behaviour. Nonetheless, experimental testing was carried out at ambient room temperature throughout this thesis, allowing a wider range of testing to be carried out and increased data output still regarded as valuable to industry.

1.2.1 Tempered martensite formation

The tempered martensitic stainless steels used in turbine blade applications are typically low carbon steels (between 0.05 and 0.15 wt. %) and are therefore hypo-eutectoid in nature and can be represented by the iron-carbon phase diagram. The formation of tempered martensite begins with an austenitisation process. The material is heated past eutectoid temperature to an austenitisation temperature typically between 1020 °C and 1100 °C. The material is held at the austenitisation temperature for a specific period, allowing carbides and nitrides to dissolve, and inducing the formation of austenite grains with a face centred cubic (FCC) structure. The material is then cooled with sufficient rapidity to induce a near instantaneous diffusionless shear transformation, characteristic of the formation of martensite. The crystal structure is transformed from FCC to a body centred tetragonal (BCT) structure. During this rapid cooling period and prior to the formation of martensite, it may be possible for α-ferrite to form at austenite grain boundaries.

The transformation of the crystal structure induces high internal residual stress due to a restriction of the volumetric change during the austenite to martensite transformation. The high internal residual stress results in a material that is very strong but undesirably brittle in

nature. A tempering process is necessary where the material is heated to below the eutectoid temperature typically between 150 °C and 850 °C (depending on the properties desired and material composition), and held for a specific period, to partially relieve the internal residual stress. During the tempering process, fine stable particles of cementite (Fe_3C) are formed within α-ferrite matrix, which alters the mechanical properties of the material and produces a characteristic tempered martensite microstructure (Figure 1-4 A). Tempering increases the ductility of the material, reduces material hardness but maintains relatively high strength and toughness properties to industrially desirable levels.

Martensite microstructure consists of martensitic laths that align parallel to each other to form blocks, although some misalignment of 2-3 degrees can be seen. The blocks are aligned parallel with each other to form packets. Groups of packets are seen typically bordering with other packets and prior austenite grain boundaries (Figure 1-4 B and C).

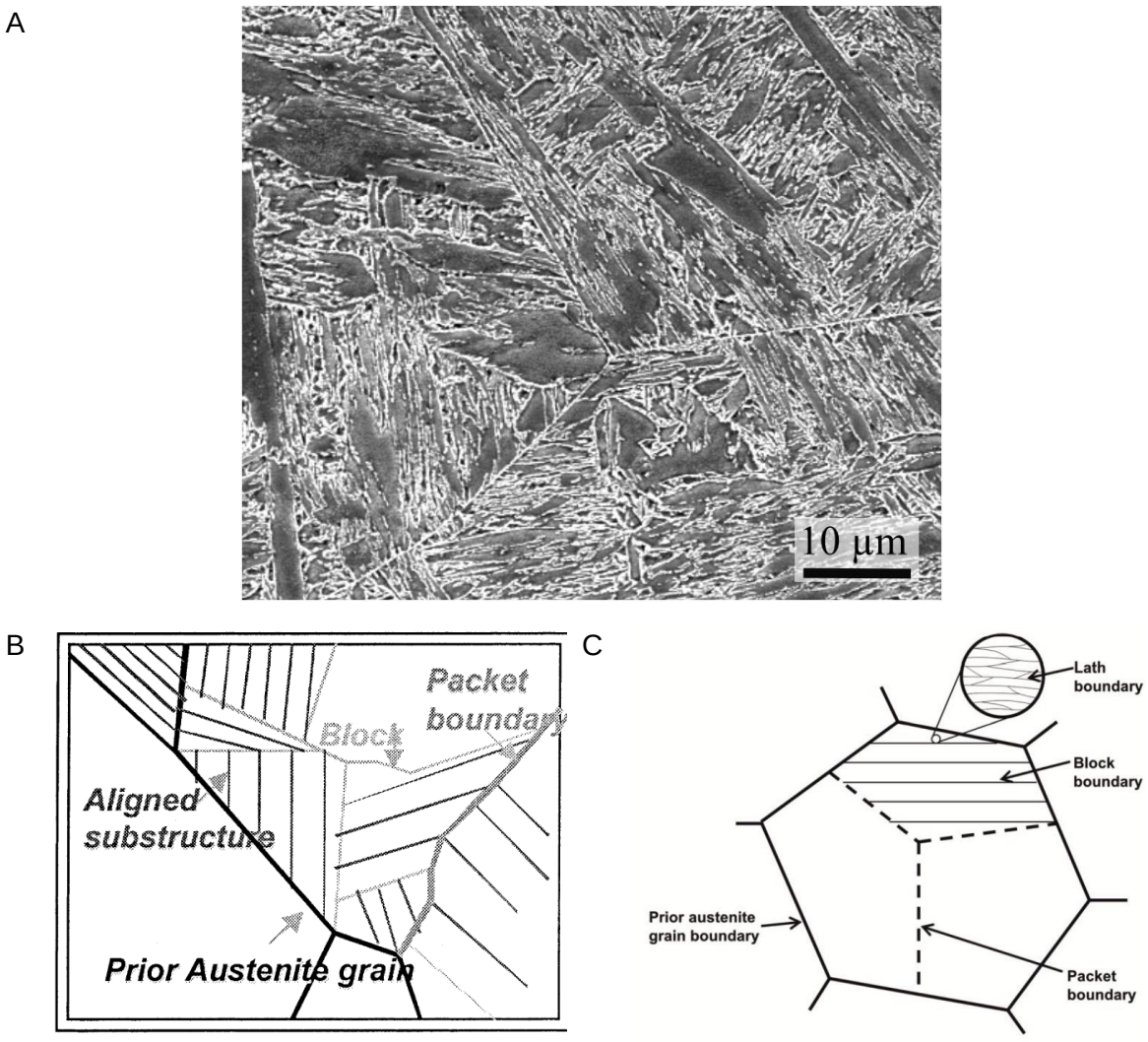

Figure 1-4: A) Scanning electron microscopy of etched FV566 material [7]. B) Schematics showing the typical three tiered microstructure of tempered martensite taken from [8] and C) Kimura [9] cited in Soady [10].

1.2.2 Effect of alloying additions

The addition of alloying elements to steels affect the eutectoid temperature. Increasing the weight % of Manganese (Mn) and Nickel (Ni), reduces the eutectoid temperature. Whereas Titanium (Ti), Molybdenum (Mo), Silicon (Si), Tungsten (W) and Chromium (Cr) increase the eutectoid temperature [11] cited in [12] (Figure 1-5). In conjunction, the isothermal transformation temperature of phases are altered, including the temperature required to start martensite transformation (Ms) (Figure 1-6). Additionally, the required tempering temperature is altered, which may help reduce costs during the manufacturing process.

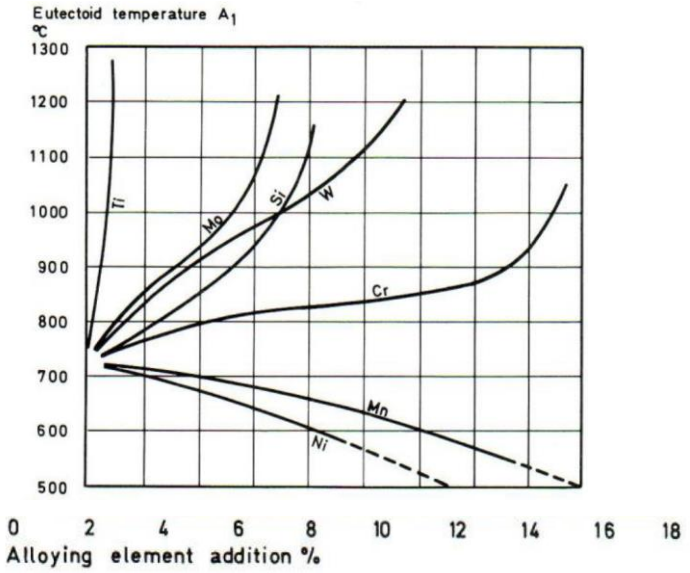

Figure 1-5: The effect of alloying elements on eutectoid temperature. Increasing amounts of Ni and Mn decrease the eutectoid temperature, while Ti, Mo, Si, W and Cr increase eutectoid temperature [11] cited in [12].

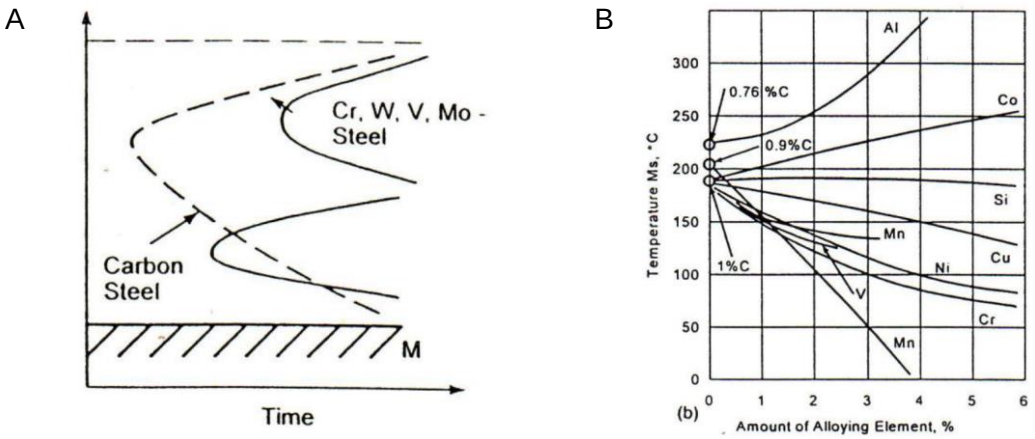

Figure 1-6: A) The effect of alloying elements on isothermal transformation temperature. B) The effect of alloying elements on the martensite transformation starting temperature (Ms) [11] cited in [12].

More importantly, the addition of alloying elements can precipitate with Fe and C during the austenitisation and tempering process, which induces the formation of secondary phase particles. These secondary phase particles can affect grain size, and act as obstacles to fatigue crack growth. Therefore, the mechanical properties such as corrosion resistance, strength, ductility, hardness (Figure 1-7) and resistance to fatigue are affected by altering the quantity of alloying elements [12].

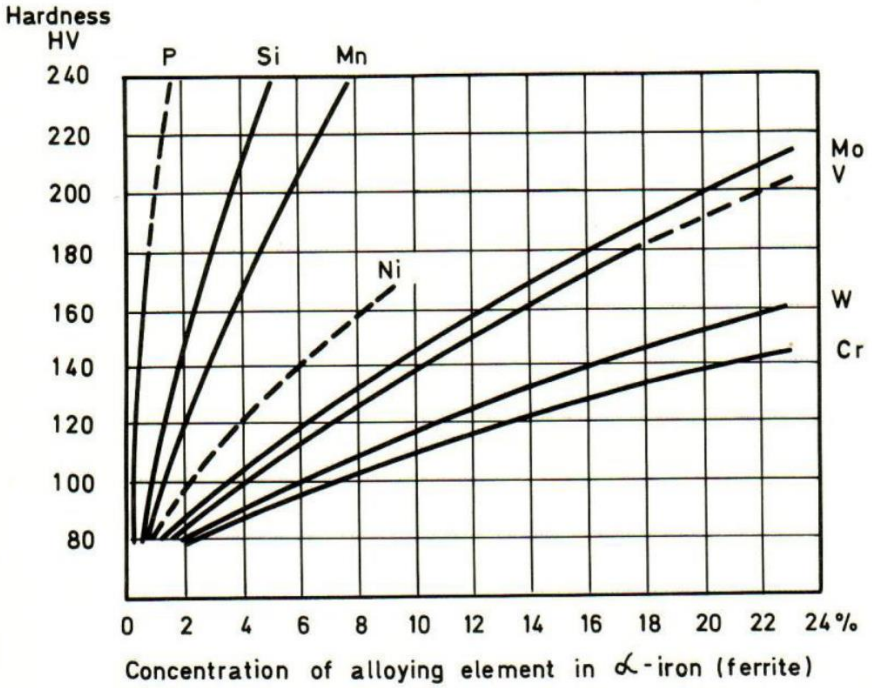

Figure 1-7: The effect of alloying elements on material hardness (Ms) [11] cited in [12].

1.2.3 Phases apparent after tempering

Three main phases are usually formed in alloy steels after tempering: MX, M_2X and $M_{23}C_6$, where M is a metallic element Cr, Fe, W, Mo, Nb or V, and X is a non-metallic element C or N. The typical constituents of each phase as well as the typical characteristics are outlined in Table 1-2. Other phases are documented to exist such as M_3X, M_6X and M_7X_3. However, these phases require a longer tempering process than is typically carried out for the FV566 stainless steel of interest and therefore will not be discussed further.

Phase Structure	M & C constituents	Characteristics
MX	V and Nb	Very small dispersoid particles Precipitates slowly at dislocations in sub grains Dominant at temp > 700 °C Precipitation hardening effect by obstructing dislocation motion
M_2X	Mo, W, Cr and Nb	Small dispersoid particles Precipitates quickly at dislocations in sub grains Dominant at tempering temperature < 700 °C Precipitation hardening effect by obstructing dislocation motion
$M_{23}C_6$	Cr, Mo, Fe and W	Large Particles Precipitates slowly Forms mainly at grain and sub grain boundaries Seen at all tempering temperatures May stabilise martensitic lath boundaries Small precipitation hardening effect They are known as equilibrium carbides due to their stability at lower temperature

Table 1-2: Typical phases seen in 9–12 % Cr martensitic stainless-steel material along with typical composition and characteristics. M elements are typically metallic alloying elements, while X elements are typically Carbon or Nitrogen. Information based upon Soady [10].

1.2.4 Austenitisation on microstructure and mechanical properties

The austenite grain size of two low carbon Cr13 martensitic stainless steels were measured after the steels were subjected to austenitisation temperatures between 900 °C and 1100 °C. The chemical composition of the two materials tested were similar (Table 1-3).

Sample	C	Mn	Si	Cr	Ni	Mo	W	Cu
Wt. % (A)	0.019	0.4	0.16	11.69	4.94	2.04		
Wt. % (B)	0.022	0.41	0.17	11.86	5.14	2.17	1	1.39

Table 1-3: the chemical composition of two similar martensitic stainless steels [13].

Austenitisation temperatures below 1000 °C resulted in a smaller austenite grain size, while temperatures above 1000 °C resulted in a larger austenite grain size. Smaller grain sizes are attributed to enhanced mechanical properties due to increased resistance to dislocation movement. However, the small grain size is attributed to the partial dissolution of carbides and secondary phase particles, the presence of which restricts grain growth. Partial dissolution of carbides is undesirable despite the enhanced mechanical properties. Therefore temperatures greater than 1000 °C (optimally 1050 °C for this material, dependent upon quantity of alloying additions) are desirable to fully dissolve the carbides [13].

Sample	**Austenitisation Temperature (°C)**	**900**	**950**	**1000**	**1050**	**1100**
A	Grain size (µm)	17.4	25.9	27.0	52.0	53.8
B	Grain size (µm)	16.8	26.7	32.1	56.0	56.9

Table 1-4: Grain size in µm with increasing austenitising temperature [13].

Monotonic tensile tests were carried out on three samples by Zhao et al [14] made from AISI420 martensitic stainless steels with austenitising temperatures of 980 °C, 1015 °C and 1050 °C for a holding time of 60 minutes each. After austenitisation, the three samples were subjected to tempering at 200 °C for 60 minutes. Austenitizing at a temperature of 1050 °C, followed by tempering, resulted in a higher ultimate tensile strength. The authors suggest that the increase in ultimate tensile strength is attributed to the dissolution of $M_{23}C_6$ within the matrix, which increased lattice distortion within the martensite. The increase in lattice distortion together with an increase in the number of twin boundaries, increased the resistance to dislocation movement, increasing ultimate tensile strength. Thomson and Bhadeshia [15] found that a prolonged austenitization process of 12Cr1MoV steel resulted in relatively large grain growth and the formation of the δ-ferrite phase, considered undesirable.

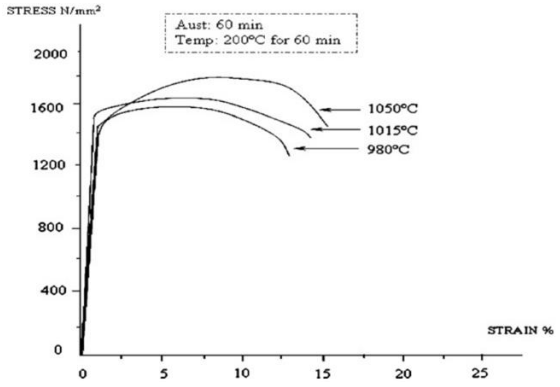

Figure 1-8: Stress versus strain relationships for monotonic tensile tests of AISI420 at various austenitising temperatures, with a 60 minute holding time, followed by tempering at 200 °C with a 60 minute holding time [14].

1.2.5 Effect of tempering on microstructure and mechanical properties

Samples made from 00Cr13Ni4Mo 'supermartensitic' stainless steel (very low carbon content) were austenitised at 1040 °C for 1 hour. Some samples received different tempering heat treatment with varying temperatures between 500 °C to 750 °C held for 3 hours. The retained austenite content percentage peaked at a tempering temperature of 600 °C (Figure 1-9 A) [16] and was therefore considered optimum for this material. Similarly, Liu [13] carried out a very similar set of tests on two similar 00Cr13 'supermartensitic' materials, and investigated the material properties. It is well known that retained austenite is softer, weaker and more ductile than martensite. Therefore, as the retained austenite percentage initially increases with tempering temperature, the materials hardness and strength decrease, while ductility (elongation) increases (Figure 1-9 B and C). A relationship also seen in FV566 material [17].

A

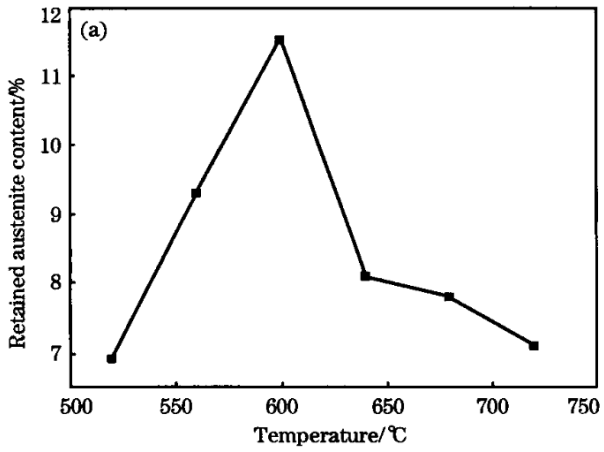

B

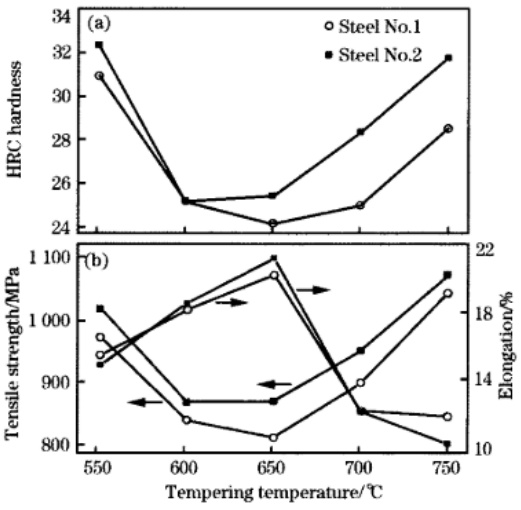

C

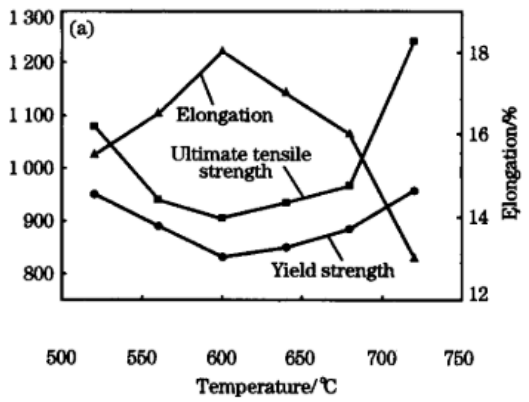

Figure 1-9: A) Retained austenite content % in 00Cr13Ni4Mo after tempering at various holding times at 600 °C [16]. B) The interaction between various mechanical properties of two Cr13 supermartensitic stainless steels at various tempering temperatures by [13] and C) by [16].

Since the optimum tempering temperature of 600 °C was found for 00Cr13Ni4Mo, additional samples received were tempered at the optimum temperature with various holding times from 2 hours to 12 hours [16]. As holding time was increased, the percentage of retained austenite content increased with a characteristic elongated grain structure (Figure 1-10) towards an asymptotic saturation point (Figure 1-11 A). The reduction in hardness (Hardness Rockwell C HRC) and increase in ductility (elongation) are once again attributed to the increase in retained austenite content (Figure 1-11 B). Very similar observations were seen in a similar 'supermartensitic' stainless steels [13] and FV566 martensitic stainless steel materials [17].

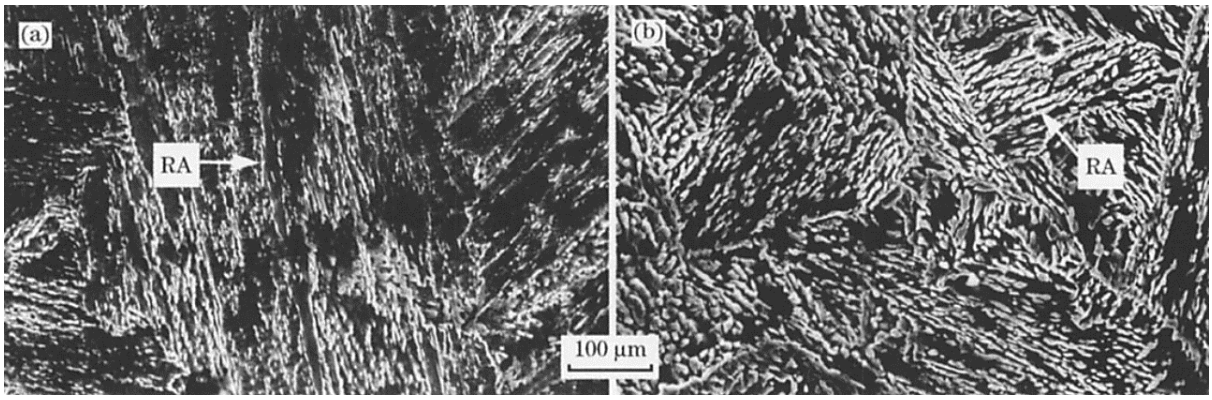

Figure 1-10: The microstructures after etching of 00Cr13Ni4Mo after tempering at 600 °C and after holding times of (a) 6h and (b) 12h [16].

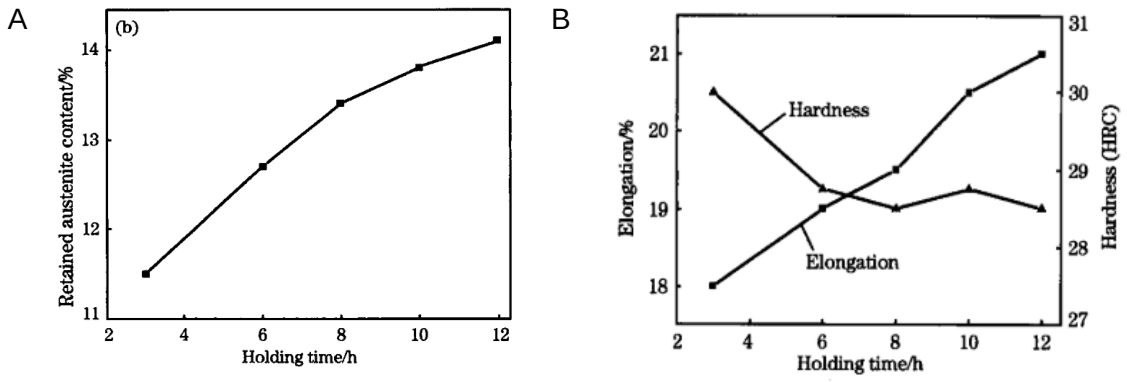

Figure 1-11: A) Retained austenite content % in 00Cr13Ni4Mo after tempering at various holding times at 600 °C [16]. B) Elongation and hardness of 00Cr13Ni4Mo samples after tempering at various holding times [16].

Zhao [14] carried out a similar investigation into the effects of tempering temperature on HRC hardness, yield strength and ultimate tensile strength on AISI420 martensitic stainless steel after austenitisation at 1050 °C for 1hr. As tempering temperature increased, the hardness, yield strength and ultimate tensile strength initially decreased. However, contrary to the findings of Zou et al [16], a small increase was seen around 500 °C (Figure 1-12). The authors speculated that the increase in strength was due to a secondary hardening phenomenon associated with the formation of M_7C_3 carbides (not seen in 00Cr13Ni4Mo due to the lack of sufficient carbon content). At tempering temperatures above 500 °C, a rapid decrease in hardness, yield and ultimate tensile strengths was observed (Figure 1-12). The authors noted a coarsening and partial transformation of M_7C_3 to $M_{23}C_6$, which was attributed to the reduction in hardness and strength. This continuing reduction in the hardness and strength properties at higher tempering temperatures was not observed in Zou et al [16], although the authors acknowledge that such behaviour was expected. The composition of alloying elements, and their influence on the formation of secondary phases, can have an impact on the mechanical properties observed in the material after various tempering temperatures.

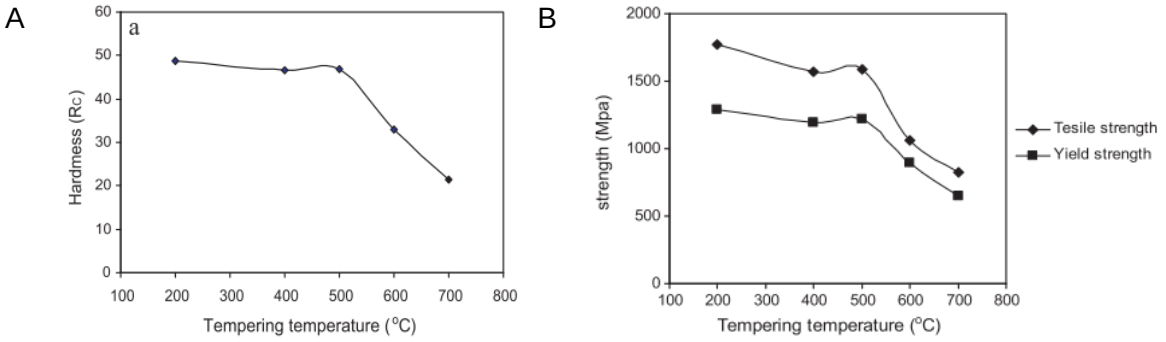

Figure 1-12: A) Effect of tempering temperature on HRC and B) yield and ultimate strengths, for AISI420 martensitic stainless steel [14].

1.2.6 Heat treatment effect on fatigue life

The effect of heat treatment on FV520B fatigue life was explored by Fan et al [18] and Guo et al [19]. Three relatively similar FV520B samples were fatigue tested under reversed loading conditions (R-ratio of -1) on a flat dog bone specimen. Only the heat treatment processes differed and subsequently the yield and ultimate tensile strengths (Table 1-5). FV520B samples subjected to heat treatments, resulted in a higher yield and ultimate tensile strength, and became more brittle [18].

FV520B	Source	Heat Treatment	Yield Strength 0.2 % (MPa)	UTS (MPa)
Type A	[18]	As-Received	880	1050
Type B	[18]	1050 °C (2 hr) 850 °C (2 hr) 480 °C (2.5 hr)	1080	1300
Type C	[19]	1050 °C (1 hr) 850 °C (2 hr) 480 °C (3 hr)	1095	1340

Table 1-5 Three samples of FV520B from two sources were subjected to different heat treatments, which subsequently resulted in different yield and ultimate tensile strengths (UTS).

The resistance to fatigue increased with increasing yield and ultimate tensile strength. The higher strength of material inhibited crack initiation, resulting in longer overall lifetimes (Figure 1-13). Since most of the tests were carried out in the high cycle fatigue regime, crack initiation behaviour becomes more important, in the low cycle fatigue regime, the fatigue lifetimes were similar. Clark [20] carried out a similar set of tests on FV520B. A heat treatment similar to type B was carried out with the slightly lower aging temperature of 450 °C, held for a longer period of 4 hours. A major substantial difference was the geometry of the specimen. A cylindrical dog-bone specimen was used as opposed to the flat dog bone specimens in Table 1-5. The cylindrical geometry of the specimen was more resistant to fatigue than the flat geometry. A much higher stress limit of 500 – 640 MPa was observed as opposed to the 275 – 360 MPa observed in Types A to C. Crack initiation appeared to favour the corner of flat dog-bone specimens, which acted as stress concentration sites, reducing the specimen's resistance to crack initiation. Whereas the cylindrical dog-bone geometry did not contain such stress concentration sites. These results highlight the importance of sample geometry to the sensitivity of fatigue life, especially in high cycle fatigue regime where initiation behaviour strongly influences fatigue lifetimes.

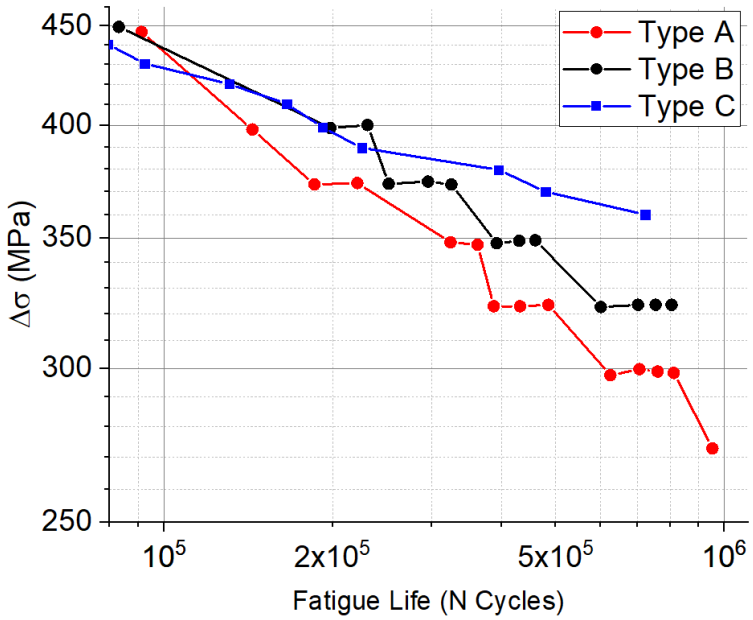

Figure 1-13: Stress range versus fatigue life for three flat dog-bone specimens made from FV520B with various heat treatments and mechanical strength properties outlined in Table 1-5 [18, 19].

It is reasonable to assume that the martensitic stainless steels provided for this thesis, have been subjected to near optimum austenitisation and tempering temperatures, according to their corresponding manufacturing standards.

1.2.7 Material property response to cyclic loading

During strain-controlled cyclic loading of ductile steel materials, the load required to achieve the desired maximum strain initially rapidly decreases due to high dislocation movement activity. After this ‘shakedown’ period, the required load either increases known as cyclic hardening (Figure 1-14 A) or decreases known as cyclic softening (Figure 1-14 B).

Cyclic hardening behaviour is characterised by an increasing load requirement to maintain constant strain amplitude due to dislocation ‘pile-up’ and dislocation-precipitate interactions (inhibiting dislocation movement) until a plateau is reached. After plateau, the material no longer displays any hardening or softening behaviour. After the onset of crack initiation followed by crack propagation, the test specimen becomes more compliant and the required load to maintain constant strain range decreases rapidly to failure (Figure 1-14 A).

Materials such as tempered martensitic stainless steels display cyclic softening behaviour under strain-controlled cyclic loading conditions [21-23]. Cyclic softening behaviour is characterised by a decreasing load requirement to maintain constant strain amplitude. In these materials, the dislocation movement energy is strong enough to destroy precipitates

by shearing, thereby no longer providing a barrier to dislocation movement. A quasi-plateau is realised where a reduced softening behaviour is observed. The specimen becomes more compliant with the onset of crack initiation resulting in a dramatic reduction in the required load to maintain constant strain amplitude, followed by failure (Figure 1-14 B).

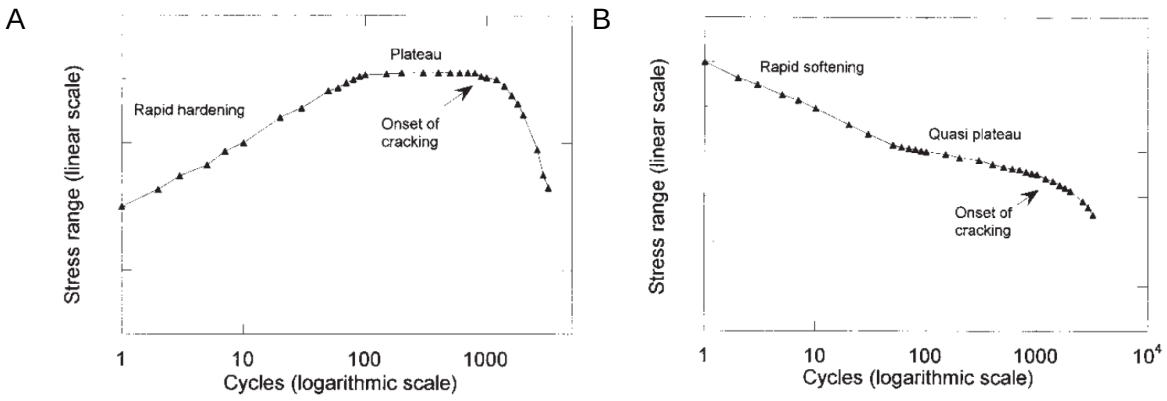

Figure 1-14 A) A typical example of strain hardening and B) strain softening material response under constant strain amplitude loading conditions from [24].

1.3 Project Plan

1.3.1 Industrial motivation

Turbine blades are subject to routine inspections where they are expected to meet health and safety standards. The original equipment manufacturer (OEM) previously recommended that inspections every 3500 start-stop-cycles cycles should be carried out approximately every 12 years. An inspection such as this can take as long as 12 weeks and result in financial loss of millions of pounds. A yearly 10 % overload test is carried out once per year or approximately every 150 cycles. The turbine is switched on and run at 110 % of its nominal daily capacity at which point it is switched off.

The generation of energy from fossil fuels releases carbon dioxide that has been stored for millions of years back into the atmosphere. There has been growing pressure towards cleaner energy sources such as renewables energy that are inherently less reliable. As renewable energy sources become more popular, more reliable energy sources such as CCGT plants must adopt more flexible operating procedures to account for the increased frequency of variability in demand. A single shift approach where turbines are switched on and off to cope with shortfalls in energy have been adopted in many power plants. It is predicted that a ‘double stage two shift’ approach is likely to be adopted in the near future whereby the turbine blades will be subjected to two start-stop cycles per day [25]. The prospect of increasing the frequency of start-stop cycles and observation of cracks has led

to the OEM recommending a reduction on the number of start-stop cycles per inspection to 1650 cycles. Consequently, energy companies are expected to carry out expensive inspections more frequently, resulting in a full blade inspection potentially being required every 2-3 years further increasing costs.

During routine inspections, short cracks at least 1 mm in length have been observed by non-destructive testing (NDT) in the fir-tree-root-fillets of in-service turbine blades (personal communication, EDF, 2018). Due to the lack of understanding of fatigue within the notched components, energy companies are adopting a conservative approach and replacing blades with cracks in the fir-tree-root-fillets before their expected service life regardless of remaining operational life at a high cost.

There is industrial motivation to increase the service life of the blades that are currently in operation. One method is to improve the understanding of the fatigue behaviour of blades in service to allow the development of a lifetime prediction model. More specifically, a more comprehensive understanding of the crack initiation and surface cracks (short cracks) on the notch surface could lead to a “largest safe crack size” potentially increasing the service life. Another method could be to introduce a lifetime extension strategy such as grinding away existing cracks followed by a fatigue enhancement surface modification process such as shot peening (Figure 1-15). It is not clear whether a lifetime strategy such as this is beneficial or detrimental to fatigue life due to many competing factors Figure 1-16. The work comprised in this thesis focuses on the development of these ideas to help energy companies reduce costs.

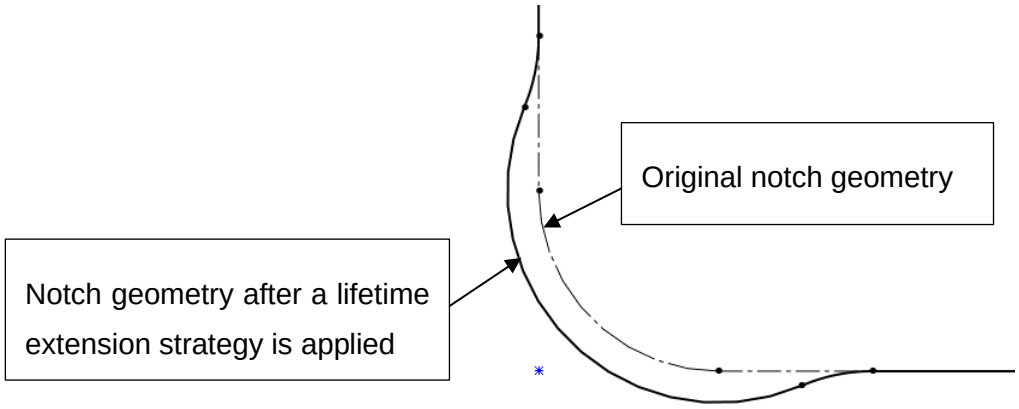

Figure 1-15 A representation of a typical fillet geometry such as the fir-tree-root-fillet geometry from a turbine blade. The dotted line shows the original notch geometry. The continuous black line shows a typical notch geometry after a lifetime extension strategy is applied, such as grinding existing cracks followed by shot peening.

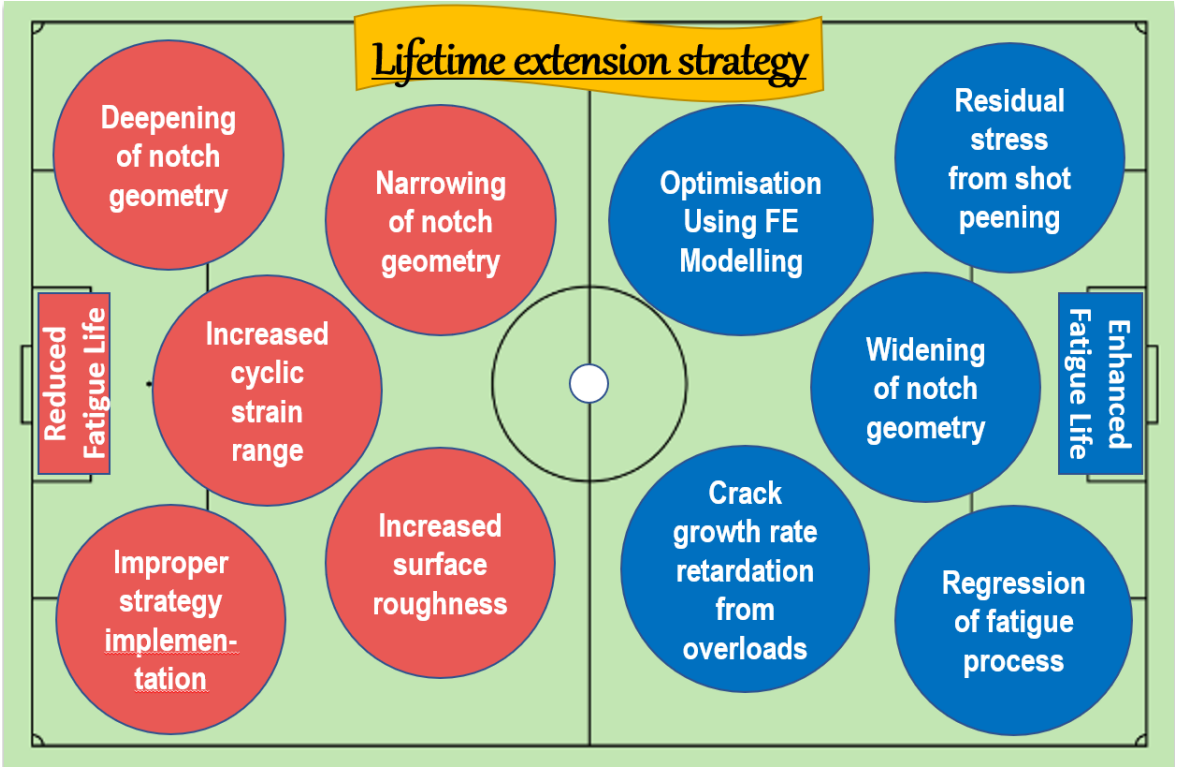

Figure 1-16 The proposed lifetime extension strategy involving grinding out existing cracks followed by shot peening results in several competing alterations both beneficial for fatigue (blue side) and detrimental to fatigue (pink side).

1.3.2 Research Question

Based upon the industrial motivation, the subsequent requirement for an advancement in knowledge, and a development of an appropriate lifetime extension strategy, an overall research question was conceived:

> *"How is crack initiation and growth in a typical notch geometry affected by a surface mitigation approach such as grinding out existing cracks, followed by shot peening and the typical loading patterns seen in service including minor overloads?"*

1.3.3 Project scope and thesis structure

The overall research question is complex; this question is best approached by dividing the questions into manageable tasks and subtasks. A review of current knowledge is presented in Chapters 1 and 2, while the main bulk of the experimental work is presented in Chapters 3 to 6. The final concluding remarks and recommendations for industry and future work are presented in Chapters 7 and 8.

A detailed project scope and the thesis structure are outlined below and further illustrated in Figure 1-17:

1. Introduce the project (Chapter 1):
    - Explain what turbine blades are, their geometry, how they are assembled, what they are for and what they are made from.
    - Introduce the industrial motivation for this project.
    - Project scope and thesis structure. How do we answer the overall research question?
    - Briefly introduce the turbine blade material, how it is made and how the formation process can affect its material properties.
2. Literature review (Chapter 2):
    - Introduce and provide up to date information on the key topics and tools that are used to answer the overall research question.
    - Fatigue behaviour in metals and lifetime prediction approaches.
    - Explain how introducing a U-notch may affect the fatigue behaviour based on previous research.
    - Investigate what is known about the effects of overloads on fatigue behaviour in steel materials.
    - What is known about notch geometry effects on fatigue behaviour?
    - A review of the literature on shot peening procedures and effects on fatigue.
3. Material characterisation and Finite Element model development (Chapter 3):
    - Investigate the baseline microstructural, mechanical and fatigue properties of ex-service FV566 martensitic stainless steel blade material.
    - How do the properties of FV566 compare with known similar turbine blade materials such as FV448 and FV520B?
    - Develop a finite element model that is based upon the baseline material properties. A tool to be used to investigate and estimate the stress and strain on the surfaces of various U-notch geometries during cyclic loading.
4. Fatigue life-cycle in U-notch geometry and overload effects on fatigue behaviour and life-cycle (Chapter 4):
    - Carry out initial fatigue tests under constant amplitude loading conditions and establish the life-cycle of U-notched bend bar samples made from FV566.
    - Understand the effect of changing the strain range on fatigue behaviour.
    - Introduce overload cycles of varying magnitude to explore the effect of overloads on fatigue and life-cycle behaviour.
5. Changing the notch geometry (from grinding out existing cracks) - effect on fatigue and life-cycle behaviour (Chapter 5):

- Develop and validate a finite element model to estimate the stress and strain distribution within the notch field to investigate the possible effects of altering the notch geometry on fatigue behaviour.
- Carry out experimental testing on U-notch samples with constant surface conditions and various relevant geometries expected after grinding out existing cracks. Followed by an investigation into the effects of changing notch geometry on fatigue and life-cycle behaviour.

6. Shot peen the U-notch surface and investigate the effects of shot peening on fatigue and life-cycle behaviour (Chapter 5):
   - Apply shot peening to U-notch samples with original and modified U-notch geometries (from grinding out existing cracks) made from FV566.
   - Measure, after shot peening, the surface roughness on the notch surface and compressive residual stress profile and within the notch field.
   - Carry out experimental testing of shot peened U-notch samples to understand the effect of shot peening on the fatigue and life-cycle behaviour.
7. Develop a prediction model capable of estimating the improvement of fatigue and service life of turbine blades following the lifetime extension strategy (Chapter 6):
   - Split the fatigue life-cycle of U-notched samples into separate phases that can be independently evaluated, so that the number of cycles to grow a surface crack to a specific length can be predicted.
   - Develop a total life model that can predict the total fatigue life of both non-shot peened and shot peened U-notch samples.
   - Combine both prediction models to create a lifetime prediction model capable of estimating the number of cycles to total failure for a U-notch sample that has been subjected to the proposed lifetime extension strategy.
   - Carry out experimental testing on U-notch samples subjected to the lifetime extension strategy under both constant amplitude and with overload cycles, and compare the experimental lifetimes with lifetime predictions.
8. Summary of the experimental work and analysis of data in this thesis, and formation of overall conclusions (Chapter 7).
9. Recommendations to industry and future work (Chapter 8):
   - Based upon the findings in this thesis, what recommendations can be made to industry to improve the service life of existing turbine blades?
   - What work is currently being carried out in parallel research studies at the University of Southampton?
   - What further work could be beneficial in the future to progress the development of an industrial solution?

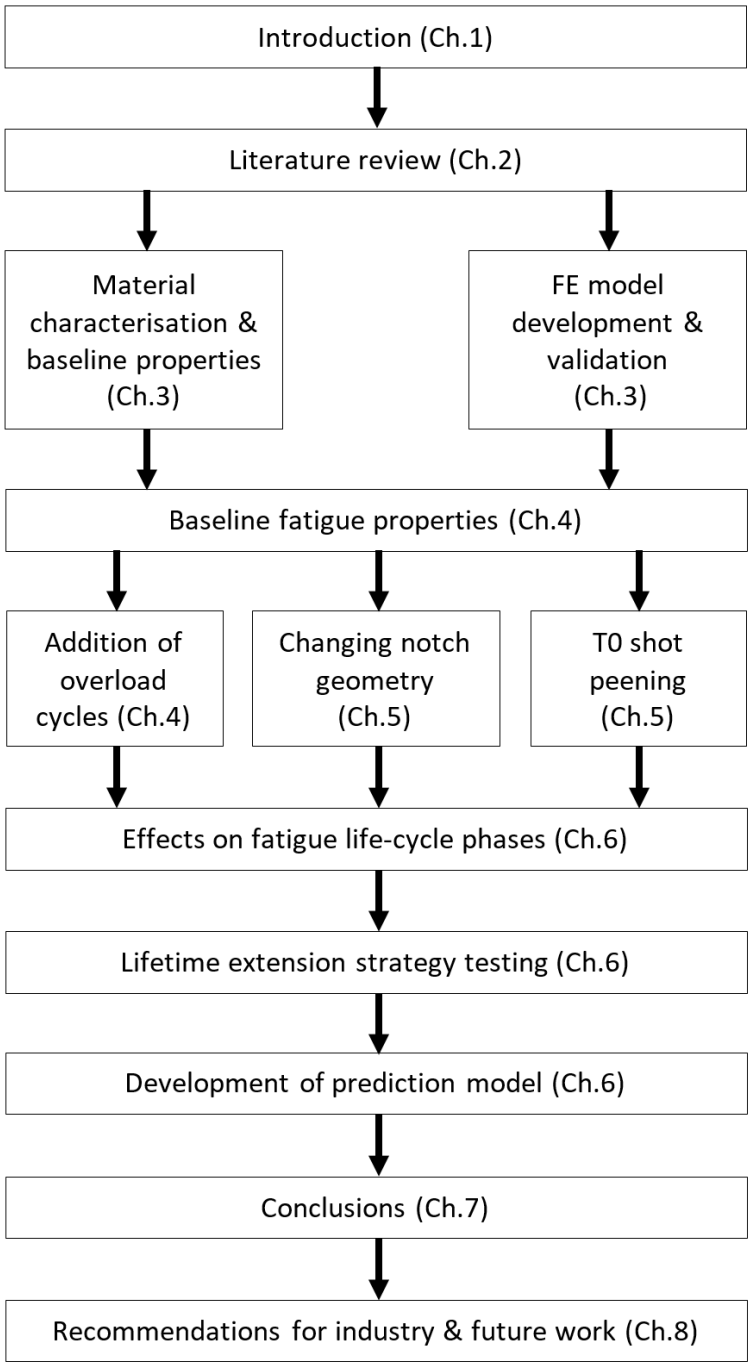

Figure 1-17: Flow chart of modelling and experimental work, and thesis structure.

Chapter 2: Literature Review

2.1 Fatigue behaviour and prediction of metallic materials

2.1.1 Introduction and definition of fatigue

Suresh [26] defines fatigue as 'changes in properties which can occur in a material due to the repeated application of stresses and strains'. Materials such as metals undergo progressive damage with the application of cyclic loading, leading to the eventual failure of the material. The process of the progression towards failure by fatigue is of interest to engineers and scientists who strive to improve identification, mitigation and ultimately the prevention of the process. If the minimum and maximum cyclic values of constant cyclic fatigue loading are known, the magnitude of the applied fatigue can be described in terms of mean cyclic value, the amplitude (half the cyclic range) of the cyclic value and the R-ratio (Figure 2-1 and Equation 2-1 to Equation 2-4). (Such cyclic values can be defined as Load, Stress, Strain or Stress intensity factor (K) discussed later in Chapter 2.1.4).

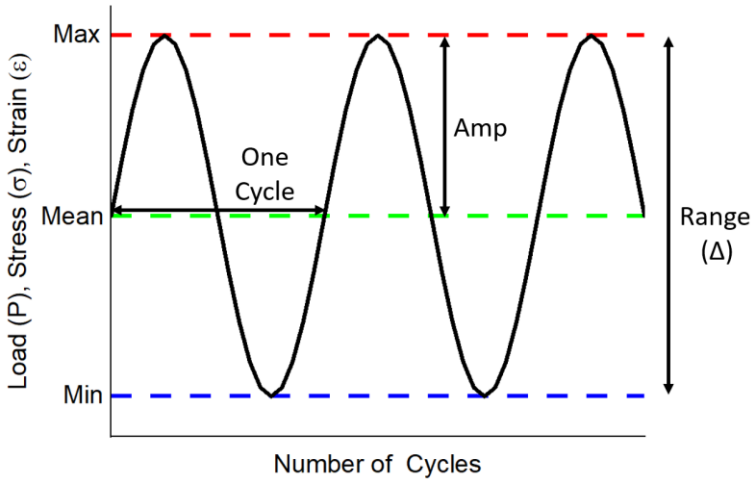

Figure 2-1: A schematic to show the maximum, mean and minimum values of constant amplitude cyclic loading conditions. The values can be Load (P), Stress, Strain or Stress intensity factor (K) discussed later in this chapter.

Mean $$Mean = \frac{Max + Min}{2}$$ Equation 2-1

Amplitude $$Ampltidue = \frac{Max - Min}{2}$$ Equation 2-2

Range $$Range\ (\Delta) = Max - Min$$ Equation 2-3

R-Ratio $$R = \frac{Min}{Max}$$ Equation 2-4

When the magnitude of the nominal maximum cyclic load is less than the material's yield strength, the fatigue behaviour and lifetime can be predicted from the applied stress range, known as the high cycle fatigue regime (HCF). For martensitic stainless steel materials, fatigue failure typically occurs after 100 000 cycles in the high cycle fatigue regime. When the magnitude of the nominal maximum cyclic load exceeds the material's yield strength, the fatigue behaviour and lifetime prediction must incorporate the strain range due to material plasticity. This is known as the low cycle fatigue regime (LCF), where fatigue failure generally occurs below 100 000 cycles. The majority of testing in this thesis is within the low cycle fatigue regime as this is closest to the service condition.

While other failure mechanisms such as creep and fretting fatigue can be a major contributing factor in the lifetimes of turbine blades [27], the work in this thesis will focus solely on cyclic loading and fatigue performance at low temperatures.

Throughout the literature review, fatigue testing has been carried out by many authors at various testing frequencies. Several fatigue experiments have been carried out to test the effect of cyclic frequency on fatigue behaviour from 1 Hz to 20 KHz. Cyclic frequency is known to influence fatigue life and behaviour of metallic materials exposed to high temperatures or corrosive environments. However, cyclic frequency did not significantly affect the fatigue life of metallic materials when tested in ambient conditions [28].

2.1.2 The fatigue life-cycle

The fatigue life-cycle typical of a component in tensile loading conditions with a finite width and depth (such as a plain bend bar primarily used in this thesis) can be characterised by broadly classifying the progression of fatigue into four main phases [26]:

1. Crack initiation
    - Sub-structural and microstructural changes occur within the material that cause permanent damage.
    - Microscopic cracks are created due to irreversible progress of permanent damage on the surface that are observable with use of microscopic equipment.
2. Crack propagation of short cracks
    - Microscopic flaws progressively grow in size and become short cracks.
    - Stable propagation of the macro-crack (known as short crack growth).
3. Crack coalescence

- Two or more stable macro-cracks grow towards and join each other.
- A dominant crack of unequalled size grows via propagation and coalescence until the crack length spans the width of the component, known as the main or primary crack.

4. Crack propagation of the main crack
    - The main crack grows in the depth direction (known as long crack growth) until structural instability or complete fracture occurs.

The effect of cyclic loading on each of the four phases of crack initiation, short crack propagation, crack coalescence and long crack propagation will be discussed in the following chapters.

2.1.3 Crack initiation behaviour

The surface condition of most components in industry will contain defects that act as stress concentration features. Crack nucleation will likely occur at surface defects such as inclusions, voids (such as corrosion pits), scratches caused by machining marks and other micro or macroscopic features. Initiation can occur below the free surface in martensitic stainless steel materials such as FV520B, especially under high cycle fatigue conditions [29], but has been seen in FV448 under low cycle conditions due to modification of the surface [5]. Defects such as these are likely to encourage crack nucleation and growth over fewer cycles than a ‘defect free’ surface regardless of loading conditions.

Microscopic flaws can develop as a result of cyclic loading on a defect-free, highly polished surface with no stress concentration features. Repeated cyclic straining of the material causes irreversible dislocation movement and shear displacement known as slip along preferentially oriented planes. Slip causes protrusions consisting of intrusions and extrusions at the free surface (Figure 2-2 A), leading to increased roughening of the surface. The intrusions act as ‘micro-notches’ acting as stress raisers ultimately leading to crack nucleation (Figure 2-2 B). Lines of slip within which cracks nucleate are known as persistent slip bands (PSBs) (Figure 2-2 C).

A

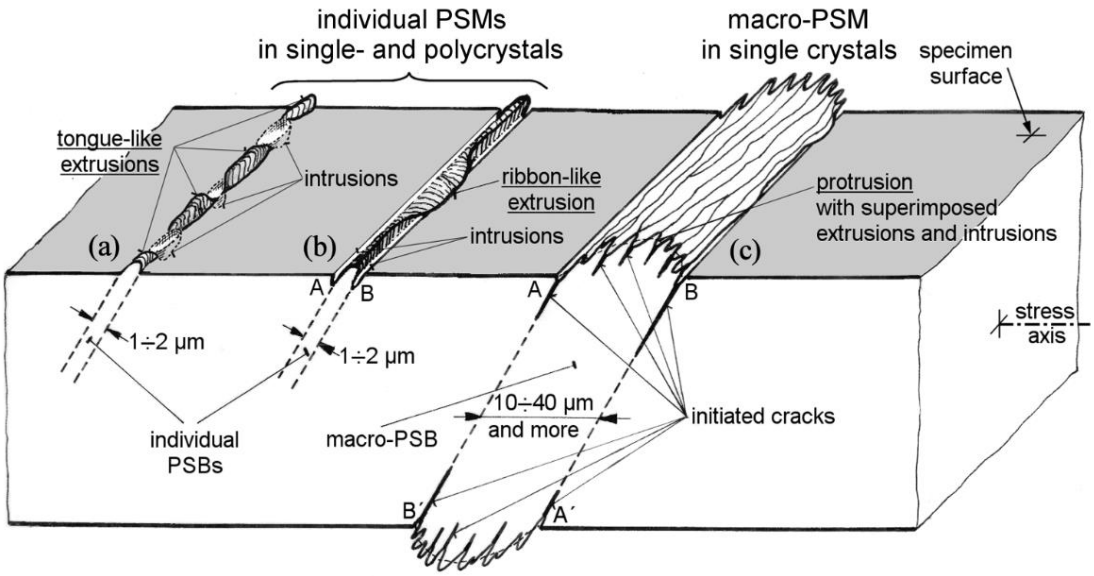

B

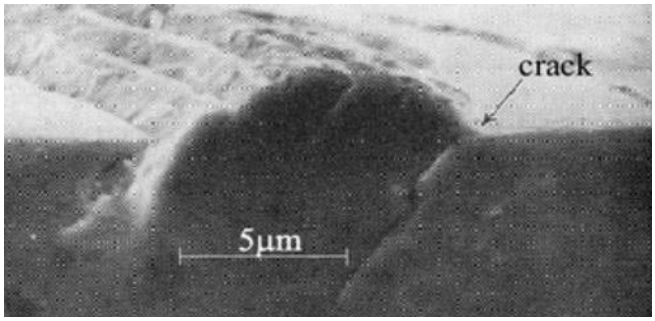

C

Figure 2-2: A) Schematic diagram of three characteristic forms of mature PSB the most common of which found in stainless steels are macro-PSB spanning the cross section of a single crystal taken from [30]. B) Persistent slip band formation taken from [26]. C) Protrusions seen on the surface within grain boundaries of an austenitic stainless steel taken from [31].

Slip band formation has been observed using atomic force microscopy and scanning electron microscopy in 316L austenitic stainless steels [30, 32-34] Slip bands tended to reveal themselves as ribbon-like surface reliefs similar to Figure 2-2 C and Figure 2-3. Extrusions were found in most cases with only a handful of intrusions that were generally either side of the extrusions. From a material science perspective, crack initiation occurs at the microstructural level from protrusions. This definition is not practical from an industrial perspective, since non-destructive testing (NDT) can only identify fatigue cracks once they have grown to 0.5 – 1 mm in length [4]. The techniques used in this project allow crack

initiation to be identified as ‘the nucleation of micrometre-sized flaws’ as short as 20 µm [26].

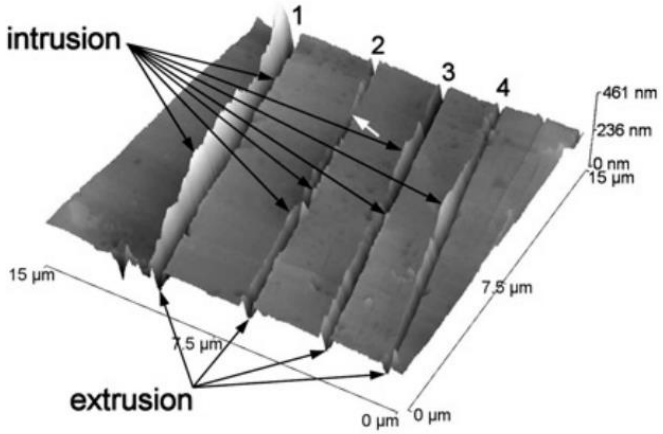

Figure 2-3 Early stages of crack initiation within a grain of 316L steel obtained using atomic force microscopy (AFM) on plastic surface replicas [35].

2.1.4 Fatigue crack propagation of long and short cracks

The application of cyclic loading produces the ‘driving force’ for crack propagation and can occur in three ways. The tensile opening mode I (Figure 2-4 A) is the most common and best describes the application of fatigue loading conditions for the tests carried out in this thesis. The other two modes are shearing modes (Figure 2-4 B and C).

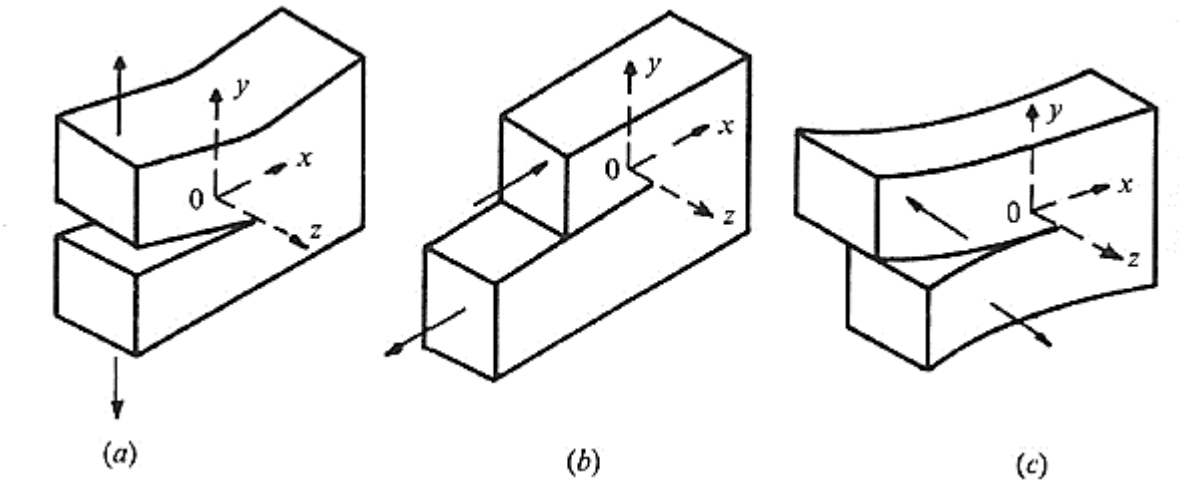

Figure 2-4: The three fundamental modes of fatigue crack driving force with a) Mode I - tensile opening, b) Mode II – In-plane sliding, c) Mode III - Anti-plane shear) taken from [26].

The magnitude of the driving force is commonly referred to as the stress intensity factor range (*ΔK*) and is related to the rate of crack propagation, which is commonly used to describe crack growth behaviour. Griffith [36] and Westergaard (1939) as cited in [26] developed the widely used linear elastic fracture mechanics (LEFM) method for calculating the stress intensity factor range for mode I opening (Equation 2-5):

$$\Delta K_I = f\left(\frac{a}{W}\right)\Delta\sigma\sqrt{\pi a} \qquad \text{Equation 2-5}$$

where $\Delta K_I = K_{Imax} - K_{Imin}$, $f\left(\frac{a}{W}\right)$ is the geometry correction factor as a function of the crack length a and the sample depth W, and $\Delta\sigma$ is the cyclic stress range. Equation 2-5 can be used to quantify the 'crack driving force' for both long cracks (Appendix A) and short cracks (Appendix C). Linear elastic fracture mechanics assumes no plasticity of material at the crack tip, resulting in infinite stress applied to an infinitely sharp crack tip. In reality, material plasticity effects will result in a finite crack tip radius and subsequent redistribution of stress around the crack tip. The radius of the plastic zone size around the crack tip under plane strain can be approximated using Irwin's approach for plain strain (Equation 2-6):

$$r_p = \frac{1}{3\pi}\left(\frac{K_I}{\sigma_y}\right)^2 \qquad \text{Equation 2-6}$$

where r_p is the radius of the plastic zone and σ_y is the yield strength of the material. LEFM does not adequately describe crack growth behaviour in the case of large scale yielding, a typical occurrence in short cracks. In such cases, elastic plastic fracture mechanics (EPFM) approaches can be adopted to account for non-linear material behaviour.

The J-integral is the energy release rate (with respect to crack advance) for non-linear elastic-plastic material behaviour, which represents the rate of change in potential energy, found by taking the line integral along any contour around the crack tip [37]. The crack tip opening displacement (CTOD) is the distance between the two crack faces (δ_t) as in (Figure 2-5) and can provide some quantification as to the amount of plastic deformation that has occurred at the crack tip [38].

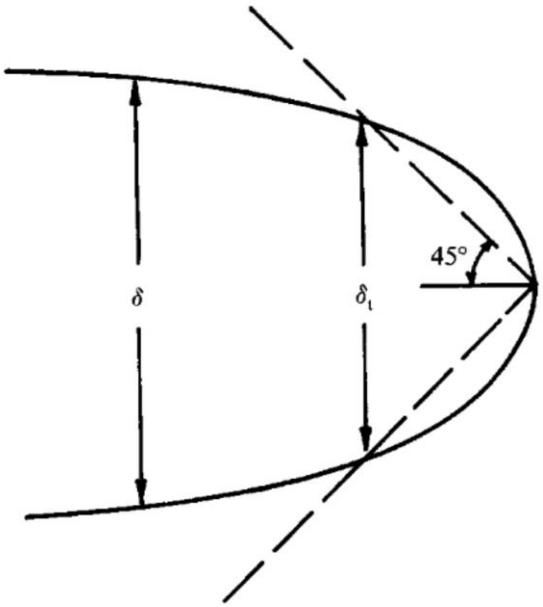

Figure 2-5: Schematic showing the definition of crack tip opening displacement (δ_t) from [26].

In cases where the crack-tip yielding is sufficiently limited (small scale yielding), the stress intensity factor still provides a good description of the overall crack tip stress state at the crack tip and can be used to define the crack growth driving force. Under elastic conditions, the J-integral (J) can be expressed as the energy release rate based upon linear assumptions ($\mathcal{G}$), and can be related to the stress intensity factor (Equation 2-7), as can the crack tip opening displacement (Equation 2-8):

$$J = \int_{\Gamma} \left(wds - \mathrm{T}\frac{\partial u}{\partial x} ds \right) \equiv \mathcal{G} = \frac{{K_I}^2}{E} (Assuming\ LEFM) \qquad \text{Equation 2-7}$$

$$\delta_t = \frac{{K_I}^2}{\sigma_y E} \qquad \text{Equation 2-8}$$

where w is the applied work, ds is a small contour line length, T is the traction vector, δ_t is the crack tip opening displacement and *E* is the Young's Modulus of the material.

Long crack growth typically refers to crack growth data obtained from samples with a pre-existing through-thickness crack where crack growth rate data is monitored as a function of *ΔK*. The typical relationship between long crack growth rate and stress intensity factor range (*ΔK*) is shown in Figure 2-6 A) where three regimes of long crack propagation exist.

Stage I crack growth (regime A in Figure 2-6 A) typically associated with near threshold (ΔK_{th}) and low *ΔK* values when the crack tip plasticity zone size is smaller than the grain

size of the material. Stage I crack growth behaviour is highly dependent upon local microstructure and can be observed in both long and short cracks. The propagation mechanism of crack growth in the stage I regime occurs by shear de-cohesion along pre-existing slip bands and preferentially aligned slip planes, which extends across several grains and transfers to stage II crack growth. In long crack samples, this regime is often evaluated by careful load-shedding practices to identify the $\Delta K_{Threshold}$ (below which no crack advance is seen). The crack growth modes observed are sometimes referred to as quasi-Stage I as they often show features similar to the early stages of crack growth in a naturally initiating crack, but in a long crack test, the actual da/dN values observed are linked to the prior crack path history (including closure effects). The low ΔK values of short cracks are often seen to have faster growth rates than longer cracks due to the greater influence from the limitations of linear elastic fracture mechanics assumptions on short cracks as well as the lack of closure [26].

Stage II crack growth (regime B in Figure 2-6 A) is typically observed at higher ΔK levels, where the crack has grown across multiple grains, and becomes less dependent upon microstructure (Figure 2-6 B). Stage II crack growth tends to grow perpendicular to the direction of longitudinal tensile stress and is observably less tortuous than stage I crack growth. The relationship between crack growth rate and ΔK follows a power law relationship and can therefore be modelled with the Paris-law fit (Chapter 2.4.3). Striations can sometimes be observed using scanning electron microscopy (SEM) equipment on the fracture surface due to repeated opening and blunting of the crack tip followed by closing and re-sharpening [39] (Figure 2-6 C), described by the Laird-smith model of crack propagation [40]. The transition from stage I to stage II crack growth behaviour can occasionally be observed directly [41] (Figure 2-6 B).

In stage III crack growth (regime C in Figure 2-6 A), the crack growth rate increases rapidly due to monotonic bursts of plastic failure at higher ΔK values near the end of fatigue life and is sometimes characterised by beachmarks on the fracture surface [42].

Observations of the fracture surfaces of FV566 as a result of stage II and stage III long crack propagation indicates a mixture of transgranular and intergranular crack growth (Figure 2-6 D) [43] and quasi-cleavage fracture (a combination of dimple rupture and cleavage) (Figure 2-6 E) [14, 44].

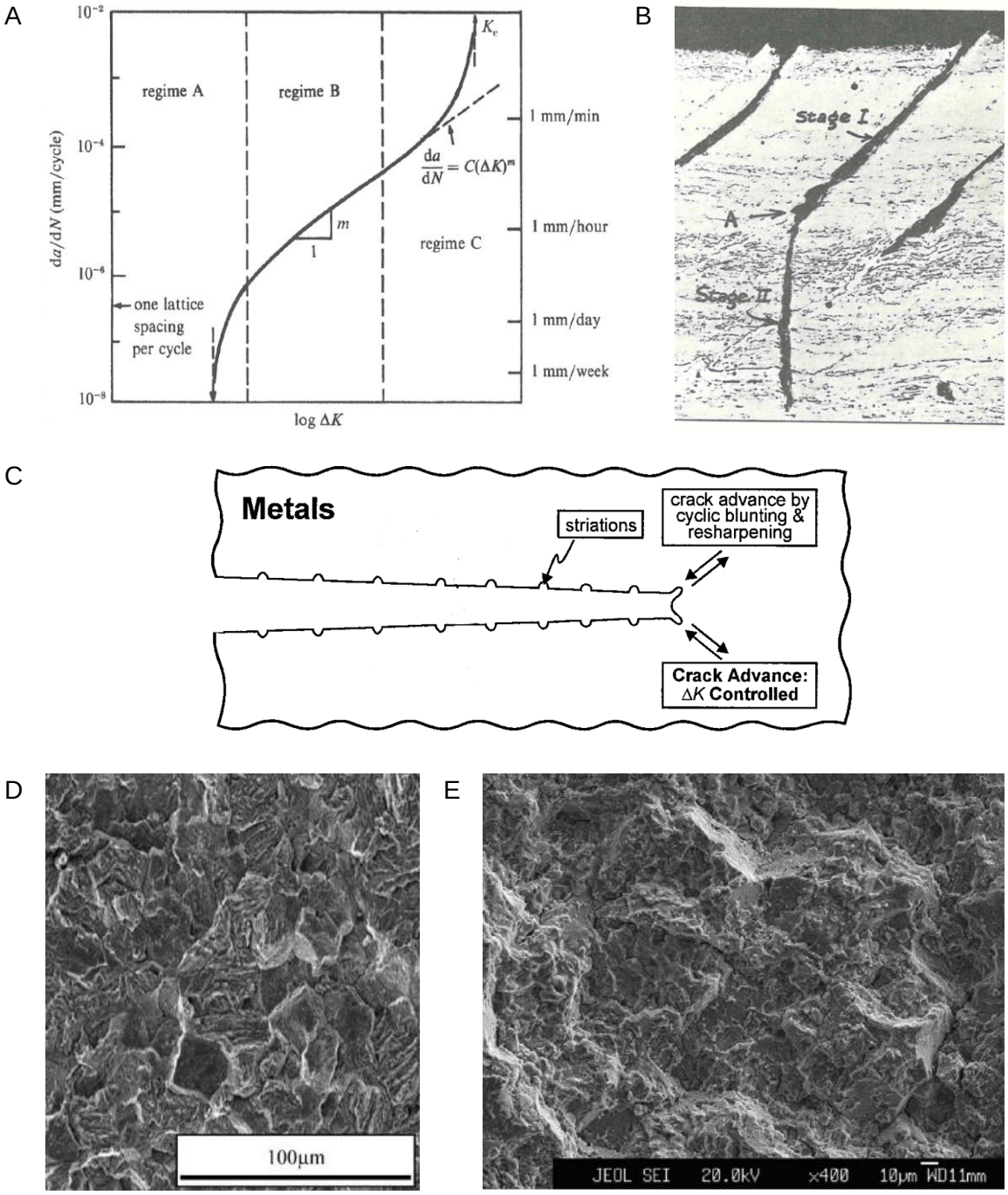

Figure 2-6: A) Log *ΔK* versus crack growth rate illustrating the three regimes of typical long crack growth taken from [26]. (Regime A is also known as stage I, regime B is also known as stage II and regime C is also known as stage III). B) Stage I and stage II crack propagation in pure aluminium magnification x 200 taken from [41]. C) Schematic illustration of crack advancement in a ductile metal showing striations due to periodic blunting and re-sharpening of the crack tip [39]. D) and E) Fracture surfaces of FV566 martensitic stainless steel indicating a combination of intergranular and transgranular quasi-cleavage fracture [43] and [44].

Immediately after crack initiation, cracks grow both along the top surface (perpendicular to the tensile axis) and in the depth direction, producing a semi-elliptical fatigue surface characteristic of short crack propagation. Four types of short crack exist in metallic materials from [26] depending on the length of the short crack, size of microstructural features and the ambient conditions:

1. 'Microstructurally small cracks':- After initiation, short crack growth begins with microstructurally short cracks that are smaller than the grain size of the material. The crack growth rates of microstructurally short cracks are affected by microstructural features such as grain boundaries, inclusions and precipitates that act as barriers to crack growth, in some cases arresting for temporary periods before propagating again [45]. Additionally, microstructurally short cracks tend to grow along slip bands. The accumulation of these influencing factors produces crack growth behaviour that is typically intergranular and tortuous in nature.
2. 'Mechanically short cracks' have a surface length comparable to the near tip plasticity zone size. These cracks are generally larger than microstructurally short cracks and are less influenced by the material's microstructure. Both microstructurally and mechanically short cracks are known to propagate at a higher rate than long cracks at similar low ΔK levels for most metallic materials under linear-elastic fracture mechanics assumptions, and is known as the short crack problem [46, 47] (Figure 2-7). The increase in the growth rate of these short cracks is attributed to propagation mechanisms such as growing along slip bands and also to the simplification and limitations of the linear-elastic fracture mechanics approaches. The application of elastic-plastic fracture mechanics approaches have been found to produce results akin to long crack growth behaviour [48, 49].
3. 'Physically short cracks' are generally smaller than 1 mm in length and have little dependence on plastic zone size, which is comparably negligible to the crack length. Physically short cracks are less tortuous, and the crack growth behaviour can be appropriately described by the principles of linear elastic fracture mechanics. Physically short cracks may not induce significant crack wake, and so may exhibit less closure than longer cracks.
4. 'Chemically short cracks' show unpredictable propagation behaviour due to the varying influence of environmental factors at the size scale of the crack and is not considered further in this thesis.

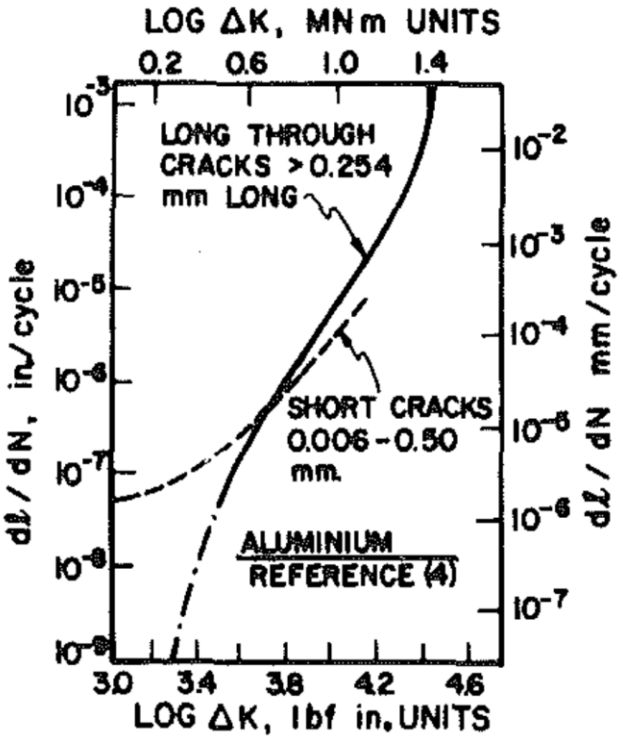

Figure 2-7: Crack growth rate versus *ΔK* for long and short crack aluminium alloy BSL65 [47].

The short crack shape is often characterised as the ratio of half the short crack surface length to its semi-ellipse depth, known as the a/c ratio (Figure 2-8 and Figure 2-9). Semi-ellipse *a/c* ratios of 1 are typically expected for test specimens subjected to tension. However, specimens subjected to bending loading conditions are expected to have lower a/c ratios due to the decreasing stress range gradient as the crack grows towards the neutral axis. The *a/c* ratios were measured from the fracture surface of FV448 martensitic stainless steel cuboidal specimens subjected to three-point bending fatigue testing. It was found that *a/c* ratios were generally between 0.9 and 1.2. The authors suggested that the *a/c* ratios were higher than expected due to microstructural features such as stringers encouraging a deep semi-ellipse shape [5]. The expected a/c ratio (approximately 0.8 which reduces with increasing short crack surface length) for a specimen in three point bending conditions has been found based upon the necessary semi-elliptical shape required to achieve a constant *ΔK* around the crack tip perimeter [50, 51].

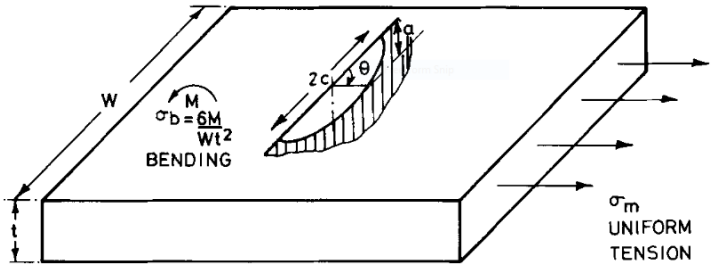

Figure 2-8 A schematic showing the semi-elliptical fatigue surface from short crack propagation in a flat plate under uniform tension. The total short crack surface length is defined as *2c* while the total short crack depth is *a* [52].

Holdbrook and Dover [53] and Scott and Thorpe [52] found that the stress intensity factor ΔK for short cracks in a finite plate under bending load conditions can be related to its surface length (Appendix C). The *a/c* ratio of the short crack is an important consideration in the calculation of $\Delta K_{Surface}$. Therefore the calculation of $\Delta K_{Surface}$ is expected to be inaccurate immediately after short crack coalescence, since the *a/c* ratio temporarily reduces dramatically (Figure 2-9).

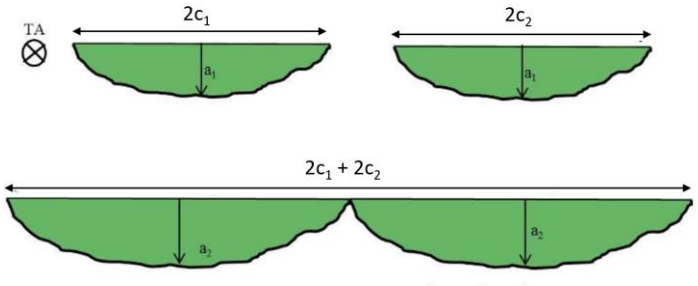

Figure 2-9 Two semi-elliptical cracks coalescing, thereby greatly increasing the short crack surface length while the depth does not change. The *a/c* ratio is therefore temporarily much lower immediately after coalescence adapted from [5].

2.1.5 Crack growth rate retardation mechanisms

There are many internal and external influences that can induce measurable transient retardation effects (including full crack arrest) in the crack growth rate during cyclic loading. The mechanisms of these retardation effects in martensitic stainless steels of relevance to this thesis are:

- Plasticity-induced crack closure
- Roughness induced crack closure
- Variable amplitude loading
- Crack deflection

- Crack bridging
- Crack shielding.

2.1.5.1 Plasticity-induced crack closure

The concept of crack closure was introduced by Elber [54]. If a crack is prevented from fully closing, or prematurely closes before full cyclic unloading, then the effective *ΔK* range is reduced (known as ΔK_{eff}). Therefore, the crack 'driving force' is subsequently reduced, that results in a retardation effect during crack growth rate propagation, described in Equation 2-9 and Figure 2-10:

$$\Delta K_{eff} = K_{max} - K_{op} \qquad \text{Equation 2-9}$$

where K_{op} (also known as K_{cl}) is the maximum stress intensity factor at which the crack is still closed and is always greater than K_{min} when closure effects are present [55-58].

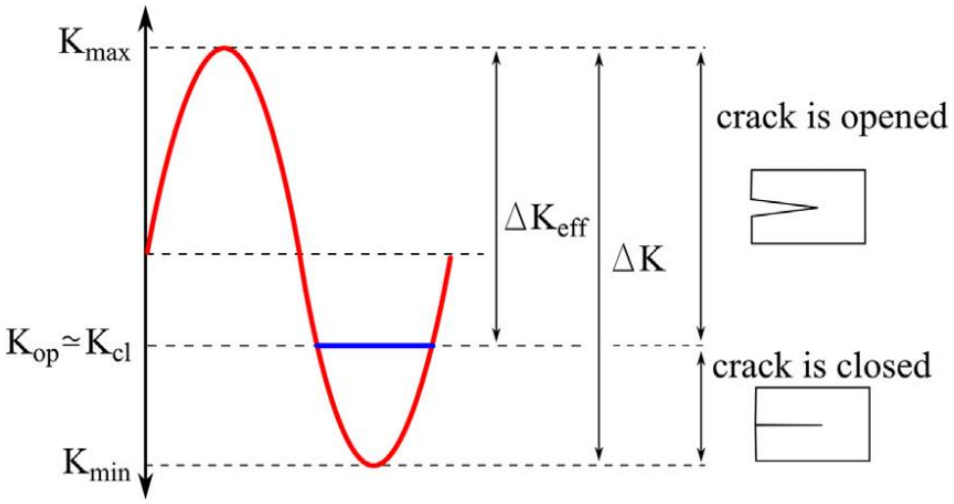

Figure 2-10 Schematic showing the closure effect where ΔK_{eff} is smaller than ΔK as a result of closing of the crack part way during cyclic unloading, reducing the effective driving force for crack propagation [59].

During cyclic loading, a small amount of material plastically deforms at the crack tip plastic zone at K_{max}. A small wedge shaped protrusion is produced due to the plastically deformed material, preventing the crack from 'fully' closing. This induces a crack closure mechanism, which effectively reduces the 'driving force' for crack advance [56]. As the crack propagates, a trail of plastically deformed material is formed, known as a plastic wake. In constant amplitude loading conditions, the plastic wake increases in size as the crack advances due to increasing *ΔK* (Figure 2-11).

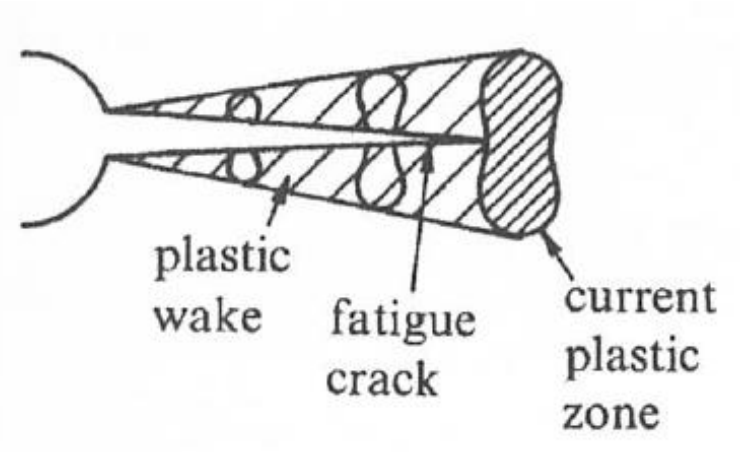

Figure 2-11: Schematic showing the current plastic zone size increases with increasing fatigue crack length, the deformed material known as the plastic wake responsible for crack closure is occasionally visible on the sample from [26].

The effects of plastic closure were most prominently observed at low R-ratios in various low carbon steels [60-62]. Shin and Smith [63] found that R-ratios less than 0.2 were required to induce crack closure effects in a AISI 316 stainless steel. A similar threshold was observed in a Ti-6Al-4V material [64], with R-ratios less than 0.25 required to retard long crack growth rate that was attributed to plasticity-induced crack closure effects. The R-ratio applied to tests in this thesis were 0.1 and therefore the effects of plasticity-induced crack closure may be apparent. The magnitude of plastic closure (and closure effects in general) is typically calculated using Equation 2-10 [63].

$$U = \frac{K_{max} - K_{op}}{K_{max} - K_{min}} = \frac{\Delta K_{eff}}{\Delta K}$$ Equation 2-10

2.1.5.2 Roughness induced crack closure

A crack that advances with intergranular propagation in a coarse grained structure, results in a fatigue surface with a potentially large surface roughness. Misalignment of the fracture surface can cause a reduction in crack opening displacement inducing a closure effect in mode I loading conditions, although the closure effect is more pronounced for Mode II shearing fatigue conditions [56]. The effects of roughness induced crack closure are typically seen at low R-ratios such as 0.1 in coarse grained austenitic and pearlite steels structures [57]. Tempered martensitic stainless steels with relatively high martensite content, long holding times and reduced cooling rates can be affected by roughness induced crack closure [65].

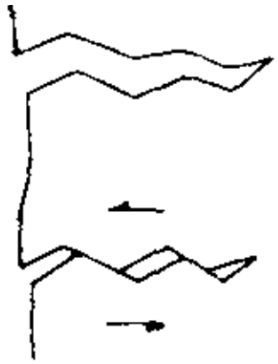

Figure 2-12: A schematic showing the mechanism of surface-induced crack closure. The large surface roughness of the fatigue surface can induce a closure effect from [56].

2.1.5.3 Variable amplitude loading

Increasing or decreasing the minimum and maximum values of cyclic loading during fatigue can alter the crack growth rate due to changing plasticity induced crack closure levels and from compressive residual stress developed ahead of the crack tip. The effects of variable amplitude loading with specific focus on single periodic tensile overloads are discussed more in Chapter 2.2.

2.1.5.4 Crack deflection

Obstacles within the material microstructure, such as inclusions and grain boundaries, can act as barriers to crack propagation and cause a crack to deviate from an otherwise straight path perpendicular to the tensile axis (Figure 2-13). The location and size of the obstacles can affect crack tortuosity. A retardation in the projected crack growth rate is seen since an increasing tortuosity means a longer overall crack length is needed to achieve the same projected crack length. Additionally, a deflected crack growth results in a smaller ΔK component acting as the 'driving force' in the direction of crack propagation, and the effective ΔK is reduced. Crack deflection in the form of intergranular crack propagation behaviour has been observed in early short crack growth in FV448 material [5].

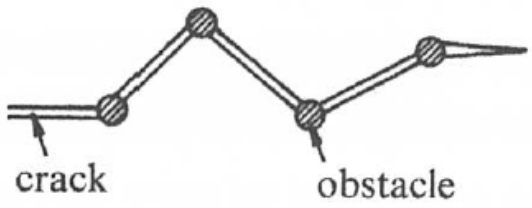

Figure 2-13: A schematic showing obstacles causing crack deflection and subsequent crack growth retardation from [26].

2.1.5.5 Crack shielding and acceleration

Crack shielding can be characterised by a retardation or arresting of crack tip growth due to the presence of neighbouring cracks reducing the stresses and strains at the crack tip, this is often observed during short crack coalescence events. If cracks are aligned such that their crack tip stress-strain fields overlap, then crack acceleration can also be observed. The effect of crack coalescence on short crack fatigue behaviour and propagation rates is further discussed in Chapter 2.1.6.

2.1.5.6 Oxide and Viscosity induced crack closure

Other reasons for transient retardation effects in crack growth rate, considered of little relevance to this thesis, include:

- Oxidation induced crack closure – an oxidised layer forms on the fracture surface during cyclic loading while the crack is open that results in closure effects. Oxidation induced crack closure occurs in martensitic stainless steels subjected to high temperature fatigue testing conditions. Since the tests performed as part of the experimental work of this thesis are carried out in ambient temperature conditions, oxidisation induced crack closure is not considered to impact crack growth rates.
- Viscosity induced crack closure – A fluid such as oil may reduce the crack growth rate due to closure effects by increasing hydrostatic pressure at the crack tip during unloading [66]. It is possible therefore, that silicone material applied for surface replication purposes, may seep in between cracks and induce a similar viscosity induced crack closure effect. However, no work, to the author's knowledge, has been carried out to study such phenomenon, and any viscosity induced crack closure effects are thought to have a negligible impact on growth rates [26].

An up to date review on fatigue crack closure with particular interest in plasticity-induced, roughness-induced and oxide-reduced closure effects on various materials and environmental conditions was carried out by Pippan and Hohenwarter [67].

2.1.6 Crack coalescence behaviour

The simplest form of coalescence is when two 'in-plane' cracks coalesce to form a single crack. Short crack coalescence events are known to affect the growth rates of neighbouring cracks (Figure 2-14 A). In the approach to crack coalescence (between N_b and N_c in Figure 2-14 A and stages I to II in Figure 2-14 B), the crack growth rate of the crack tips approaching each other initially increases due to the heightened localised stress at the crack tips. After coalescence has occurred at N_c, the crack has increased length (a_1 to a_2)

but with an abnormal fatigue region shape resulting in a low *a/c* ratio (Figure 2-14 B II). The crack growth rate of a_2 retards temporarily since the driving force for crack growth is biased towards the depth direction (Figure 2-14 B II to III). The ΔK values during the transition between stage II and III has been investigated by Kamaya [68] and Tan and Chen [69]. As the depth of the coalesced crack increases to equilibrium based *a/c* ratio values (N_c to N_a Figure 2-14 A), the crack growth rate of the crack approaches that of a single crack of length a_2 (Figure 2-14 A and B IV).

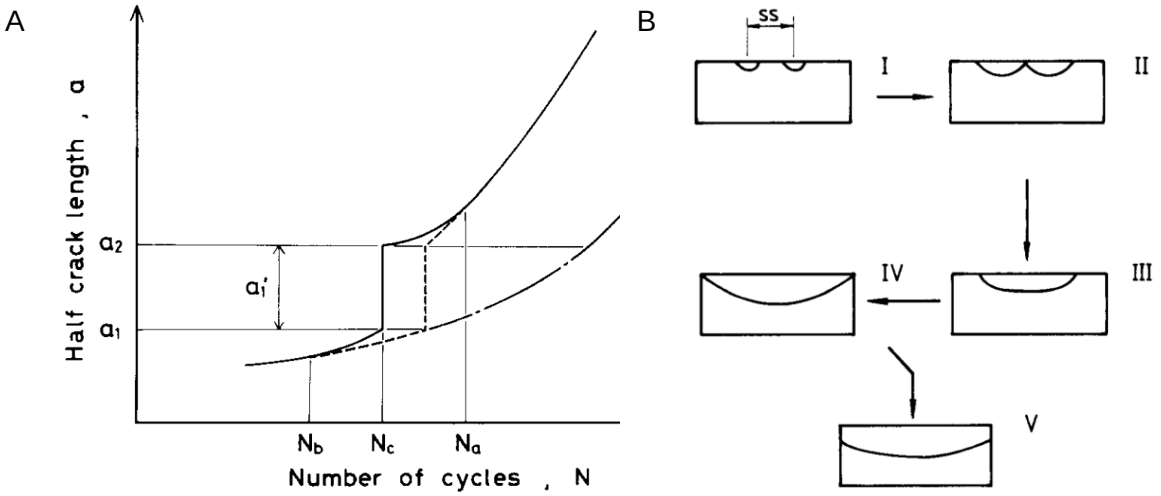

Figure 2-14 Theoretical half short crack length (also known as *c*) versus number of cycles for a crack with coalescence (solid line) and without coalescence (dashed line) from [70]. B) Schematic of the progress of two in-line short cracks (I) meeting followed by coalescence (II) and unification of the semi-elliptical fatigue region (III), followed by crack growth as if a single short crack (IV) and followed by long crack growth (V) from [71].

It is unlikely that multiple short cracks will grow 'in-plane', instead they are likely to grow 'out-of-plane' with each other (Figure 2-15 A), especially on a flat surface or notch surface with a large radius (Figure 2-15 B).

A

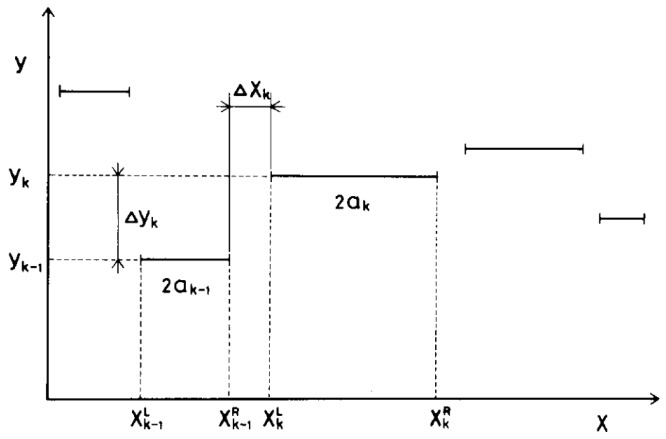

B

Figure 2-15 Schematic showing the 'out-of-plane' distance between neighbouring cracks ΔY_k and the crack tip distance between neighbouring cracks from [70]. B) Example of short crack growing 'out-of-plane' in a U-notched FV448 material with radius of 2.25 mm [72].

The relationship between the crack growth rates of out-of-plane cracks has been investigated by several authors. A single crack redistributes stress on and below the surface, causing a stress concentration at the crack tips and region of reduced stress adjacent to the fatigue region (Figure 2-16 A). When cracks overlap one another, the overlapping crack tips grow through the region of reduced stress (known as a shielded zone) and the stress range at the crack tip is reduced [73]. Conversely, the opposing crack tip stress ranges increases in intensity as the two cracks coalesce into a larger single crack (Figure 2-16 B).

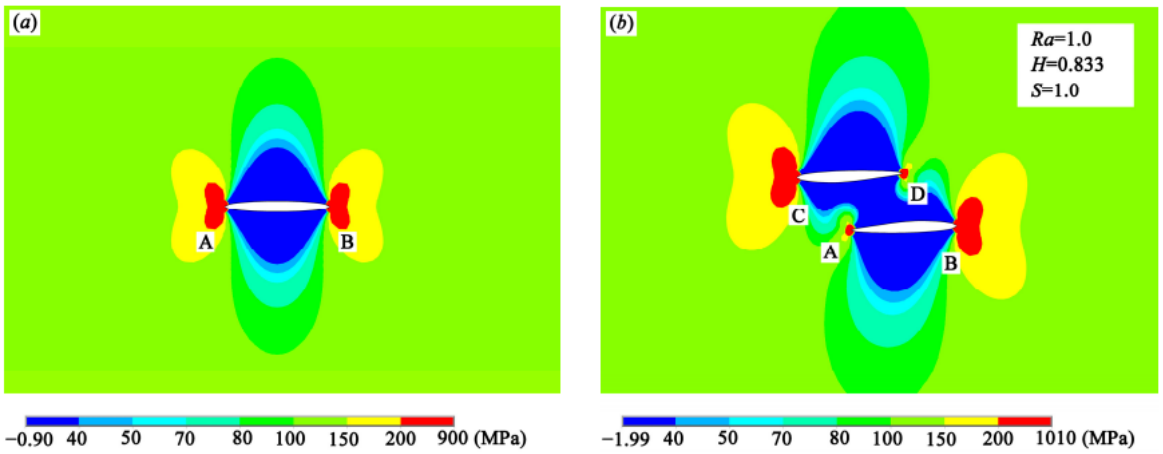

Figure 2-16 Tensile stress distributions around the crack tips of a) a single crack and b) two cracks that are overlapping from [73].

Lefebvre and Sinclair [74] recorded crack tip growth during coalescence of two short cracks growing out-of-plane in a 2024-T351 aluminium material. The two short cracks overlapped each other causing shielding effects (Figure 2-17 A). Crack tips 1A and 2B grew into the other cracks shielded region and the crack growth rate was retarded. However, the opposite crack tip ends 1B and 2A continued to grow and experienced an accelerated growth rate (Figure 2-17 B). This shielding effect and coalescence behaviours are typical for polycrystalline materials [75].

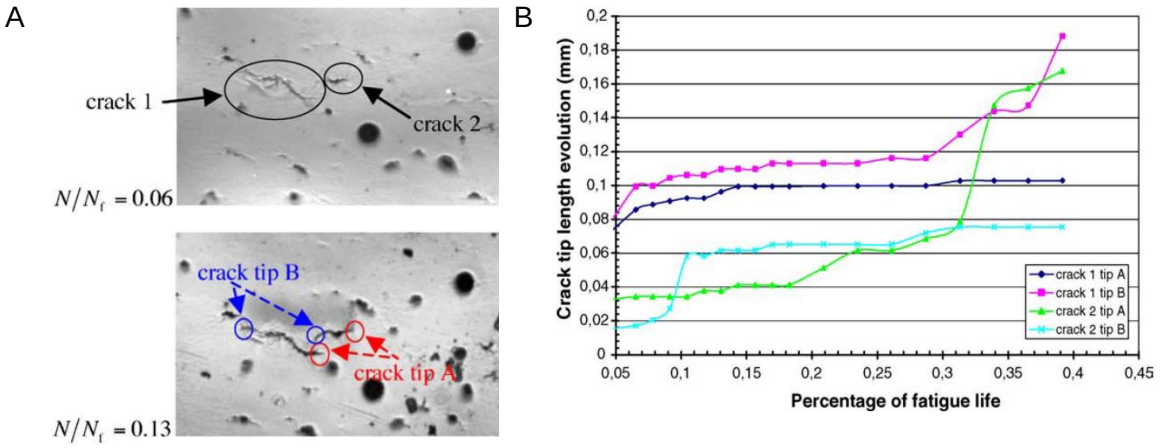

Figure 2-17: A) Two overlapping short cracks prior to coalescence in a 2024-T351 aluminium and B) corresponding crack tip growth from a fixed reference point for the two near coalescing cracks [74].

An idealized short crack evolution and interaction schematic was constructed to show how multiple short cracks interact with other over the whole surface of a sample. The 5 mm by 1 mm flat plate made from 99.98 % copper material was cyclically loaded with a strain range of 0.42 % (in the low cycle regime). The surface was replicated using acetyl cellulose with methyl acetate approximately 20 times during the fatigue life [70]. At 0 % crack propagation life (the number of cycles to crack initiation have been ignored), multiple short cracks were apparent, indicating that many cracks initiated in between replicas. Cracks can be seen coalescing at 36 % propagation life. A mixture of short crack growth and coalescence behaviour were observed until 73 % crack propagation life. By 94 % propagation life, all short cracks had coalesced to form a main crack that continued to propagate until the full width of the specimen.

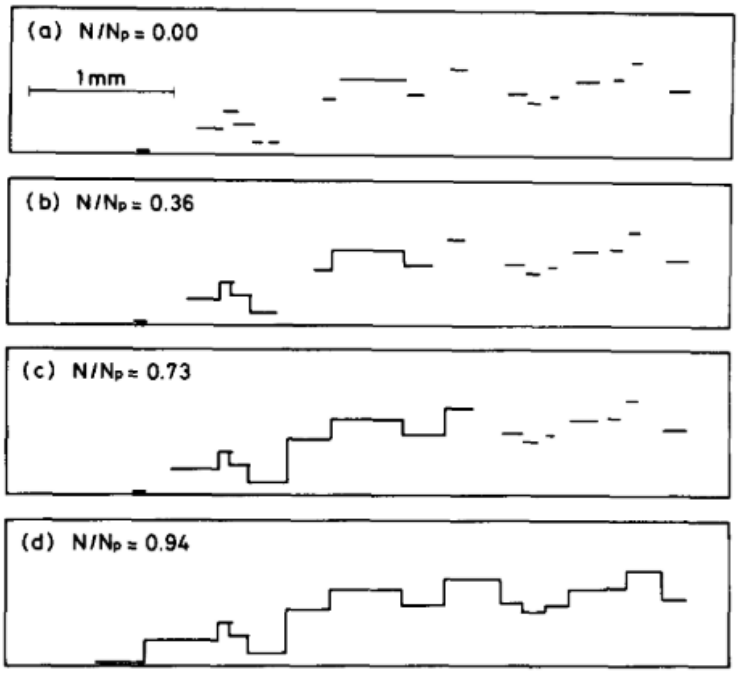

Figure 2-18 Short crack growth evolution in 99.98 % copper material, showing short crack growth followed by coalescence events at 36 % of fatigue life. The short cracks have coalesced into a near full width crack by 94 % of crack propagation life [70]. Only cracks that coalesced with the main crack were included in this schematic.

The effect of out-of-plane distance between neighbouring cracks (ΔY) with coalescence behaviour was investigated [70, 75] on a flat surface. The larger the out-of-plane distance, the larger the sum of the two coalescing cracks was required to initiate coalescence (Figure 2-19 A). This relationship was also observed for a wide range of crack lengths on two alloy steels subjected to corrosion stress cracking (Figure 2-19 C and D). The ratio between the lengths of joining cracks did not seem to affect this behaviour (Figure 2-19 B). The characteristic short crack coalescence behaviour appears to be consistent across various materials (such as copper, steel and aluminium) and loading conditions (such as cyclic fatigue, stress corrosion cracking or creep fatigue) [70, 75-80].

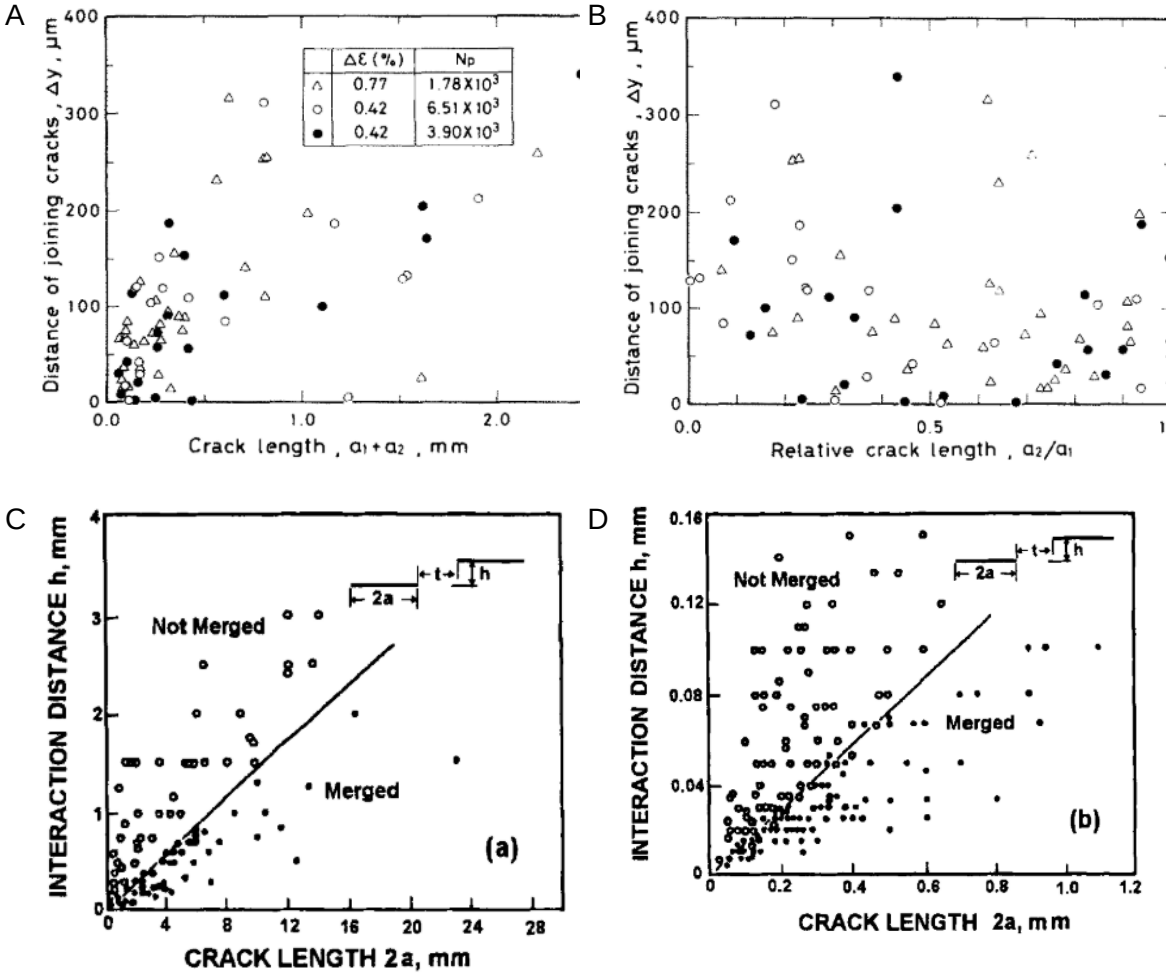

Figure 2-19 Out-of-plane distance between neighbouring cracks versus total crack length (after coalescence) and B) relative crack length ratio between the two coalescing cracks from [70]. C) Out-of-plane distance with surface crack length for particularly long corrosion cracks in a Mn-Cr steel exposed to deionised water at 70 °C and D) smaller short cracks in a Ni-Cr-No-V steel in NaOH solution [75].

2.1.7 Fatigue behaviour in notches

It is well known that notches are a common feature in engineering components, the presence of which are detrimental to fatigue life. Notches induce stress redistribution, creating a localised area of concentrated stress above the nominal stress (known as the notch field). The magnitude of the notch field is dependent upon the notch radius, notch depth to sample thickness ratio and the applied stress. The maximum stress typically occurs on the notch surface (assuming linear stress-strain material behaviour) (Figure 2-20) and can be estimated using Peterson's stress concentration factors using Equation 2-11 [81]:

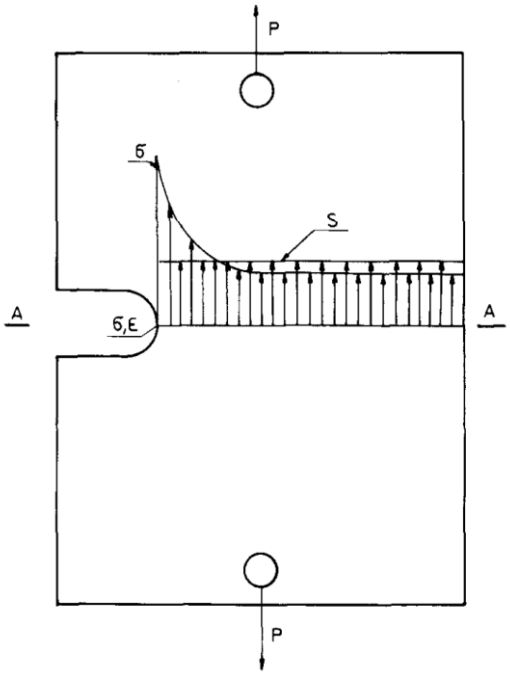

Figure 2-20: 2D view of a U-notch under uniform tension with a schematic stress field distribution from [82].

$$k_t = \frac{\sigma_{max}}{S}$$ Equation 2-11

where σ_{max} is the local stress and S is the nominal stress.

Short crack behaviour can differ in notches due to the presence of the notch field (Figure 2-21). The short crack rate is expected to be higher initially due to the high localised stress near the notch surface. As the crack grows, the short crack growth rate will increase due to the increased ΔK, but additionally the stress gradient decreases as the crack grows through the notch stress field. These competing factors mean that linear-elastic fracture mechanics is unlikely to describe the early stage I growth behaviour of short cracks in notches presented schematically in (Figure 2-21) [45]. Once the short cracks have grown through the notch field, the crack growth behaviour tends towards stage II crack growth for un-notched specimens [60, 83].

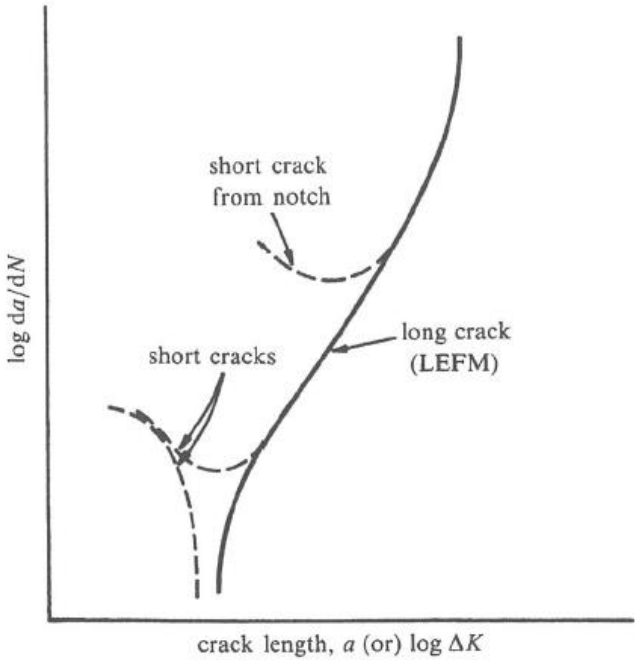

Figure 2-21: A schematic to show *ΔK* versus crack growth rate for long cracks, short crack and short cracks in notches using linear-elastic fracture mechanics assumptions from [26].

This typical short crack effect in notches has been observed in double edge notch specimens made from AISI stainless steel material with a thickness of 2.6 mm [63]. The growth rate of short cracks in a notched specimen was higher than that of an un-notched specimen (Figure 2-22 A), assumed to be due to the increased stress range from the notch effect. The magnitude of plastic closure 'U' was calculated for both samples, but no difference was observed indicating that plastic closure may not contribute towards the notch effect (Figure 2-22 B).

A

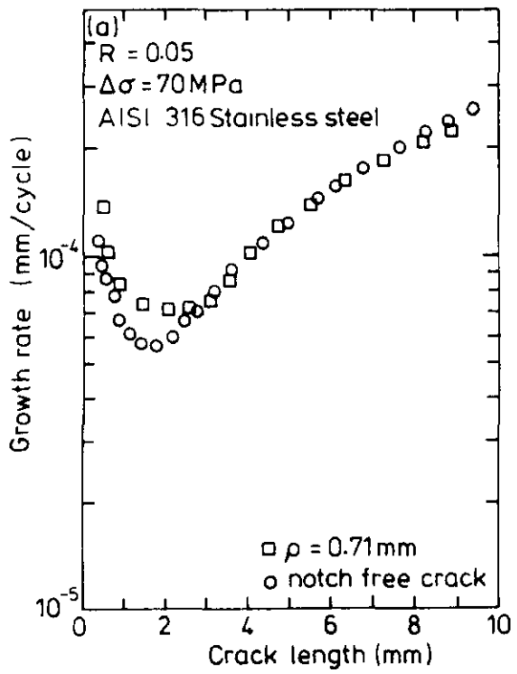

B

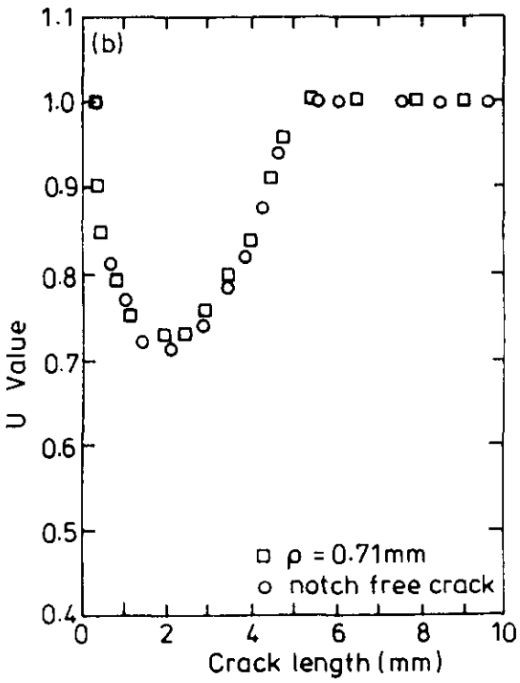

Figure 2-22 A) Short crack growth rate versus crack length for AISI 316 stainless steel with and without a notch at R-ratio of 0.05 and stress range of 70 MPa and B) with the corresponding U Value indicating plastic closure effects [63].

The effects of plastic closure on the short crack behaviour in notches was investigated in hot-rolled 1026 steel material with a yield strength of 322 MPa [61]. The magnitude of the plastic closure was compared with crack tip opening displacement. Plastic closure effects were observed in specimens under fully reversed loading conditions (R-ratio of -1). The authors noted that the short crack notch effect was less pronounced at higher R-ratios such as 0 and 0.1. This observation was also captured by Shin and Smith; [63] at high R-ratios, the short crack effect was reduced and almost eliminated (Figure 2-23 A). At R-ratios of 0.05 the short crack effect was observed under different stress ranges (Figure 2-23 B).

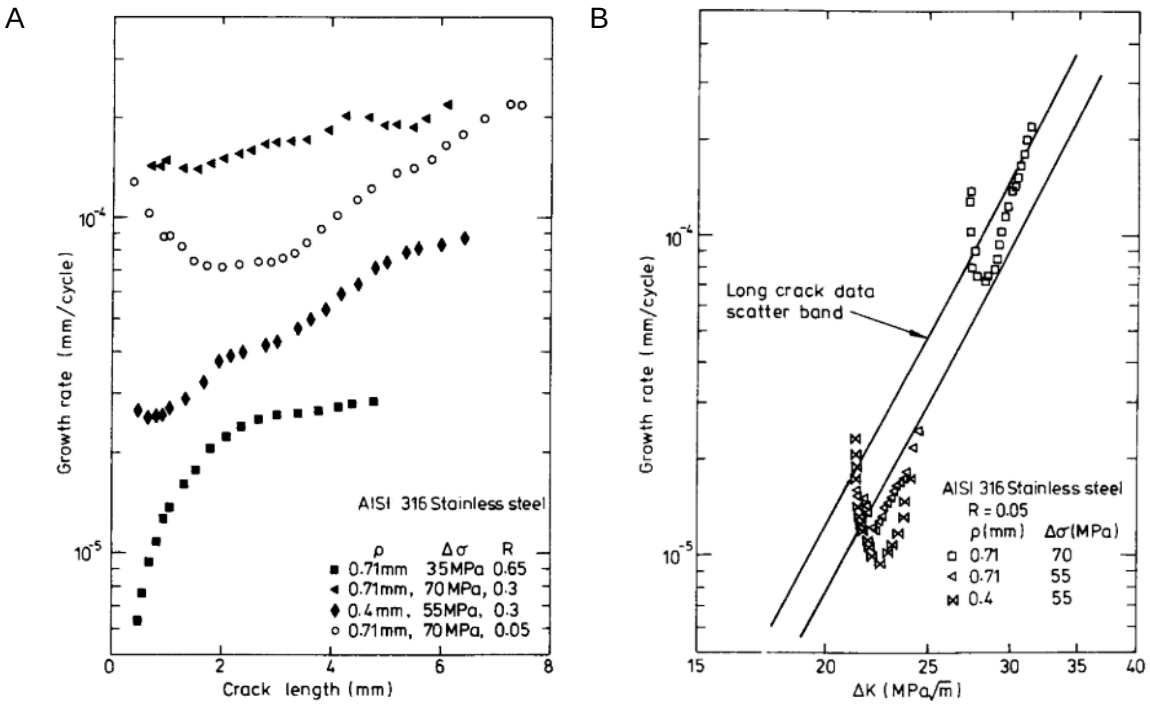

Figure 2-23 A) Short crack growth rate versus short crack length for different notch radius under various loading conditions with different stress ranges and R-ratios and B) versus ΔK at R-ratio of 0.05 from [63]

Accounting for the effects of plastic closure and crack tip opening displacement into the linear-elastic fracture mechanics approach can help better describe the early mode I stage II short crack behaviour typically seen in notches, but not entirely [63, 83]. Sadananda [84] suggests that the lack of similitude between crack growth rates versus ΔK relationship between short and long cracks cannot be fully explained by plastic closure or microstructural features acting as obstacles alone. Instead, internal or residual stresses within the notch field from material manufacturing, machining and loading past material yield within the notch field should also be taken into account.

Fatigue testing was carried out on a single edge notch tension specimen with thickness of 5 mm made from GH4169 alloy material with a yield strength of 1045 MPa at R-ratio of 0.1 under constant amplitude conditions [85]. One set of samples was tested as-received, with residual stresses from machining processes between -200 MPa and -370 MPa. While the others were heat treated after machining to relieve residual stresses. The authors suggested that removing the residual stress resulted in a slight increase in short crack growth rate under 380 MPa. Once the cracks grew to 500 µm, no difference in crack growth rates were observed. This result may indicate that compressive residual stress from machining process may have contributed towards the increased crack growth rate. However, no difference was observed under 410 MPa loading, where a similar effect would

be expected. It is possible that other crack growth rate factors such as crack shielding from neighbouring cracks may have affected the results. In shot peened U-notched FV448 martensitic stainless steel specimens, the compressive residual stress and strain hardening from the shot peening process had a clear retardation effect on short crack growth rates [50] (more information can be found in Chapter 2.3.3).

2.1.7.1 Stress and strain distribution estimations within the notch field

A linear distribution of the stress within the notch field was seen in Figure 2-20. When the maximum stress at the notch surface exceeds the yield strength of the material, the distribution of the stress within the notch field changes (to the red line in Figure 2-24) [86]. The maximum stress is typically seen at some depth beneath the notch surface due to 'notch-constraint' effects of surrounding material.

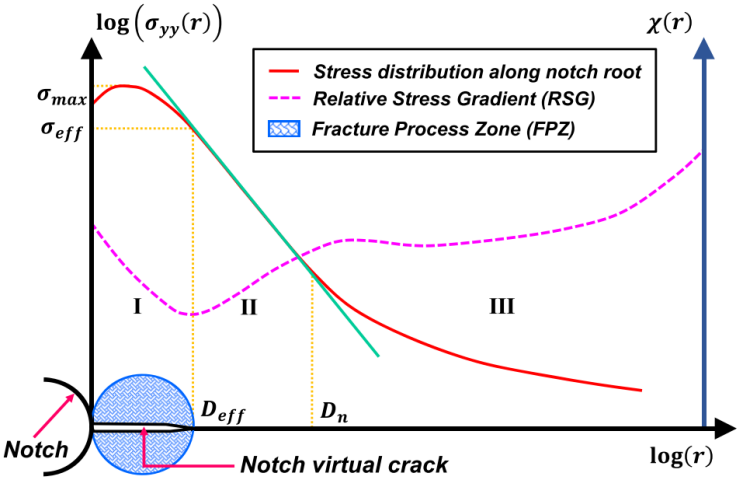

Figure 2-24 Stress distribution versus notch depth based upon elastic-plastic material behaviour assumptions in the notch field (with no crack present) shown as the red line from [86].

The stress distribution can be obtained using the FE modelling method, which can be computationally expensive and not immediately accessible for industry use. An attempt to save computation time and increase practicality to industry was made by using Glinka's rule with the aim of predicting the stress distribution within the notch field as part of this thesis study. The Ramberg-Osgood fitting method [87] was used to model existing monotonic tensile data for FV556 (personal communication, FNC, 2018) using Equation 2-12:

$$\varepsilon = \frac{\sigma}{E} + \left(\frac{\sigma}{H}\right)^{\frac{1}{n}}$$ Equation 2-12

where ε is the strain, σ is the stress, E is the Young's modulus of the material, H is the monotonic strength coefficient and n is the strain hardening exponent. A 'double' Ramberg-Osgood approach was used where two Ramberg-Osgood curves were required to capture both the elastic to plastic transition and material behaviour at higher strains (Figure 2-25 A), which reduced the error considerably (Figure 2-25 B).

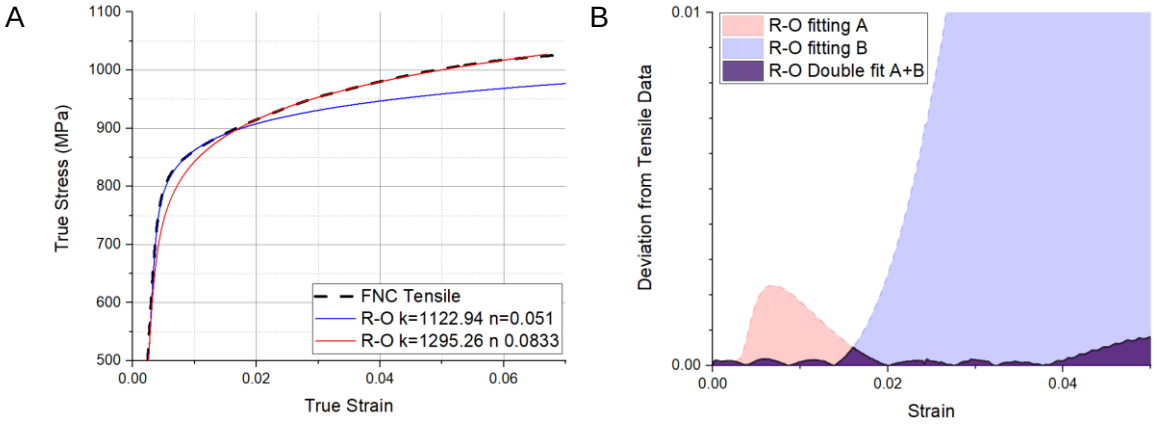

Figure 2-25 A) A 'double' Ramberg-Osgood fit for existing monotonic tensile data to achieve a greater representation of the monotonic tensile results. B) The deviation of the Ramberg-Osgood fit from the strain results obtained through monotonic tensile testing. The purple area shows that a double Ramberg-Osgood method reduced the error considerably.

The stress at the notch surface can be estimated using Glinka's rule (Equation 2-13), a development of the well-known Neuber's rule [88], that assumes that the energy to achieve a particular stress and strain at the notch surface is equivalent between linear and monotonic elastic-plastic material behaviours.

$$\sigma^2 + \frac{2E\sigma}{n+1}\left(\frac{\sigma}{H}\right)^{\frac{1}{n}} = (Sk_t)^2 \qquad \text{Equation 2-13}$$

Glinka's rule is considered more accurate than Neuber's rule since integrating the Ramberg-Osgood relationship to calculate the energy accounts for energy dissipation during the elastic to plastic transition, a consideration omitted from Neuber's rule assumptions (Figure 2-26 A). A comparison has been made between Neuber's rule, Glinka's rule and FE modelling approach predictions [10]. It was found that Glinka's rule was in agreement with FE modelling predictions, while Neuber's rule typically slightly over-estimated the stress and strain at the notch surface (Figure 2-26 B).

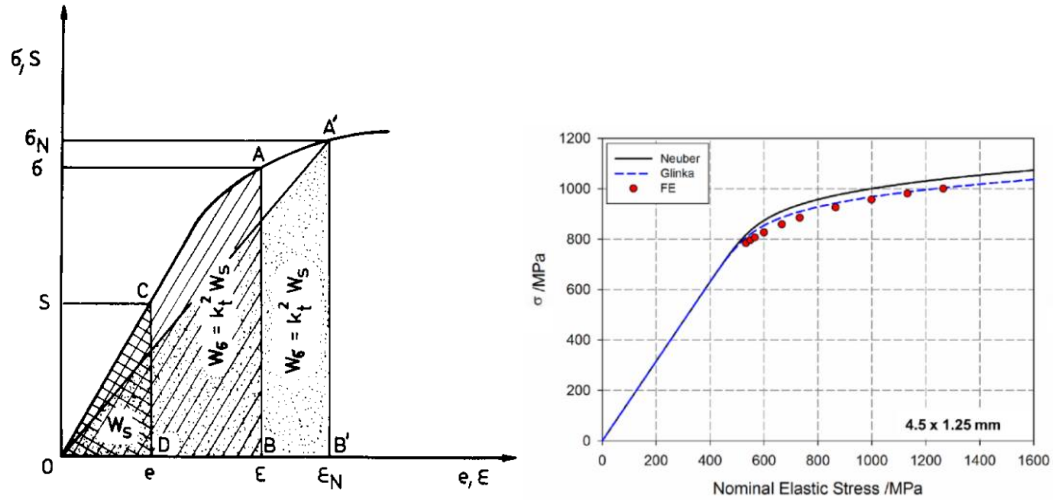

Figure 2-26 A) A comparison between Neuber's and Glinka's rule approach for predicting the maximum stress and corresponding strain at the notch surface from existing tensile data [82]. B) Neuber's and Glinka's rule used to predict the longitudinal stress at a notch surface and compared with FE modelling [10].

A comparison was made between the tensile stress distributions within the notch field using FE modelling with elastic and elastic-plastic material modelling, Glinka's rule was then applied and compared with the FE modelling predictions. While Glinka's rule appears to accurately predict the stress at the notch surface as expected, the stress distribution within the notch field is not accurately captured (Figure 2-27). The FE modelling approach is required since 'notch-constraint' effects are accounted for, a consideration not captured by application of Glinka's rule.

The stress distribution within the notch field was investigated using the FE modelling method in a U-notched specimen made from FV448 with notch depth of 1.25 and with notch radii of 4.5 mm and 10.5 mm [10]. The maximum strain at the notch surface was identical for both notch geometries. The shaper notch geometry had a slightly larger maximum stress that was nearer to the notch surface and the notch field was smaller overall. Additionally, the neutral axis was slightly closer to the notch surface.

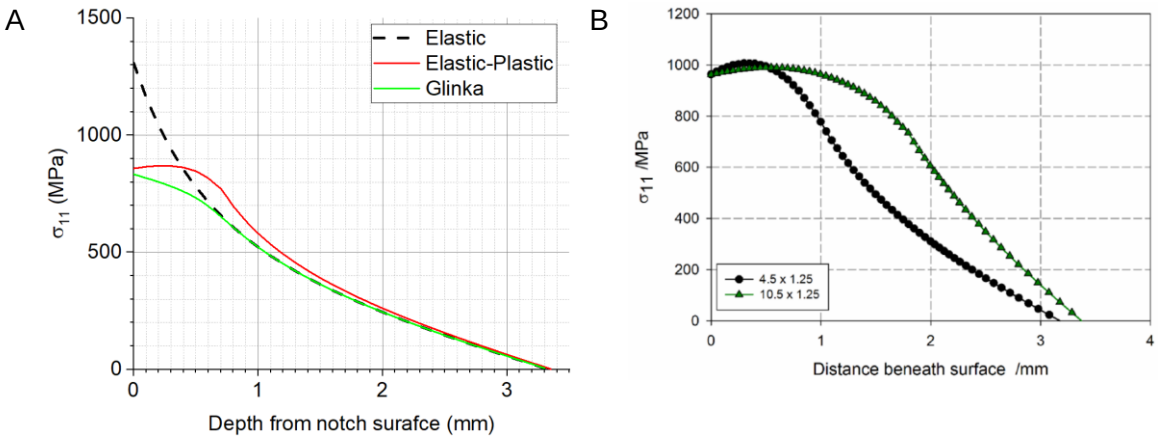

Figure 2-27 FE modelling used to predict the stress distribution in the notch field using elastic and elastic-plastic material modelling assumptions and compared with the Glinka's rule approach. B) Stress versus distance beneath the notch surface showing the distribution of stress within the notch field for U-notched specimens made from FV448 with notch depth of 1.25 mm and notch radii of 4.5 mm and 10.5 mm [10].

2.2 Effects of overload cycles on fatigue behaviour

2.2.1 Introduction

Under the constant amplitude cyclic loading conditions discussed thus far, the mean stress and stress amplitude remain constant throughout the duration of fatigue. In reality, components are more likely to be subjected to more complex and less consistent variable amplitude loading conditions such as overloads, underloads or a combination of random loading. Variable amplitude loading conditions can occur from routine inspections such as over-speed testing of a power plant turbine known as single periodic tensile overloads [89] (Figure 2-28 A).

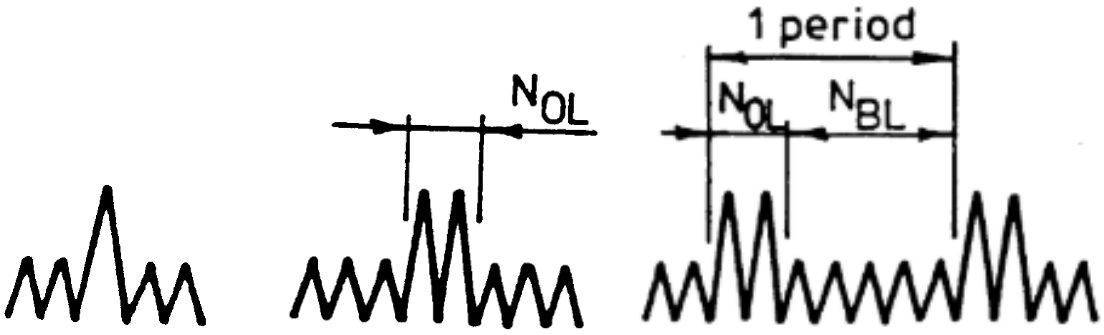

Figure 2-28: A) A Single overload is applied amongst constant amplitude baseload cycles. B) An overload block consisting of more than one overload N_{OL} are applied consecutively. C) An overload block with N_{OL} overload cycles is applied periodically every N_{BL} (in this case five) baseload cycles [89].

The magnitude of a single periodic tensile overload can be defined as a percentage increase above the maximum baseload (Equation 2-14) [90]. However, it is more common to define the magnitude of a single periodic overload in terms of the overload ratio (OLR) accounting for the minimum load of the baseload (Equation 2-15) [62]:

$$\%\, overload = 100 \times \frac{P_{OL} - P_{max}}{P_{max}} \qquad \text{Equation 2-14}$$

$$OLR = \frac{P_{OL} - P_{min}}{P_{max} - P_{min}} \qquad \text{Equation 2-15}$$

where P_{OL} is the maximum load from the overload cycle, P_{max} is the maximum load from the baseload cycle and P_{min} is the minimum load from the baseload cycle.

2.2.2 Effects of overloads on crack growth propagation

Numerous authors have investigated the effects of single periodic tensile overloads on fatigue crack growth behaviour. The majority of the literature suggests a notable lifetime extension effect due to a temporary retardation in the growth rate of long cracks, especially in steel materials [62, 89-98]. Four possible retardation behaviours have been identified [90] discussed below:

- No/little effect - No retardation effect is seen; the overload cycle did not produce an observable change in the crack growth rate (Figure 2-29 A).

- Retardation – A temporary reduction in the crack growth rate is seen immediately following the overload. This is followed by an equivalent increase in crack growth rate to constant amplitude levels. The temporary retardation effect results in a decrease in the average crack growth rate of the crack overall (Figure 2-29 B).
- Delayed retardation – The crack growth rate remains constant for a short period [99] or increases immediately after the overload [100], followed by a delayed decrease in crack growth rate. The retardation effect of the overload is typically greater than the initial increase resulting in a decrease in the average crack growth rate overall (Figure 2-29 C).
- Lost retardation – A retardation or delayed retardation effect is observed, followed by an increase in the crack growth rate. The increase in crack growth rate is sufficiently large to increase the crack growth rate past constant amplitude levels, resulting in no effect on the average crack growth rate overall (Figure 2-29 D).

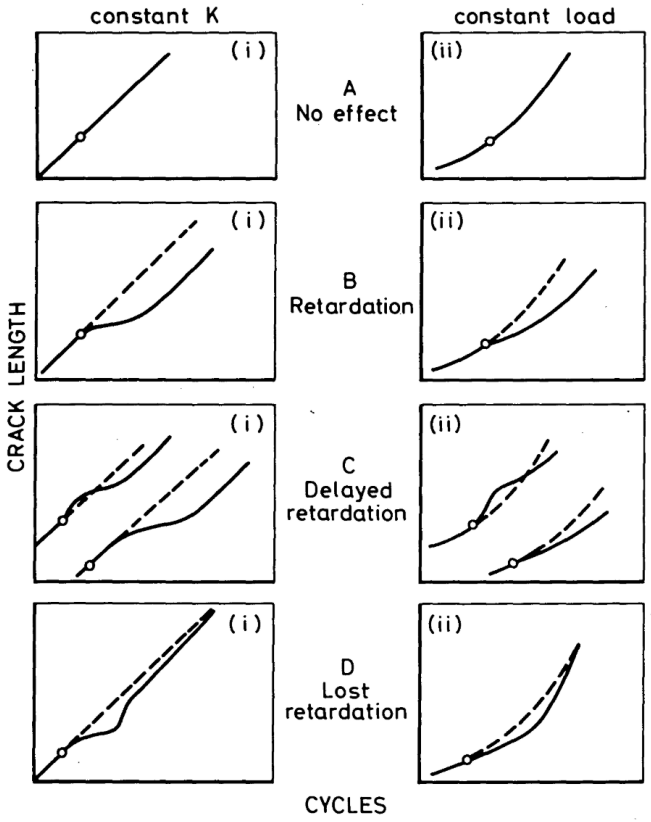

Figure 2-29: Crack length versus number of cycles for four main types of fatigue crack growth retardation behaviours from a single periodic overload cycle such as A) no/little effect, B) crack growth retardation that may extend fatigue life, C) initial increase in crack growth rate followed by delayed retardation that may extend fatigue life and D) initial retardation of crack growth followed by an increase in crack growth rate as if no overload was applied, resulting in lost retardation and no effect on fatigue life [90].

B.M.D. Cunningham

Delayed retardation crack growth behaviour is typically exhibited following an overload in steel materials [62, 89, 101] (Figure 2-30).

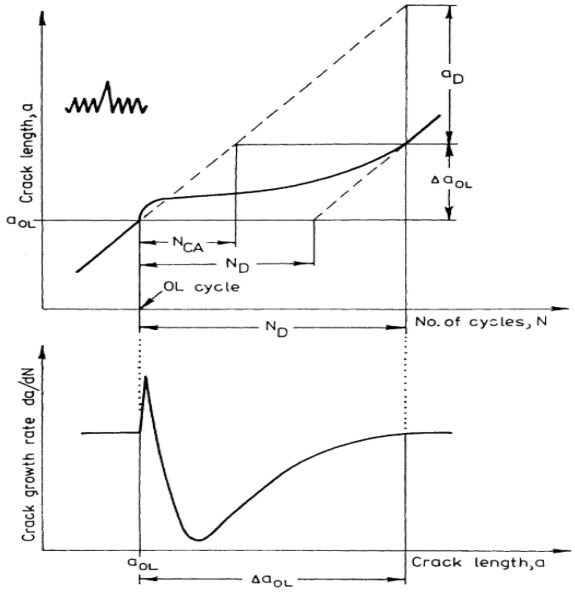

Figure 2-30: Schematic showing a typical example of the crack length and crack growth rate versus number of cycles for a delayed crack retardation effect (with initial increase in crack growth rate followed by retardation) following an overload cycle [89].

2.2.3 Factors influencing fatigue crack growth behaviour following overloads

Shin and Hsu [62] applied overloads of varying OLRs to compact tension (CT) specimens with thickness of 6 mm and width of 50 mm made from AISI 304 stainless steel material at different ΔK values. Varying the baseload ΔK between 16 $MPa^{0.5}$ and 22 $MPa^{0.5}$, did not appear to affect the crack propagation retardation effect following an overload with OLR of 2 at R-ratio of 0.1 (Figure 2-31 A). On the other hand, the magnitude of the overload had a significant impact on the amount of retardation observed when OLRs of 1.5 and 2 were applied. An increase in the OLR from 1.5 to 2 while maintaining a constant ΔK of 22 $MPa^{0.5}$ resulted in a decrease in the minimum crack growth rate by a factor of six (Figure 2-31 B). The increasing retardation effect with increasing OLR is a common observation [62, 89, 102-104]. Interestingly, the authors observed that the effect carried on for roughly the same number of cycles until the pre-overload crack growth rate was restored.

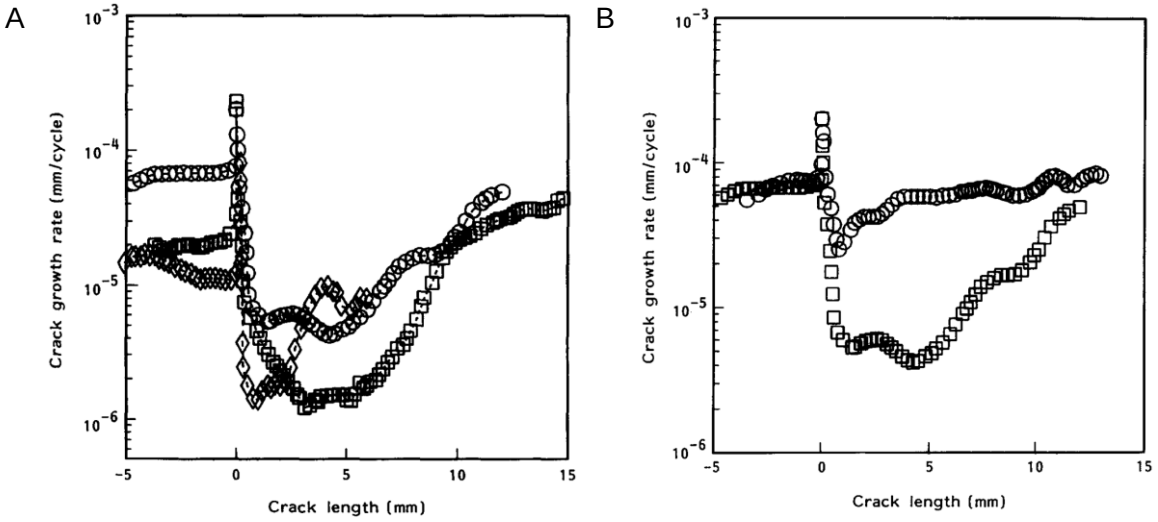

Figure 2-31: Crack growth rate in mm per cycle versus relative crack length following an overload cycle A) at different baseline ΔK values of 22 MPam$^{0.5}$ (circle symbols), 19 MPam$^{0.5}$ (square symbols) and 16 MPam$^{0.5}$ (diamond symbols) and B) at different OLRs of 1.5 (circle symbols) and OLR of 2 (square symbols) for AISI 304 stainless steel at R-ratio of 0.1 and ΔK of 22 MPam$^{0.5}$ [62].

Jones [105] applied overloads to Ti-6Al-4V under constant amplitude loading conditions with an R-ratio of 0.1. A retardation effect can clearly be seen with 100 % (OLR of 2.11) and 70 % (OLR = 1.78) overloads as expected. However, 50 % (OLR = 1.56) and especially 20 % (OLR = 1.22) overloads did not appear to have any retardation effect on crack growth propagation (Figure 2-32).

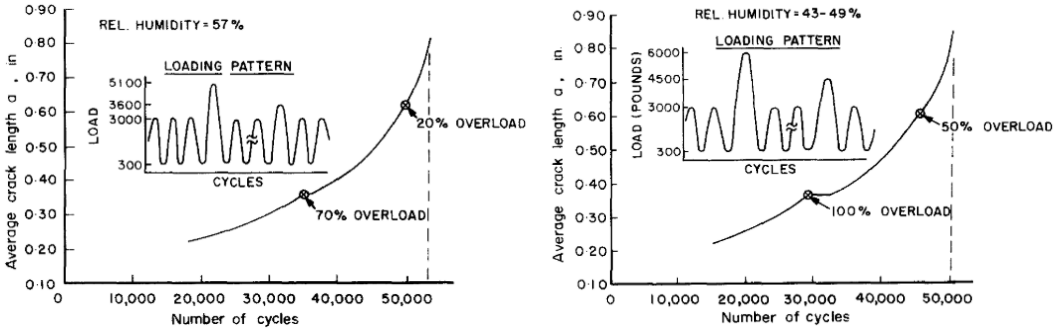

Figure 2-32: Crack length versus number of cycles for a Ti-6Al-4V titanium alloy under cyclic loading at R-ratio of 0.1 with overloads of 20 % to 100 % applied from [105].

An apparent overload threshold was investigated by Bernard et al [90] on FV520B martensitic stainless steel with yield strength of 940 MPa and Ducol W30B with a yield strength of 366 MPa. It was found that tensile overloads less than 35 % applied at baseline R-ratio of 0.05 (OLR of 1.37) did not produce a measurable retardation effect on crack growth propagation for FV520B. A higher R-ratio reduced the overload threshold to

approximately 20 % (Figure 2-33 A), however, the equivalent OLR was approximately the same (OLR of 1.4). Decreasing the thickness of the FV520B specimen from 25 mm to 5 mm slightly reduced the number of cycles exhibiting a retarded crack growth rate by approximately 20 %, but the overload threshold value appeared to be unaffected (Figure 2-33 B).

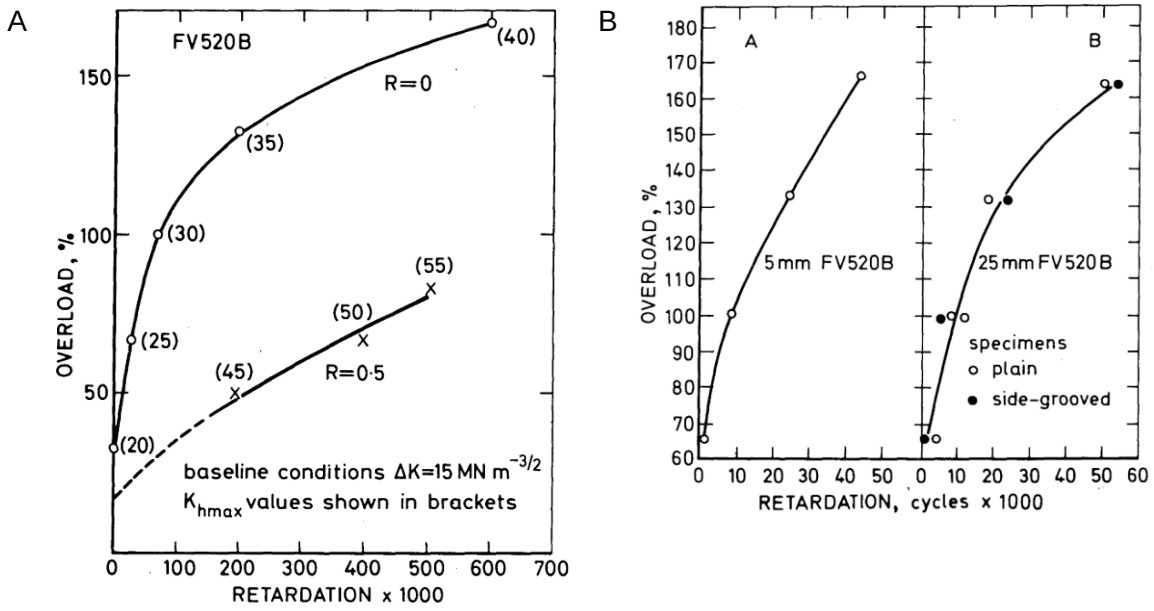

Figure 2-33 A) Overload (%) versus number of cycles with a retarded crack growth at different R-ratios of 0.05 and 0.5 for FV520B with a thickness of 25 mm and baseline ΔK of 15 MPam$^{0.5}$ and B) for different thicknesses of 5 mm and 25 mm with R-ratio of 0.05 and constant baseline ΔK of 30 MPam$^{0.5}$ from [90].

The lower yield strength of the Ducol W30B resulted in more significant specimen thickness effects on the number of cycles with retarded crack growth rate following an overload cycle and a lower overload threshold value of 30 % (Figure 2-34 A). As specimen thickness increases, so the number of cycles exhibiting a retarded crack growth rate decreases, attributed to the more significant multiaxial stress state in thicker specimens. A similar relationship was observed for a high strength steel at various baseline ΔK values, R-ratio of 0.05 and OLR of 2 [106] cited in [89]. This specimen thickness effect was observed until a thickness of 10 mm to 15 mm after which increasing the thickness further did not alter the retardation behaviour regardless of baseline ΔK values (Figure 2-34 B).

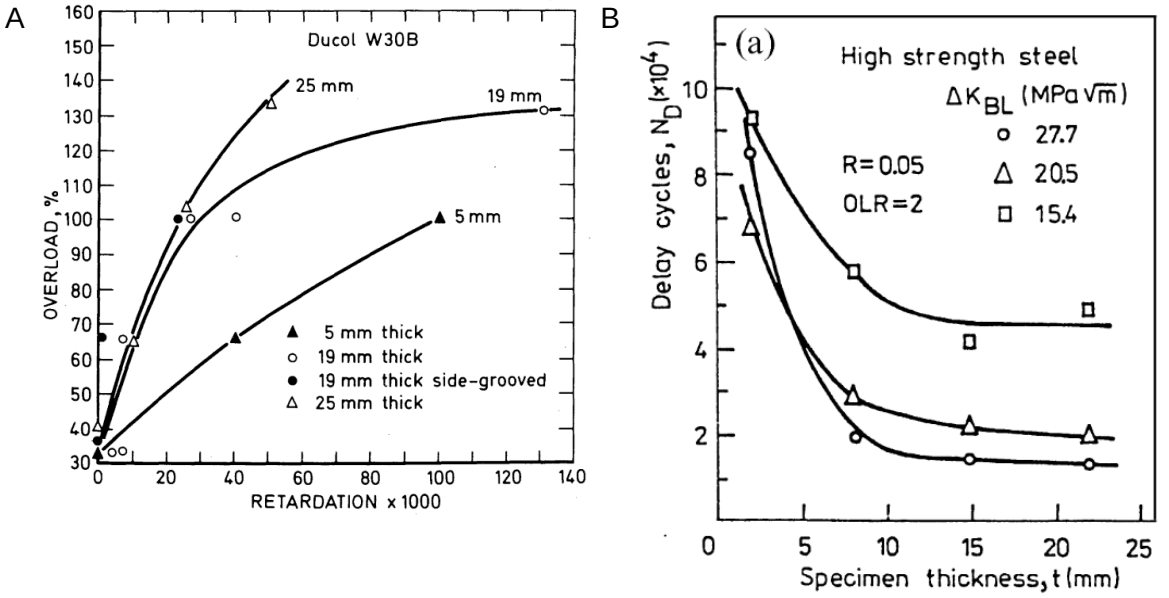

Figure 2-34: A) Overload (%) versus number of cycles with a retarded crack growth rate for Ducol W30B with various specimen thicknesses from [90]. B) Number of cycles with a retarded crack growth rate following an overload cycle with OLR of 2, versus specimen thickness for a high strength steel material under an R-ratio of 0.05 at various ΔK values from 15.4 MPam$^{0.5}$ to 27.7 MPam$^{0.5}$ from [106] cited in [89].

AISI 304 stainless steel samples were subjected to different R-ratios of 0.1, 0.45 and 0.6 at a baseline ΔK of 22 MPam$^{0.5}$ and OLR of 2 [62]. A higher R-ratio with constant OLR values resulted in less potent overloads; an R-ratio of 0.1 is equivalent to a 90 % overload, while an R-ratio of 0.6 is equivalent to a 40 % overload at OLR of 2. Therefore decreasing R-ratios caused a more significant retardation effect with a lowest crack growth rate (expressed as a percentage of the pre-overloaded crack growth rate) of 50 % for R-ratio of 0.6, 40 % for R-ratio of 0.45 and 6 % for R-ratio of 0.1. Furthermore, the number of cycles required to restore pre-overloaded crack growth rate increased with decreasing R-ratios, with approximately 2 mm required for R-ratio of 0.6, 8 mm for R-ratio of 0.45 and 15 mm for R-ratio of 0.1 (Figure 2-35).

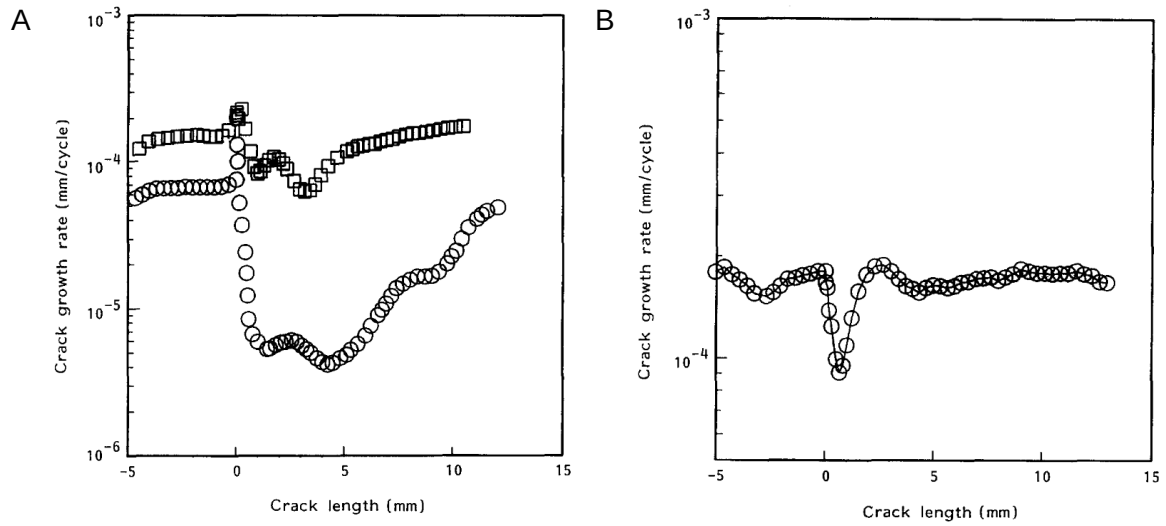

Figure 2-35 Crack growth rate versus relative crack length following an overload cycle at different R-ratios of A) 0.1 (circle symbols) and 0.45 (square symbols) and B) 0.6 for AISI 304 stainless steel with OLR of 2 and baseline ΔK value of 22 $MPam^{0.5}$ from [62].

Hammouda et al [60] investigated the effects of relatively small overloads on the short crack behaviour in the high cycle fatigue regime at different notch geometries in 3 mm thick low carbon steel with yield strength of 267 MPa and ultimate tensile strength of 381 MPa. Two samples with notch depth of 8 mm and notch radius of 2 mm (Figure 2-36 A) were subjected to constant amplitude loading with a maximum stress of 70 % of the yield stress and R-ratio of 0. The number of cycles to grow a crack 0.15 mm was 3 265 000 and 3 235 000 cycles. One sample was subjected to a single overload with OLR of 1.3 before constant amplitude loading was applied. The number of cycles required to initiate and grow a crack 0.15 mm was increased to 8 785 000 cycles. This increase in the number of cycles for crack initiation was attributed to the compressive residual stress field from the overload cycle.

The short crack growth rate following overloads with OLR of 1.1, 1.2 and 1.3 were recorded under identical loading conditions. Increasing the OLR of overloads tended to reduce the crack growth rate (Figure 2-36 B). The presence of the notch appeared to reduce the overload threshold, this may be due to the increased stress concentration factor on the notch surface, the particularly soft ductile material being tested or due to particularly localised compressive residual stress field due to notch geometry constraint effects.

An overload with OLR of 1.3 was applied to notched samples with notch depth of 4 mm and notch radius of 1 mm under baseload cyclic loading at R-ratio of 0 and maximum stress of 74 % of the yield stress at various crack lengths (L). The application of the overload cycle

induced an initial increase in crack growth rate followed by delayed retardation crack growth behaviour (Figure 2-36 C).

The effect of R-ratio on short crack growth behaviour following an overload with OLR of 1.3 was also explored in a sample with 8 mm notch depth and 2 mm notch radius with maximum load at 70 % yield stress. The overload cycle applied at crack length (L) of 0.6 to 0.62 mm, appears to produce a small delayed retardation effect at all R-ratios tested between 0 and 0.3.

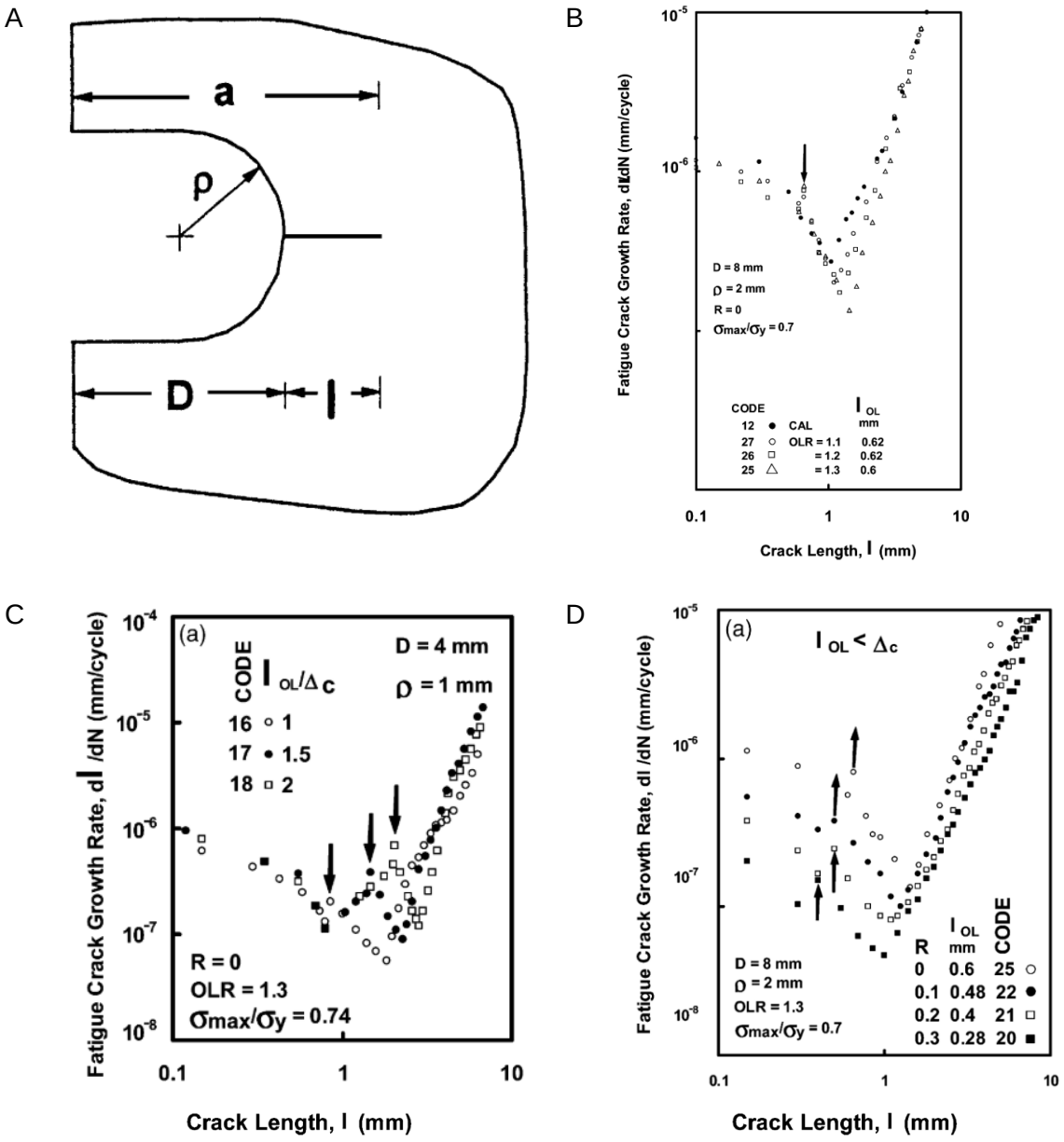

Figure 2-36 A) Notched plate with thickness of 3 mm showing dimensions for notch depth (D), notch radius (ρ), crack length (a-D = L). B) Crack growth rate versus crack length (L) for various overloads applied after some crack length (L) and for C) a different notch geometry and for D) different R-ratios from [60]. The arrows in (B to D) indicate when overloads were applied.

2.2.4 Mechanisms of fatigue crack retardation effects following overloads

Many reasons for the retardation effect from the overload cycle have been proposed, summarised by Shin and Hsu [62] including:

- Crack tip strain hardening
    - The application of the overload and resulting plastic deformation increases dislocation density and dislocation pile up within the crack tip of the material. This strain hardening of the material may increase resistance to crack propagation.
- Plasticity-induced crack closure
    - Material deformation at the crack tip causes closure effects retarding crack growth (Chapter 2.1.5.1), the overload cycle may increase the amount of plastic deformation leading to temporary decrease in the crack growth rate.
- Crack tip blunting
    - The increased plastic deformation at the crack tip experienced from the overload cycle, results in an increase in the radius of the crack tip notch. This consequently would lead to a temporary reduction in the crack growth rate.
- Compressive residual stress ahead of the crack tip
    - The increased plastic deformation experienced at the crack tip from the overload cycle induces a relatively large compressive residual stress field within the crack tip plastic zone. The compressive residual stress induces a superposing effect on the cyclic stress range, effectively reducing the mean stress and crack tip opening displacement, inducing a quasi-closure effect.

Jones [105] investigated the effect of strain hardening on the crack growth rate in Ti-6Al-4V sheet material, heat treated to MILT9046F specifications. One sample was left as-received, while several specimens were deformed in tension to various percentages of plastic strain to induce strain hardening. The specimens were subjected to constant amplitude cyclic loading with maximum load of 3000 lb with an R-ratio of 0.1. An increased crack growth rate was observed in pre-strained specimens when compared to as-received specimens. Nonetheless, a crack growth rate retardation effect was still seen after an overload was applied (Figure 2-32). Therefore, the author concluded that strain hardening within the crack-tip plastic zone was unlikely to contribute towards the crack growth retardation effect following an overload, but this was not tested experimentally. Based upon this hypothesis, materials that exhibit increased resistance to fatigue with higher yield strengths and brittleness may exhibit an enhanced crack growth rate retardation effect following an overload cycle.

Shin and Hsu [62] attempted to recreate the effects of plastic closure in AISI 304 stainless steel. An overload cycle with OLR of 1.5 and 2 were applied to two specimens after an initial crack length had been grown (original image in Figure 2-31 B) and the U value for plastic-closure effects were calculated (Figure 2-37 A). On one other specimen, epoxy resin was vacuum infiltrated into the crack at the crack tip during constant amplitude loading at R-ratio of 0.1 and ΔK of 26 MPam$^{0.5}$ while held at a 90 % of the maximum load. The resin was allowed to harden and constant amplitude loading recommenced.

The crack growth rate immediately reduced to similar levels seen following an overload cycle with OLR of 2, followed by an increase to pre-infiltrated levels. The authors suggested that plasticity induced closure was present and was the main contributing factor to crack growth rate retardation following an overload, with crack tip blunting and compressive residual stress playing a secondary role. However, the crack growth rate behaviour from epoxy resin infiltration differs somewhat to the behaviour following an overload cycle. The crack growth rate does not initially increase and the retardation effect is not sustained for the same period of cycles.

The impact of R-ratio on plasticity-induced crack closure has been investigated by several authors on several materials [60-64]. Plasticity-induced crack closure effects appear to diminish following an overload cycle in steel with cyclic loading at high R-ratios of 0.2, partly due to the reduced stress range but also partly due to the reduced severity of the overload cycle. Instead, the retardation behaviour is generally attributed to compressive residual stress ahead of the crack tip.

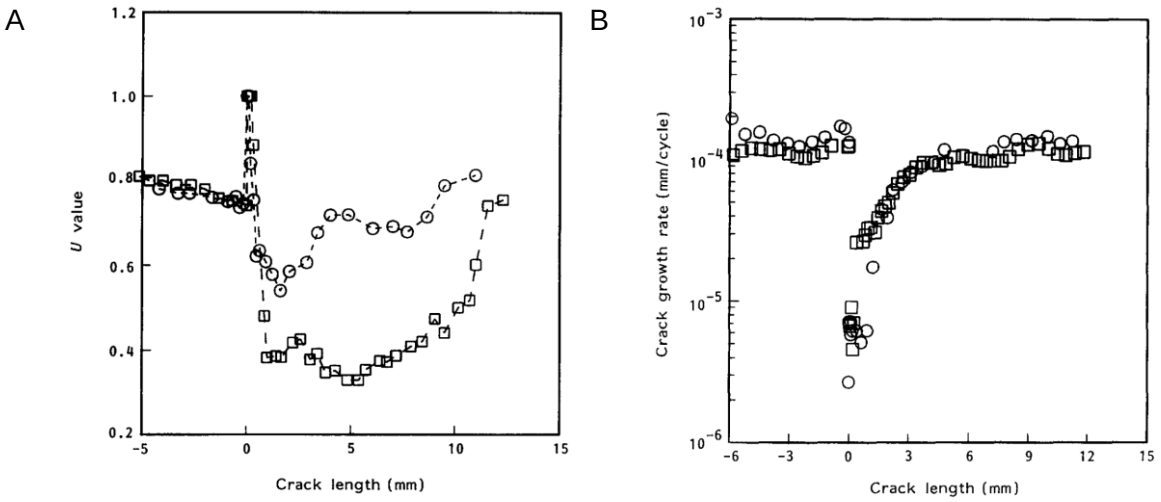

Figure 2-37: Crack closure U value versus relative crack length following an overload cycle for OLRs of 1.5 (circle symbols) and OLR of 2 (square symbols) for AISI 304 stainless steel at R-ratio of 0.1 and ΔK of 22 MPam$^{0.5}$. B) Crack growth rate versus relative crack length following an overload for a specimen infiltrated with epoxy resin at R-ratio of 0.1 and ΔK of 26 MPam$^{0.5}$ [62].

Damri and Knott [97] attempted to investigate the role of compressive residual stress on the crack growth rate retardation behaviour following a overload cycle in a low carbon steel with yield strength of 240 MPa. Specimens were subjected to cyclic loading with R-ratio of 0.2 at 12 $MPam^{0.5}$. An overload with OLR of 2.5 was applied at 9 mm crack length where crack tip blunting effects were observed, accompanied by a large crack growth retardation effect (Figure 2-38). The test was repeated, but the specimen was extracted immediately following the application of the overload cycle, and heat treated to remove internal residual stress induced by the overload cycle. No retardation effect following the overload was seen in the crack growth rate subsequent to heat treating (Figure 2-38). Despite the presence of crack blunting, the authors attributed the retardation effect in crack growth rate following an overload on compressive residual stresses ahead of the crack tip. More recent studies on aluminium material tend to agree with these conclusions and disregard plastic closure effects [107].

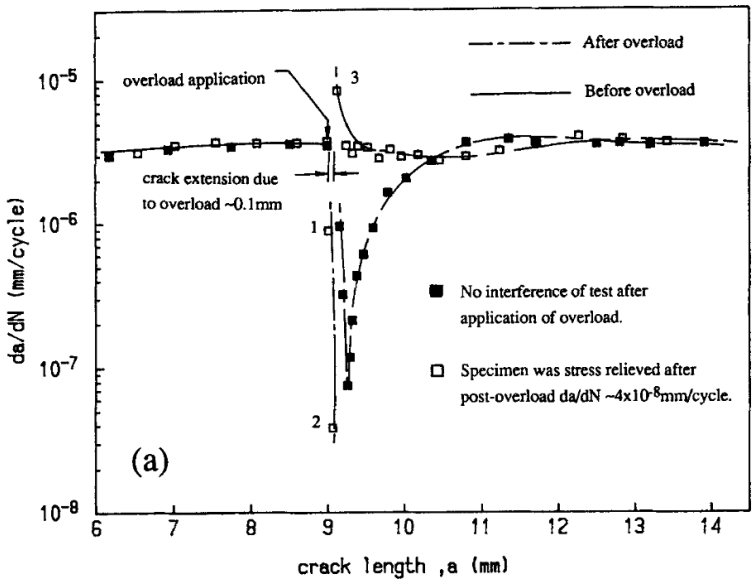

Figure 2-38: Crack growth rate versus crack length following an overload cycle (applied at 9 mm crack length) for an un-interfered specimen and a specimen that received a stress relieving operation.

Duquesnay, et al [108] tested notched specimens (Figure 2-39 A) made from 2024-T351 aluminium with 380 MPa yield strength with periodic underloads resulting in compression every 1000 cycles (Figure 2-39 C). The stress range versus cycles to failure relationship was similar for all specimens regardless of notch size and suggested a slight decrease in the lifetimes when compared with un-notched samples (Figure 2-39 B). A similar result was found on notched 1045 steel materials with compressive underloads [94]. The authors suggested that plastic closure effects were negated and possible tensile residual stress at the crack tip may have accelerated crack growth rate which contributed to the reduction in

lifetimes. It is possible however, that the reduced thickness of the cross section (and therefore less crack growth required for failure) may have contributed towards the reduction in fatigue life.

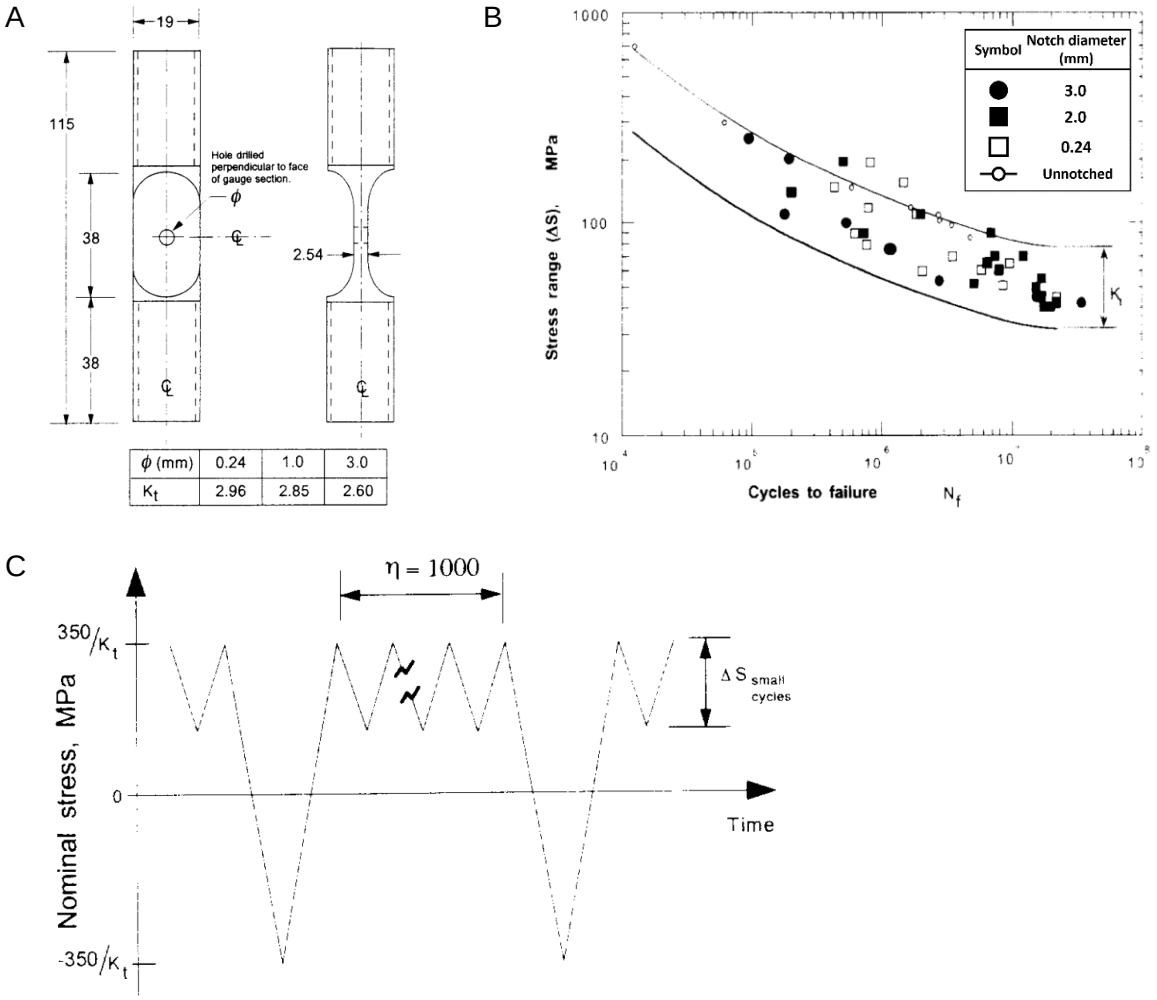

Figure 2-39: A) Notched specimens with various notch sizes from 0.24 mm to 3 mm diameter made from 2024-T351 aluminium. B) Stress range versus cycles to failure for notched specimens and un-notched specimens. C) Cyclic amplitude loading conditions with maximum load (of 100 % yield stress) and minimum load chosen depending on the stress concentration factor of the notch geometry. Single periodic underloads resulting in R-ratio of -1 were applied every 1000 cycles from [108].

Robin et al [109] cited in Skorupa's comprehensive review [89], applied a combination of tensile and compressive overloads and underloads in 316L austenitic stainless steel material. Tensile overloads caused the most retardation in crack growth rate. The presence of additional underloads either before or after the tensile overload resulted in less retardation effect being exhibited. It is thought the underload may cause residual stress

relaxation effects that diminish the retardation effect caused by compressive residual stress induced by the tensile overload.

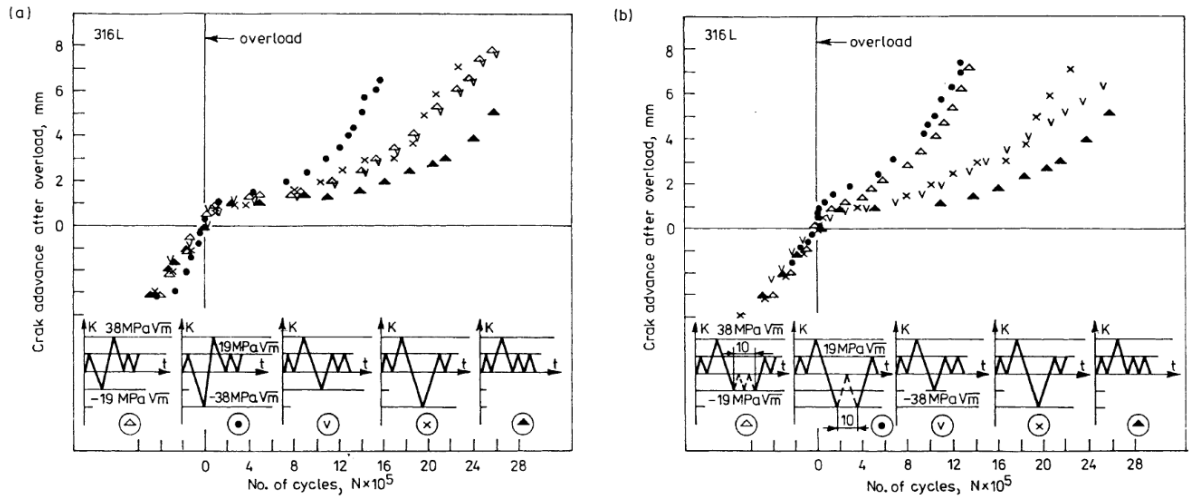

Figure 2-40: Crack growth retardation following different combinations of compressive and tensile underloads and overloads [109] as cited in [89].

Although the evidence appears to bias towards compressive residual stress ahead of the crack tip as the cause of crack growth rate retardation following an overload cycle, the debate continues [110]. Since both plastic-closure and compressive residual stress ahead of the crack tip are produced from similar conditions, it is entirely possible that both mechanisms exists simultaneously, each contributing towards the crack growth rate retardation effect. The ratio of each mechanism's contribution is unclear and likely to be affected by individual loading/environmental conditions and material properties. Crack tip blunting and plastic closure are common features observed in lower R-ratios and materials with relatively low yield strength. Less common is investigative work on higher yield materials, where the increased resistance to plastic deformation may reduce the impact of these mechanisms. Instead, it is more likely that compressive residual stress ahead of the crack tip be responsible for the crack growth rate retardation effect in materials such martensitic stainless steels.

Multiple studies on single periodic overloads in stainless steel materials show that a retardation effect of crack growth exists that has the effect of lengthening the number of cycles to failure in multiple materials [62, 89-98]. To the author's knowledge, no cases of decreased lifetime have been found with periodic tensile overloads in steel material under ambient conditions without additional interference that subsequently removed closure mechanisms or compressive residual stress.

2.3 Effects of shot peening on fatigue behaviour and life

2.3.1 Shot peening characterisation

Shot peening is a cold work surface treatment usually applied locally to stress concentration features on engineering components such as fir-tree-root-fillets of turbine blades. The process of shot peening involves the bombardment of spherical shots onto the free surface. The kinematic energy from each impinging shot deforms the surface causing significant localized plastic deformation in the form of dimples on the surface (Figure 2-41). After the initial shot impact, the elastically deformed material is prevented from returning to its original shape by the plastically deformed material and a misfit strain (known as an eigenstrain) is produced.

The shot peening process can be controlled by modifying its intensity and coverage. The intensity of the shot peening process is further controlled by three variables: the material hardness of the shot, shot size and shot velocity. The shot peening intensity is characterised by the impact that shot peening has on one side of an Almen strip (made from SAE1070 spring steel material with known material properties and known thickness of either A, C or N). A shot peen intensity value of '10A' means a 0.010" deflection of an Almen strip with a thickness 'A' [111]. Coverage is a measure of the shot peened area measured as a percentage of the area that has been shot peened. If it takes time t to apply a 100 % coverage, then a coverage of 200 % would mean a shot peening time of $2t$.

It is well known in the literature that the application of shot peening induces three important effects on and beneath the surface that have implications on the resistance to fatigue of the material. These are:

- A considerable increase in the surface roughness due to the large plastic deformations produced from the spherical shot.
- The large deformation at the surface increases the density of dislocations that impair dislocation movement causing a hardening of the material as well as increased yield strength, especially near the surface (known as strain hardening).
- A resulting compressive residual stress field beneath the shot peened surface (Figure 2-41), followed by a counterbalancing tensile residual stress field further below the surface.

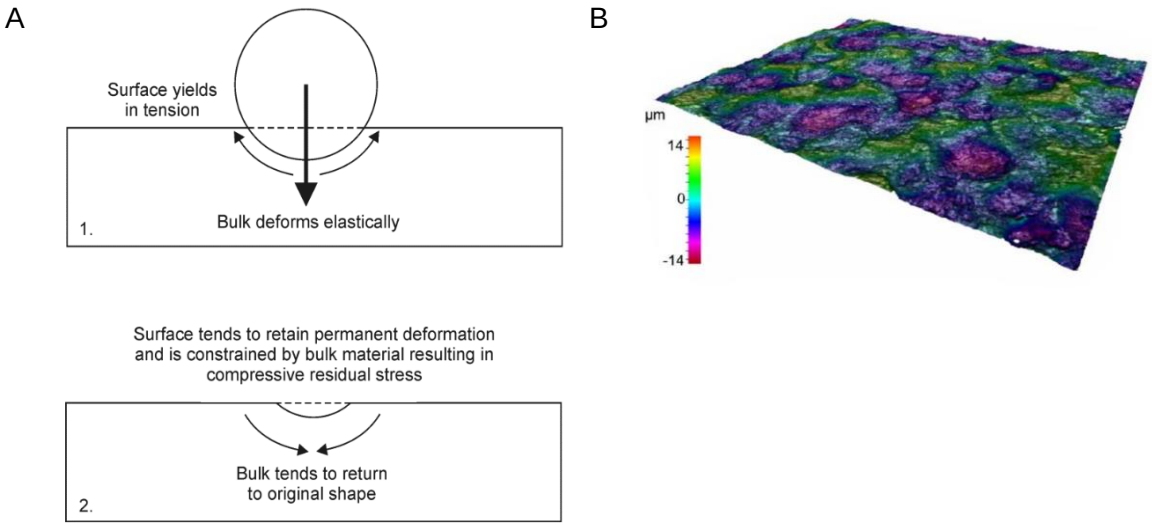

Figure 2-41: A) Mechanism of formation of compressive residual stresses during shot peening. B) Surface topology of FV448 after T0 shot peening from [10].

2.3.2 Surface roughness

The effect of surface roughness on number of cycles to crack initiation and fatigue life is well known across various materials [112-115]. A higher surface roughness encompasses a higher density and intensity of micro stress concentration features, thus reducing the number of cycles to initiation and consequently overall fatigue life. Shot peening is known to increase surface roughness which is considered to be detrimental to fatigue resistance.

The surface of U-notched samples made from FV448 were subjected to four typical shot peening treatments with known intensity and coverage, readily available in industry (Table 2-1). The surface roughness of an as-received ground surface condition 'G' was also tested for comparative purposes.

Process	Designation	Intensity	Coverage (%)	Shot diameter (mm)	Shot hardness (HRC)	Shot velocity (ms^{-1})
MI110R 04A 200%	T1	4A	200	0.28	45–52	26
MI230R 13A 200%	T0	13A	200	0.58	45–52	57
MI330R 13A 200%	T2	13A	200	0.84	45–52	35
MI330R 18A 200%	T3	18A	200	0.84	45–52	54

Table 2-1: Various shot peening process parameters applied to U-notched FV448 specimens from [22].

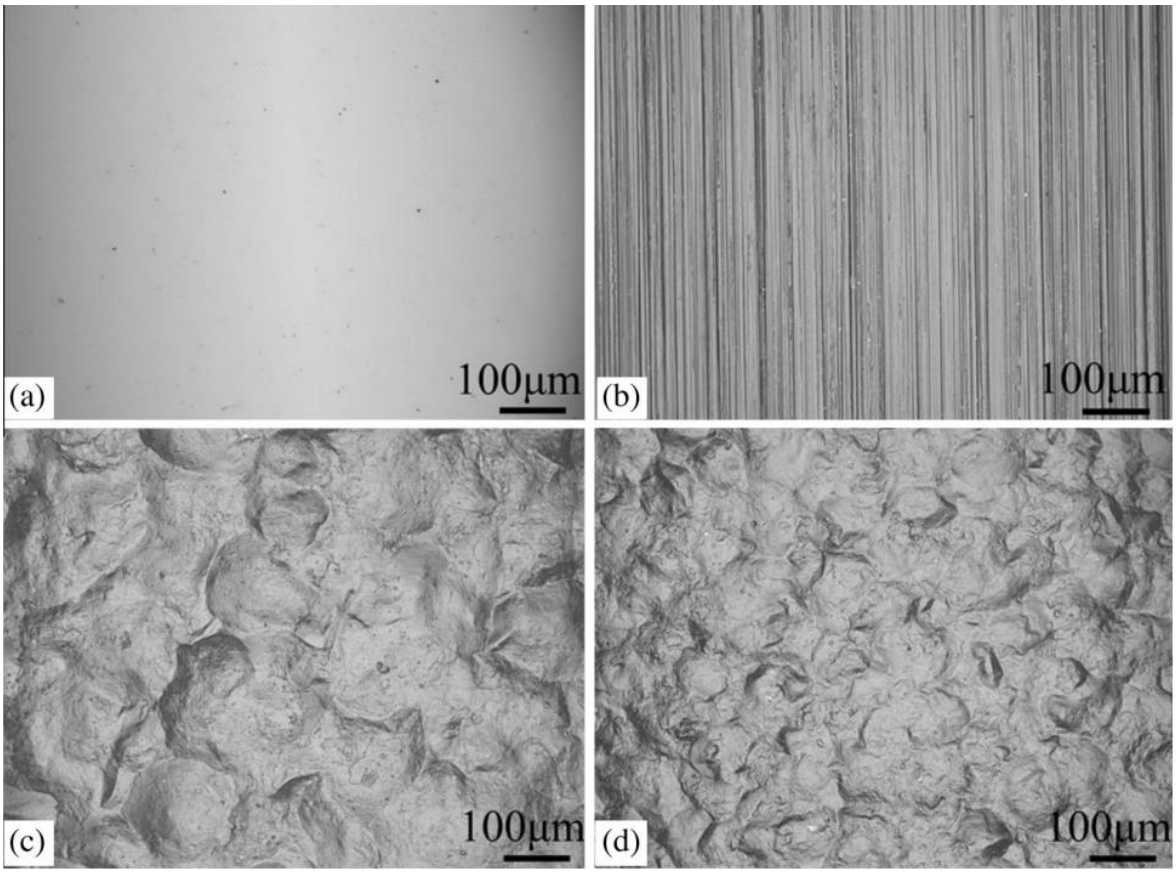

Figure 2-42 A) Polished surface condition with R_a typically less than 0.1 µm. B) Ground surface condition with R_a of approximately 0.6 µm. C) T0 shot peened surface condition with R_a of approximately 3.4 µm and D) T1 shot peened surface condition with R_a of approximately 1.2 µm [50].

The surface roughness R_a (defined as the arithmetic mean deviation from the mean line over the length of the profile [116] Equation 2-16) of a ground and polished surface condition using tactile measurement methods was approximately 0.6 µm and typically less than 0.1 µm. Shot peening the surface with a relatively low intensity of 4A resulted in an increase in surface roughness with R_a of 1.2 µm. More intense shot peening processes increased the surface roughness considerably with R_a values between 3 µm and 4 µm (Figure 2-42 and Figure 2-43). However, increasing shot peening intensity further is not expected to increase surface roughness values, which plateau after a particular shot peening intensity depending on material properties [117].

$$R_a = \frac{1}{l}\int_0^l |y(x)|dx \qquad \text{Equation 2-16}$$

Where l is the length of the profile and y is the length deviation measurement of the surface from the mean line.

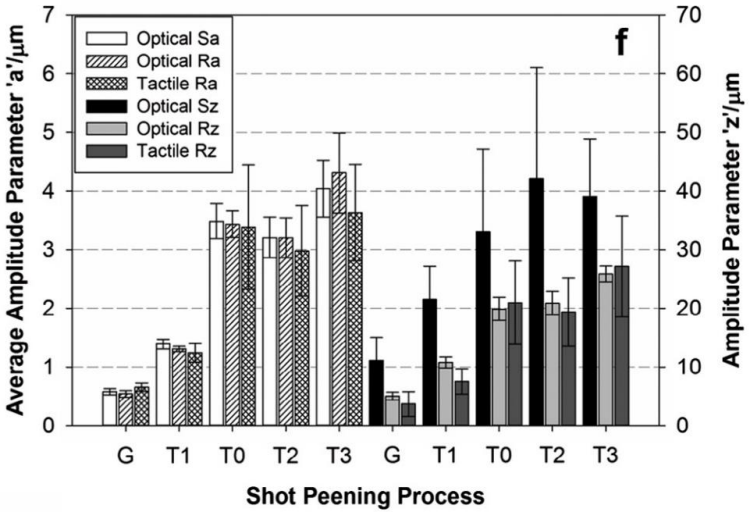

Figure 2-43: Tactile and areal surface roughness measurements for each surface condition (where G is ground and T1, T0, T2 and T3 are different shot peening process) from [22].

2.3.3 The induction of strain hardening and residual stress from shot peening

The impact of shot peening on the surface induces some quantity of measurable plastic deformation, and therefore some quantity of plastic strain and corresponding residual stress. Three popular methods for quantifying the true plastic strain and residual stress versus depth from surface profiles, from shot peening, have been explored by Soady [10, 22] and are briefly discussed below.

- Microhardness: Traverse technique

Microhardness measurements were taken conforming to *BS EN ISO 6507-1:2008* [118] at progressively increasing depths from the shot peened surface. The true plastic strain profile with depth can be determined from the microhardness measurements assuming microhardness is proportional to yield strength and using a calibration technique described in [10]. The microhardness traverse technique has been used to establish strain hardening profiles with varying degrees of success.

- X-ray diffraction (XRD)

X-ray beams impact the surface of a specimen at various angles (typically ± 45 °) the rebounding X-rays superimpose in particular locations, creating a constructive interference X-ray diffraction pattern. The well-known Bragg's-Law (Equation 2-17) can be used to determine fundamental information about the material's crystal structure, such as the atomic plane d-spacing, to establish plastic strain at the surface. Incremental layer removal of the surface material, followed by repeated XRD testing, along with the full width half at half maximum (FWHM) calibration technique, produces strain and residual stress versus depth

profiles. A full explanation of the derivation of strain and stress from XRD measurement information can be found in [10] along with relevant additional literature.

$$n\lambda = 2d\sin\vartheta \qquad \text{Equation 2-17}$$

Where n is an integer multiple of the wavelength, λ is the wavelength of the X-ray, d is the distance between crystallographic (hkl) planes and ϑ is the angle of X-ray penetration with the surface where constructive interference occurs.

- Electron Backscatter Diffraction (EBSD)

Electron beams are used as opposed to X-rays using a similar technique to the XRD method which provides fundamental information about the crystallographic orientation. The misorientation of this crystal orientation can be used to measure the extent of strain hardening. More information regarding the application and quantification of the true plastic strain can be found in [10] along with relevant additional literature.

- Hole-drilling

The residual stress versus depth profile can be established by drilling a hole into the shot peened surface of the specimen and measuring the resulting deformation around the hole using a configuration of several strain gauges. The residual stresses with depth are then determined using calibrations determined empirically or, more recently, through FE modelling [119]. Repeatability studies indicate hole-drilling typically produces a larger range of values at the surface which quickly diminish at a depth of 0.3 mm [120].

Three techniques (excluding hole drilling) were carried out on flat and U-notched surfaces of FV448 martensitic stainless steel and compared (Figure 2-44 A and B). The true plastic strain versus depth profile using microhardness measurements could not be established within the first 100 μm from the surface since the unconstrained free surface causes an underestimation in material hardness values. In addition, the true plastic strain was overestimated compared to XRD or EBSD methods due to the additional resistance to indent deformation from compressive residual stress, a result also seen in other work [121, 122]. The corresponding estimated increase in the yield strength of the material is seen when calculated from empirical fitting of the Ramberg-Osgood relationship to monotonic tensile data (Figure 2-44 B).

The angle of X-ray beams for the U-notched sample was restricted to ± 30 ° due to notch shadowing effects. Despite this, the results from XRD and EBSD were similar and found to produce both strain hardening profiles and residual stress profiles with relatively high

confidence (Figure 2-44 A and B). The option to choose one method over another depends on material and equipment availability considerations.

The strain hardening profiles between a ground surface and shot peened surface obtained via XRD show that shot peening induces a considerable strain hardening effect. Additionally, the ground surface indicated some small strain hardening at the surface, which may be indicative of measurement error (expected to be higher at the surface) or effects induced from the grinding process. The strain hardening profiles for a flat surface and U-notched surface were also considered and compared. A reduced true strain versus depth profile was obtained for the notched specimen. However, an increased residual stress versus depth profile was obtained for the notched specimen. Material constraint effects from the notch geometry may explain these results, although the difference in the results may be within the expected scatter range [10, 22, 123]. The true strain versus depth profiles are larger for more intense shot peening processes as expected (Figure 2-44).

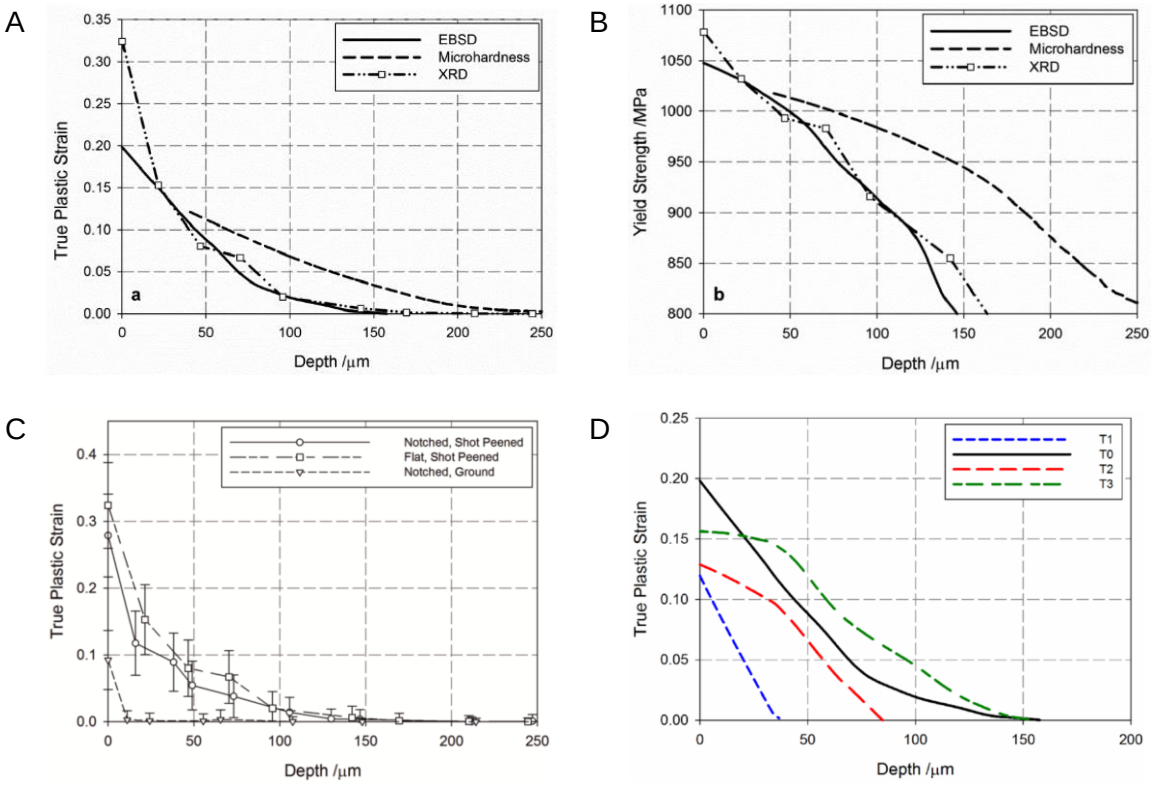

Figure 2-44: True plastic strain versus surface depth profiles produced using EBSD, XRD and microhardness methods. B) The expected yield strength of the material from the true plastic strain versus depth profiles from a Ramberg-Osgood fit of monotonic tensile data of FV448. C) True plastic strain versus depth profiles produced using XRD for a non-peened U-notch surface, shot peened U-notch surface and shot peened flat surface. D) True plastic strain versus depth produced using EBSD for four different shot peening process from [10].

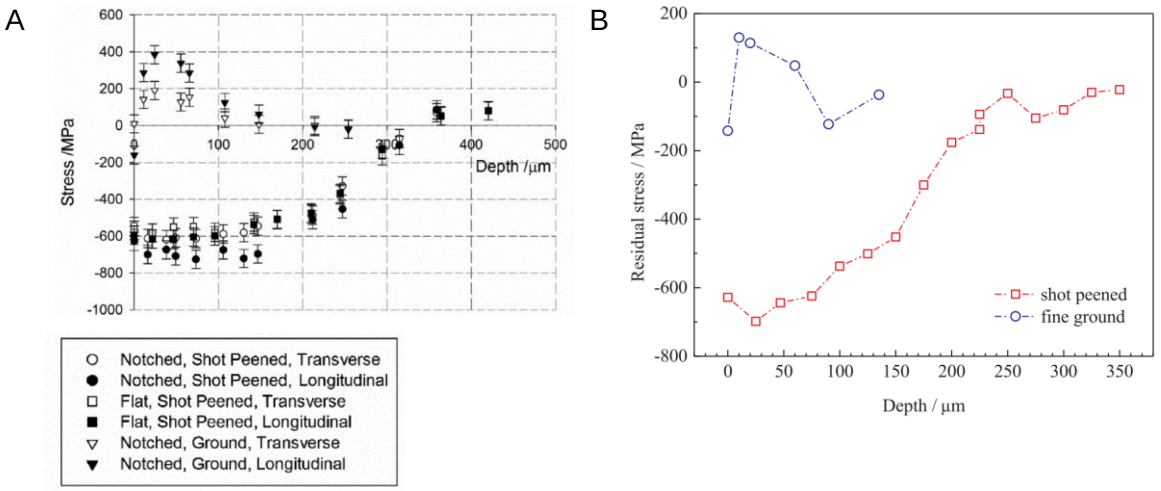

Figure 2-45: Residual stress profiles for notched and flat samples obtained via XRD before and after T0 shot peening from [10]. B) Residual stress profile of FV566 obtained via XRD before and after S170 8-12A shot peening from [124].

2.3.4 Shot peening effects on fatigue behaviour

The shot peening process caused significant deformation at the edges of fatigue specimens made from FV448, inducing the formation of edge 'lips' (Figure 2-46) on plain bend bar specimens. The lips acted as stress concentrations which influenced the crack initiation behaviour by increasing the probability of edge crack initiations. The 'lips' were removed by grinding which restored the typical crack initiation locations on the notch surface.

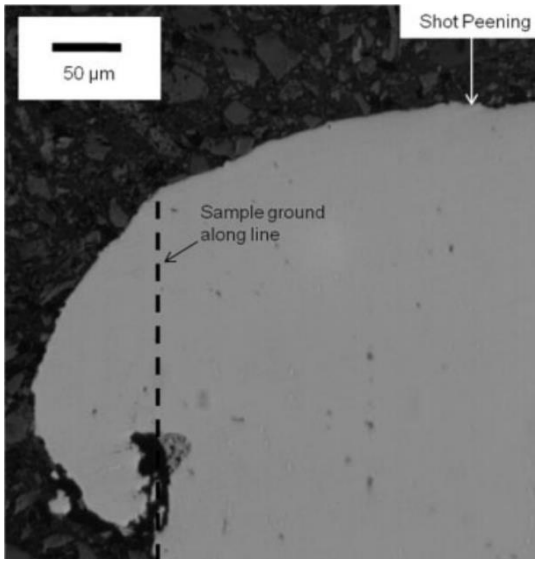

Figure 2-46 Lips produced at the edge of specimen as a result of large deformation of the surface due to shot peening, increasing the probability of edge crack initiations from [72].

Increasing the strain range at the surface of a 2.25 mm radius by 1.25 mm deep notch, increased the number of crack initiation events in FV448. Interestingly, a high intensity shot peen such as T0, increased the quantity of crack initiations observed on the surface. It was noted by the authors [50] that the less intense T1 shot peen induced apparent sub-surface crack initiations. The T1 shot peen, induced a strain hardening and compressive residual stress, which increased the resistance to crack initiation on the surface, leading to fewer crack initiation events. However, additional surface damage from large plastic deformation such as folding of material and pre-existing cracks on the surface were observed, due to the higher intensity T0 shot peen. This increase in surface damage increased the number of crack initiation events, and also resulted in increased tortuosity of short cracks less than 500 µm. While the surface damage decreased resistance to crack initiation, an increased crack tortuosity may contribute towards the retardation of short crack growth rates.

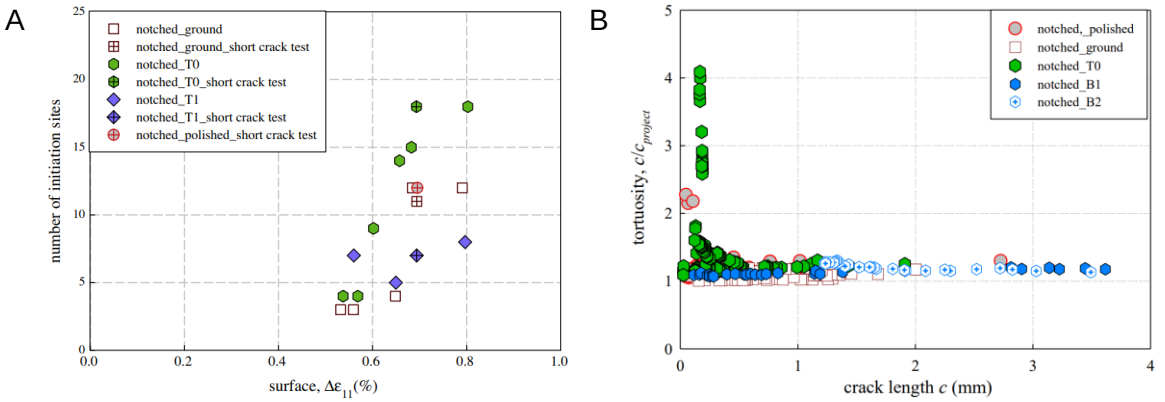

Figure 2-47 A) The number of initiation events verses the notch surface strain range for non-peened and shot peened surface conditions from [50]. B) Tortuosity as a ratio of total crack length to projected crack length versus projected crack length for non-peened and shot peened surface conditions from [5].

Short crack depth to half short crack surface length (*a/c*) ratios (Figure 4-10) for FV448 specimens with polished and shot peened surfaces were compared [50]. The *a/c* ratios on the fracture surfaces of specimens with polished surfaces were typically in agreement with expected values found by applying theoretical equilibrium assumptions and combined with FE modelling (Figure 2-48) [51-53, 125]. Particularly high *a/c* ratios were observed that were greater than 1 and attributed to stringers oriented unfavourably, encouraging particularly rapid crack growth in the depth direction. On the other hand, the compressive residual stress field from shot peening resisted crack growth in the depth direction causing lower *a/c* crack ratios (Figure 2-49 and Figure 2-50 A).

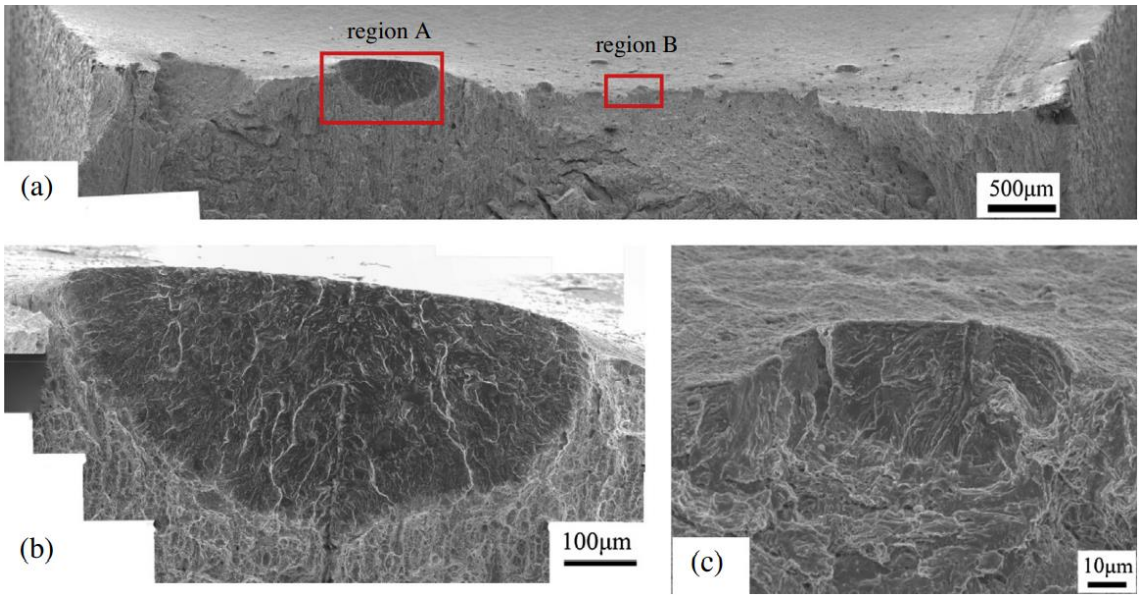

Figure 2-48 A) Low magnification SEI image of the fracture surfaces of a polished specimen showing two semi-elliptical fatigue regions that are shown at a higher magnification in B) and C) from [50].

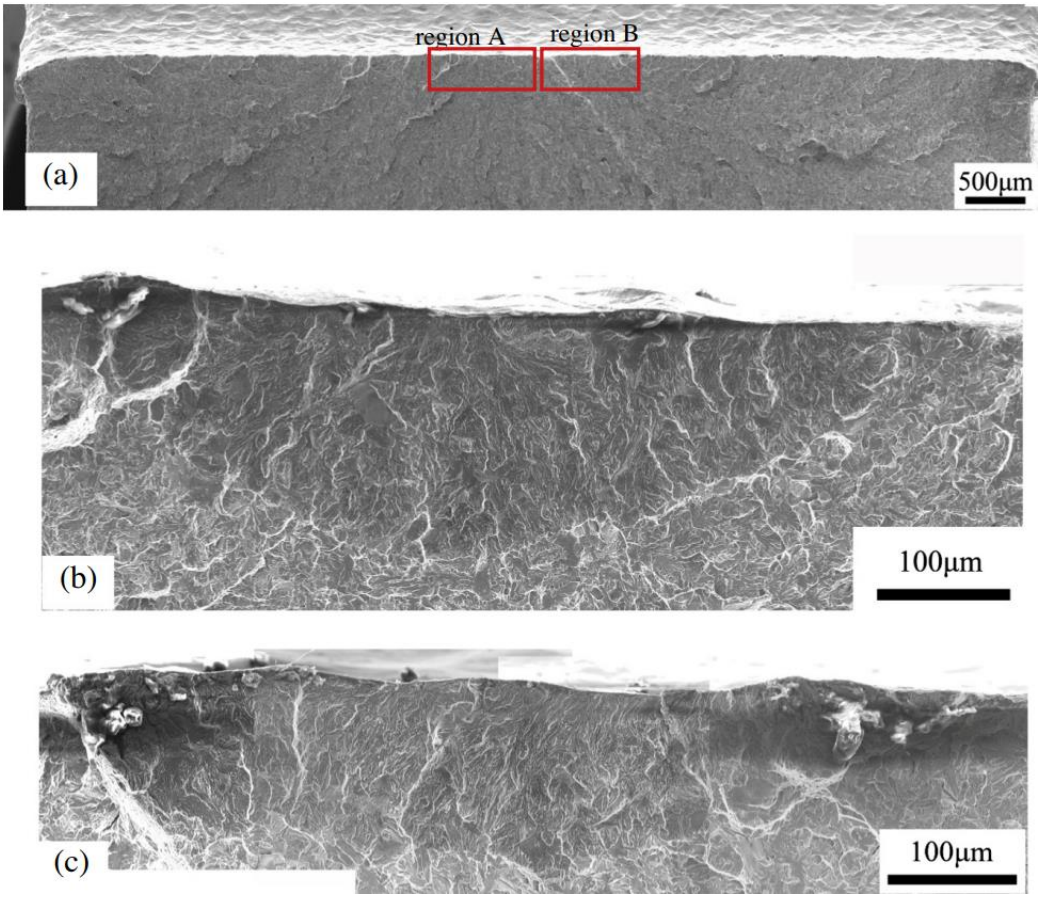

Figure 2-49 A) Low magnification SEI image of the fracture surface of a T0 shot peened specimen showing two semi-elliptical fatigue regions that are shown at a higher magnification in B) and C) from [50].

The short crack growth rate versus $\Delta K_{Surface}$ relationship was obtained via surface replication techniques in ground and shot peened U-notch specimens with 2.25 mm radius and 1.25 mm depth made from FV448 material. The compressive residual stress field and strain hardening on and beneath the notch surface induced by the T0 shot peening process, retarded the short crack growth rate, especially for low ΔK values (Figure 2-50 B and C). The reduction in short crack growth rates (by an average of approximately between 10 to 15 times compared with non-peened and long crack results), despite possible decreased resistance to crack initiation, increased the fatigue life of specimens, especially for lower fatigue strain ranges at the notch surface (Figure 2-50 D).

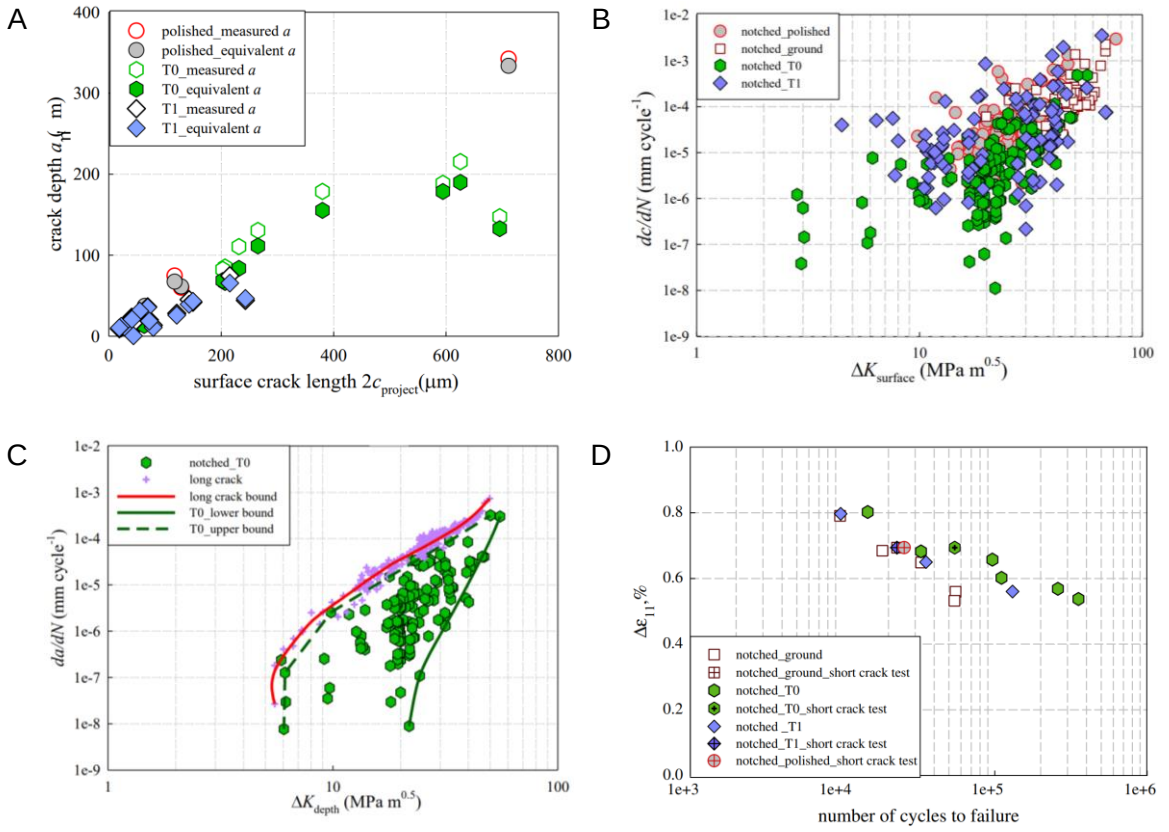

Figure 2-50 A) Crack depth (a) versus projected surface crack length ($2c_{project}$) for polished and shot peened U-notch surface conditions from [5]. B) Short crack surface growth rate versus $\Delta K_{Surface}$ for non-peened and shot peened U-notch surface conditions from [50]. C) Short crack surface growth rate versus $\Delta K_{Surface}$ for long crack (and approximate non-peened surface condition) and T0 shot peened surface condition from [50]. D) U-notch surface strain range versus number of cycles to failure for non-peened and shot peened U-notch surface conditions from [50].

2.3.5 Cyclic loading conditions on shot peening fatigue life extension

The true plastic strain versus depth profiles from the surface of a non-peened and T0 shot peened notch with 2.25 mm radius and 1.25 mm depth were obtained using XRD before fatigue testing, after one cycle and after 50 % of the expected lifetime under constant amplitude with a strain range of 0.68 % and R-ratio of 0.1. A reduction in the amount of strain hardening was seen after one cycle in both the non-peened and peened sample. After 50 % of the total lifetime, strain hardening from shot peening was effectively diminished to pre-peened levels, an expected result considering the typical cyclic softening behaviour displayed by FV448 and similar martensitic stainless steels [21-23].

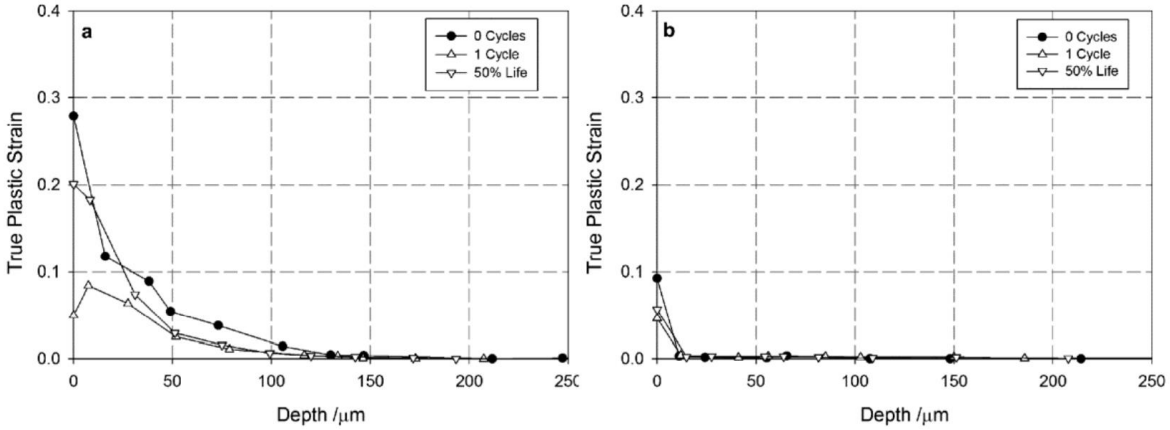

Figure 2-51 The relaxation of strain hardening profiles before cyclic loading, after one cycle and after 50 % expected lifetime at 0.68 % strain range at the surface of a 2.25 mm radius x 1.25 mm deep notch after A) T0 shot peening and B) grinding from [10].

The residual stress profiles of a T0 shot peened U-notch with 2.25 mm radius and 1.25 mm depth were measured using XRD before fatigue testing, after one cycle and after 50 % of the expected lifetime under constant amplitude with a strain range of 0.68 % and R-ratio of 0.1 [10, 126]. Some residual stress relaxation was observed in the transverse direction after one cycle which appeared to stabilise for at least approximately 50 % of expected life (Figure 2-52 A). The residual stress in the longitudinal direction (along the tensile axis) was maintained despite the presence of cyclic loading in the LCF regime (Figure 2-52 B).

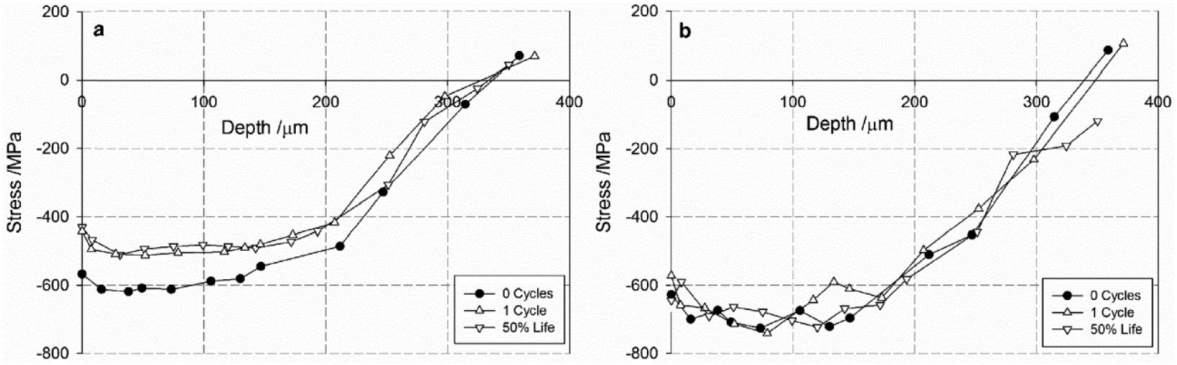

Figure 2-52 The relaxation of residual stress profiles before cyclic loading, after one cycle and after 50 % expected lifetime at 0.68 % strain range at the surface of a T0 shot peened 2.25 mm radius x 1.25 mm deep notch in the A) transverse direction and B) longitudinal direction from [10].

Similar testing was carried out on non-peened U-notch specimens and the residual stress measured using XRD [10, 126]. A tensile residual stress was seen in the transverse direction but was greater in the longitudinal direction due to the notch machining process. Tensile loading past the yield strength of the material in the longitudinal direction meant that a large compressive residual stress was formed in the longitudinal direction (Figure 2-53 B). Due to the unidirectional application of the load, only a small compressive residual stress was induced in the transverse direction after one cycle (Figure 2-53 A). The longitudinal compressive residual stress after one cycle was accurately predicted using a kinematic-isotropic hardening material model in ABAQUS, especially near the notch surface.

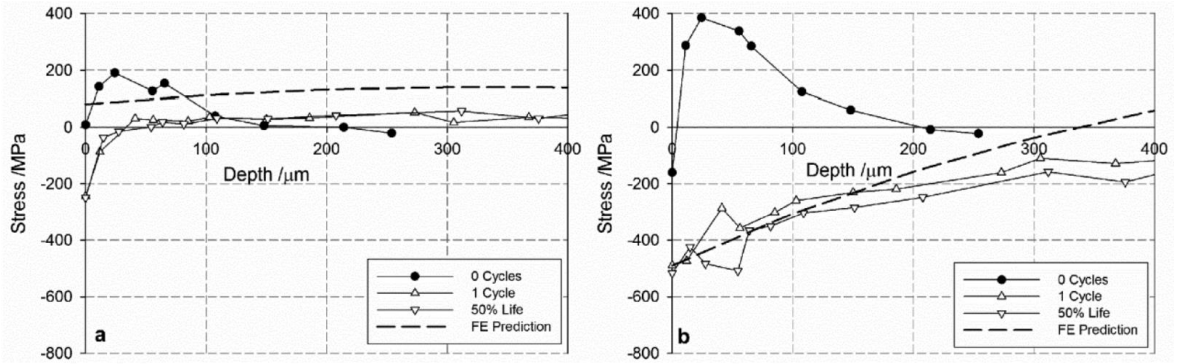

Figure 2-53 The relaxation of residual stress profiles before cyclic loading, after one cycle and after 50 % expected lifetime at 0.68 % strain range at the surface of a ground 2.25 mm radius x 1.25 mm deep notch in the A) transverse direction and B) longitudinal direction from [10].

You [125, 127, 128] developed the FE model from Soady [10, 126] further to allow relatively confident predictions of the residual stress profiles in different sample geometries and at different strain ranges using the eigenstrain approach. Residual stress profiles in the

longitudinal and transverse directions from a T0 shot peened plain bend bar and U-notch after one fatigue cycle at 0.63 % strain range and R-ratio of 0.1 were modelled using FE modelling and validated with experimentally obtained data. The FE model prediction of residual stress was in good agreement with experimental testing (Figure 2-54). The FE model was then used to predict residual stress profiles after one cycle at different strain ranges in the plain bend bar and in the U-notch specimen. In both cases, residual stress relaxation was most prominent in the transverse direction. A greater amount of residual stress relaxation was seen in the plain bend bar as opposed to the U-notch specimen (Figure 2-54). The material constraint effects from the U-notch geometry, maintain the residual stress induced from the shot peening process. A greater lifetime extension effect from shot peening might therefore be expected in U-notched specimens.

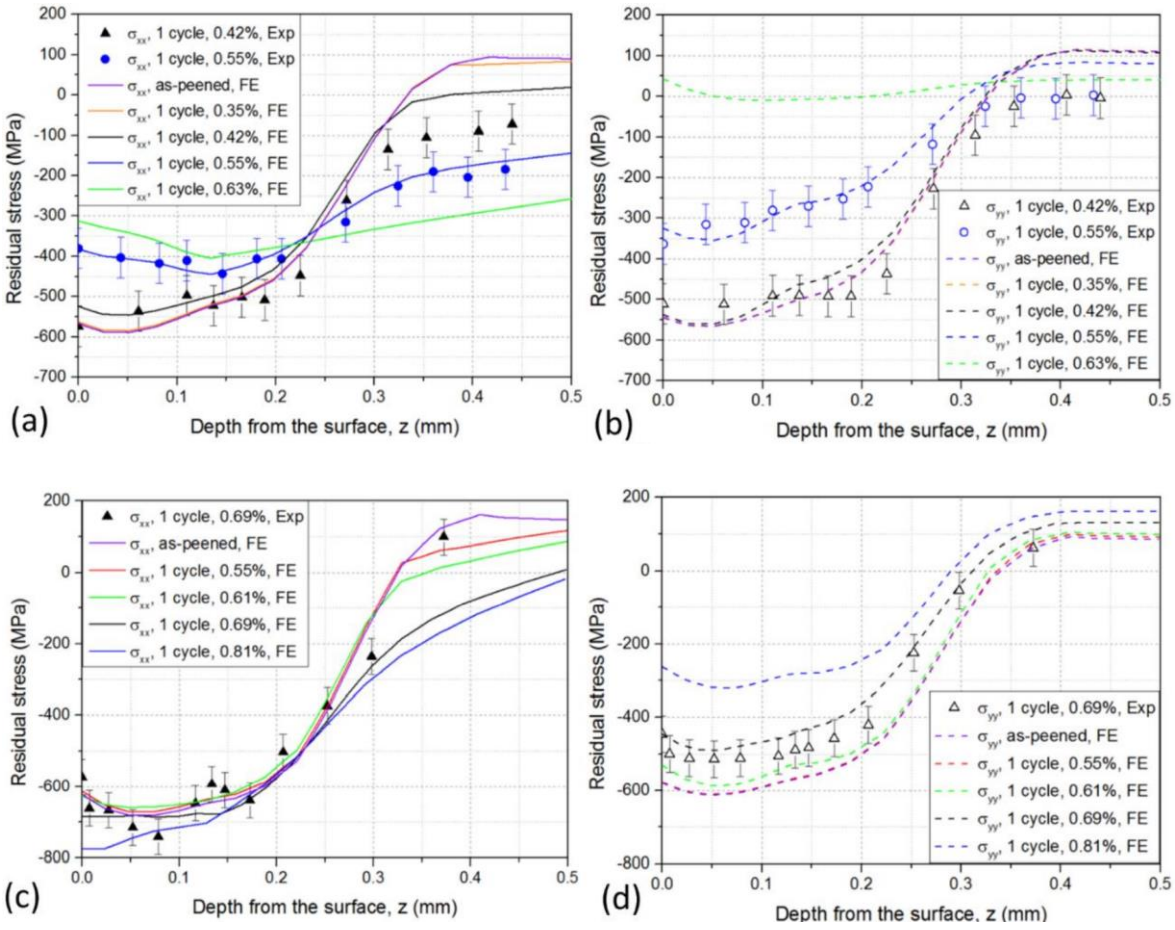

Figure 2-54 Simulated residual stress relaxation after one cycle compared with experimental results for A) T0 plain bend bar in the longitudinal direction and B) the transverse direction and C) T0 shot peened 2.25 mm radius x 1.25 mm deep notch in the longitudinal direction and D) the transverse direction from [125].

The compressive residual stress profiles of shot peened (with 0.5 mm radius shot and velocity between 25 ms^{-1} and 100 ms^{-1}) AISI 4340 high strength material with yield strength of 1248 MPa was measured after 30 constant amplitude fatigue cycles at various stress

ranges with R-ratio of -1 [129] (Figure 2-55 A). A maximum stress between 112 % and 153 % of the yield strength of the material was required to induce residual stress relaxation effects. However, fully reversed loading induces a greater residual stress relaxation response due to the compressive loading response (Figure 2-55 B), as seen with compressive overloads.

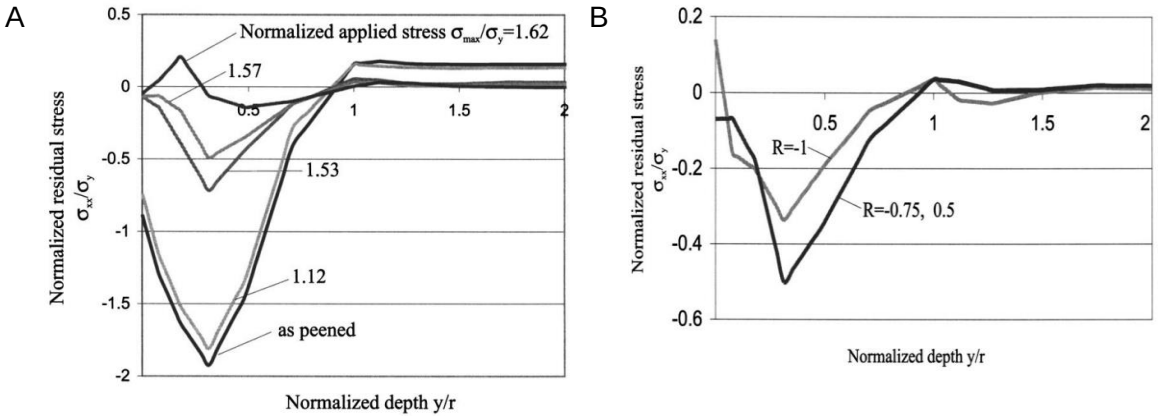

Figure 2-55 A) Compressive residual stress profiles after 30 cycles at R-ratio of -1 in high strength AISI 4340 from [129]

The influence of residual stress relaxation effects on the fatigue life of non-peened and peened normalized steel with yield strength of 600 MPa was carried out [130]. Cylindrical specimens were subjected to shot peening with approximately 16A intensity and 200 % coverage. The compressive residual stress profiles of the specimens were measured before fatigue and after various number of fatigue cycles had been applied with various strain ranges under fully reversed loading. It is clear that increasing the strain range induces more prominent residual stress relaxation effects (Figure 2-56 A). At 0.4 % total strain amplitude and R-ratio of -1, the lifetime extension benefit from shot peening is diminished (Figure 2-56 B) despite only partial residual stress relaxation of the specimen (Figure 2-56 A).

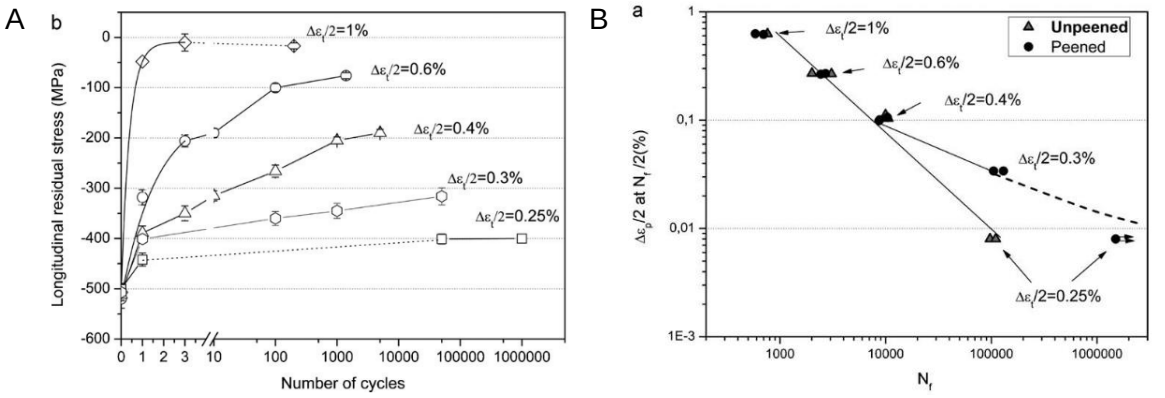

Figure 2-56 A) Longitudinal compressive residual stress versus number of cycles for different strain ranges. B) Plastic strain amplitude versus fatigue life for peened and non-peened specimens from [130].

The application of T0 shot peening on plain bend bars made from FV448 marginally increased the total fatigue lifetime, although a clear lifetime extension effect can be seen at lower strain ranges. However, a more prominent fatigue lifetime extension can be observed for specimens with a notch of 2.25 mm radius and 1.25 mm depth. The amount of lifetime extension compared with non-peened specimens is similar to Dianyin [131], who found that shot peening extended the fatigue lifetime of a turbine blade by a factor of 5. The increase in lifetime extension in the U-notch geometry is attributed to notch constraint effects which significantly increase the resistance to residual stress relaxation effects. With increasing strain range, the lifetime extension benefit from shot peening decreased, where increased cyclic softening and residual stress relaxation is expected at higher strain ranges (Figure 2-56). A sharper notch geometry, with a lower radius, increased the lifetime extension effect due to increased notch material constraint effects [10, 126] (Figure 2-57 B).

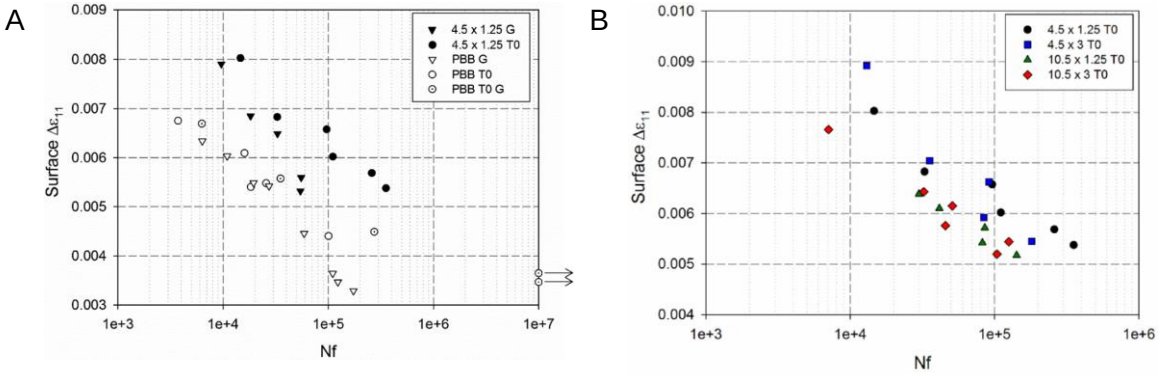

Figure 2-57 Surface strain range versus total life for ground and T0 shot peened plain bend bars and U-notched (2.25 mm radius x 1.25 mm deep notch) specimens and B) T0 shot peened specimens with different notch geometries (radius of 2.25 mm and 5.25 mm and depths of 1.25 mm and 3 mm). R-ratio is 0.1, from [10].

The effect of a single overload under various loading sequences at the beginning of fatigue tests (Figure 2-58) on the lifetimes of shot peened cylindrical specimens made from normalized steel under fully reversed loading were investigated by Dalaei [130]. The lifetimes for peened and non-peened specimens subjected to constant amplitude of 0.3 % (baseload) and 0.6 % (overload) total strain amplitude were carried out. Full residual stress relaxation was seen at 0.6 % total strain amplitude while the compressive residual stress from shot peening increased the lifetime of the specimen considerably compared to the non-peened surface condition. The lifetimes of specimens were significantly reduced when a tensile overload was immediately followed by a compressive overload (TX), as opposed to when the compressive overload was applied before the tensile overload (CX) (Figure 2-59). The application of the compressive overload after the tensile overload, resulted in a relaxed residual stress for the remainder of the test, reducing the lifetime. On the other hand, when the compressive overload is applied before the tensile overload (CX), the

residual stress was initially relaxed, but the tensile overload then reapplied some compressive residual stress. Therefore, a larger compressive residual stress was apparent for the remainder of the test, slightly improving fatigue lifetime over (TX) overload applications. The application of 1000 baseload cycles before overloading, allowed some initial residual stress relaxation before the application of the fully reversed overload (C1000). The initial residual stress relaxation reduced the tensile overload's ability to reapply the residual stress.

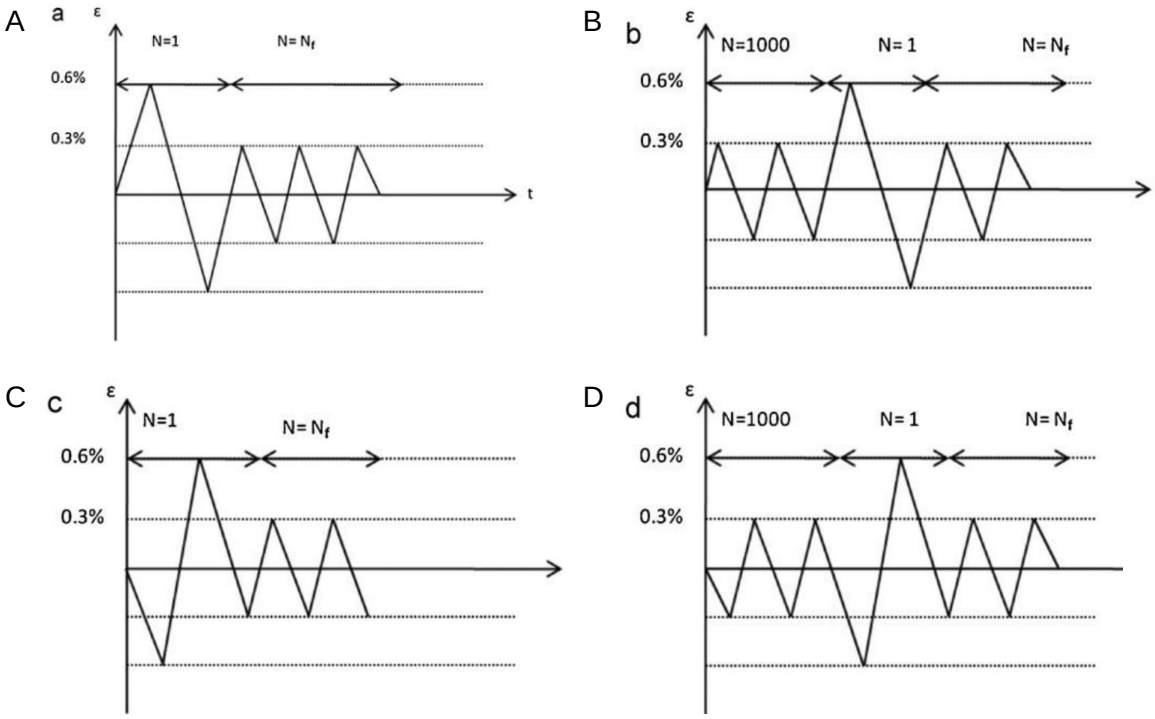

Figure 2-58 Strain % versus time for A) a tensile overload followed immediately by a compressive overload at the start of the test followed by constant amplitude loading for the remainder of the test (T1), B) 1000 baseload cycles followed by a tensile overload followed immediately by a compressive overload cycle followed by constant amplitude loading for the remainder of the test (T1000), C) a compressive overload followed by a tensile overload cycle at the start of the test followed by constant amplitude (C1), D) 1000 baseload cycles followed by a compressive overload followed by a tensile overload followed by constant amplitude loading (C1000) from [130].

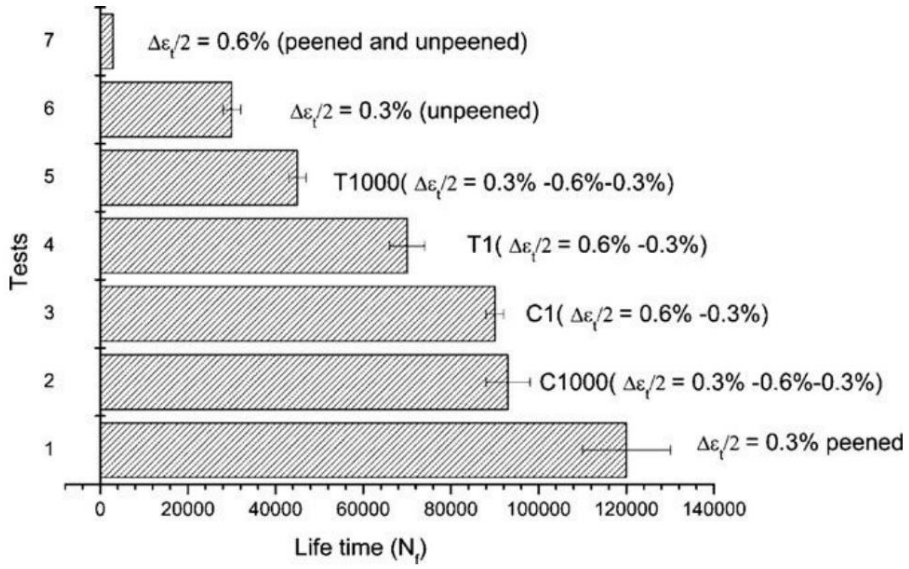

Figure 2-59 The fatigue lifetime for specimens subjected to different surface and loading conditions from [130].

2.4 Life prediction approaches

2.4.1 Introduction

Fatigue life prediction is an important industrial tool that can provide an estimated time frame to failure and aid in the decision-making process, potentially reducing costs. Life prediction is generally approached in one of two ways [26]:

- The total life approach;
    - The total life approach is a prediction of the entire lifetime of a specimen and requires a number of tests to produce useful data, which is typically presented as in a stress versus cycles to failure (S-N) graph.
    - The total life approach is typically used to predict the total life of a component (N_f) subjected to a particular stress amplitude and is a less flexible prediction approach.
- The damage tolerant approach;
    - The damage tolerant approach splits the fatigue lifecycle into the four fatigue phases (initiation, short crack growth, coalescence and long crack growth) to predict the number of cycles for specific fatigue progression behaviours.
    - The damage tolerant approach requires less testing to produce useful data and is a more flexible prediction approach, allowing for specific scenarios such as number of cycles to produce a particular crack length.

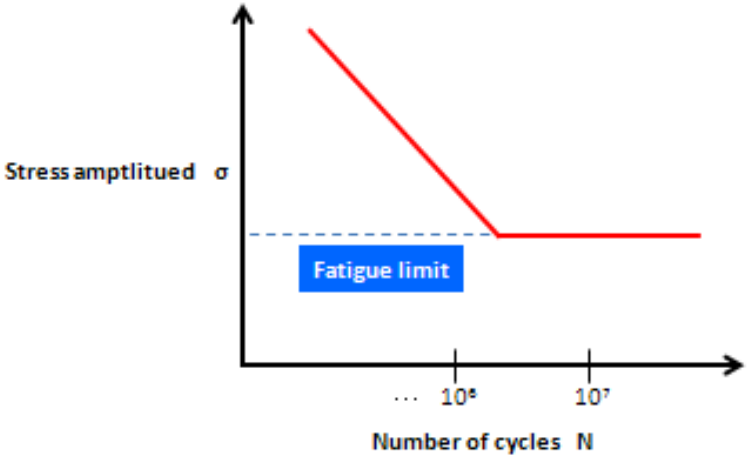

Figure 2-60: An example of a typical S-N graph for steel materials showing the number of cycles to failure increasing as the cyclic stress amplitude decreases to an asymptotic value known as the fatigue limit [132].

2.4.2 Total life approach

The relationship between cyclic stress amplitude and total number of cycles to failure can be represented by the Basquin's [133] power law relationship, for high cycle fatigue conditions (Equation 2-18):

$$\frac{\Delta\sigma}{2} = \sigma_a = \sigma'_f (2N_f)^b \qquad \text{Equation 2-18}$$

where σ'_f is the fatigue strength coefficient and b is the fatigue strength exponent (both constants are found empirically).

A similar power law relationship (Equation 2-19) was found for cyclic plastic strain range and total number of cycles to failure by Coffin and Manson [134, 135], a common characteristic observation in the low cycle fatigue regime where the yield strength of the material is often exceeded. Basquin and Coffin-Manson are often combined to offer a relationship between both stress and strain with total number of cycles to failure (Equation 2-20):

$$\frac{\Delta\varepsilon_p}{2} = \varepsilon'_f (2N_f)^c \qquad \text{Equation 2-19}$$

$$\frac{\Delta\varepsilon}{2} = \frac{\sigma'_f}{E}(2N_f)^b + \epsilon'_f (2N_f)^c \qquad \text{Equation 2-20}$$

where $\Delta\varepsilon_p$ is the plastic strain range, ε'_f is the fatigue ductility coefficient and c is the fatigue ductility exponent.

The process of shot peening produces a compressive residual stress field beneath the notch surface that extends fatigue life by effectively reducing the mean stress. Many approaches have been adopted to account for mean stress in total life prediction approaches such as Gerber [136], Goodman [137], Soderberg [138] and Smith-Watson-Topper (SWT) [139]. The most widely applied mean stress correction for shot peened components is the modified SWT approach (Equation 2-21) [139], which has been used alongside FE modelling approaches with reasonable accuracy [140].

$$\sigma_{max}\varepsilon_a = \sigma_{max}\frac{\Delta\varepsilon}{2} = \frac{\left(\sigma'_f\right)^2}{E}\left(2N_f\right)^{2b} + \varepsilon'_f\sigma'_f\left(2N_f\right)^{b+c} \qquad \text{Equation 2-21}$$

A damage accumulation rule (Equation 2-22), proposed by Palmgren [141] and then developed by Miner [142] is a popular approach to fatigue life prediction accounting for variable amplitude loading conditions.

$$D = \sum_{i=1}^{i=m}\frac{n_i}{N_i} = 1 \qquad \text{Equation 2-22}$$

Where m is the total number of different cyclic load states, n_i is the number of cycles carried out at load state i, N_i is the total number of cycles to failure at a single load level and D is the sum of relative lives at each load state which should be equal to 1.

The damage accumulation rule assumes that the larger the load the larger the amount of fatigue damage will be inflicted. Therefore, the presence of overloads that are larger than the baseload is predicted to result in shorter lifetimes. However, it has been shown in Chapter 2.2.4 that the presence of overloads often has the opposite effect in stainless steel materials, due to closure and residual stress effects that retard crack growth propagation.

It is well known that the Palmgren-Miner rule is not necessarily reflective of reality with some *D* values being calculated as low as 0.03 and as high as 22.8 [143]. Many authors have attempted to develop the Palmgren-Miner approach [143] cited in [144]. However, the increasing complexity from the development of the approach does not outweigh the reduction in prediction error to satisfy industrial practicality. Others have attempted to apply statistical probability modelling to offer some confidence level to lifetime predictions [145-147]

2.4.3 Damage tolerant approach

2.4.3.1 Crack initiation life

Tanaka and Mura [148] developed a prediction model to predict the number of cycles for crack initiation to occur in polycrystalline materials such as stainless steels (Equation 2-23). The model predicts that cyclic loading induces progressive dislocation pile-up due to irreversible dislocation movement. The accumulative pile-up is associated with the progression of extrusion and intrusion formation. When the accumulation of stored energy from irreversible dislocation movement reaches a critical value, crack initiation has occurred. The model was later corrected and has been further developed in terms of plastic strain for low cycle fatigue conditions by Wu [149]. The model developed by Wu has been validated using 316 stainless steel samples with two surface roughness conditions. The author states that this prediction model can be used in industrial conditions without the need for further experimental testing. While such confidence in a prediction model is ultimately desired, the importance of experimental testing procedures within industry should not be understated.

$$N_c = \frac{8(1-\nu)w_s}{\mu b \Delta y^2} \qquad \text{Equation 2-23}$$

Where ν is the Poisson's ratio, w_s is the surface energy, μ is the shear modulus, b is the Berger's vector and y is the shear strain.

2.4.3.2 Crack propagation prediction modelling

In Chapter 2.1.4 it was shown that the crack growth rate of a stage II propagating crack tends to increase with *ΔK* typically following a power law relationship and is therefore predictable. The well-known Paris-law [150] (Equation 2-24) is typically used to describe this relationship:

$$\frac{da}{dN} = C\Delta K^m \qquad \text{Equation 2-24}$$

where the constants C and m are found empirically. The effects of closure can be accounted for by substituting for the effective *ΔK* in Equation 2-25.

$$\frac{da}{dN} = C(\Delta K_{eff})^m \qquad \text{Equation 2-25}$$

Stage I and stage III crack growth behaviour can be modelled but is rarely used in industrial applications [151]. The total number of cycles to grow a crack from some initial crack length a_1 to some final crack length a_2 can be achieved by integrating the Paris-law [152] (in its most simple form Equation 2-26):

$$N = \frac{1}{C}\int_{a_2}^{a_1} \frac{1}{\Delta K(a)^m}\, da \qquad \text{Equation 2-26}$$

where $K(a)$ is the stress intensity factor described as a function of crack length a. Typically, ΔK is a function of the geometry factor which includes crack length. For complex geometry factors this approach may need to be calculated using iterative methods.

2.5 Literature review summary

A background/literature review of fundamental and relevant aspects of fatigue has been revisited. The fatigue lifecycle of specimens/components with sufficient width can be split into four stages, namely: crack initiation, short crack propagation, crack coalescence and long crack propagation until failure. Cracks in martensitic stainless steels tend to initiate from slip bands, surface features and sub-surface (as a result of some lower intensity shot peening processes). The early short crack growth rate is typically higher than long cracks at similar ΔK levels. This is well known as 'the short crack problem', attributed to LEFM limitations to fracture mechanics and partially resolved by adopting EPFM approaches.

The stress distribution in the notch field accounting for material plasticity has been briefly explored, work exploring the effect of various industrially relevant notch geometries on the stress distribution within the notch field is currently lacking. A small project as part of this thesis revealed that Glinka's rule, while proficient at predicting notch surface stress and strains accounting for material plasticity, was not able to accurately predict stress distributions in the notch field. Instead, FE modelling must be used to accurately capture the distribution accounting for the notch material constraint effects.

Crack coalescence behaviours are well known and documented in several materials. The effect of coalescence parameters such as crack shielding effects on short crack growth rates and fatigue lifetime is also well explored. However, the effect of changing notch geometry on crack coalescence, such as 'out-of-plane' distance of surface cracks, is not well known. Short crack growth evolution diagrams including short crack growth and coalescence, give good insight into the interactions between cracks over the full width of the specimen. This approach has only been found on copper material and not within a notch geometry.

B.M.D. Cunningham

Tensile overloads are well known to retard both short and long crack growth rates. This retardation phenomenon has been thoroughly investigated in many materials including stainless steel. The effects of parameters such as OLR magnitude, R-ratio, baseline loading range (ΔK) and various overload sequences have been explored, with most of the literature occurring in the late 20th century. Plasticity-induced crack closure and compressive residual stress are considered the main reasons for the temporary retardation in crack growth. The debate as to the mechanism behind the retardation effect continues. However, for high strength martensitic stainless-steel materials, compressive residual stress is expected to be the primary mechanism contributing towards the retardation of both long and short cracks. The effects of tensile overloads on the crack initiation behaviour within the notch field and contribution to fatigue life are not currently fully explored.

The effects of shot peening on fatigue behaviour and lifetimes within the notch geometry of martensitic stainless steels such as FV448 have been extensively researched. Shot peening increases the surface roughness considered detrimental to fatigue life, and induces a compressive residual stress field shown to be beneficial to fatigue life. The additional effect of strain hardening at and slightly beneath the surface is debated, but for materials exhibiting cyclic softening behaviour, the effect could be deleterious to fatigue life. The residual stress induced by shot peening significantly retarded short crack growth rate and was the main contribution towards fatigue life extension. Residual stress relaxation effects within the notch geometry have also been extensively explored. Notch geometry constraint effects increased the resistance to residual stress relaxation, increasing lifetimes over un-notched specimens. At higher strain ranges, the beneficial effect from shot peening was diminished due to residual stress relaxation, especially for plain bend bars and fully reversed loading conditions.

Sufficiently large overloads can reduce the lifetime extension benefit from shot peening. It is well known that compressive loading can increase residual stress relaxation effects. However, tensile overloads (which induce some level of compressive residual stress of their own) do not have such a prominent deleterious effect on the compressive residual stress relaxation. The effects of overloads with fully reversed loading conditions has been studied, but the effects of R-ratios of 0.1 within the notch geometry are not explored and may not impact lifetimes significantly.

The lifetimes of samples have been adequately predicted using well known total life approaches such as Coffin-Manson, the Palmgren-Miner rule accounting for overloads, Smith Watson Topper accounting for mean stress effects in the LCF regime. In addition, damage tolerant approaches such as the Paris-law describing the relationship between crack growth rate and ΔK and the Tanaka-Mura model for number of cycles to crack

initiations have been used to predict and describe particular stages of fatigue. The use of such methods simultaneously is relatively uncommon, but required for specialised complex fatigue predictions, such as the predicted lifetime extension from grinding out existing cracks, followed by shot peening within the notch geometry.

The typical fatigue behaviour of martensitic stainless steels in notches and the notch stress field has been reviewed. It is known that tensile overloads retard crack growth rates in stainless steel materials due to compressive residual stress ahead of the crack tip and from plasticity-induced closure mechanisms. The influence of the overload on initiation behaviour within a notch and how this may impact fatigue lifetime has been less explored. The stress distribution within the notch field accounting for material plasticity within the notch field has only recently been explored. However, the effect of changing the notch geometry on the distribution of stress and strain in the notch field has not been investigated. The mechanism of lifetime extension from shot peening in a notch is thoroughly understood. However, the reduced residual stress relaxation from shot peening leading to increased fatigue life in sharper notch geometries at identical strain ranges may be better understood by such investigations. Lastly, total life and damage tolerant fatigue life prediction approaches have been reviewed. Such prediction approaches may be used in conjunction with one another to provide a life prediction of complex fatigue situations, such as adopting a lifetime extension strategy with additional overload cycles.

Chapter 3: Material Characterisation and Baseline Properties

3.1 Introduction

In this chapter material characterisation of FV566 in terms of microstructure, mechanical strength and some aspects of fatigue behaviour are investigated and compared with FV448 (from previous work [5, 10, 125]) and FV520B, a comparator material being studied in a companion PhD project. FV566 is the main material of interest for this study. The FV566 samples were extracted from multiple low pressure turbine blades. Extracting samples from multiple blades provides more samples for testing, however, any findings or conclusions derived from samples extracted across multiple blades is subject to blade variability. FV566 samples from multiple blades were therefore compared to also investigate blade variability and the validity of cross blade testing.

FV448 has been extensively studied including material characterisation and fatigue testing [5, 10, 125]. Such extensive information on such a comparator material provides a useful reference against which a direct comparison with FV566 can be made. Microstructural characterisation of FV566 and comparison with other martensitic stainless steels allows an investigation into the microstructural features and provides an insight into what micromechanisms of fatigue may be expected.

Mechanical property characterisation of hardness and strength has been investigated. Hardness testing was carried out in three orthogonal planes to investigate any anisotropy within the material due to rolling procedures during turbine blade manufacture. The tensile stress-strain data obtained is also used to define elastic-plastic material behaviour for subsequent FE modelling.

Fatigue behaviour characterisation such as the evolving cyclic stress strain behaviour of multiple FV566 samples at various strain ranges was also carried out. Tempered martensitic stainless-steels tend to show cyclic-softening behaviour [21, 22, 153]. It is important to establish the extent of this expected behaviour in FV566 and the extent of any softening, a material response that can affect fatigue initiation and crack growth behaviour. The long crack growth behaviour in single edge notched bend (SENB) samples has also been investigated for both FV566 and FV520B as part of this study and compared with existing data for FV448.

In this chapter the FE model of U-notch samples tested in subsequent chapters is introduced and the material behaviour, boundary conditions, contacts, loading conditions

and mesh refinement approach discussed. Validation of the model was carried out via comparison with results from plain bend bar experimental testing. The model is subsequently used to calculate the stress/strain at a notch and investigate the effects of changing notch geometry (such as grinding out existing cracks) in later chapters.

Some of the work presented in this chapter has been published in the following paper [153]:

B. M. D. Cunningham, A. Evangelou, C. You, A. Morris, J. Wise P. A. S. Reed, A. Hamilton *'Fatigue crack initiation and growth behaviour in a notch with periodic overloads in the low-cycle fatigue regime of FV566 ex-service steam turbine blade material'*. Fatigue Fract Eng Mater Struct. 2021. https://doi.org/10.1111/ffe.13617

3.2 Experimental Methodology

3.2.1 Sample Extraction

Plain cuboidal bend bars were extracted from the fir-tree-root block of ex-service low-pressure turbine blades by water jet cutting carried out by Frazer-Nash Consultancy (FNC). The orientation of the FV566 plain bend bar (PBB) samples are shown in Figure 3-1 and FV520B samples in Figure 3-2.

A Cartesian coordinate system was introduced to define axial directions and corresponding planes relative to service conditions. The X, Y and Z directions are defined below;

- The X direction is defined as the direction of blade rotation.
- The Y direction is parallel with the axis of rotation.
- The Z direction is defined as the direction of centripetal acceleration.

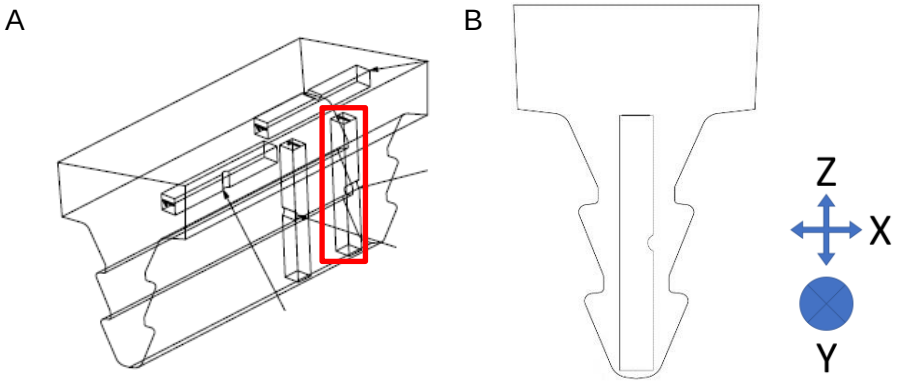

Figure 3-1: A) Sample extraction from Alstom English Electric turbine blade fir-tree-root-fixing. Samples were extracted in the orientation highlighted by the red box. B) Side view showing the orientation of the sample.

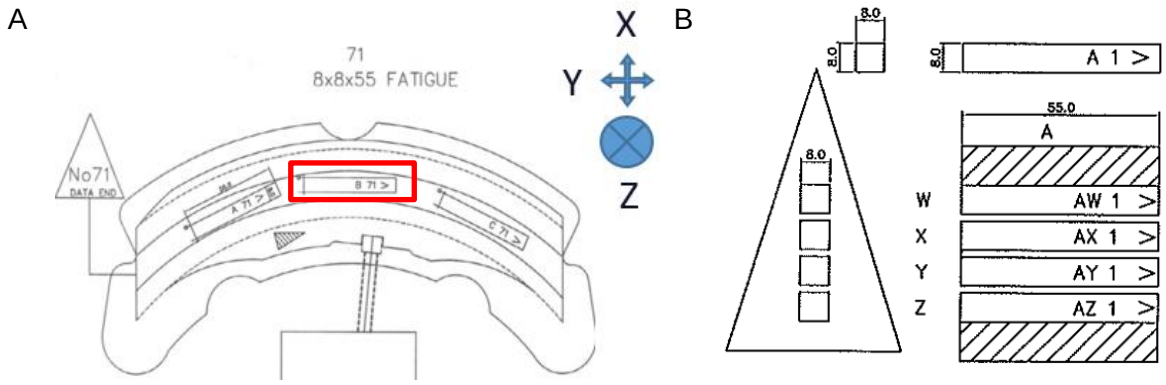

Figure 3-2: Schematic drawings showing FV520B sample extraction in the form of plain bend bars from the LD66 turbine blade fir-tree-root-fixing. A) Sample orientations within the fir-tree-root of blade number 71. B) Sample depth position within the fir-tree-root.

3.2.2 Sample preparation

It is understood from the sponsor supplying the ex-service turbine blades that this material will have been austenitised at 1050 °C and oil quenched, followed by tempering at 650 °C [154]. A wet sectioning saw was used to cut the FV566 and FV520B samples into three planes. A hot mounting press was used to mount the samples in conductive Bakelite. Grinding with progressively finer silicon carbide grinding paper followed by polishing with progressively finer suspensions finishing with 1 µm diamond suspension was carried out for microscopy and hardness testing.

3.2.3 Microstructural characterisation

Vilella's etching reagent (1 g Picric acid, 5 ml HCl and 95 ml ethanol) was applied for approximately 40 - 60 seconds to reveal the martensitic microstructure. The polished samples were observed at various magnifications using an Olympus BX51 optical microscope to show microstructural features enhanced by the etching process. Secondary Electron Imaging (SEI) and Backscattered Electron Imaging (BEI) using a JSM 6500F field emission gun scanning electron microscope (FEG-SEM) was used to observe the microstructure. Energy Dispersive X-ray Spectroscopy (EDS/EDX) was used to determine the chemical constituents of microstructural features such as inclusions. A sample of FV566 was sent to Southdown Materials Testing Ltd for spectrographic analysis to determine the material composition.

3.2.4 Mechanical properties

3.2.4.1 Hardness testing

Plain bend bars made from FV566 and FV520B were cut with a wet sectioning saw to produce three perpendicular planes (Figure 3-3) and prepared using the procedure detailed in section 3.2.2. A micro hardness tester (Future-Tech FM-300) was used to apply hardness indents with 200 g and a dwell time of 15 seconds. The indent dimensions were measured, and the hardness value found using the microhardness machines' in-built function. Sixty-four indents were carried out in the middle of the polished sample and with horizontal and vertical spacing greater than 100 µm to avoid any influence of plastically deformed material from surrounding indentations (*BS EN ISO 6507-1:2008* [118]). Hardness measurements outside the upper and lower quartiles (Q1 and Q3) of the data were regarded as anomalies but included in average hardness measurements.

Three FV566 samples from separate blades (M06, M08 and M09) on the YZ surface plane were prepared using the procedure detailed in Chapter 3.2.2. Ten hardness indents were applied with 500 g loading and 15 second dwell time. The indents were measured, and the hardness values obtained to *BS EN ISO 6507-1:2008* [118]. The average hardness values with error of one standard deviation were compared to test blade hardness variability.

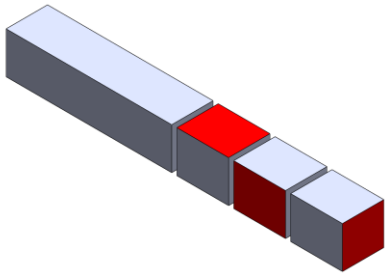

Figure 3-3 The plain bend bar (PBB) was cut three times to produce three cubes. The cubes were mounted and prepared for hardness testing on three perpendicualr planes, highlighted in red.

3.2.4.2 Tensile testing

Three cylindrical dog-bone tensile specimens from three blade root sections (M01, M02 and M03) were machined from FV566 by TWI (Figure 3-4). The tensile test specimens were subjected to monotonic tensile testing at a constant strain rate of 1.8 $x10^{-4}$ s^{-1} throughout the elastic to plastic transition. After a total strain of 3%, the strain rate was increased for the remainder of the test. All tensile testing was carried out to *BS EN 6892-1* [155].

A

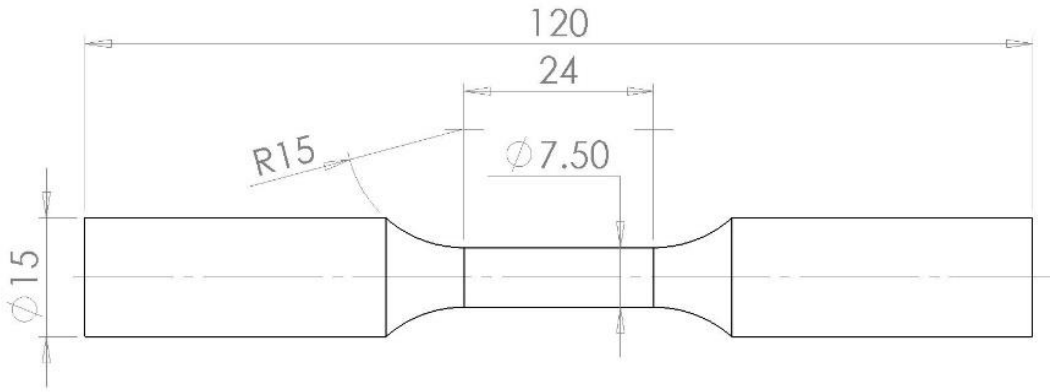

B

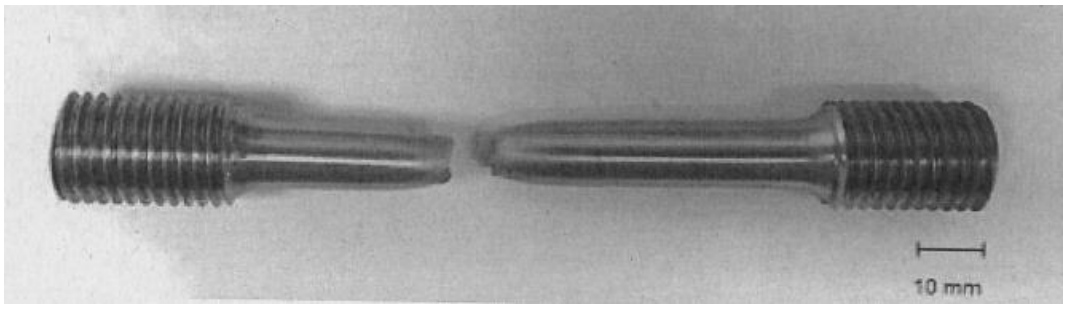

Figure 3-4: A) Cylindrical dog-bone tensile specimen dimensions. B) The tensile specimens were prepared and tested by Frazer-Nash Consultancy. Note that the same specimen geometry was also used for fully reversed strain controlled cyclic loading tests.

3.2.5 Fatigue properties

3.2.5.1 Cyclic stress-strain behaviour

Cylindrical dog-bone specimens were machined from FV566 fir-tree-root block (blades M11 – M15) identical to Figure 3-4. Strain controlled fully reversed (R = -1) axial cyclic load testing was carried out by FNC with various strain ranges 0.6 %, 0.8 %, 1 %, 1.2 % and 1.8 % until failure to *BS ISO 12106:2017* [156].

All surfaces of a PBB made from FV566 (blade M08) were ground and polished using 1 µm suspension. A strain gauge of length 2 mm was placed in centre of the PBB. The plain bend bar was loaded in 4-point bending on a servo-hydraulic dynamic cyclic testing machine with a top roller span of 50 mm and bottom roller span of 10 mm (Figure 3-5). The strain gauge was connected to software (StrainSmart®) converting electrical resistance to mechanical axial strain in the longitudinal direction. The PBB was cyclically loaded with a total of 4000 cycles with four strain ranges of 0.3 %, 0.4 %, 0.6 % and 0.85 % (1 000 cycles at each strain range).

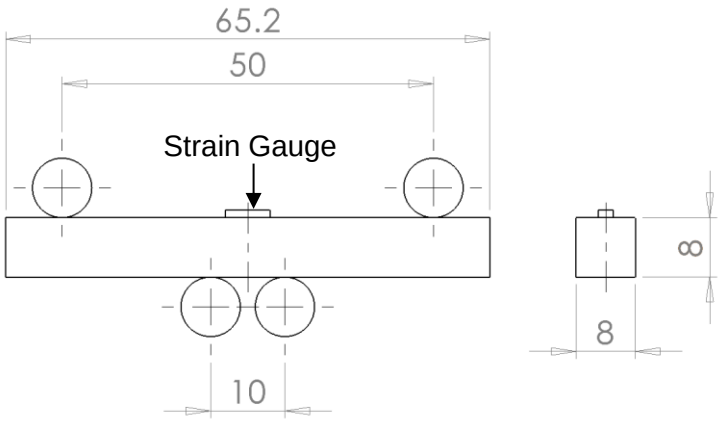

Figure 3-5 PBB dimensions and 4-point bending set-up for cyclic strain testing of FV566. The strain gauge was placed at the centre on the top face of the sample.

3.2.5.2 Long crack growth rate

Two plain bend bars made from FV520B (blade 71) and FV566 (blade M06) were notched with a single edge notch as per British Standards *BS EN ISO 12108:2012 [157]* using a wire cutter (Figure 3-6 and Table 3-1). All six sides of the sample were ground using 800 and 1200 grit paper, and further polished using 6 µm and 1 µm diamond suspension. The samples were cleaned using ethanol before testing.

The sample was loaded in 3-point bending on a servo-hydraulic dynamic cyclic testing machine (INSTRON 8502) at room temperature with sinusoidal wave form at 10 Hz and a top roller span of 40 mm (Figure 3-6). The stress intensity factor ΔK was calculated using the method in Appendix A. The sample was cyclically loaded with R-ratio of 0.1 at an initial ΔK of 15 MPam$^{0.5}$ to initiate crack growth. The crack length was monitored throughout the test using the direct current potential drop (DCPD) method. Pre-cracking was carried out to ensure that the long crack had grown through at least six monotonic plastic zone sizes calculated using the Irwin approximation of plane strain [158] (Equation 3-1).

$$r_p = 6 \times \frac{1}{3\pi}\left(\frac{\Delta K}{(1-R)\sigma_y}\right)^2 \qquad \text{Equation 3-1}$$

The load was altered during the test to ensure a constant ΔK ± 1 % to assess crack growth rates at lower ΔKs. For threshold testing, a load shedding procedure was carried out whereby the ΔK was dropped in 10 % decrements after the crack growth rate had been determined via growth through six monotonic plastic zone sizes at the previous ΔK. This series of decreasing ΔK values and associated *da/dN* values was monitored to determine the near threshold region and approximate ΔK_{th}. Once the ΔK_{th} was found, grow-out testing

was carried out whereby ΔK was increased to 12 MPam$^{0.5}$ to induce crack growth. The cyclic load range was kept constant for the remainder of the test (ΔK increased with crack length) to achieve a full range of da/dN versus ΔK behaviour until sample failure. The Paris-law constants were determined using an empirical fit to the data and the materials compared.

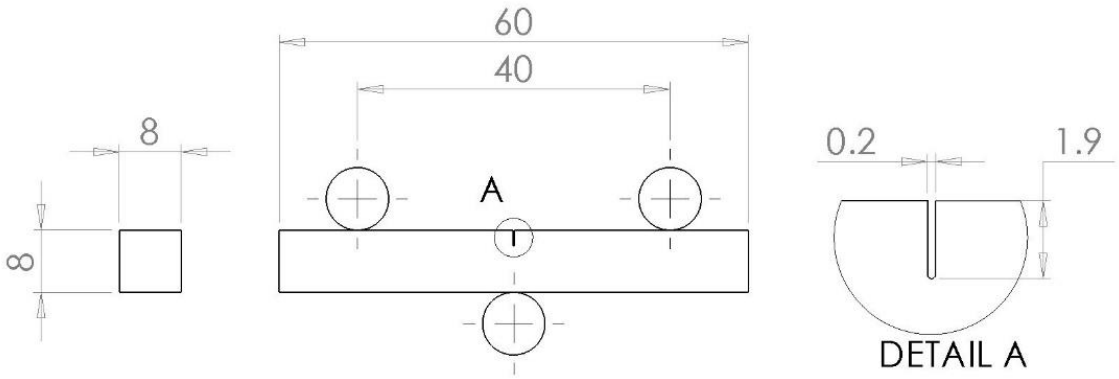

Figure 3-6: SEN sample dimensions and 3-point bending set up for long crack testing of FV566.

Material	Width (mm)	Breadth (mm)	Notch depth (mm)
FV566	8.0	8.0	1.9
FV520B	6.8	7.5	1.5

Table 3-1: SEN samples had different geometries depending on the material due to sample extraction constraints.

3.2.6 Development of FE model

A 3D quarter-model of the PBB in 4-point bending with roller supports modelled as 3D discrete rigid bodies was created in ABAQUS (Figure 3-7 A) with the aim of comparing FE modelling results with experimental data for validation purposes.

An elastic-plastic material model was used to define the material behaviour. The true stress-strain curve from monotonic tensile testing of M02-02 performed by FNC (Figure 3-12) was used as the input conditions for the material behaviour model using Equation 3-2. The yield stress for this model was found to be 678 MPa defined at the beginning of the elastic to plastic transition at 0.002 % plastic strain.

$$\varepsilon_{Plastic} = \varepsilon_{True,Total} - \frac{\sigma_{True}}{E} \qquad \text{Equation 3-2}$$

Full integration quadratic hexahedral mesh elements (C8D20) were used for the model. The non-linear effects due to large displacements (Nlgeom) had a minimal effect on the stress

and strain output at the surface of the notch and was therefore not used. The mesh was refined in influential areas such as the contact locations and surrounding material (Figure 3-7 B) and in the centre of the PBB, especially in the region of interest. A mesh convergence analysis was carried out to ensure the mesh was of adequate refinement Appendix B.

A fixed support constraint was placed in the centre of the support roller. Symmetry constraints were applied on symmetry planes required for quarter-model construction. A constraint was placed in the centre of the load roller to allow only unidirectional movement in the Y direction (Figure 3-7 C). A load was defined in the centre of the roller in the Y direction to simulate the maximum load applied during cyclic testing. A frictionless 'hard' tangential contact was created between the roller and PBB surface with finite sliding constraints. An initial 'pre-loading' step was applied whereby the top roller was displaced by a small amount (0.04 mm) to activate the contact between the roller and PBB. The load was applied in stepped increments of 5 % of the total load during an analysis run to account for non-linear behaviour of the model.

A

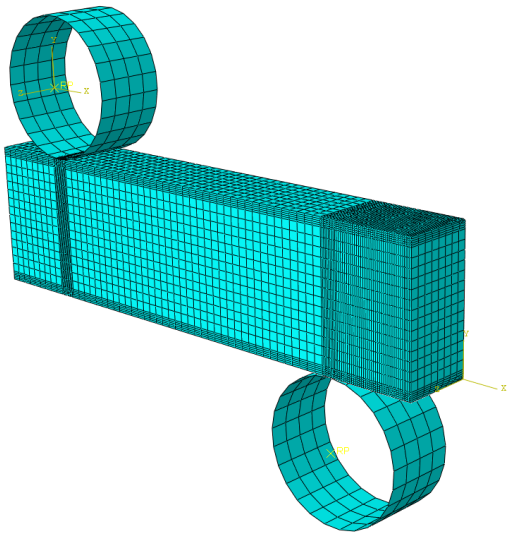

B

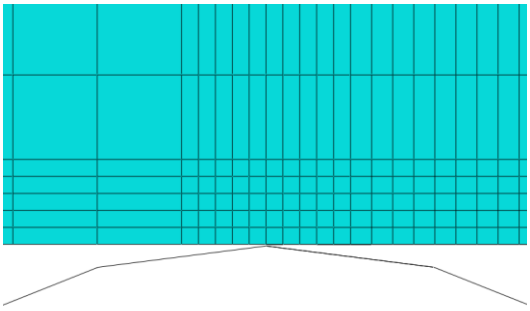

C

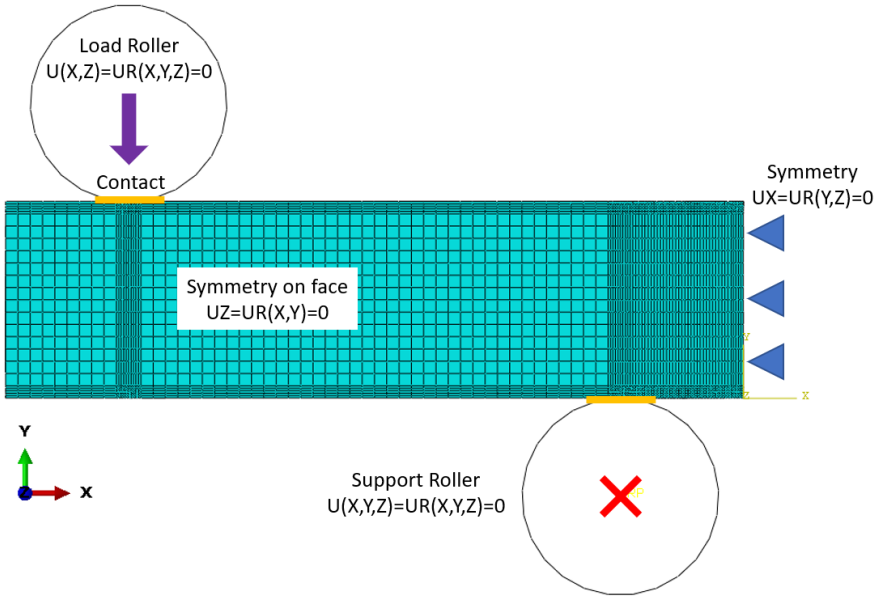

Figure 3-7 A) An isometric view of the ABAQUS 3D quarter-model of the PBB in 4-point bending with rollers and mesh (ranging from 0.1 mm to 0.5 mm). B) A close-up view of the mesh at the contact point between the bottom support roller and the bottom surface of the PBB. C) The boundary conditions for the model where U is degree of freedom of unidirectional movement along an axis and R is the degree of freedom of rotation around an axis.

3.3 Experimental Results

3.3.1 Chemical composition

The chemical element composition of the material seen in Table 3-2 was obtained using spectrographic analysis by Southdown Materials Testing Ltd [153].

Element	C	Si	Mn	P	S	Cr	Mo	Ni	V	N	Fe
%-wt	0.1	0.4	0.68	0.02	0.004	11.4	1.76	2.38	0.33	0.05	Bal

Table 3-2: Composition of FV566 found using spectrographic analysis by Southdown Materials Testing Ltd.

3.3.2 Microstructural characterisation

FV566 has a microstructure typical of martensite with prior-austenite grain boundaries, packets, and laths (Figure 3-8 A). Evidence of inclusions and stringers aligned with the Z-direction comprising Aluminium Oxide (Al_2O_3) and Manganese Sulphide (MnS) can be seen in Figure 3-8 B). A lower magnification BEI (Figure 3-8 C) of FV566 shows a visual overview

of the typical density and distribution of inclusions (seen as black spots) within the microstructure. Inclusions seen were Aluminium Oxide (Al_2O_3) ranging from 1 µm to 10 µm diameter appearing within the matrix of the material (Figure 3-8 D and E). A less common Manganese Sulphide (MnS) inclusion was seen (Figure 3-8 F and G). A δ-ferrite phase formed during the pre-heat-treatment manufacturing process was observed (Figure 3-8 H). The BEI image shows that the phase was surrounded by secondary phase particles containing alloying elements of higher density (lighter colour) than the surrounding matrix, the phase itself was of similar density to the surrounding matrix (Figure 3-8 J). A silicon Oxide (SiO) inclusion was identified as a cause of crack initiation on a fracture surface (detailed further in Chapter 4.4.3).

A

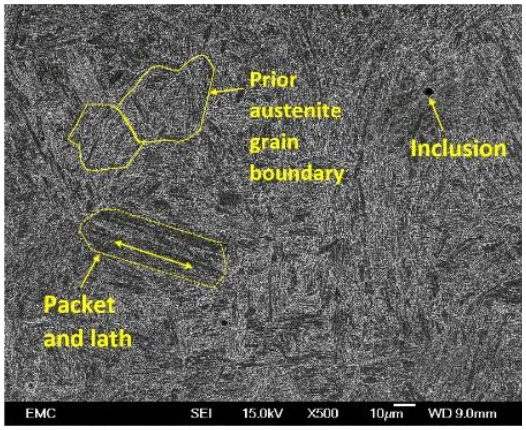

B

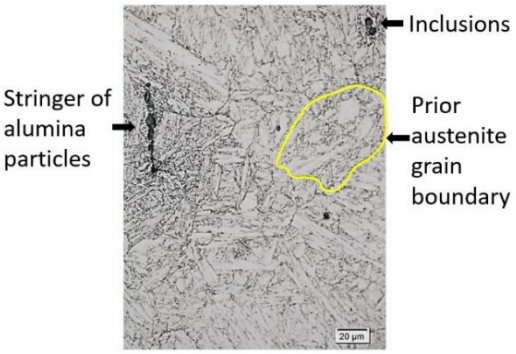

C

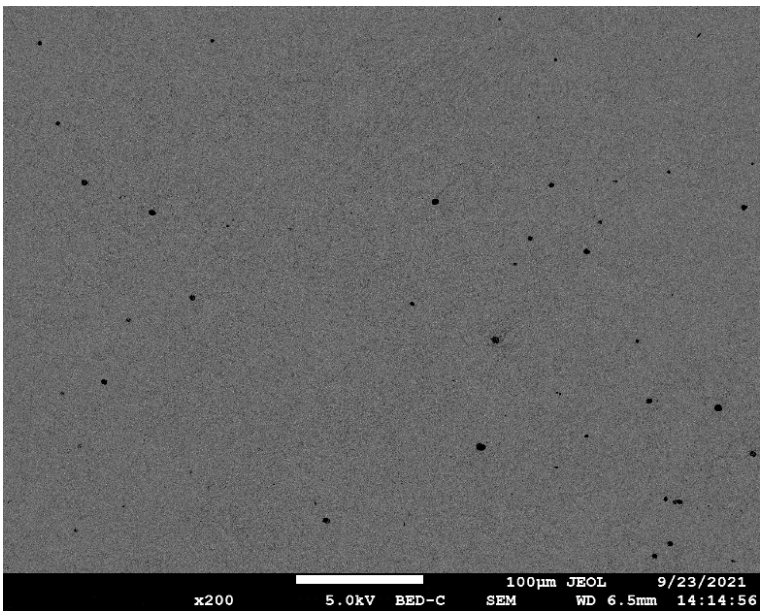

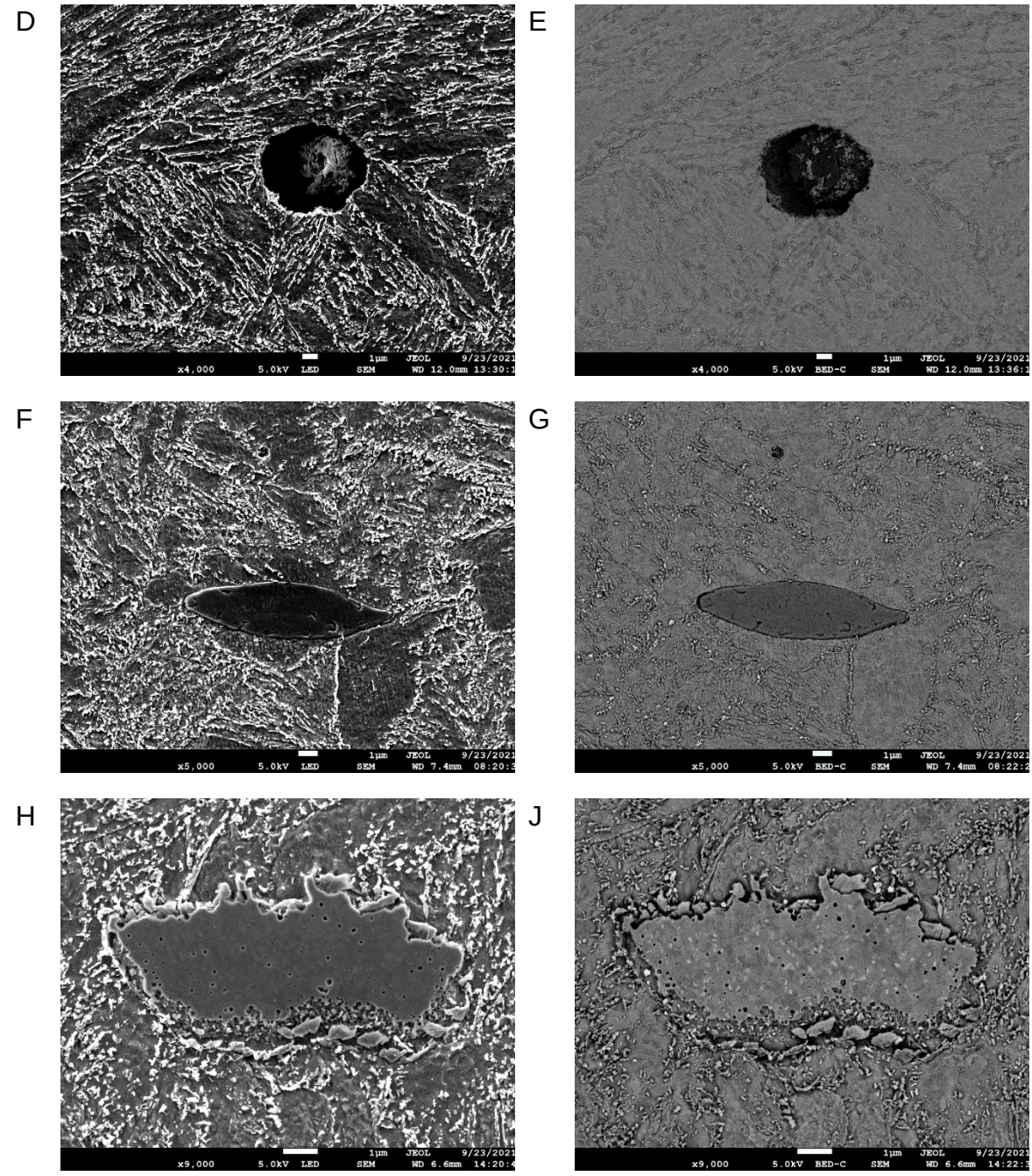

Figure 3-8 A) SEI image showing the martensitic microstructure of FV566. B) OM image showing the martensitic microstructure of FV566 and features such as stringers. C) BEI image of FV566 showing inclusions as black spots. D) A high magnification image of an inclusion made from Al_2O_3. E) The BEI image shows the inclusion in D has a lower density (darker colour) than the surrounding matrix material. F) An inclusion likely consisting of MnS and G) its corresponding BEI image. H) A region of δ-ferrite likely formed during manufacture of the material prior to heat treatment. J) BEI image of δ-ferrite showing a similar density to the surrounding matrix and surrounding secondary phase particles seen as white dots and therefore higher density than the surrounding matrix.

B.M.D. Cunningham

A 3D microstructure view of three perpendicular etched planes was constructed for three blades made from FV566 (M06, M08 and M09) and for FV520B for comparative purposes (Figure 3-9 and Figure 3-10). There is little notable variability between the microstructures of the three blades of FV566 with similar grain size and similar microstructural features such as inclusions composed of aluminium oxide and white patches of retained austenite observed. FV520B has a similar microstructure to FV566, the prior-austenite grain boundaries were not shown by etching. The rolling direction of all four samples is not particularly evident although the XZ plane of FV520B does appear to differ from the other planes.

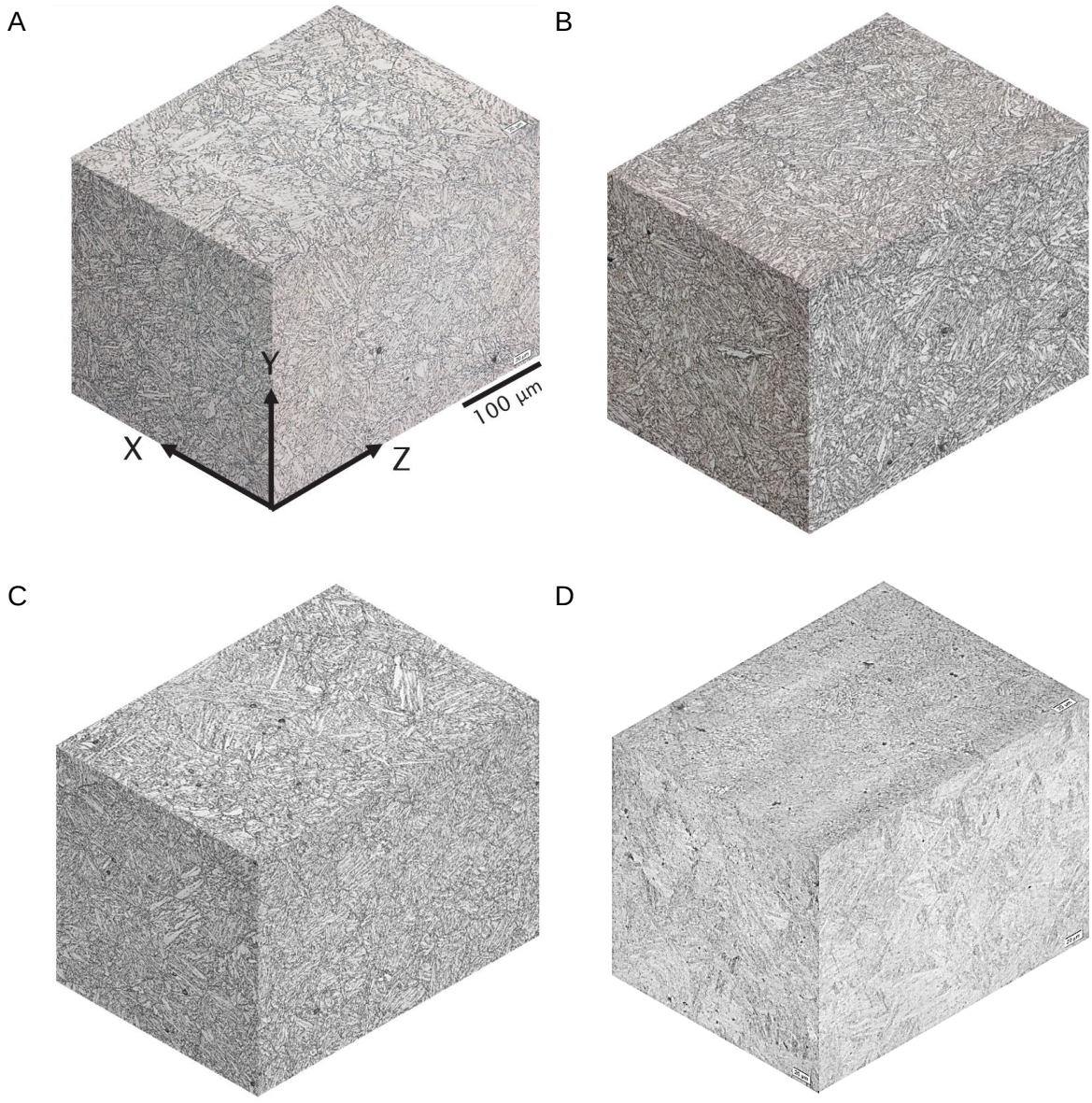

Figure 3-9: 3D microstructures from OM images in three perpendicular planes of A) FV566 Blade M06, B) FV566 Blade M08, C) FV566 Blade M09 and D) FV520B.

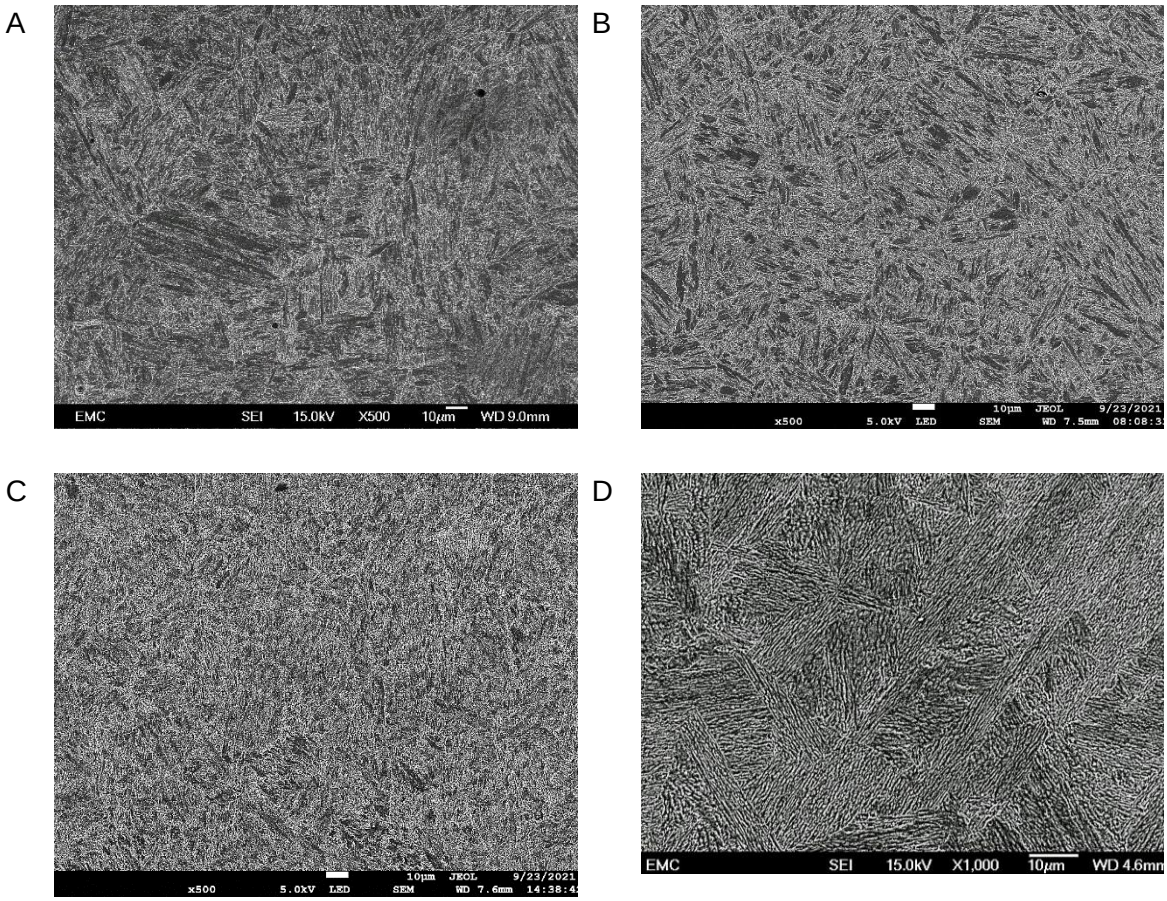

Figure 3-10: SEI images of microstructures of A) FV566 Blade M06, B) FV566 Blade M08, C) FV566 Blade M09 and D) FV520B.

3.3.3 Hardness comparison

The baseline hardness values of FV566 and FV520B were measured (Table 3-3). The results suggest that there is almost negligible variability in hardness between the three FV566 blades tested with values falling within the typical error range. Hardness testing on three perpendicular planes of both FV566 and FV520B revealed one particularly hard plane (Figure 3-11), shown by the higher density of red squares showing higher hardness values possibly indicative of rolling direction.

Material	**Baseline Hardness (HV)**
FV566 Blade M01 [a]	317
FV566 Blade M02 [a]	325
FV566 Blade M03 [a]	320
FV566 Blade M04 [a]	320
FV566 Blade M05 [a]	324

Material (continued)	Baseline Hardness (HV)
FV566 Blade M06 (500 g loading)	313 ± 6 (10 indents)
FV566 Blade M08 (500 g loading)	322 ± 5 (10 indents)
FV566 Blade M09 (500 g loading)	316 ± 3 (10 indents)
FV566 Blade M06 (200 g loading)	354 ± 15 (196 indents)
FV520B Blade 71 (200 g loading)	377 ± 17 (196 indents)

Table 3-3 Average baseline hardness results from FV566 and FV520B. A comparison of three blades made from FV566 is shown based upon 500 g loading. A comparison between FV566 and FV520B is shown based upon 200 g loading over a higher number of indents. [a] the microhardness indentation testing was carried out by FNC with unknown load.

Figure 3-11: Microhardness results in Vickers hardness (HV) on three perpendicular planes of A) FV566 and B) FV520B shown as colour maps. One plane was found to be particularly hard in both materials possibly indicative of rolling direction.

3.3.4 Tensile testing

FV566 monotonic tensile testing was carried out by FNC, the stress-strain curves were plotted in Figure 3-12 and mechanical properties extracted (Table 3-4). Blade variability in the mechanical strength properties was found. The tensile data collected from blade M02-02 was used to define the material behaviour in the FE model since it will produce more conservative fatigue lifing results in terms of strain range in the notch root.

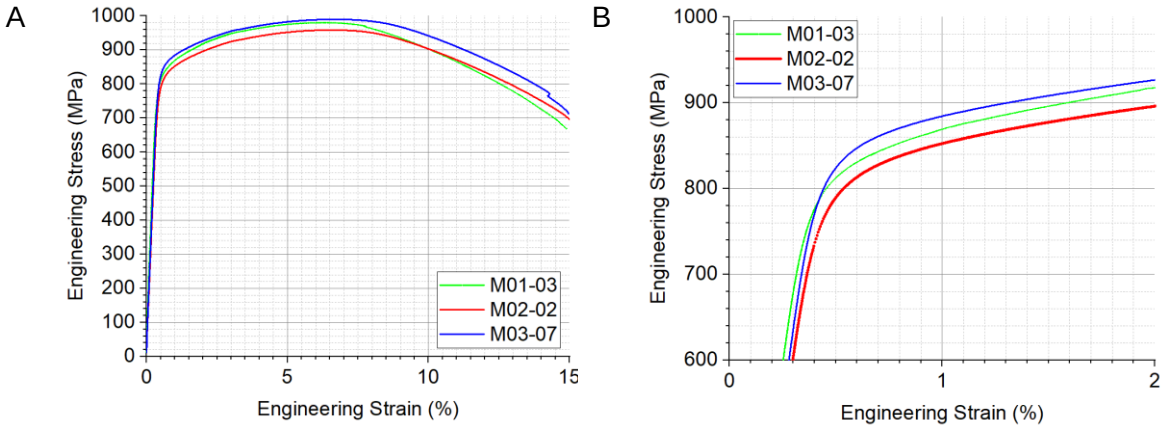

Figure 3-12: A) Stress vs strain from three monotonic tensile tests performed by Frazer-Nash Consultancy on three separate blades (M01, M02 and M03) made from FV566. B) A closer view of the elastic-plastic transition for the three tensile curves.

Blade	Young's Modulus (GPa)	Yield Strength (MPa)	Ultimate Tensile Strength (MPa)	Elongation to Failure (%)
M01-03	226	825	980	14.9
M02-02	197	815	959	15.1
M03-07	210	848	990	15.0

Table 3-4 Material strength properties found from the tensile testing performed by FNC of FV566 from three separate blades.

3.3.5 Cyclic stress strain data

Strain-controlled cyclic fatigue testing was carried out by FNC on FV566 samples from five separate blades with various constant cyclic strain ranges. The variation of maximum (tensile) and minimum (compressive) stress values during each cycle versus number of cycles shows that FV566 cyclically softens during cyclic loading in the LCF regime. FV566 cyclically loaded at a constant total strain range of 1 % shows initial cyclic softening behaviour (decreasing maximum stress with number of cycles) within the first 100 cycles. The softening behaviour decreases in intensity and stabilises although softening behaviour is seen throughout the entire fatigue test. Crack initiation at approximately 2293 cycles resulted in an increase of the material compliance and a reduction in the force required to induce 1 % strain range resulting in a reduced maximum stress. The sample became increasingly compliant (stiffness decreased) as the crack(s) grew until failure occurred at 3295 cycles (Figure 3-13 A). Initial cyclic tensile softening behaviour and subsequent stabilised softening behaviour was observed for total strain ranges of 0.8 % and higher. As the strain range increased above 0.8 %, the softening behaviour becomes more marked. At strain ranges of 0.6 % and lower, the material does not exceed the yield strength of the material and any softening or hardening behaviour that occurs becomes negligible (Figure 3-13 B). Three FV566 samples from separate blades were subjected to a constant cyclic total strain range of 1.2 % fatigue testing (Figure 3-13 C). Blade variability in cyclic softening behaviour was seen with a variation in stress over 70 MPa after 100 cycles. The blade variability seen helps explain why the M11 blade at 1 % appears identical to M15 at 1.2 % in Figure 3-13 B).

Load controlled testing was carried out on a PBB made from FV566 in 3-point bending with a centrally positioned strain gauge. A load versus maximum total strain graph (Figure 3-13 D) was chosen for direct comparison with FE modelling. At maximum total strain of 0.035 and lower, the material is within the elastic regime and no cyclic hardening effects were observed. At maximum total strain of 0.043, the material is mostly within the elastic regime, however small cyclic hardening effects were seen. At a total strain of 0.057 and above, clear cyclic hardening effects can be seen at each strain level. The cyclic stress strain response was stable after the 50^{th} cycle.

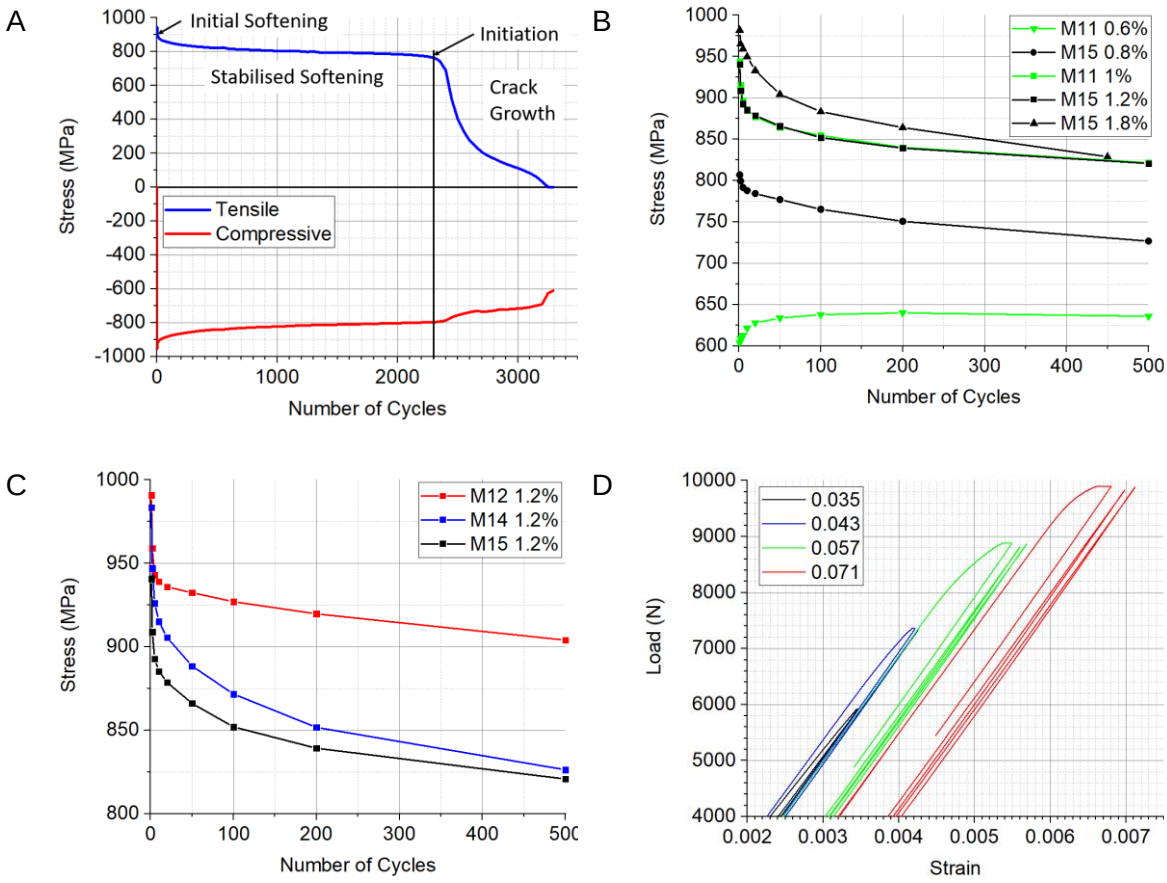

Figure 3-13 A) Stress in MPa versus number of cycles from a strain-controlled fatigue test at 1 % constant total strain range. B) Tensile stress versus the initial 500 cycles for strain-controlled fatigue tests at various strain ranges. C) Tensile stress versus the initial 500 cycles for strain-controlled fatigue tests of three different blades made from FV566 at 1.2 % constant strain range (A, B and C were performed by Frazer-Nash Consultancy on FV566 blade M11). D) Load vs Strain for the PBB cyclic loading test. The results show the 1st, 10th and 50th cycles at each strain range.

3.3.6 Long crack growth rate

Two long crack tests from SEN bend bars made from FV566 and FV520B were carried out in laboratory ambient air conditions and the results compared with FV448 obtained using Paris-law constants [10] for comparison (Figure 3-14). The noise contained in the raw data was smoothed using the Loess function with 0.1 sampling size and a 4th degree polynomial [159] for mid-range ΔK values. The Paris-law constants were found by empirical fitting of the smoothed data collected during the grow-out stage of the test. The ΔK_{th} was found by noting the value of ΔK below 10^{-7} mm/cycles. FV566 and FV520B were found to have similar

long crack growth behaviours. FV448 by comparison displayed lower crack growth rates at identical *ΔK* values when compared with FV566 and FV520B.

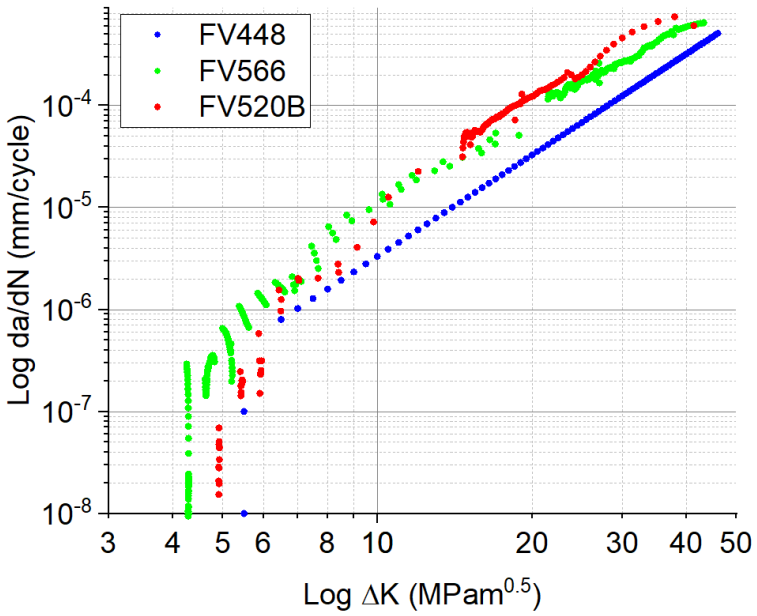

Figure 3-14: *ΔK* versus crack growth rate for long crack testing of FV566 and FV520B compared with FV448 [10].

Material	***C***	***m***	ΔK_{th}**(MPa√m)**
FV 448 [10]	1.7 x 10^{-9}	3.3	5.5
FV 566	7.3 x 10^{-9}	3.1	4.3
FV 520B	1.2 x 10^{-8}	3.1	4.9

Table 3-5: The Paris-law constants as measured from Figure 3-14 and from [10]

3.3.7 FE model Validation

FEA data was compared to experimental data for validation purposes. The reaction force at the support roller and longitudinal stress at the extreme fibre in the mid length of the PBB (Figure 3-15 A) for each time step was recorded. The load versus total strain during the 4-point cyclic strain experimental test on FV566 was recorded for the 50th cycle at each strain range (Figure 3-15 B) and compared with FE modelling results. The FE model predicts a higher strain for load values exceeding the yield strength of the material. The higher the load, the higher the error between the FE model and experimental data. Despite the discrepancy, this FE model can still be used to estimate the strain range of the notch surface experienced during experimental testing as discussed further in Chapter 3.4.3.

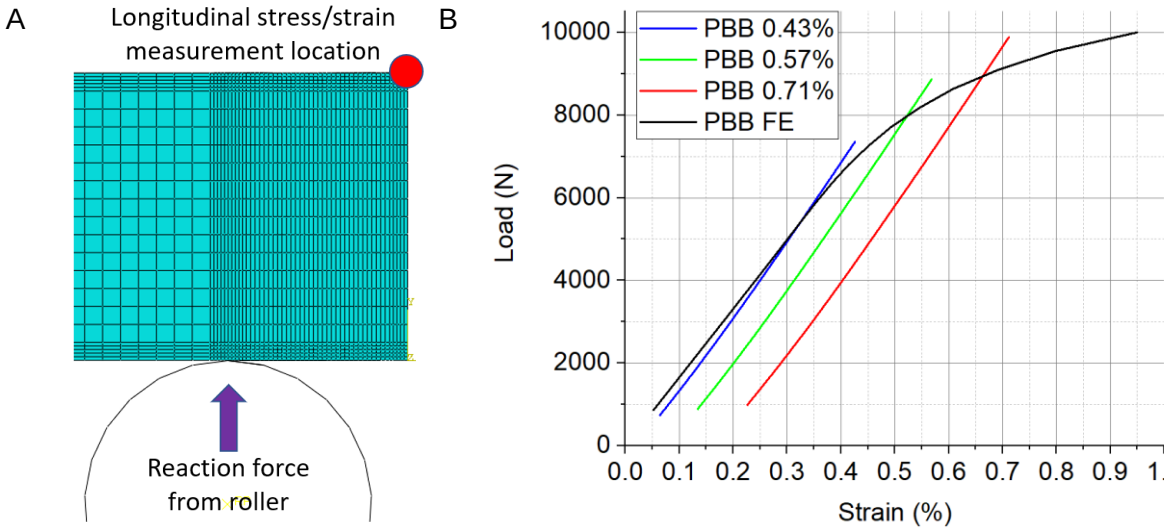

Figure 3-15 Load versus strain (%) for stabilised experimental data after the 50th cycle compared with FE modelling.

3.4 Discussion

3.4.1 FV566 composition and microstructural characterisation

The chemical composition of FV566 was compared with two other similar martensitic stainless steels FV448 [10] and FV520B [160] as well as data available on FV566 [43] from the literature (Table 3-6 and Figure 3-16). All three martensitic stainless-steels contain similar ratios of alloying elements and the FV566 studied is typical of an 11-15 % Cr martensitic stainless-steel material. Elements such as C (added to encourage interstitial solid solution strengthening and formation of beneficial carbides) and Cr (to increase steel hardenability and corrosion resistance) are common to all three materials, whereas Cu and W are unique to only one material. It is apparent that even in the same FV566 material there were still notable differences in chemical composition such as V and Nb (included to encourage more carbon to contribute to solid solution strengthening and restrict austenite grain growth, increasing steel toughness). The chemical composition analysis of FV448 shows a lack of Sulphur, however precipitates containing Sulphur such as MnS were identified within the material [10]. The variability in chemical composition shown in these results may be influenced by the error and limitations of the chemical composition analysis and reporting methods.

Material	C	Mn	Cr	Mo	Si	Ni	V	Nb	S	P	Cu	W
FV448 [10]	0.12	0.94	11	0.58	0.31	0.74	0.31	0.34	x	x	x	< 0.01
FV520B [160]	0.047	0.81	14.61	1.62	0.61	5.53	x	0.34	0.009	x	1.5	x
FV566 [43]	0.1	0.61	11	1.35	0.35	2.4	0.15	0.28	0.01	0.02	x	x

Table 3-6: Chemical composition in weight % of three similar martensitic stainless steels including FV566 from the literature for comparison with the material studied (Figure 3-16).

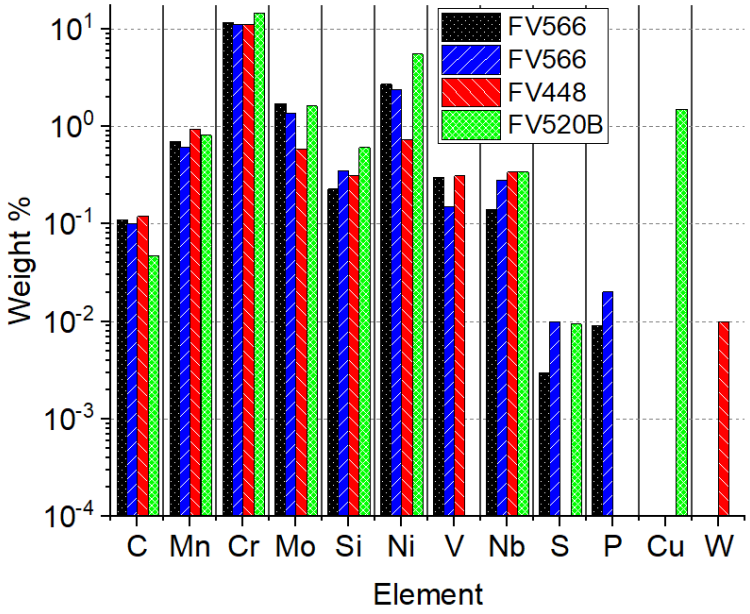

Figure 3-16: Alloying additions in weight % for FV566 obtained from spectrographic analysis by Southdown Materials Testing Ltd (black), compared with FV566 (blue), FV448 (red) and FV520B (green) from literature (Table 3-6). A log scale has been used for clarity.

The microstructure of FV566 is similar to FV448 with similar features such as prior-austenite grain boundaries of similar size as well as martensite features such as packets and Laths [22] (Figure 3-17). Common martensitic features are present in FV520B but the prior-austenite grain boundaries and inclusions were not exposed by the etching process and are less visible than in the FV448 and FV566 materials. The rolling direction could not be identified in the FV566 material by observing microstructure alone, a similar conclusion was found in FV448 [10]. However, FV520B appeared to indicate a clear observable difference in the microstructure in the XZ plane that may be indicative of rolling direction but could also be due to slight variations in the etching process on each plane.

The stringers observed in the FV448 material were found to be aligned parallel to the rolling direction [10]. From this, it can be deduced that the rolling direction in the FV566 material

studied was most likely aligned parallel to the Z-direction (direction of centripetal acceleration). The FV448 material was obtained from a rolled block rather than a turbine blade component. As a result, stringers were more frequently found with a very strong alignment and the material was not from an ex-service turbine blade.

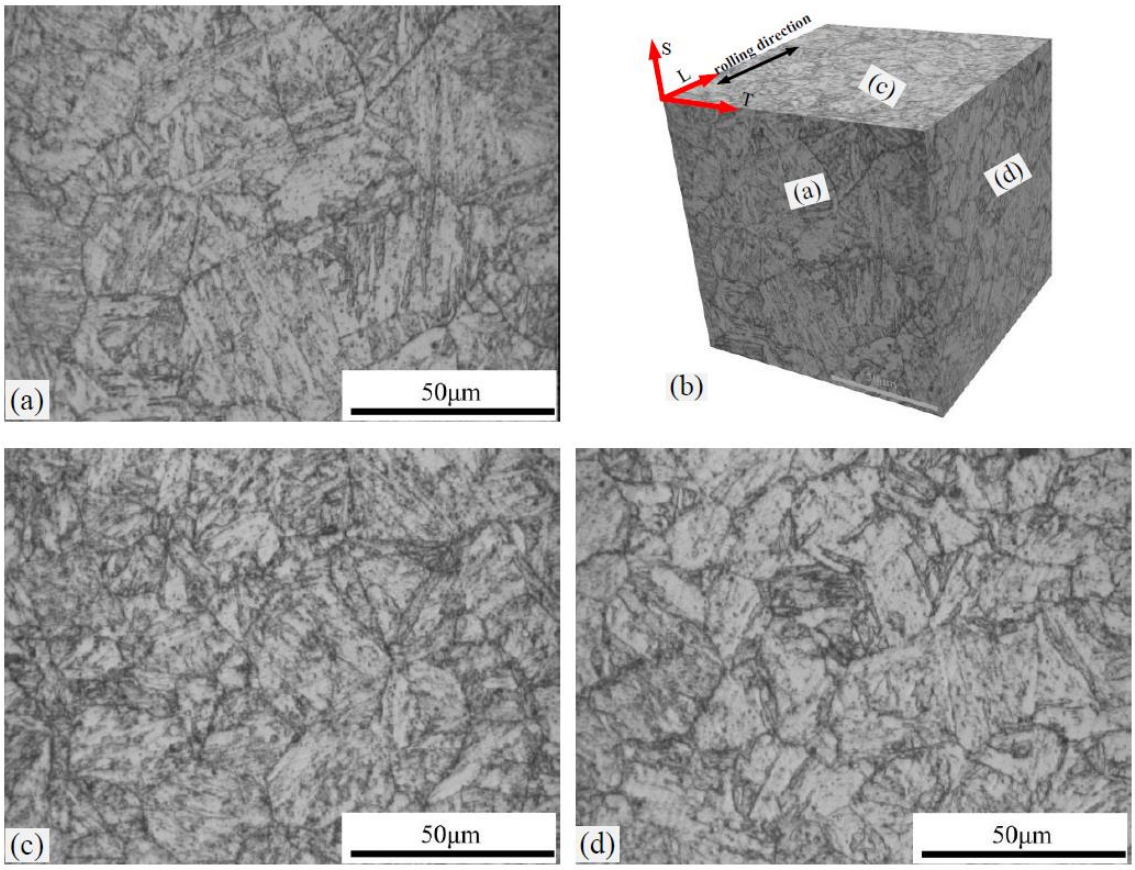

Figure 3-17: 3D OM microstructure image of FV448 (b) and the corresponding three planes (a), (c), (d), image taken from [5].

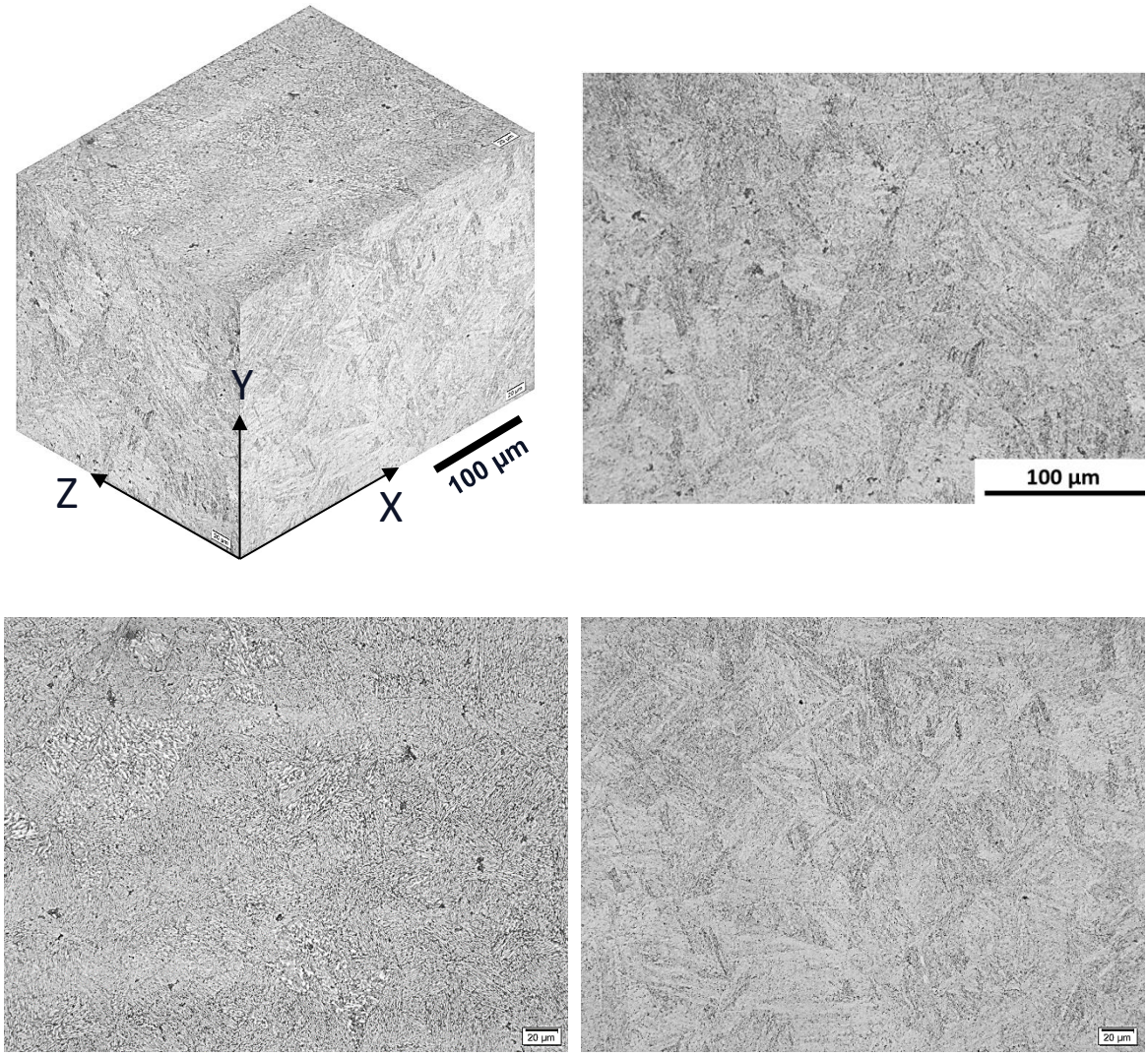

Figure 3-18: 3D OM microstructure image of FV520B and the corresponding three planes.

Inclusions were found in the FV566 studied including a stringer within the material microstructure. Similar features were seen in FV448 material [50, 161]. The inclusion in Figure 3-8 B) somewhat resembles Figure 3-19 A) identified as Aluminium Silicon Oxide by EDS (Figure 3-19 E). Figure 3-19 B and D) are both identified as Aluminium Oxide by EDS and Figure 3-19 C) and Figure 3-19 G) are both identified as Manganese Sulphide by EDS (Figure 3-19 H). Stringers of both Aluminium Oxide and Manganese Sulphide were also found in another FV566 ex-service blade (Figure 3-20) [162]. A proposed δ-ferrite phase was observed in the microstructure of FV566. This phase is typically formed at very high temperatures (above 1500 °C) during the early material manufacturing stage and is considered undesirable. Once formed, the δ-ferrite phase is difficult to remove using conventional heat treatments. An example of a possible δ-ferrite phase was seen in a 13Cr4Ni0.02C martensitic stainless steel after tempering at 770 ° (Figure 3-21). The δ-ferrite phase shown in the image closely resembles the proposed δ-ferrite in Figure 3-8 H) and J) with similar size and similar distribution of precipitates along the phase boundary.

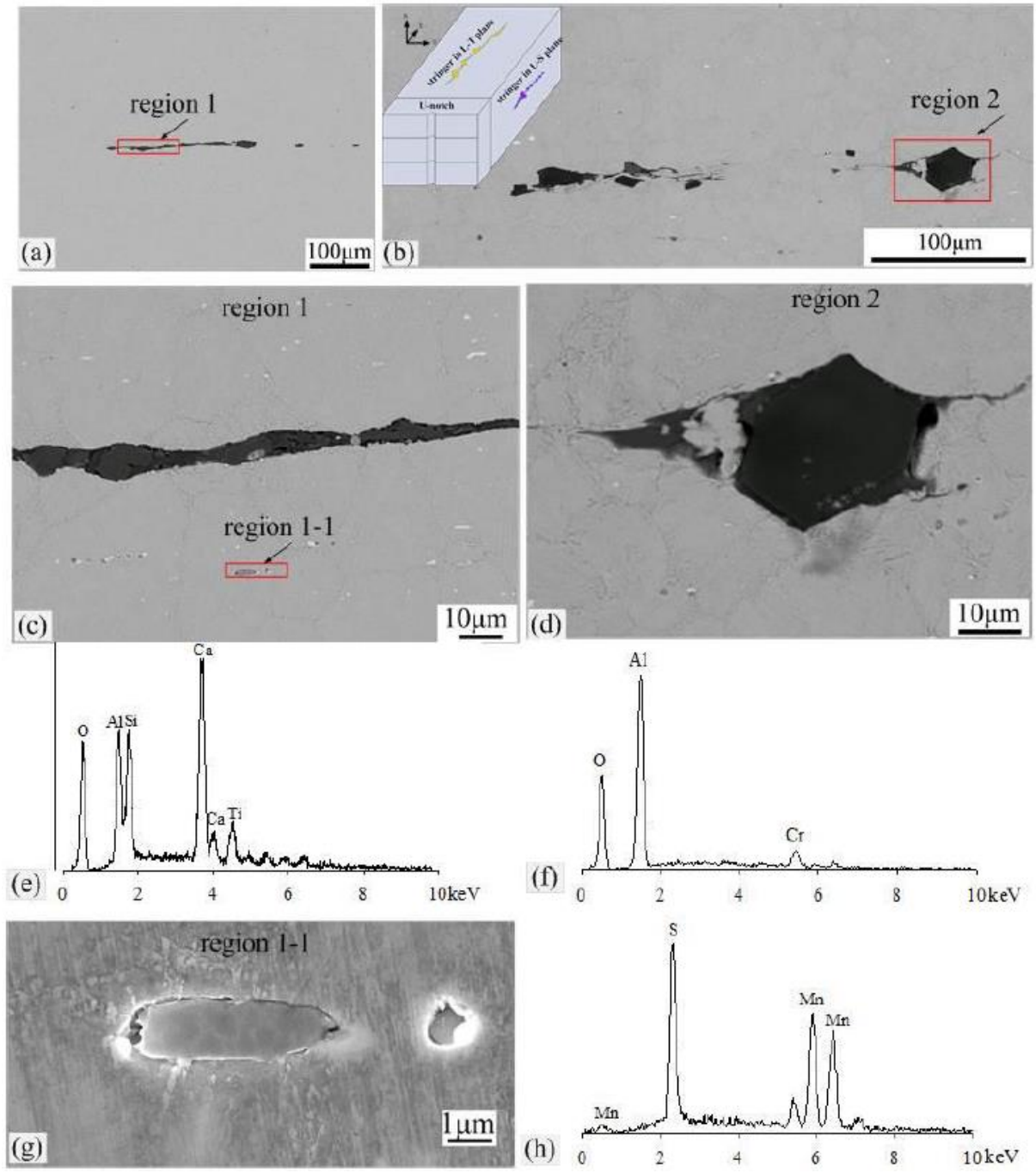

Figure 3-19: a) Stringer labelled as region 1, b) Inclusion labelled as region 2, c) Magnified image of the area enclosed within the red box on image a) showing smaller inclusion labelled as 1-1, d) magnified image of the area enclosed within the red box on image b), e) EDS results of stringer labelled as region 1, f) EDS results of the inclusion labelled region 2, g) magnified image of the area enclosed within the red box on image c), h) EDS results of the inclusion labelled as region 1-1 [5].

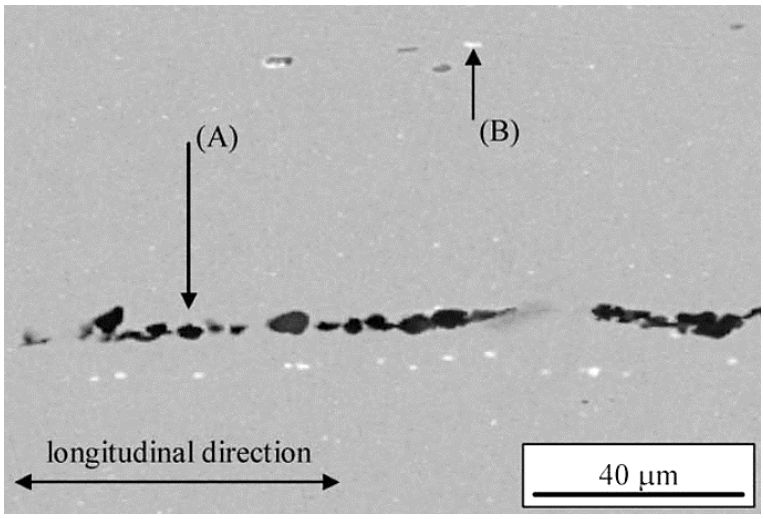

Figure 3-20: Stringers made from (A) Aluminium Oxide and (B) Manganese Sulphide in FV566 material [162].

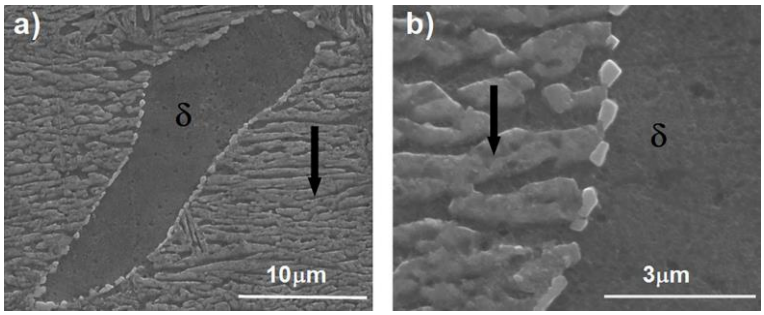

Figure 3-21: (a) SEM image showing a region of δ-ferrite after tempering at 770 °C of 13CrNi 0.02C steel. (b) A higher magnification image shows precipitate detail at the δ-ferrite boundary [163].

The minimal variability between three blades made from FV566 based upon microstructural observations suggests that fatigue testing of samples from multiple blades can be cross compared.

3.4.2 Hardness and mechanical properties

The baseline hardness values in Hardness-Vickers with 200 g load (HV 0.2) of FV566 and FV520B are compared with FV448 [126] (Table 3-7). The baseline hardness of FV448 was 301 ± 5 HV 0.2 and softer than FV566 and FV520B possibly due to a higher proportion of softer retained austenite in the microstructure from the tempering process (Chapter 1.2.5). FV566 is harder than FV448 but slightly softer than FV520B, suggesting that the material hardness properties are typical of a martensitic stainless steel. The standard deviation of the hardness results are represented as the error values for each baseline hardness value. The baseline hardness of FV448 was found by taking a lower number of indents on a single

plane, reducing the amount of variation in hardness due to plane variability, and therefore the error range is lower than observed in FV566 and FV520B which reflects hardness variation between three perpendicular planes.

The baseline hardness values for FV566 and FV520B are further broken down into their constituent perpendicular planes (Table 3-7). The box and whisker diagram shows the statistical distribution of the hardness data for each plane (Figure 3-22). In both materials, the XY plane appears to be relatively hard when compared with the XZ and YZ planes. This is most notable in FV520B material. The increased hardness may be indicative of the rolling direction but this is not clear due to the complex 3-dimensional characteristic of the hardness indent measurement. Figure 3-22 shows that many particularly soft areas were measured that fell outside the 10^{th} – 90^{th} percentile range. These are significant due to the lack of equally hard anomaly values. These softer areas are attributed to indents being taken in areas of retained austenite that are softer than the more abundant surrounding matrix (Chapter 1.2.5). The microhardness values obtained, and conclusions derived from observations for FV566 and FV520B are considered statistically significant due to the large number of indents collected (64 indents for each individual plane).

Material	**Hardness (HV 0.2)**			
	XZ plane	**XY plane**	**YZ plane**	**Baseline**
FV448	X	X	X	301 ± 5 [10]
FV566	341 ± 7	372 ± 9	351 ± 7	354 ± 15
FV520B	369 ± 7	396 ± 11	364 ± 8	377 ± 17

Table 3-7 The baseline hardness in HV 0.2 for FV448 [126], and for FV566 and FV520B in order of hardness from softest to hardest. The baseline hardness of FV566 and FV520B for each perpendicular plane is presented.

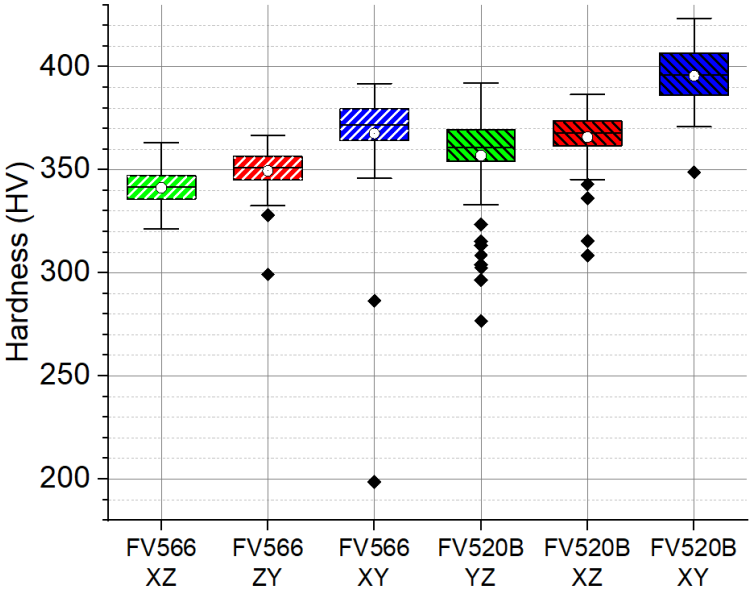

Figure 3-22: Box and whisker diagrams showing the distribution of the data obtained from Figure 3-11. The black central horizontal line shows the median value. The maximum and minimum values of each box show the first and third quartiles. The white circle represents the mean value. The outer horizontal lines show the 10th and 90th percentiles. The outlier diamonds (outside the 10th and 90th percentile range) indicate particularly soft measurements due to testing on areas of softer austenite phases.

Hardness indentation testing was carried out on FV520B with various applied loads from 50 g to 500 g loading. Twenty hardness indents were applied for each load. A smaller applied load tended to produce higher hardness values; a 15 HV difference in mean hardness was seen between 200 g and 500 g load (Figure 3-23). This relationship between applied load and hardness value is commonly known as the 'hardness indentation size effect' [164]. A wider variation in hardness values was found with lower loads due to increased human error when measuring indent size by eye. Secondly, a lower load and therefore smaller indent size is more likely to account for variation of hardness values as a result of microstructural features such as areas of softer austenite phases and harder inclusions. An eye piece x 50 magnification was used for 50 g - 200 g loads. An eye piece x 10 magnification was used for 300 g and 500 g loads resulting in increased measurement error. As the load was increased, the plastic 'pile-up' surrounding the edge of the indentation also increased. This pile-up material obscured the indent edge and ultimately increased measurement error. It is possible that the pile-up material induced a softer reading due to the raised material above nominal surface height increasing the perceived size of the indent.

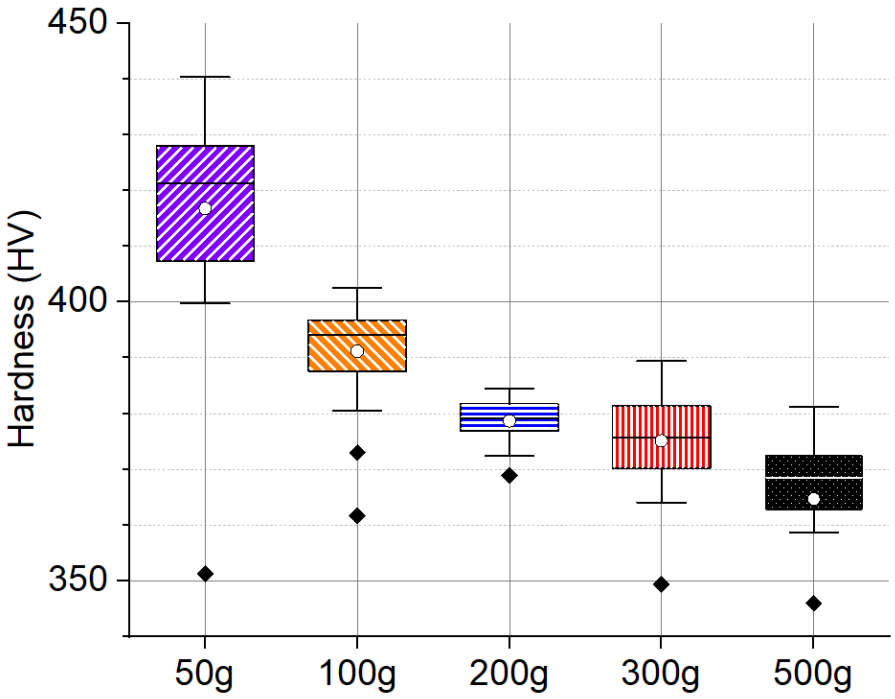

Figure 3-23 Box and whisker diagram showing the hardness (HV) of FV520B taken with five different loads. As the load increases, the hardness value decreases for an identical material commonly referred to as indentation size effect.

An important consideration is whether the grinding and polishing process during sample preparation had any effect on measured hardness values. In other work, eleven TiAl6V4 samples were each subjected to a grinding process where the surface of the sample was subjected to grinding stages [165]. Each new grinding stage was carried out with a new silicon carbide paper of increasingly finer grit size (decreasing particle size) from 80 – 4000 grit papers (equivalent to 200 μm to 5 μm grain size) at 150N force for 3 minutes. The final grinding stage of each sample was carried out with increasing grit paper size. The macro-hardness (H_0) of the material surface was taken for each sample (Figure 3-24). At grit paper sizes 320 and coarser, the large material deformation on the surface causes a relatively rough surface that may influence macro-hardness measurement results. Secondly, large deformation of the material surface may cause some strain hardening on the surface. At 800 grit paper size the hardness values appear to be stabilising with an anomalous result at 1200 grit paper size. Although this work was carried out on a different material to the FV566 studied, the results suggest that a grinding and polishing process with decreasing particle size to 1 μm is not expected to influence the hardness measurements of the material surface via strain hardening effects.

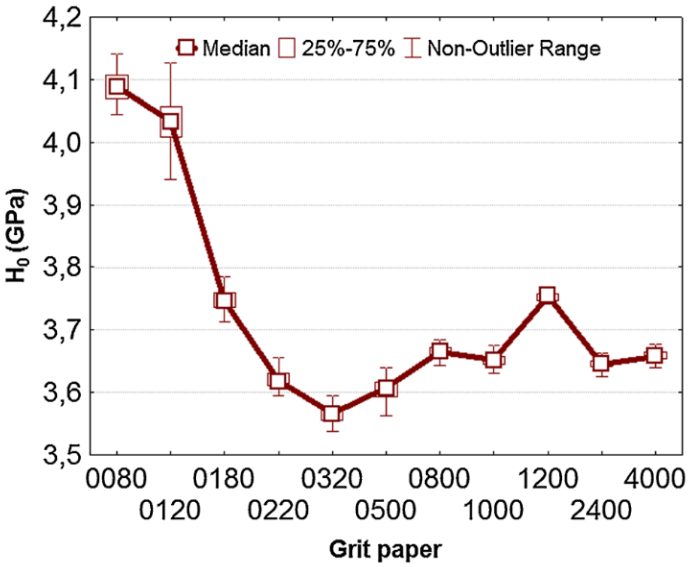

Figure 3-24: The macro-hardness H_0 on the surface of TiSl6V4 versus grit paper size [165].

Turbine blades are exposed to harsh atmospheric conditions and high thermal fluctuations during operation. Such conditions could result in localised changes to the materials hardness due to in-service operating conditions. In other work, the fir-tree-root-fixing of a third-stage (low-pressure) turbine blade made from Inconel 738 after 22 400 hours of service was cut, exposing the tree shape of the blade root (equivalent to the XZ plane), followed by polishing and etching with Aqua regia (Figure 3-25). Several microhardness indents were carried out over the fir-tree-root cross sectional area and hardness values in HV measured. The micro-hardness value (HV) tended to increase with fir-tree-root depth (Figure 3-25 B) and was attributed to thermal gradients during operation [27]. A similar effect might have influenced the results for FV566 and F520B turbine material. However, the orientation of the sample extracted from the FV520B fir-tree-root (Figure 3-2) should negate the effects of a thermal gradient, yet a harder plane was still identified in this material.

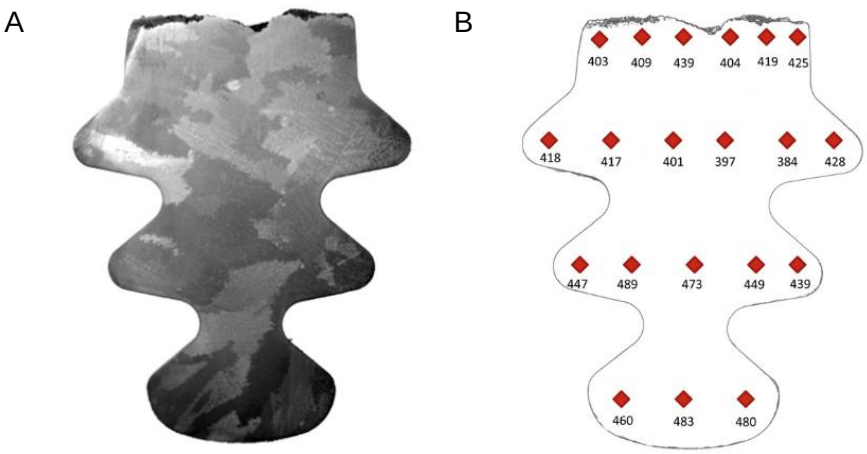

Figure 3-25: A) An etched cross section of a fir-tree-root-fixing made from Inconel 738. B) Corresponding hardness indent locations and hardness values in HV [27].

Tabor [166] argues that microhardness indentation is 'essentially a measure of the plastic yield stress of the material'. Hardness measurements obtained from indentation methods such as Hardness-Vickers have been shown to be linearly proportional to the yield strength and ultimate tensile strength in steel materials [167, 168]. Additionally, numerical modelling of hardness indentation shows that applying a linear relationship between hardness and material strength may be a suitable assumption for estimating material properties from hardness data such as yield strength and ultimate tensile strength [169]. Linear relationships between material hardness and strength was found from linear regression fitting with experimental data [167] (Figure 3-26). The strength of steel material can be estimated with standard error of approximately ± 100 MPa using Equation 3-3 (to estimate yield strength) and Equation 3-4 (to estimate ultimate tensile strength):

$$\sigma_y \pm 100\ MPa = -90.7 + 2.876H_v \qquad \text{Equation 3-3}$$

$$\sigma_T \pm 100\ MPa = -99.8 + 3.7346H_v \qquad \text{Equation 3-4}$$

where σ_y is the yield strength of the material in MPa, σ_T is the ultimate tensile strength of the material in MPa and H_v is the hardness of the material in HV. Hardness in HV from indentation measurement is subject to error from the indentation size effect. The load used for estimating tensile strength properties in this thesis was 500 g since the load used for hardness measurements upon which the relationships were derived are not specified in Pavlina and Tyne [167].

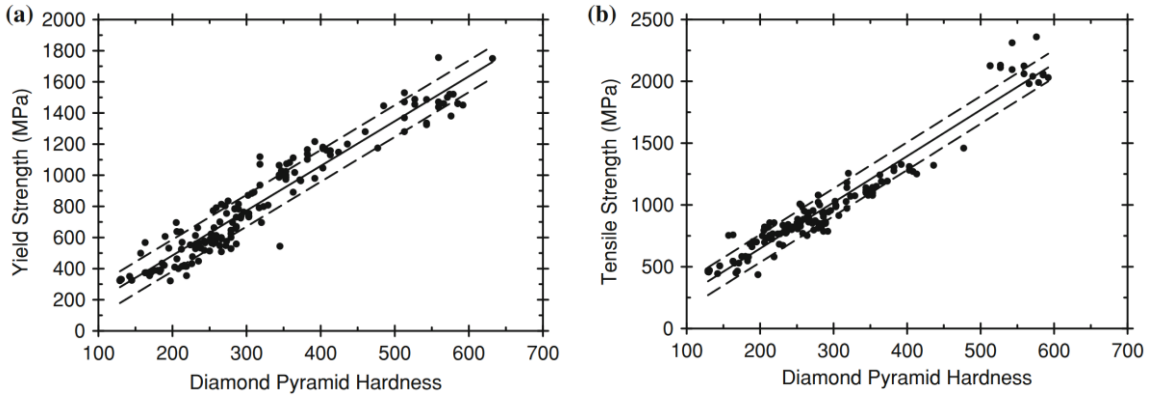

Figure 3-26: A) Relationship between yield strength (MPa) and Diamond Pyramid Hardness (HV) for various medium-carbon steels with a linear regression fit and standard error lines of ± 100 MPa. B) Relationship between tensile strength and HV [167].

Tensile testing of FV448 was carried out by Soady [10] using a dog-bone sample (Figure 3-27). The rate of tensile displacement was 0.3 mmmin^{-1}. Tensile testing of FV520B was carried out on cylindrical dog bone specimens with similar geometry to Figure 3-4 A) [20].

The stress strain curve is not available for FV448 or FV520B; the Young's modulus, 0.2 % proof yield strength and elongation to failure are reported in Table 3-8 and compared with averaged FV566 tensile data.

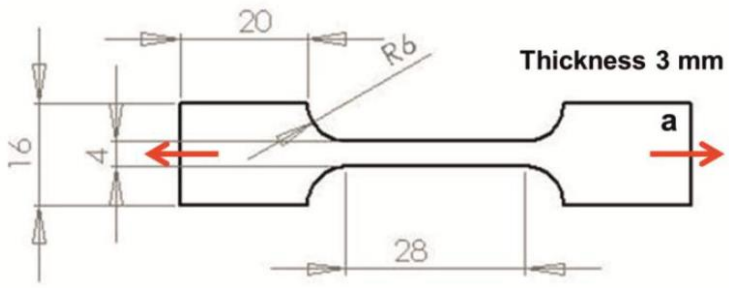

Figure 3-27: Tensile dog-bone sample used by Soady [10].

Some blade variability was found between three blades made from FV566. A relatively high range in Young's modulus of 29 GPa was seen, the reason for this high range is unclear but could be attributed to strain measurement error such as slight slipping of the extensometer during testing. A relatively small range in 0.2 % yield strength and ultimate tensile strength of 30 MPa was seen. The range in mechanical strength is likely due to variation in the material properties and less likely due to testing error. Some blade variability in mechanical strength properties has been identified. The strain to failure was consistent between the three blades and therefore negligible blade variation in ductility was found.

The mean HV 0.5 value across all the FV566 blades from Table 3-3, the mean HV 0.5 value of FV520B (Figure 3-23), and HV 0.2 value for FV448 (since HV 0.5 is unavailable) were used to estimate the yield and ultimate tensile strengths of all three materials using Equation 3-3 and Equation 3-4. The estimated yield strengths were found to match measured values experimentally with an accuracy within ± 5 %. However, ultimate tensile strength tended to be overestimated by at least 10 %. It is therefore expected that the ultimate tensile strength for FV448 is lower than the estimated value proposed.

A difference of 50 MPa was seen between FV448 tensile data taken in the transverse and longitudinal direction. This apparent anisotropy of the mechanical strength of the material is attributed to the rolling process during manufacture of the material. FV448 was found to have lowest hardness and strength, while FV520B has the highest hardness and strength. The variation in mechanical properties seen between the three materials is likely most affected by different heat treatment processes. It is well known that the strength and hardness of martensitic stainless-steel material is directly affected by the proportion of softer reverted austenite (than the ferrite matrix) affected by temperature and holding time during the tempering process [13, 16].

Material	Source	Young's Modulus (GPa)	0.2 % Proof Stress (MPa)	UTS (MPa)	Strain to Failure (%)
FV448	Soady [10]	201	806 ± 6 [a] 858 [b] 775 ± 100 [c]	1025 ± 100 [c]	12
FV566 (M01)	FNC	226	825	980	14.9
FV566 (M02)	FNC	197	815	958	15.1
FV566 (M03)	FNC	210	848	990	15
FV566 (averaged)	FNC	211	830 830 ± 100 [c]	976 1100 ± 100 [c]	15
FV520B	Clark [20]		957 950 ± 100 [c]	1020 ± 40 1250 ± 100 [c]	

Table 3-8: The results from tensile testing for FV448, FV566 and FV520B materials. [a] Yield stress for FV448 in the transverse direction. [b] Yield stress for FV448 in the longitudinal direction. [c] Estimated stress from hardness measurements [167].

Cyclic stress-strain testing of cylindrical dog-bone specimens made from FV448 was carried out by Soady [22] with four strain ranges of 0.005, 0.008, 0.011 and 0.0155 with R-ratio of -1. Each strain range was applied to four separate samples to eliminate possible coaxial effects due to ramping. A similar cyclic softening behaviour was also observed in FV448 and other tempered martensite materials with non-symmetric loading such as R = 0.1 [6, 21]. Cyclic softening behaviour was therefore expected in the FV566 material.

3.4.3 Applicability of FE model

The strain at the mid length of a PBB sample where maximum strain and fatigue is expected to occur was measured during a 4-point bending test. A FE quarter-model with identical loading and geometry conditions to the 4-point bending test was produced and compared with the experimental test. A discrepancy between FE modelling and experimental testing was observed. For example, at a load of 10 000 N, the FE model predicts a 30 % higher strain than experimental testing. However, the FE model is considered an appropriate representation of notched samples in 3-point bending for the following reasons.

- You [125] carried out a 3-point bend test on a U-notched geometry of 9 mm radius and 2.5 mm deep (Figure 3-28 A) and measured the strain using a strain gauge in

the centre of the notch. It was found that a PBB geometry (Figure 3-28 B) was more sensitive to boundary conditions than a U-notched geometry (Figure 3-28 C). FE modelling of U-notched geometry was found to match nominal stress-strain curves with more accuracy (48 % for a PBB model and 12 % for a U-notched model). The improvement in accuracy for U-notched models may be attributed to localised material notch constraint effects especially at the notch centre. Despite the lack of agreement between experimental and FE modelling for a PBB, the FE model is expected to be more accurate for U-notched models. Furthermore, the U-notch geometry used for the remainder of this PhD has a sharper radius, enhancing the local material constraint effect and potentially improving the agreement between FE modelling and experimental testing further.

- Coaxial effects may have been experienced by the PBB during the 4-point bending test due to ramping (increasing strain range in steps after stabilisation of the material has occurred for each strain range for the same test specimen) [170]. Coaxing produces the effect of hardening and increasing fatigue limit of the material. If coaxing effects are removed, the stabilised load-strain curve from experimental testing would slightly shift towards the load-strain curve predicted by FE modelling, slightly improving agreement between the FE model and experimental testing.
- Results and conclusions obtained via FE modelling based upon comparative testing will be less affected by FE modelling assumptions and limitations since material behaviour modelling and boundary conditions remain identical for each test.

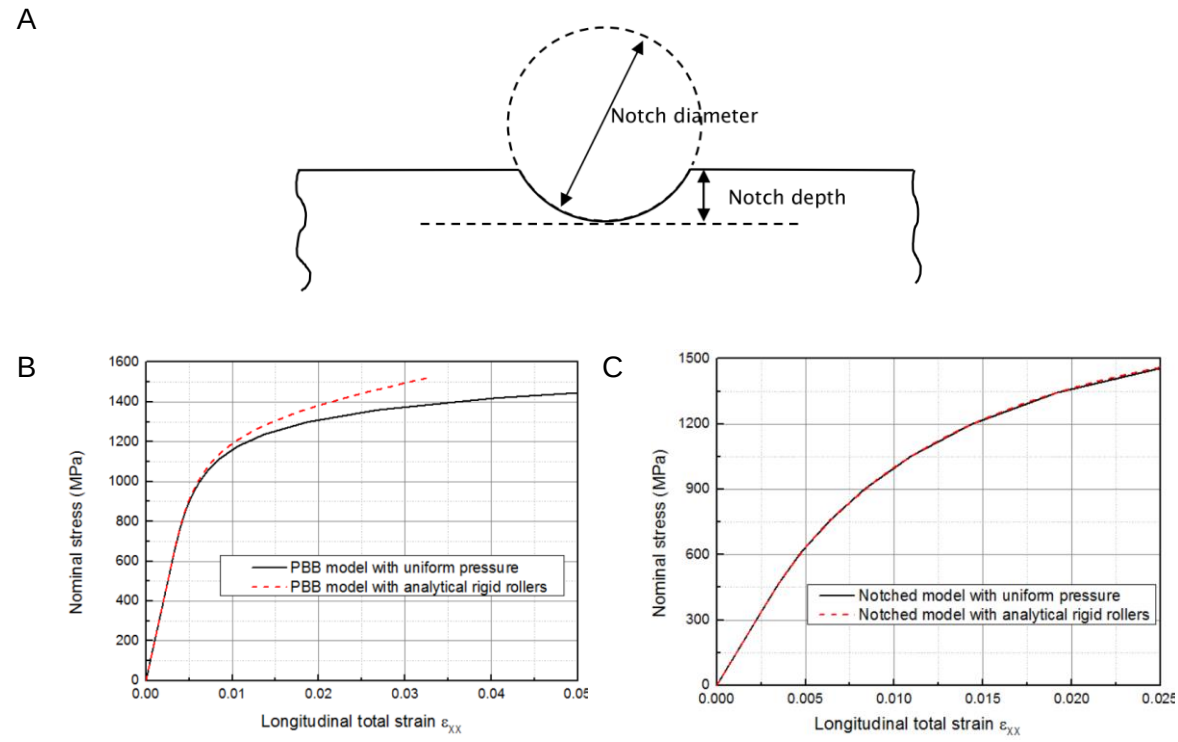

Figure 3-28 A) FE modelling for a PBB with uniform pressure applied to the top surface (black) and with rigid rollers (red). B) FE modelling for a notched geometry with uniform pressure and with rigid rollers. The U-notch geometry is less sensitive to modelling assumptions due to localised material notch constraint effects [125].

3.4.4 Fatigue properties

The long crack growth behaviour, Paris-law constants and ΔK threshold of FV566 and FV520B were found and compared with FV448 material from literature [10]. The fracture surfaces of FV566 and FV520B long crack samples (Figure 3-29) are symmetrical, indicating that the long crack grew uniformly across the width for both tests, providing a suitable comparison between the two materials. The results in Figure 3-14 and Table 3-7 suggest that a softer material with reduced strength provides a higher resistance to long crack (and short crack) growth at identical ΔK. This result is not surprising since a softer and more ductile material would induce higher energy dissipation around the crack tip and plastic zone resulting in lower energy available for driving crack growth. In Figure 3-29, a transition line can be seen indicating very slow crack growth near the ΔK_{th} on the FV520B material. A less clear indication of this transition can be seen on the FV566 material. It is possible that the higher hardness and strength of the FV520B material is responsible for the visibility of this transition on the fracture surface. The fatigue surface was found to have

quasi-cleavage fracture characteristics typical of fatigue in martensite and did not observably change in appearance or surface roughness with increasing ΔK values.

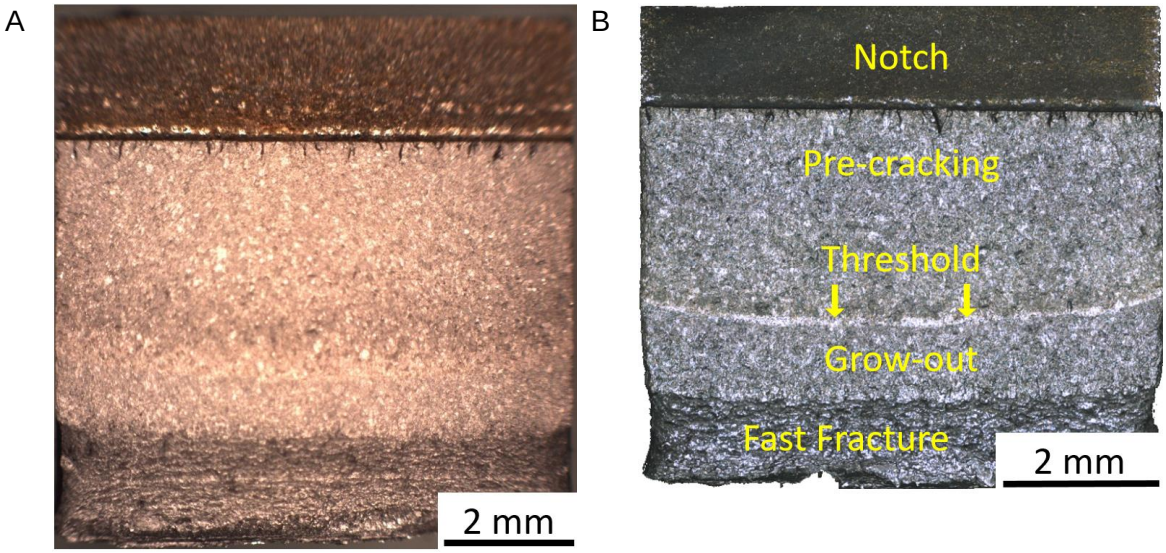

Figure 3-29: Fracture surfaces of SEN samples after long crack testing to threshold of (A) FV566, (B) FV520B.

3.5 Summary and conclusions

The microstructure, mechanical properties, and fatigue properties of three 11-15 Cr tempered martensitic stainless-steel materials (FV448, FV566 and FV520B) were compared. FV566 extracted from several ex-service turbine blades were compared to investigate blade variability and the efficacy of cross blade testing.

The microstructure of all three materials was typical of tempered martensite with similar features such as inclusions, prior-austenite grain boundaries and stringers. The microstructural features were less noticeable in the FV520B material. An undesirable δ-ferrite phase was observed in FV566 microstructure.

Hardness indentation testing and tensile testing revealed anisotropy in mechanical properties of FV448 and FV566, attributed to the rolling process during manufacture of the material. Hardness measurements were used to estimate yield strength were successful with an accuracy of ± 5 % but ultimate tensile strength was overestimated by at least 10 %. FV520B was found to be the hardest and strongest material with FV448 the softest and weakest. Tensile testing of three FV566 materials revealed some small variation in mechanical properties between blades.

Cyclic softening behaviour was seen in FV566, a typical feature of 11-15 Cr tempered martensitic stainless-steel material.

Long crack testing showed a relationship between material strength and long crack growth rate in stage II crack growth. FV448 (the softer material) showed higher resistance to long crack growth attributed to dissipation of energy at the crack tip and plastic zone.

An elastic-plastic FE model was produced based upon tensile data of FV566. Despite the lack of agreement between FE modelling and experimental results of a PBB geometry, the model was deemed to be acceptable especially for U-notched sample geometry (a common test geometry for the remainder of the thesis).

Slight blade variability in mechanical strength properties of FV566 was found across three blades. Conservative tensile data obtained from the weakest blade (M01) was used for the FE material model. The slight blade variability found is considered to have a minimal effect on fatigue behaviour and allows for cross blade testing.

Chapter 4: Overload effect on fatigue behaviour

4.1 Introduction

It was discussed in Chapter 1.3.1 that in-service low-pressure steam turbine blades typically made from martensitic stainless steels are being increasingly exposed to cyclic fatigue conditions due to the drive towards cleaner alternative renewable sources of energy. A typical turbine is currently subjected to 150 start-stop cycles and a 10 % over-speed test per year. During inspections cracking has been observed in the fir-tree-root-fillets of the last stage low-pressure steam turbine blades. A lack of understanding of short crack growth behaviour in the notch stress field with the small over-speed overloads may be resulting in over conservatism in the lifing approaches applied (personal communication, EDF, 5th January 2018). The chapter aims to investigate the impact of service-relevant overloads on notch fatigue behaviour including crack initiation, coalescence, and propagation with within steam turbine blade materials.

Variable amplitude cyclic loading is a common loading condition experienced by many engineering components. In some instances, the variable amplitude loading is well defined, such as a routine over-speed test of a turbine in a power plant that constitutes a single tensile periodic overload [89]. Many studies have shown tensile overloads can extend the fatigue life of various metallic materials such as aluminium and steel including within notched samples [60, 62, 90-94, 96-98, 102, 105, 108, 171-174]. It is widely reported that overloads tend to reduce crack growth rates and affect the growth rate of both long and short cracks during cyclic loading. Many explanations to why the crack growth rate reduces have been suggested and tested by different authors with strain hardening, compressive residual stress ahead of the crack tip and closure effects being most widely accepted in most metallic fatigue tests under ambient air conditions (Chapter 2.2.4).

Studies have demonstrated that an overload threshold exists whereby the lowest OLR that produces a clear effect (retardation of long crack growth rate) from an overload cycle for R-ratio of 0.1 is between 1.44 and 1.55 in a martensitic stainless steel and a Ti-6Al-4V titanium alloy [90, 105]. The fatigue behaviour expected with smaller 6 % and 10 % overloads every 150 baseload cycles will not differ significantly from constant amplitude loading conditions. Therefore, an additional 50 % overload (OLR of 1.56) was introduced to induce a change in fatigue behaviour, especially for crack initiation and propagation.

One might expect a slowing of the crack growth rate to be the main contributory factor to un-notched samples in the HCF regime. On the other hand, a notched sample in the LCF regime will have additional complexities arising from material plasticity and resulting residual stress on the notch surface. An independent finite element analysis by FNC

(personal communication, FNC, Feb, 2018) showed that the fir-tree-root-fillets may undergo localised plastic deformation during in-service loading conditions in the LCF regime. Offcuts from ex-service blade fir-tree-roots have therefore been subjected to hardness testing to identify possible areas of localised strain hardening at the fir-tree-root-fillets from in-service loading conditions.

Short crack growth behaviour in notches is well known. Crack initiation and small crack growth in high stress concentration areas, such as the notch geometry of fir-tree-root-fillets, is believed to control the fatigue behaviour in gas turbine blade components. A surface replication technique has therefore been used to observe the surface of the notch at regular cyclic intervals to investigate initiation, short crack growth, and coalescence behaviour in U-notched samples under constant amplitude loading and with 50 % overloads. Depending on the length of the crack, short cracks are affected by local microstructural features, the relative crack tip plastic zone size compared to the crack length, the surrounding material's plasticity levels (e.g. the surrounding notch stress field) and may not always be well described using linear elastic fracture mechanics assumptions. To the author's knowledge, initiation behaviour within U-notch geometry with the presence of overloads has not been fully investigated within the literature.

This work investigates the effect of relatively small single periodic tensile overloads on each stage of the fatigue process in a FV566 martensitic stainless-steel material, to better account for the effects of overloads on observed and predicted lifetimes. Notched specimens were subjected to cyclic loading in the LCF regime, where plasticity, strain hardening and residual stress, are expected to affect lifetime. A surface replication technique was used to observe the surface of the notch at regular cyclic intervals to investigate initiation, short crack growth, coalescence, and finally long crack growth behaviour.

Some of the work presented in this chapter has been published in the following paper [153] and is presented here with additional analysis of published data:

B. M. D. Cunningham, A. Evangelou, C. You, A. Morris, J. Wise P. A. S. Reed, A. Hamilton *'Fatigue crack initiation and growth behaviour in a notch with periodic overloads in the low-cycle fatigue regime of FV566 ex-service steam turbine blade material'*. Fatigue Fract Eng Mater Struct. 2021. https://doi.org/10.1111/ffe.13617

4.2 Experimental methodology

Details regarding material extraction in the form of plain bend bars of FV566 from ex-service low-pressure turbine blade root-fixings (LD 66) is available in Chapter 3.2.1. An additional

offcut from the fir-tree-root-fixing including the fillet notch geometry was provided (Figure 4-1).

4.2.1 Hardness Testing

An offcut from an ex-service blade fir-tree-root was cut into three parts using a wet sectioning saw (Figure 4-1 A). The offcut containing the fir-tree-root-fillet was mounted in Bakelite using a hot mounting press. Grinding with progressively finer silicon carbide grinding paper followed by polishing with progressively finer suspensions, finishing with 1 µm diamond suspension, was carried out for hardness testing (Figure 4-1 B). A finite element analysis (FEA) performed by FNC (personal communication, FNC, Feb, 2018) on a typical fir-tree-root geometry revealed three locations of interest outlined by the three yellow boxes in Figure 4-1 C). Hardness indentation testing was carried out to British Standards *BS EN ISO 6507-1:2008* [118] on a (Future-Tech FM-300) microhardness tester. Twenty-four microhardness indents (four rows by six columns) with 500 g loading and a dwell time of 15 seconds were carried out (Figure 4-1 D). The indent dimensions were measured, and the hardness value in Vickers Hardness (HV) found using the microhardness machines' in-built function.

A

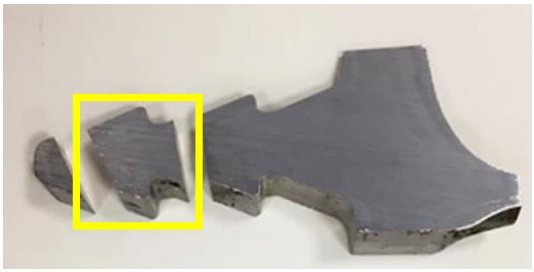

B

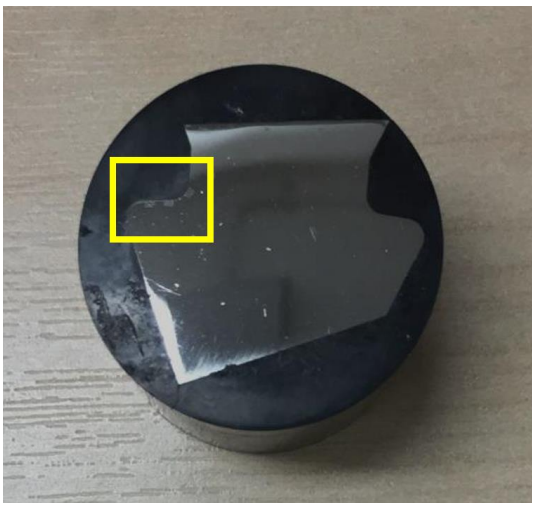

C

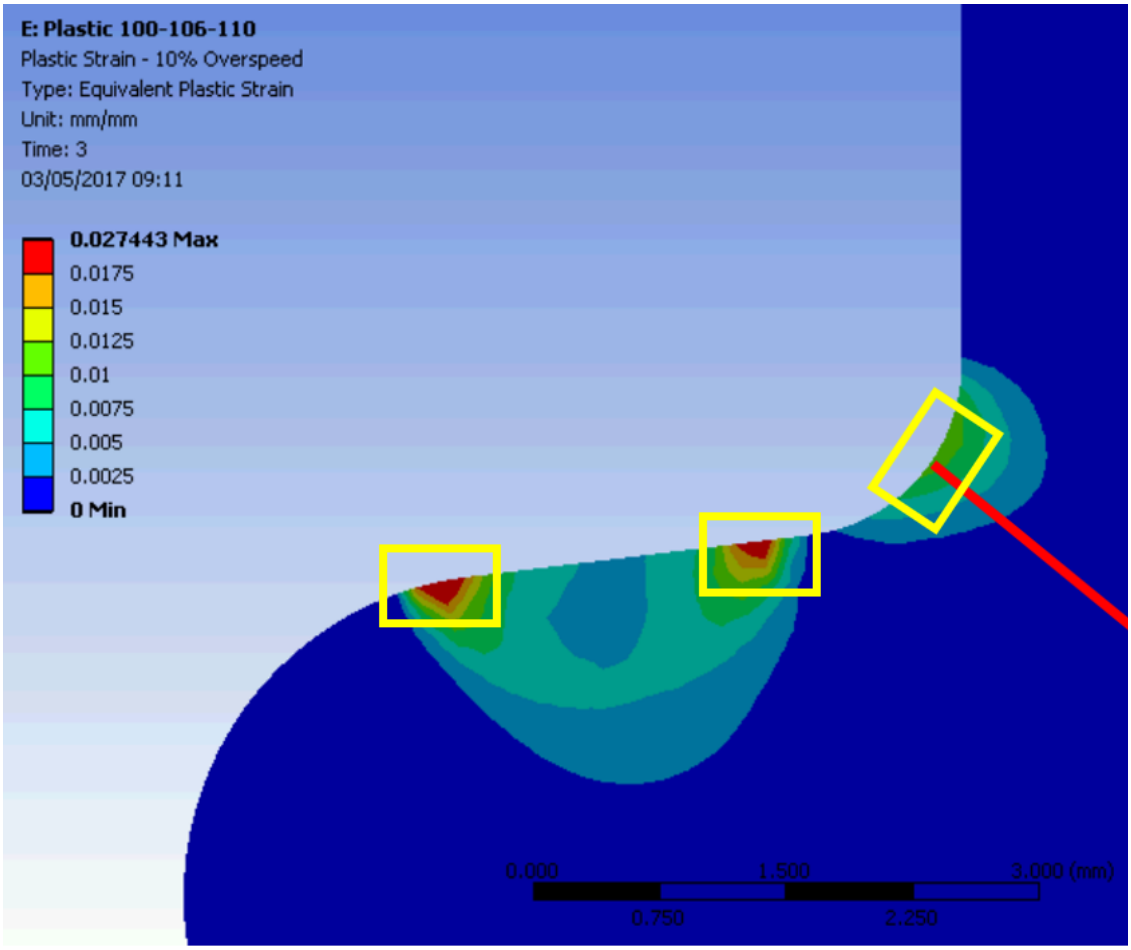

D

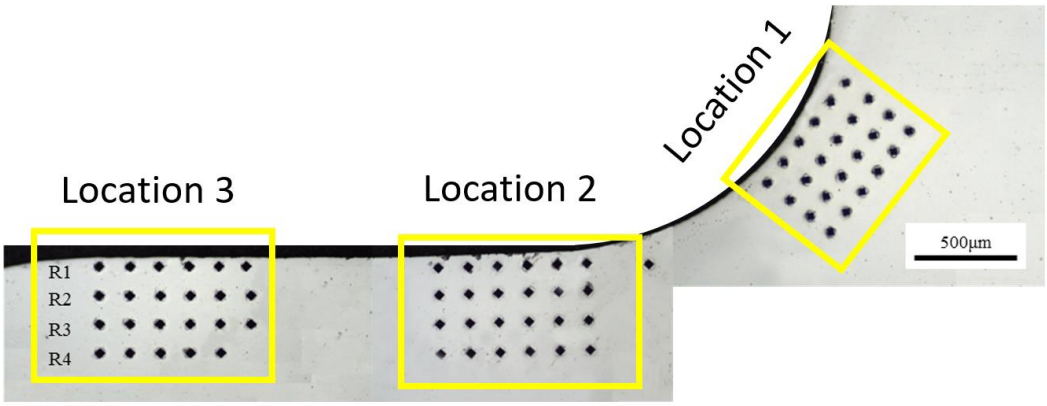

Figure 4-1 A) An offcut from the fir-tree-root of an FV566 blade (M06) cut into three separate parts. The yellow box indicates the offcut used for hardness testing. B) The offcut mounted and polished for hardness testing. C) FEA performed by FNC of identical fir-tree-root geometry showing the plastic strain expected from 10 % over-speed testing. Three areas of interest were identified for hardness testing. D) Twenty-five micro-hardness indents were taken at the three locations of interest on a fir-tree-root-fillet.

4.2.2 Short crack testing

4.2.2.1 Sample preparation

Plain bend bars from blade M06 made from FV566 had a U-notch with industry relevant dimensions (2.25 mm radius and 1.25 mm deep) machined in the centre of the sample (Figure 4-2). The U-notch geometry is representative of in-service turbine blade fir-tree-root fillets with a stress concentration factor of 1.6. The orientation of the notch was chosen to induce representative fatigue behaviour expected from in-service fir-tree-root-fillets. The samples were left in ambient conditions for several months before being cleaned with acetone in an ultrasonic bath and stored in a desiccator after signs of corrosion were observed.

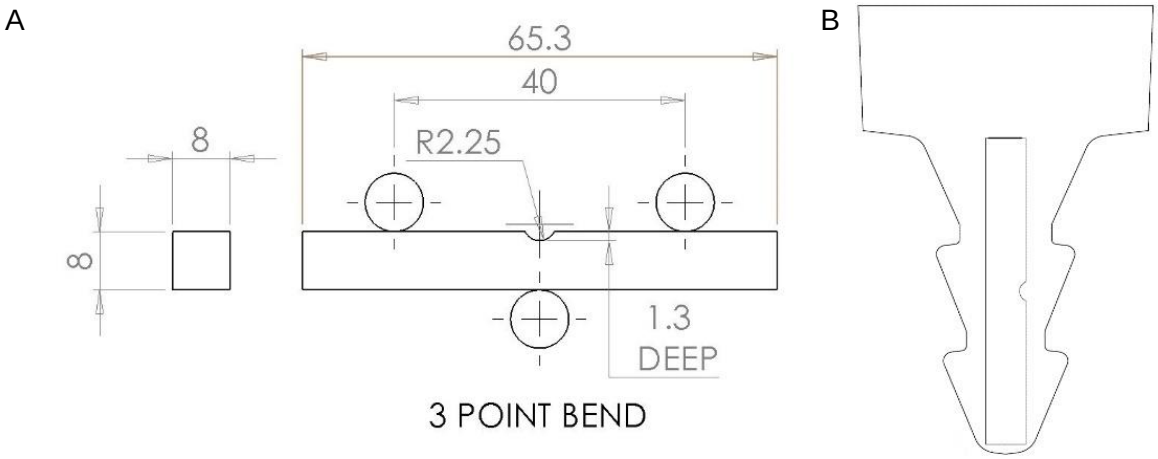

Figure 4-2: A) U-Notch sample dimensions and 3-point bending set up for short crack testing of FV566. B) The orientation of typical U-notched samples. The notch orientation is representative of in-service turbine blade fir-tree-root-fillets.

4.2.2.2 Notch surface characterisation

Two U-notch surface conditions were tested as shown in Figure 4-3. The as-received surface condition contained corrosion pits from long term exposure to ambient conditions on the surface of the U-notch resembling a likely representative in-service fir-tree-root-fillet surface condition. Machining marks were also seen running perpendicular to the tensile axis. Polishing of the notch surface was carried out with 9 µm diamond suspension using a rotary power tool (Dremel) to remove machining marks and corrosion pits. Some light polishing lines can be seen running parallel to the tensile axis on the polished notch surface.

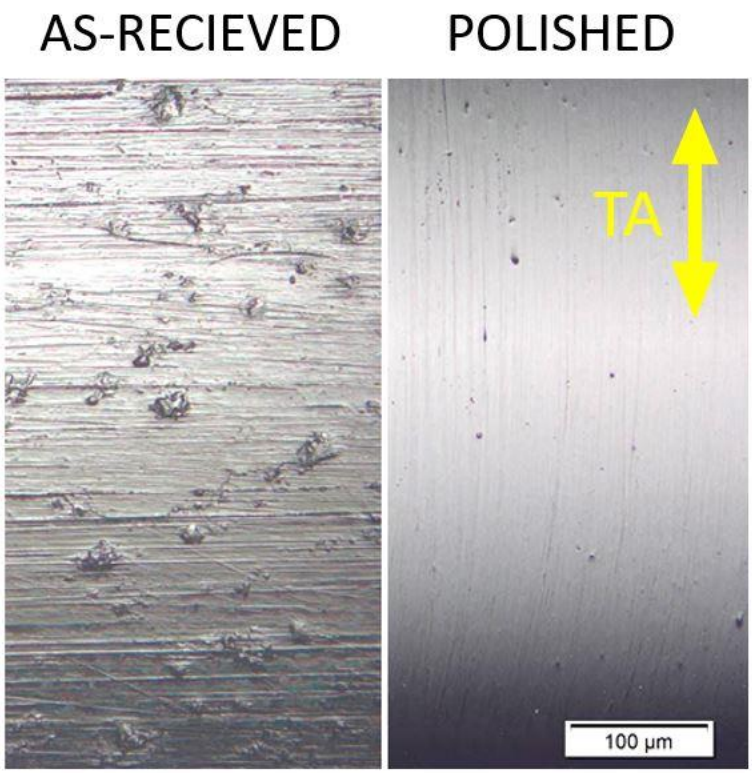

Figure 4-3: The as-received surface condition contained corrosion pits due to the surface being exposed to ambient air conditions, machining marks can be seen running perpendicular to the tensile axis (TA). The polished surface condition was polished using 9 µm suspension, some residual corrosion pitting can still be seen along with polishing marks running parallel to the TA.

Fifteen random corrosion pits where characterised using optical profilometry (Alicona). The projected surface area and depth of several corrosion pits were estimated. An *a/c* ratio was calculated where *a* is the maximum pit depth (crack depth equivalent) and *c* is the radius of the pit (half of the total projected surface crack length) to allow a comparison between pit and short crack *a/c* ratios (Figure 4-10).

Surface roughness R_a measurements were taken using a profilometer (Infratouch) in accordance with *BS EN 4288: 1998* [175] to compare the roughness of the as-received and polished U-notch surface condition. A measurement length of 5 mm and *Lc* value of 0.8 was applied in the traverse direction (perpendicular to the tensile axis) for all notch surfaces.

4.2.2.3 Determination of the cyclic baseload

A 3D quarter-model of the U-notch sample in 3-point bending was developed using ABAQUS software using the method as described in Chapter 3.2.6. The boundary conditions for the U-notch geometry are shown in Figure 4-4. The loads required to produce a total strain range of approximately 0.75 % with R-ratio of 0.1 at the centre of the notch was found using the FE model.

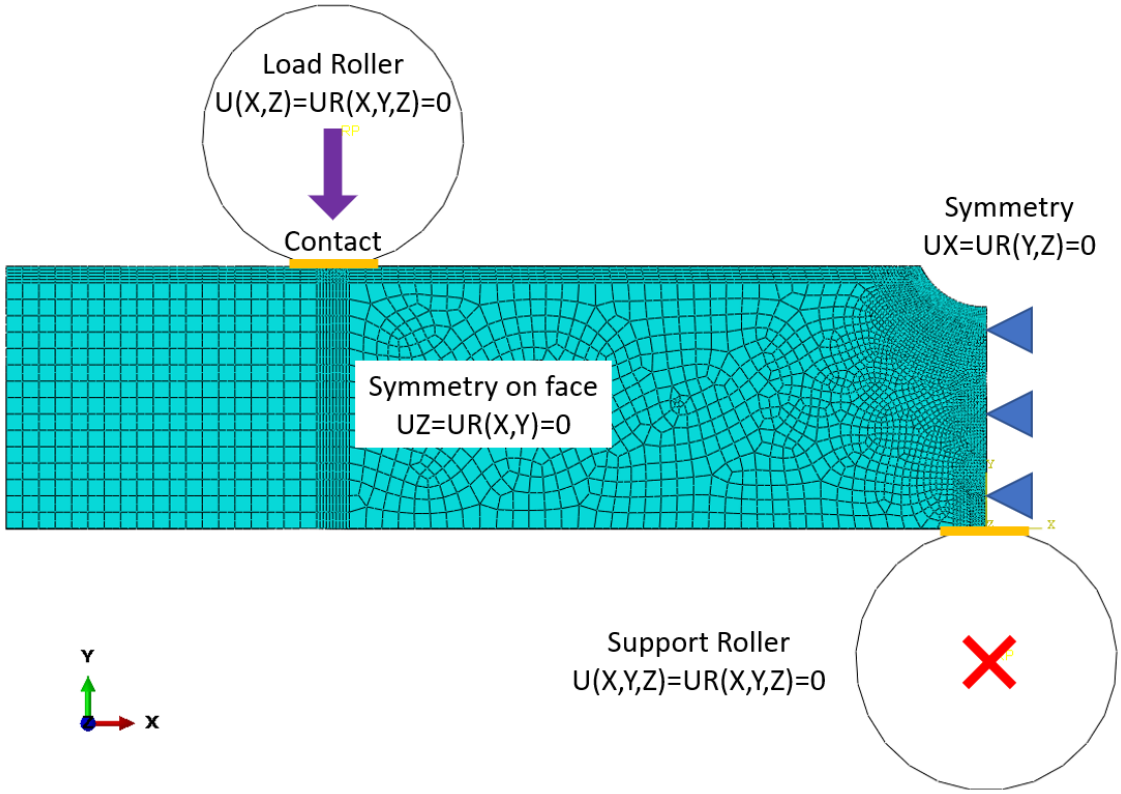

Figure 4-4 The boundary conditions for the U-notch model where UX is the degree of freedom of unidirectional movement along an axis X and RX is the degree of freedom of rotation around an axis X.

4.2.2.4 Continuous and interrupted fatigue testing of U-notch samples

Fatigue testing of U-notch samples was carried out under 3-point bend loading conditions on an Instron 8502 servo-hydraulic machine at room temperature using a sinusoidal waveform at 10 Hz frequency at a baseline R-ratio of 0.1. Single tensile periodic overload cycles were applied with a slower frequency of 1 Hz. The magnitude of a tensile single periodic overload known as the overload ratio (OLR) was calculated using Equation 4-1. Where P_{OL} is the maximum load during the overload cycle, P_{max} is the maximum load during the baseload cycle and P_{min} is the minimum load during the baseload cycle. An overload 50 % above the maximum base load P_{max} has an equivalent OLR of 1.56.

$$OLR = \frac{P_{OL} - P_{min}}{P_{max} - P_{min}} \qquad \text{Equation 4-1}$$

U-notch samples were subjected to constant amplitude loading conditions and to a single periodic overload with OLR of 1.56 every 150 baseload (constant amplitude) cycles (Figure 4-5). The overload frequency was chosen to represent in-service over-speed test operating conditions.

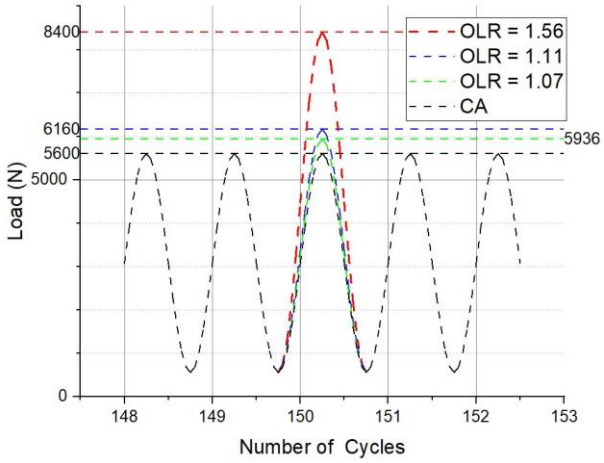

Figure 4-5: A visual schematic of the application of an overload cycle with OLR of 1.07, 1.11 and 1.56 every 150 baseload cycles.

U-notch samples were tested to obtain representative lifetimes under various loading conditions (continuous lifetime tests) while some were interrupted during fatigue cycling (Figure 4-6) to enable regular surface replication of the notch root using Repliset-F5 (Struers Ltd) silicone material with a resolution of 0.1 μm (interrupted lifetime tests). Interrupted lifetime testing allowed the recording of crack initiation and evolution mechanisms on the surface of the U-notch at regular intervals during fatigue cycling. The replicas were subsequently analysed using an Olympus BX51 optical microscope and FIJI Image software. Backtracking of surface replicas allowed identification of crack initiation events and short surface crack growth rate.

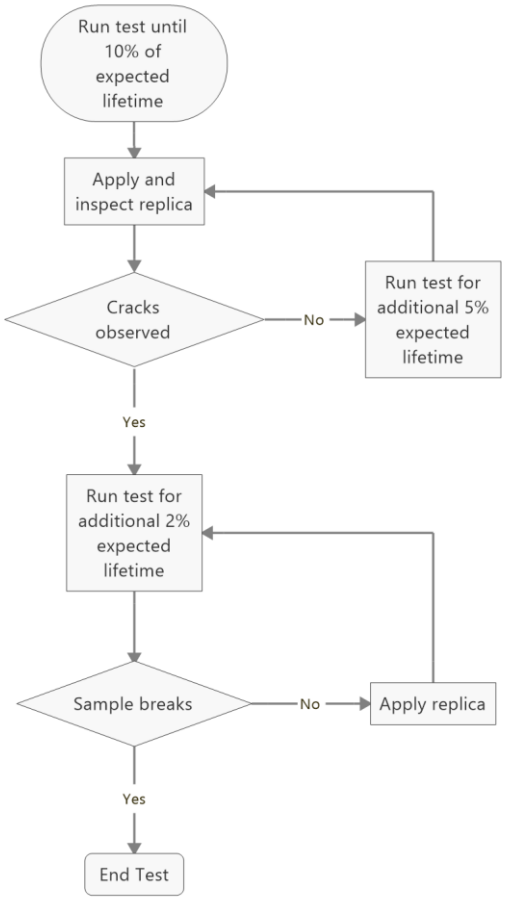

Figure 4-6: A decision map showing the surface replication method applied for suitable collection of short crack growth data providing the expected number of cycles to failure can be estimated.

4.2.2.5 Post-test analysis

Projected crack lengths $2c_{project}$ parallel to the tensile axis (Figure 4-7) were measured for several cracks for each replica using a “best estimation” method (Figure 4-8). A visual representation of the short crack growth and coalescence evolution during fatigue was created from the replicas using animations in Microsoft PowerPoint. A record of crack length, $c_{project}$, versus number of cycles, N for each crack, was constructed for short crack growth rate determination. Projected surface crack growth rates dc/dN were calculated using the secant method and compared for U-notch specimens tested under constant amplitude (CA) and for an OLR of 1.56 (applied every 150 baseload cycles). The ΔK values for both primary (the main crack that grows the entire width of the sample) short surface cracks and secondary short surface cracks (Figure 4-9) were calculated using the methodology described in Scott and Thorpe [52] and Holdbrook and Dover [53] (Appendix C). The a/c ratio (Figure 4-10) used for this study was calculated using 4-2 based on the study by He et al. [50].

$$a/c\ ratio = 0.824 - 8.45 \times 10^{-5}(2c) + 5.19 \times 10^{-9}(2c)^2 \quad 4\text{-}2$$

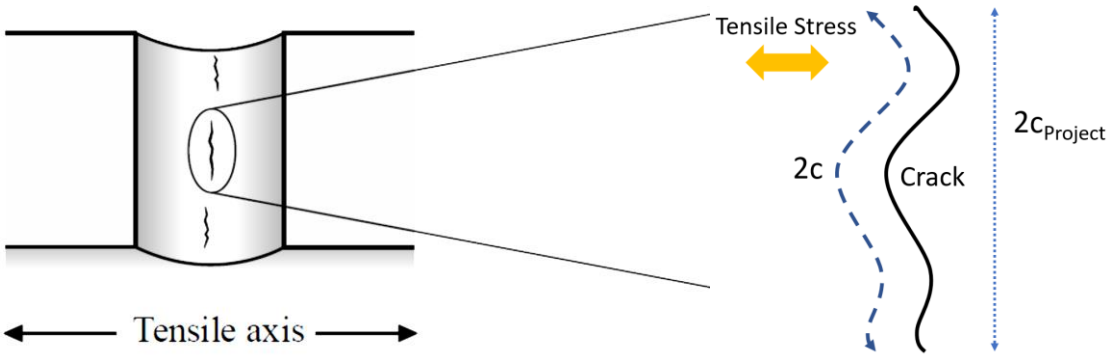

Figure 4-7: Schematic showing tensile axis direction (in the longitudinal direction) that is perpendicular to projected surface crack growth. The total length of the tortuous crack is *2c* while the lower projected length of the crack is $2c_{Project}$. All measured crack lengths are projected crack lengths, image taken from [5].

Figure 4-8 A short crack approximately 800 µm in length. The two green arrows show the approximate crack tip locations upon which the crack length is estimated.

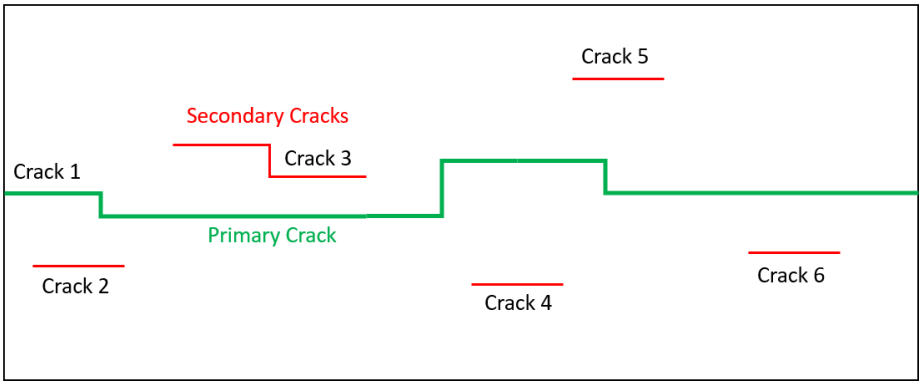

Figure 4-9: A schematic of the notch surface with the primary crack spanning the entire width of the sample (shown in green) and secondary cracks (shown in red).

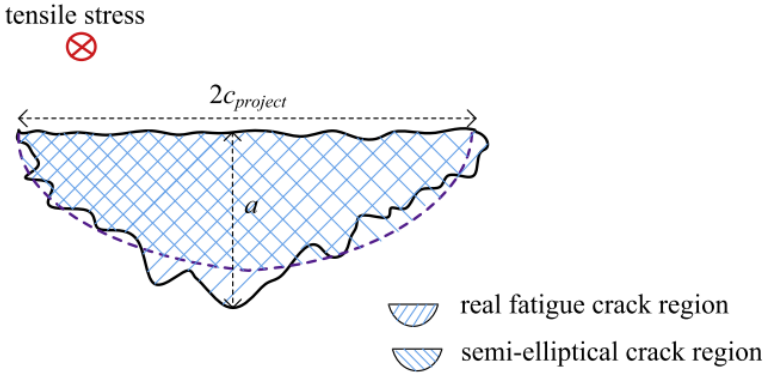

Figure 4-10 A schematic showing the characteristic semi-circular shape of the fatigue region from a short surface crack seen on the fracture surface. 'a' is the crack depth and '$2c_{Project}$' is the projected length of the surface crack. Image taken from [5].

4.2.3 Fractography

The fracture surfaces of all U-notch and SEN bending tests were observed using a JSM 6500F field emission Scanning Electron Microscope (SEM) to observe beachmark features and identify chemical constituents of inclusions using energy dispersive X-ray spectroscopy (EDX). Initiation events were identified using surface replica data. For U-notched samples subjected to continuous lifetime testing and therefore with no surface replication data, an optometry surface profiling microscope (Alicona Infinite Focus) was used to identify ratchet marks. The fracture surface height was recorded across the width of the sample near the notch surface over approximately 4000 data points. The height difference between data points was plotted in a height difference versus width graph (Figure 4-11). Clusters of height differences of greater than 4 µm were found to accurately identify ratchet mark locations caused by the coalescence of short cracks. A height difference cut-off of 4 µm was found by adjusting the height difference cut-off point until the number of clusters exceeding the cut-off point (estimated number of ratchet marks) was equal to the actual number of initiation events plus one for a sample with a known number of initiation events from surface replica data. The number of initiation events that form the primary crack can be estimated by adding one to the total number of estimated ratchet marks (Figure 4-11).

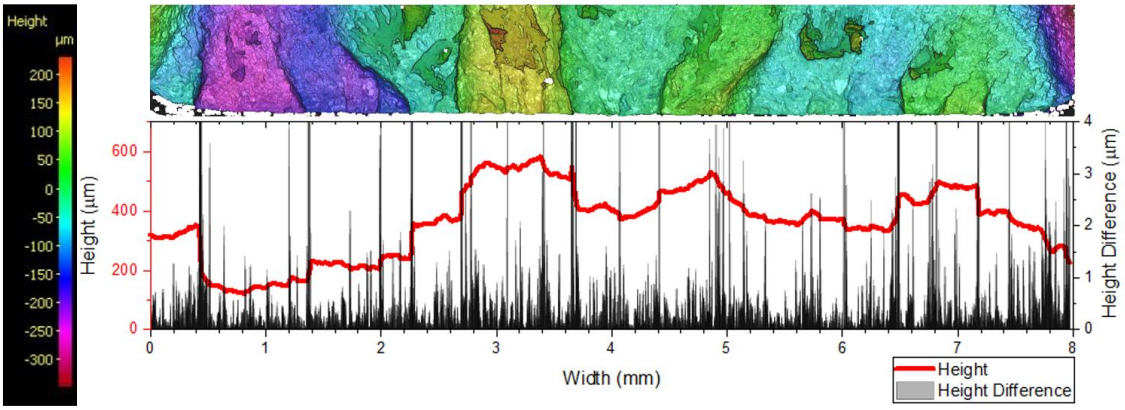

Figure 4-11: An optometry profile image created using an Alicona Infinite Focus optical microscope showing plane heights of the fracture surface of the as-received continuous lifetime sample with 0.75 % strain range. The ratchet marks are identified when the average height difference between nearby data points consistently exceeds 4 µm.

4.2.4 Long crack testing

Plain bend bar samples from FV566 blade M06 were prepared for long crack testing following the same methodology detailed in Chapter 3.2.5.2. Single periodic tensile overload cycles with OLRs of 1.07, 1.11 and 1.56 (Chapter 4.2.2.4) were applied every 150 baseload cycles with a frequency of 1 Hz to three samples. The Paris-law constants (*C* and *m*) were found and compared with constant amplitude loading results from Chapter 3.3.6.

4.3 Experimental results

4.3.1 Hardness testing

Hardness testing was carried out on a fir-tree-root offcut at three notch locations of interest Location 1 suggests consistent hardness values between 332 HV – 338 HV for all notch surface distances. Location 2 also suggests consistent hardness values, a higher range of hardness values was observed 100 µm from the notch surface. A relatively low hardness of 320 ± 5 HV was found 100 µm from the notch surface suggesting softening of material at the notch. From 350 µm to 650 µm the hardness values are consistent with observations made for locations 1 and 2. The results presented are inconclusive and do not suggest any strain hardening or softening of material near the notch surface.

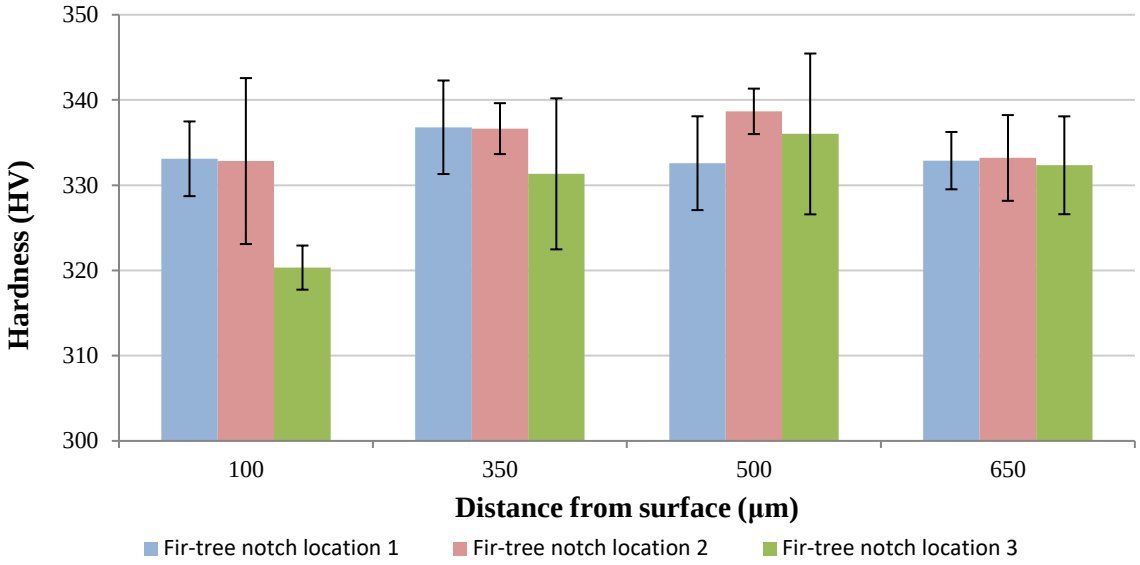

Figure 4-12: Hardness in Hardness Vickers (HV) from indents taken at three notch locations at increasing distance from the notch surface.

4.3.2 U-notch short crack testing

4.3.2.1 Notch surface characterisation

The polished notch surface had an average R_a surface roughness of 0.094 µm ± 0.031 µm (one standard deviation) with occasional shallow residual corrosion pits that were not fully ground away. The as-received notch surface had an average R_a surface roughness of 0.14 µm ± 0.087 µm (Figure 4-13). A wide range of corrosion pit shapes and sizes were observed from 350 µm^2 to 7000 µm^2 diameter and *a/c* ratios between 0.06 and 0.3.

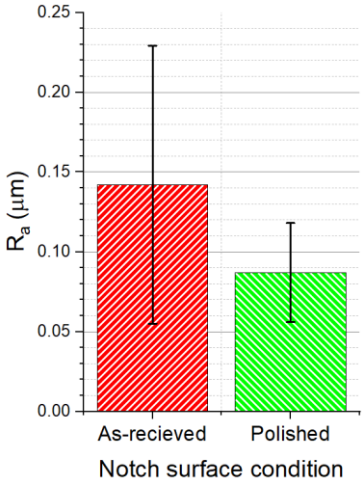

Figure 4-13 Surface roughness R_a of As-received (with corrosion pits) and polished (with 9 µm suspension) notch surface conditions.

4.3.2.2 Crack initiation behaviour

The number of crack initiation events causing the primary crack in U-notch specimens is displayed in Figure 4-14. A crack initiation was counted only if the crack was observed to grow in subsequent replicas and eventually became part of the main crack via coalescence. Many surface features such as slip bands were observed that did not contribute to fatigue and were therefore not considered as crack initiations. Applying higher constant cyclic $\Delta\varepsilon$ under CA increases the number of crack initiation events on the surface of the notch (Figure 4-14 A). The addition of an overload cycle every 150 base load cycles appears to also increase the number of crack initiation events (Figure 4-14 B). Polishing the surface of the notch resulted in more observed crack initiation events.

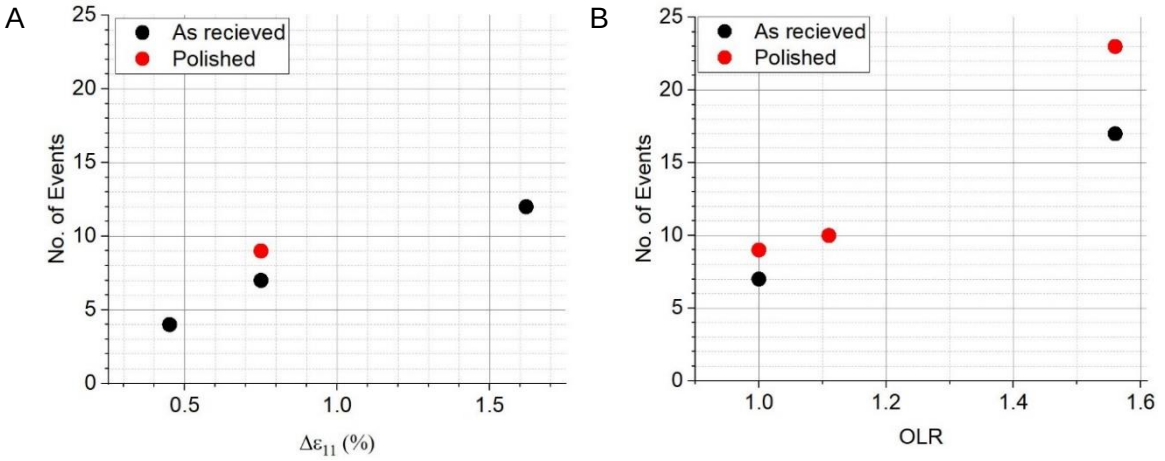

Figure 4-14. A) Number of initiation events for the primary crack with respect to strain range for the as-received and polished surface conditions. B) Number of initiation events for the primary crack with respect to OLR of overload cycle applied every 150 baseload cycles.

Causes of initiation were observed and counted on an as-received and polished U-notch samples under constant amplitude loading using surface replica data. The as-received surface condition contained corrosion pits (Figure 4-15 A) which accounted for the majority (80 %) of the total causes of crack initiation (Figure 4-16 A). Other causes of initiation observed were slip bands (Figure 4-15 C and Figure 4-18 A) and machining marks (Figure 4-15 B). Polishing the U-notch surface removed almost all corrosion pits resulting in slip bands becoming the dominating cause of crack initiation with inclusions contributing towards the remaining crack initiation cause (Figure 4-15 D and Figure 4-16 B). In some rare instances, locations of high concentrations of slip band activity resulted in early slip band coalescence. In these instances, slip band coalescence by several slip bands was considered a crack initiation (of relatively large crack length) (Figure 4-17).

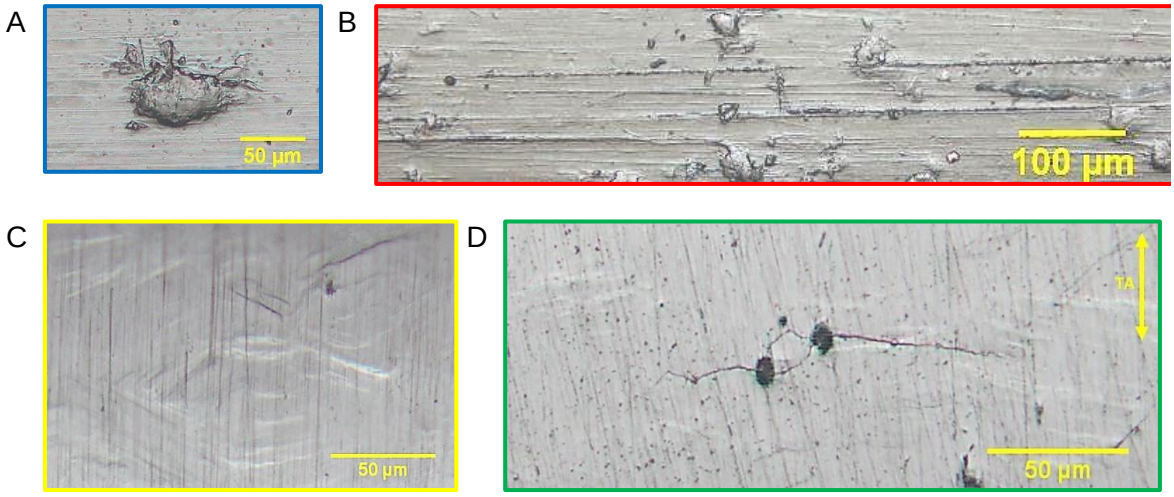

Figure 4-15: A) Crack initiation from a corrosion pit. B) Cracks running along machining marks. C) Example of slip band formation, only considered to be crack initiation if the length of the slip band continues to grow. D) Example of crack initiation from two inclusions.

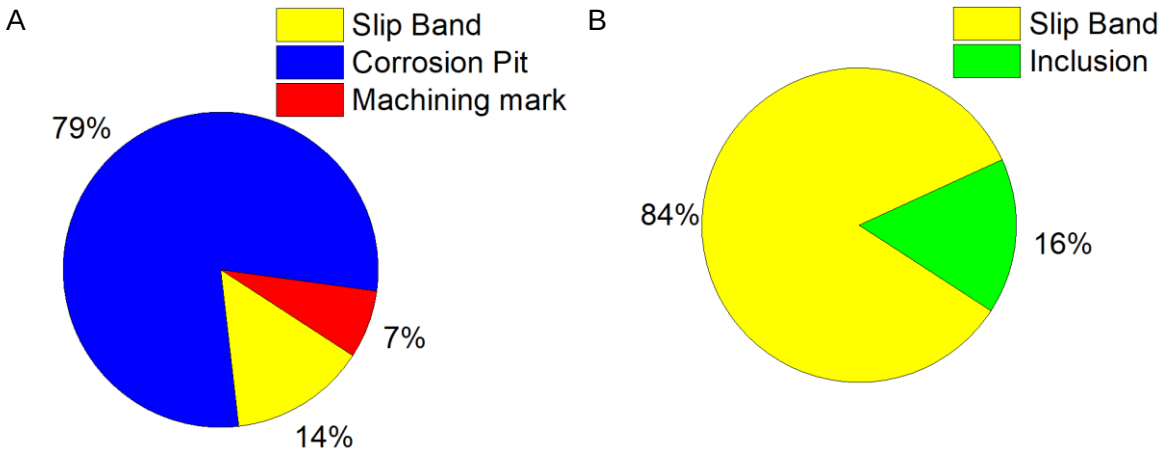

Figure 4-16: A) Percentage crack initiation cause for as-received notch surface condition. B) Percentage crack initiation cause for the polished notch surface condition.

Figure 4-17: Four slip bands that coalesced during one interval between two interruptions to produce a crack initiation with relatively large initiation length of approximately 230 µm.

4.3.2.3 Short crack behaviour and growth

Secondary cracks on a U-notched sample surface were observed with a FEG-SEM after testing. An secondary electron image (SEI) image of the crack tips of a mechanically small crack approximately 60 µm in length showed the crack was affected by microstructure and

appeared to prefer growing along prior-austenite grain boundaries (Figure 4-18 B, C and D). SEI images of the crack tips of physically short cracks at least 2 mm in length (Figure 4-18 E and F) displayed transgranular short crack growth behaviour. In one instance, a physically small crack with transgranular short crack growth grew around an inclusion (Figure 4-18 F).

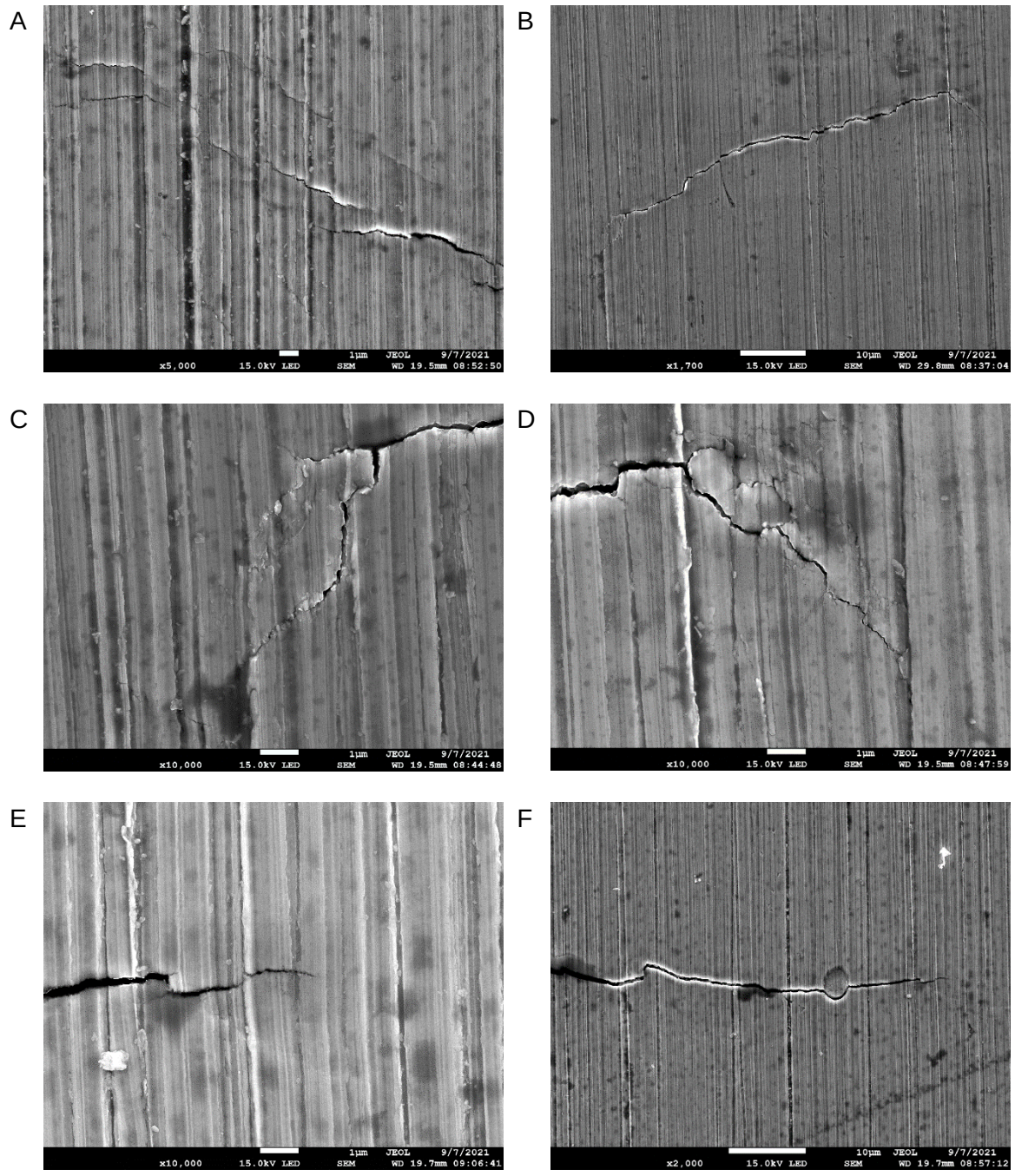

Figure 4-18 A) High magnification secondary electron image (SEI) image of slip bands. B) SEI image of crack with approximate length of 60 µm. C) and D) Close-up SEI images of crack tips from the crack in image B) displaying intergranular crack growth behaviour. E) SEI image of the crack tip for a physically short crack with approximate length greater than 2 mm, F) SEI image of physically short crack tip growing around an inclusion.

Short crack growth rate *dc/dN* versus $\Delta K_{Surface}$ was investigated for constant amplitude loading conditions for two separate total strain ranges of baseload 0.75 % and 1.62 % (OLR of 1.56 applied as a constant amplitude baseload) (Figure 4-19 A). The results suggest that short crack growth rate versus $\Delta K_{Surface}$ is independent of strain range. In Figure 4-19 B), *dc/dN* versus $\Delta K_{Surface}$ was compared between constant amplitude cyclic baseload and OLR of 1.56 applied every 150 baseload cycles. The overload resulted in less *dc/dN* data above $\Delta K_{Surface}$ of 20 MPam$^{0.5}$ as well as a greater surface crack growth rate range. There appears to be a slight reduction in short crack growth rates which has been shown to be independent of the increase in strain range from the overload cycles. Each data point shows the average crack growth rate for a given $\Delta K_{Surface}$ range (shown as X-axis error bars) and the *dc/dN* error lines show the maximum and minimum crack growth rate values (displayed as a shaded area) for each $\Delta K_{Surface}$ range. The results include arrested cracks that did not grow in between replica interruptions and therefore had a crack growth rate of zero. Only results from tests whereby the cracks were evenly distributed over the width of the sample resulting in near-symmetrical fatigue regions on the fracture surface were included.

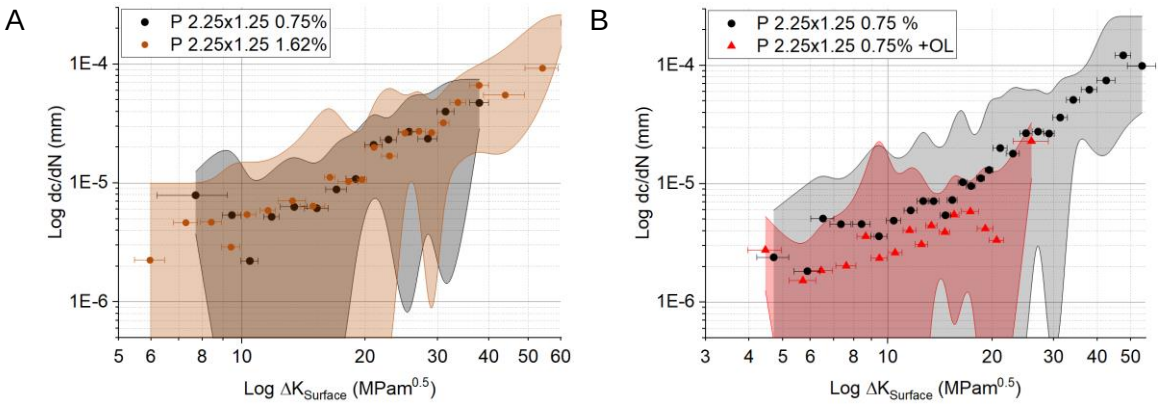

Figure 4-19 A) Surface crack growth rate *dc/dN* with respect to $\Delta K_{Surface}$ for constant amplitude loading conditions at 0.75 % and 1.62 % strain ranges. B) Surface crack growth rate with respect to $\Delta K_{Surface}$ for constant amplitude and OLR of 1.56 cycle every 150 baseload cycles. The shaded areas show the maximum and minimum crack growth rate range. Overall, there appears to be a slight reduction in short crack growth rates with the presence of an overload of OLR of 1.56 every 150 baseload cycles.

4.3.2.4 Coalescence behaviour

Crack coalescence events occurred in three ways.

- Two in-plane cracks appeared to join into one crack leaving unobservable ratchet marks on the fracture surface (Figure 4-20 A and B).

- Two out-of-plane cracks grew passed each other, followed by one crack tip changing direction and joining onto the other crack forming a T-junction (Figure 4-20 C and D).
- Two out-of-plane cracks grew past each other followed by both cracks changing direction and joining onto each other, sometimes resulting in an island of material surrounded by cracks (Figure 4-20 E and F).

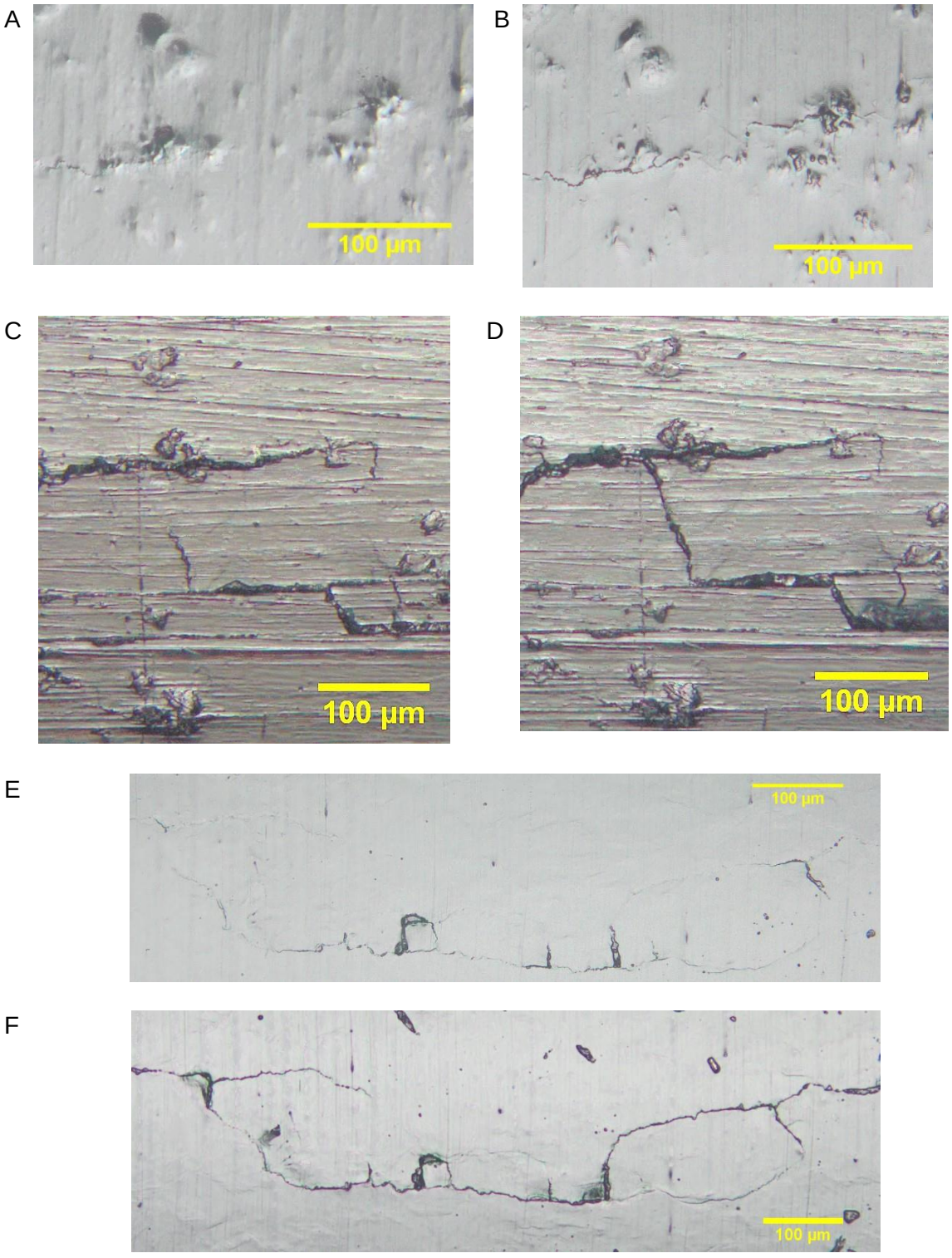

Figure 4-20 Three examples of crack coalescence observed on the surface replicas of U-notch samples.

A more detailed study of the short crack growth behaviour of the primary crack was carried out for the as-received U-notch surface with constant amplitude at 1.62 % strain range (equivalent to OLR 1.56 as the baseload cycle) (Figure 4-21 A and B) and for the polished U-notch surface with overload of OLR = 1.56 applied every 150 base load cycles (Figure 4-21 C and D). The polished surface condition delayed crack initiation whereas surface features on the as-received surface resulted in almost immediate crack initiation. Crack initiation activity intensity increases. Once cracks begin to consistently coalesce, crack initiation activity tends to decrease while coalescence activity increases. Coalescence activity overtakes initiation activity and initiation activity slows considerably. Coalescence behaviour was typically most intense in the final stages of fatigue life until the primary crack grew the entire width of the sample. The final 5 – 10 % of fatigue life was generally considered long crack growth to failure. A more detailed description of the initiation and coalescence activity for the two loading conditions follows.

The initiation and coalescence events for the primary crack on the as-received notch surface under constant amplitude loading unfolded in the following way (Figure 4-21 A and B).

- Crack initiation began around 14 % lifetime earlier than the polished surface due to the presence of corrosion pitting.
- Eight cracks had initiated from corrosion pits before 43 % lifetime
- Coalescence was then first observed around 47 % lifetime.
- Crack initiation activity was most intense very early on with most initiation activity in the first half of the lifetime.
- The highest total number of individual cracks that formed the final primary crack was ten around 55 % lifetime after which coalescence activity began to take over the fatigue behaviour.
- The last crack initiation was observed around 62 % lifetime.
- Crack coalescence activity was constant at low intensity from 60 % to 80 %.
- Crack coalescence intensity was most intense around 90 % lifetime.
- The last 9 % of fatigue life was characterised by long cracking until final failure.

The initiation and coalescence events for the primary crack on the polished notch surface with OLR of 1.56 loading conditions unfolded in the following way (Figure 4-21 C and D).

- Crack initiation first began around 43 % lifetime for the polished surface.
- Eight cracks had initiated by 62 % lifetime
- Coalescence was then first observed at 63 % and 70 % lifetime after which coalescence was not seen for another 10 % lifetime.
- Crack initiation was most intense around 75 % - 80 % lifetime.

- The highest total number of individual cracks that formed the final primary crack was twenty-seven around 82 % lifetime after which coalescence behaviour began to take over.
- Coalescence intensity was highest around 88 % lifetime.
- Coalescence activity continued with high intensity until 95 %.
- The last 5% of fatigue life comprised of long crack growth to final failure.

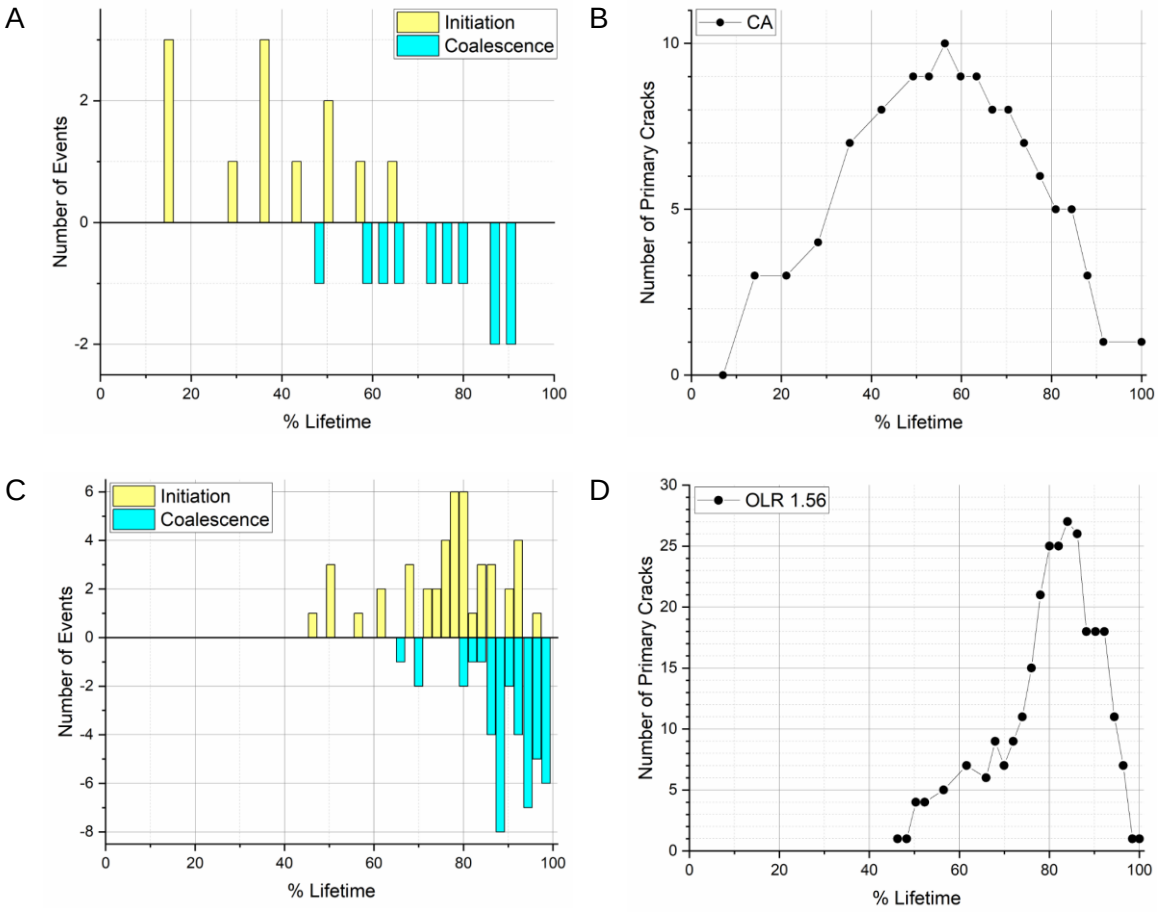

Figure 4-21 A) The number of events formed in between each replica of the as-received surface for initiation and coalescence for the constant amplitude with 1.62 % strain range (equivalent to OLR 1.56 as baseload). Initiation events in yellow adding to the number of total cracks on the surface and coalescence events in blue subtracting from the number of cracks on the surface. B) The cumulative total number of cracks on the surface with respect to lifetime. C) The number of events for the primary (main) crack formed in between each replica of the polished surface for the OLR of 1.56 every 150 baseload cycles case. D) The cumulative total number of cracks on the surface with respect to lifetime.

A PowerPoint animation approach was used to reconstruct the evolution of the short cracks on the U-notch surface during the OLR of 1.56, to gain further understanding and visualisation of the crack initiation and coalescence behaviour. The silicone replicas were used to model the cracks to scale and include a simplified crack shielding area zone (Figure

4-22). The video can be viewed here https://www.youtube.com/watch?v=-Qfrk0-6P90 and at https://eprints.soton.ac.uk/451797/. Yellow lines indicate crack initiation at slip bands, orange lines indicate crack initiation at inclusions, green lines indicate rapidly growing cracks that grew by more than 10 µm since the previous replica measurement, red lines indicate slower cracks that grew less than 10 µm since the previous replica measurement and blue lines indicate cracks that have coalesced into a single crack since the previous replica measurement.

The animation video shows crack initiation occurring seemingly randomly at first. Cracks in the initial stages after initiation appeared to stop and grow several times. When several cracks had appeared, only around half of the cracks appeared to grow at any one time. This was a common occurrence until the later stages of fatigue life (last 10 %) where coalescence and crack growth dominated. Large cracks as seen in the centre of the sample that tended to be actively growing or coalescing often did not have any crack initiation or crack growth occurring within the crack shielding zone.

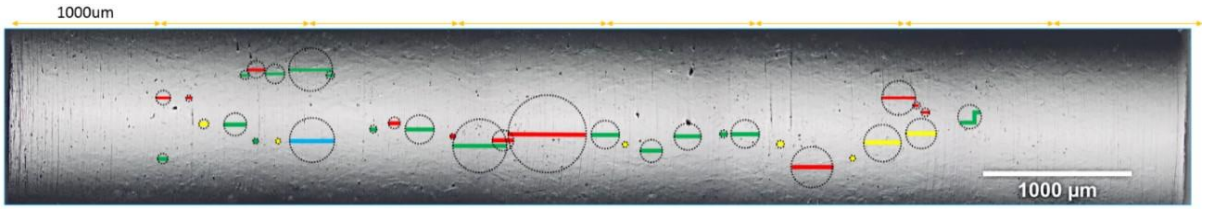

Figure 4-22 An excerpt from the crack evolution schematic.

4.3.3 Long crack growth behaviour

Four long crack tests were carried out on SEN specimens with constant amplitude loading and with OLRs of 1.07, 1.11 and 1.56 applied every 150 baseload cycles (Figure 4-23). The *da/dN* versus *ΔK* relationships for OLRs of 1.07 and 1.11 applied every 150 baseload cycles fall within the approximate error of ± 50 % estimated from Soady [10] predicted for constant amplitude loading. The results suggest that small overloads of 1.07 and 1.11 applied every 150 baseload cycles have no effect on long crack growth rate versus *ΔK*. An overload with OLR 1.56 applied every 150 baseload cycles appears to have a crack growth retardation effect on overall long crack growth, especially at lower *ΔK* values (note the much lower C and the higher m Paris-law constants in Table 4-1).

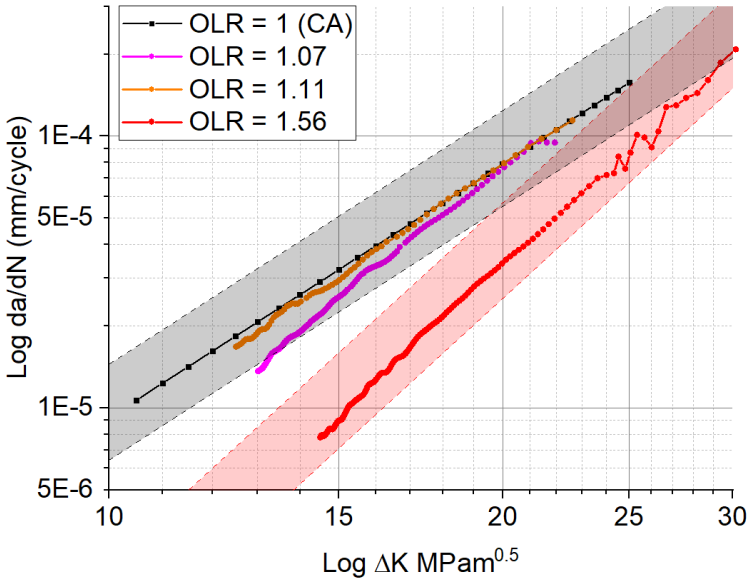

Figure 4-23: The results from four long crack tests showing crack growth rate with respect to *ΔK* for OLRs of 1 (constant amplitude), 1.07, 1.11 and 1.56 in FV566. The expected error of ± 50 % represented as dotted lines is shown for constant amplitude (CA) loading and for OLR of 1.56.

Loading condition	***C***	***m***	ΔK_{th}**(MPa√m)**
CA	7.3×10^{-9}	3.1	4.3
OLR of 1.07	1.6×10^{-9}	3.6	
ORL of 1.11	5.5×10^{-9}	3.2	
OLR of 1.56	3.3×10^{-11}	4.2	

Table 4-1: Paris-law constants calculated by extrapolating between two points on the long crack results in Figure 4-23.

4.3.3.1 Fractography

The notch surface was observed after fatigue life using an optical microscope. It appears the corrosion pits acted as high local stress concentration areas and may have encouraged crack initiation away from the neutral centre of the notch surface with large out-of-plane distances leading to particularly large ratchet marks (Figure 4-24 A). The polished sample by comparison showed a tendency for crack initiation nearer the neutral centre of the notch surface (Figure 4-24 B). No difference in crack initiation location behaviour was noticed with overloads of OLR = 1.11 applied every 150 baseload cycles (Figure 4-24 C). However, when OLR 1.56 (Figure 4-24 D) was applied, the crack initiation locations remained closer to the central axis of the notch despite an as-received notch surface condition.

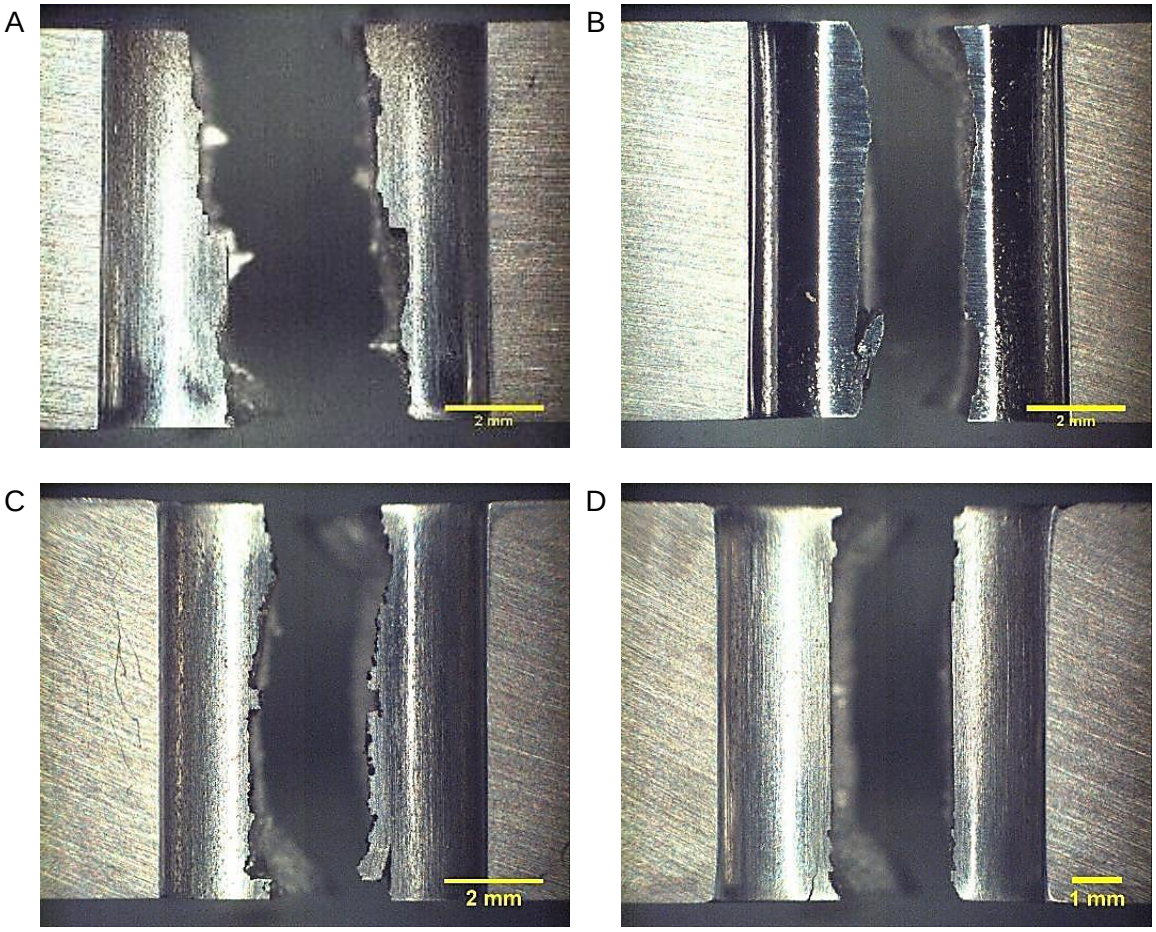

Figure 4-24 A) Notch surface after fatigue testing for CA as-received notch surface condition. Note the relatively large ratchet mark distance. B) CA polished notch surface condition. C) OLR of 1.11 applied every 150 baseload loading with as-received notch surface condition. D) OLR of 1.56 applied every 150 baseload loading with as-received notch surface condition.

The fracture surfaces of short crack tests were observed for all tests using an optical microscope, one such fracture surface can be seen in Figure 4-25. The fatigue region was clearly visible for all samples with ratchet marks indicating crack coalescence. Some fatigue region areas appeared symmetrical where crack initiation activity was uniform across the entire notch surface, and some were non-symmetrical where crack initiation activity was particularly biased towards one side of the notch surface (Figure 4-26 A). The fracture surfaces of CA loading and OLR of 1.11 applied every 150 baseload cycles appear very similar (Figure 4-26 B and C). Beachmarks were uniquely observed for OLR of 1.56 loading condition (Figure 4-26 D). The fast fracture region is identified by a darker shade of grey and contains shear lips either side of the sample. Circular features were visible on some fast fracture surfaces, possibly indicating locations of stringers in the Z-direction (Figure 3-8 B) which is considered undesirable.

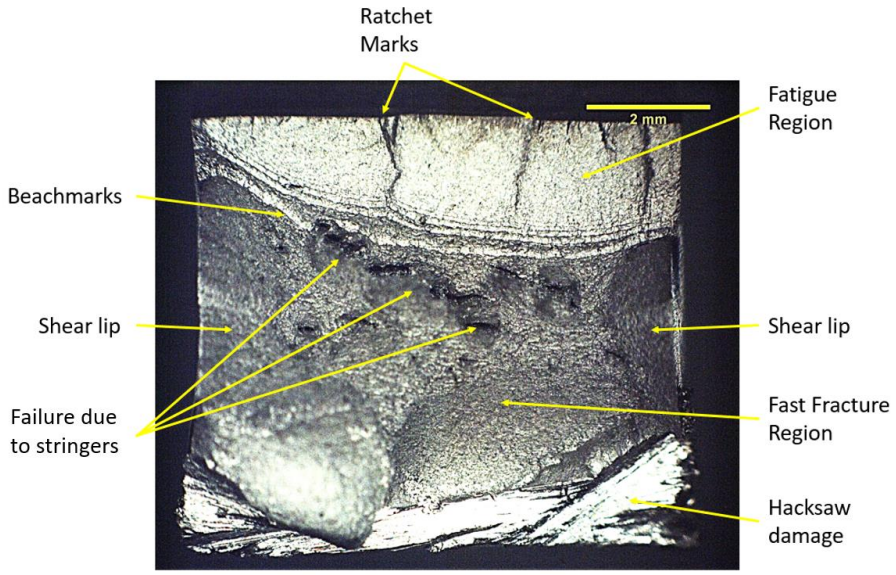

Figure 4-25: The fracture surface of a short crack test with overloads of OLR = 1.56 applied every 150 baseload cycles with features labelled.

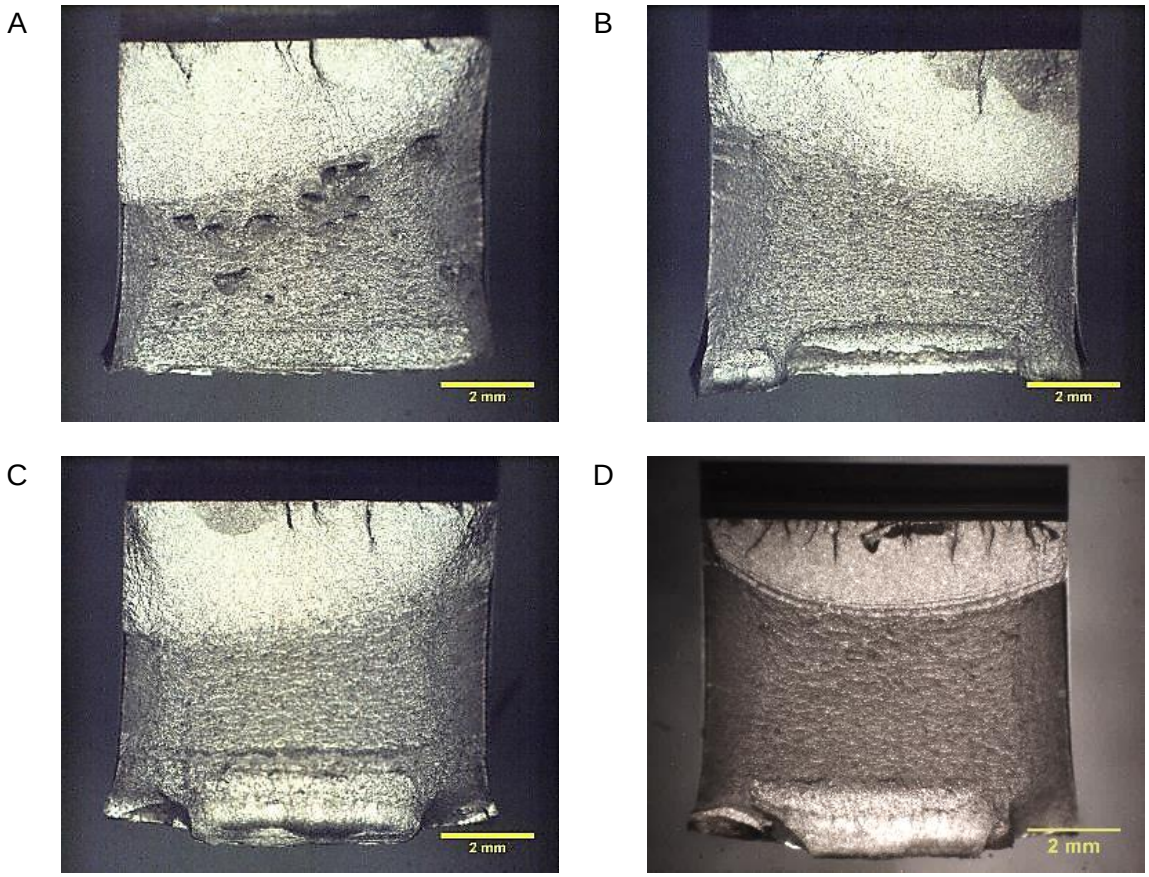

Figure 4-26: A) Fracture surface of CA short crack test on as-received notch surface, the fatigue region is uneven due to biased crack initiation and growth activity on side of the sample. B) CA short crack test with polished notch surface. C) OLR of 1.11 every 150 baseload cycles load condition. D) OLR of 1.56 every 150 baseload cycles load condition. Note the beachmarking near the end of life due to the overload cycles.

Beachmarks (or stretch marks) were observed by eye on the fracture surfaces from long crack and short crack testing near the end of fatigue life when an overload of OLR of 1.56 was applied every 150 baseload cycles indicating the fatigue to fast fracture transition (Figure 4-27 A and C). These beachmarks were not observed on the fracture surfaces of samples subjected to constant amplitude loading or small overloads with OLR of 1.07 or 1.11 (Figure 4-27 B). These beachmarks are most likely due to local high plastic deformation during the overload cycle and are not indicative of plastic closure effects.

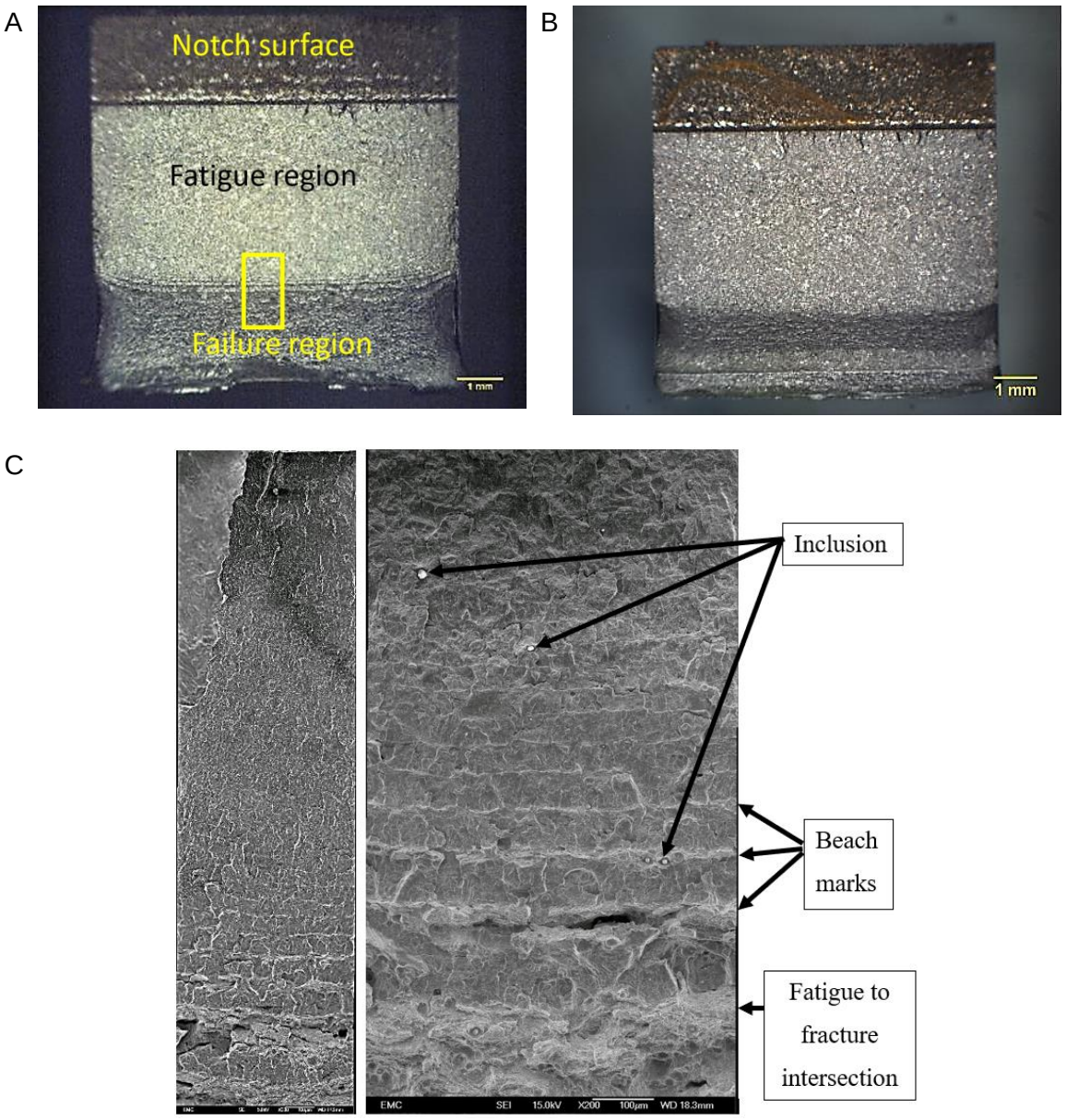

Figure 4-27: A) The fracture surface of a long crack test with overloads of OLR of 1.56 applied every 150 baseload cycles with beachmarks near the end of fatigue life observable by eye. B) The fracture surface of a long crack test with overloads of OLR of 1.11, no beachmarks were visible. C) Higher magnification SEI images of beachmarks observed on the fracture surface with microstructural features such as inclusions labelled.

4.4 Discussion

4.4.1 Notch surface strain hardening

Hardness testing at three locations did not conclusively indicate any material hardening effects near the notch surface. Compressive residual stress and strain hardening effects on and near the notch surface from plastic deformation were expected to increase resistance to hardness indentation, indicating a harder material near the notch surface. Indentations too close to the notch surface are affected by the weaker Bakelite material providing less residence to deformation and a harder indent size. Furthermore, cutting of the material may lead to relaxation of any residual stress formed at the notch surface from in-service loading conditions. A more reliable method for strain hardening or residual stress measurement may come from EBSD, XRD or hole drilling methods Chapter 2.3.3.

4.4.2 Notch surface characterisation

The notch surface roughness in R_a for FV566 was compared with an identical notch geometry for FV448 using the same equipment [5] (Figure 4-28). A possible variation in the method used to create the U-notch geometry for FV448 and FV566 samples likely accounts for the notable difference in surface roughness measurements between the two materials. A large variation in the surface roughness was found depending on whether the surface roughness measurements were taken in the longitudinal directions or in the transverse direction. This is attributed to the notch machining process and the resultant uniform directionality of machining marks. This large variation in hardness depending upon directionality was considerably reduced during the polishing process. However, it is possible that the polished notch surface roughness taken in the longitudinal direction would show a smoother surface (lower R_a values) due to polishing directionality. The error range is much higher for FV566 samples than for FV448 samples, a phenomenon for which two reasons may be apparent. Firstly, no corrosion pitting was reported to be found on the FV448 material, resulting in a more consistent surface roughness. Secondly, the surface roughness measurements for FV566 came from multiple samples (with varying degrees of corrosion) rather than from only one test possibly resulting in higher error ranges.

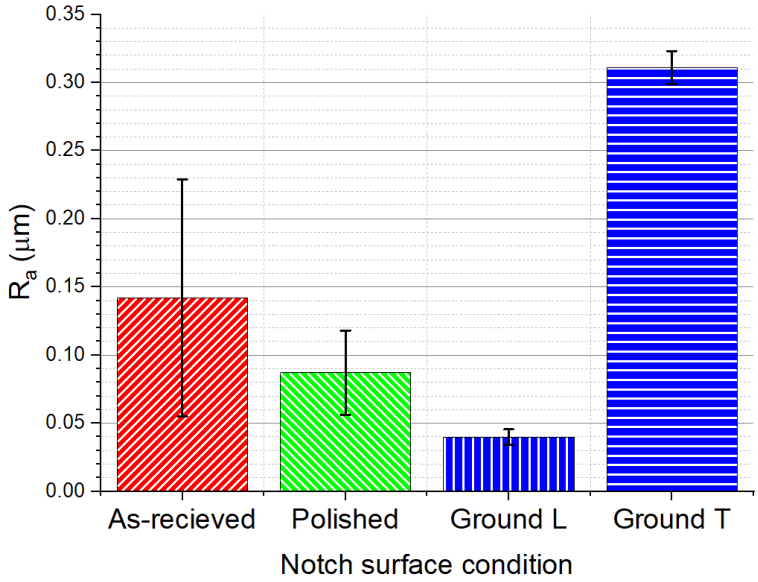

Figure 4-28: The surface roughness R_a values of the as-received and polished notch surfaces of samples from FV566 and Ground Longitudinal (L) and Ground Transverse (T) notch surface roughness measurements for FV448 [5]. The error bars represent ± one standard deviation.

The polishing process of the notch, finishing with 9 µm, is not expected to cause strain hardening or residual stress on the notch surface (as discussed in Chapter 3.4.2) and is therefore not expected to have any effect on crack initiation and short crack growth.

The polishing process of the U-notch surface removed pre-existing corrosion pits and also changed the geometry of the notch. The geometry of one U-notch before and after polishing was measured from images taken on an Olympus BX51 microscope and image analysis software (Image J). FEA using the model described in Chapter 3.2.6 comparing the two notch geometries before and after polishing showed a minimal change in the strain range of < 2.7 %. The impact of changing the notch geometry due to polishing was therefore considered negligible to fatigue behaviour and lifetimes.

4.4.3 Crack initiation behaviour

Four long crack tests with CA and OLRs of 1.07, 1.11 and 1.56 were carried out. The results suggested that the two small overloads of OLR = 1.07 and OLR = 1.11 had no effect on the long crack growth rates as expected from literature [90]. Short crack testing was carried out with constant amplitude loading and with OLR of 1.56 since the two smaller overloads are not expected to significantly affect short crack growth behaviour.

Crack initiation cause was observed to be predominantly at corrosion pits in the as-received surface condition, also observed in other steel materials [176]. This is consistent with the corrosion pits acting as stress raisers, which may be perceived as representative of expected in-service root-fillet surface conditions. When these corrosion pits were mostly

eliminated by the notch polishing process, initiation shifted preferentially to slip bands with inclusions (some composed of SiO Figure 4-29) only contributing to 16 % of total initiations. Observations via SEM did not suggest any subsurface initiation for either polished or as-received surface condition. In contrast, He [50, 72] noted that the main cause of initiation for a similar polished notch condition in FV448 martensitic stainless steel was from MnS stringers which when aligned in the crack depth direction led to higher *a/c* ratios than produced by slip band cracking. Stringers were not observed to have such a direct influence on crack initiation cause since fewer of them were observed on FV566 and the samples were extracted in a different orientation. The FV448 material studied was made from bar stock material that is representative of smaller turbine blades used in service. The observed higher density of MnS stringers in the FV448 affected initiation behaviour and early short crack growth behaviour in terms of the underlying defect distributions.

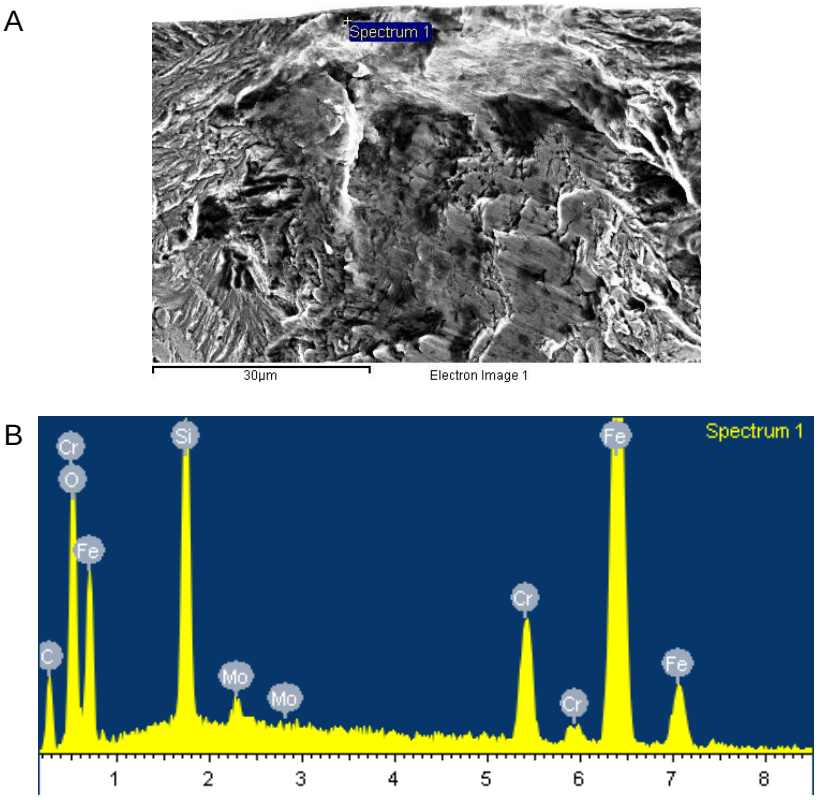

Figure 4-29: A) SEI image of one of seven inclusions on the fracture surface of a short crack with polished surface and OLR of 1.56 applied every 150 baseload cycles. The inclusion was identified as the source for the initiation of a crack and B) corresponding EDS analysis showing the chemical composition of the inclusion to be Silicon Oxide (SiO).

The cracks that made up the primary crack were used to define crack initiation, coalescence and short crack growth behaviour since the primary crack is considered to define overall fatigue behaviour and life. Secondary cracks were also observed and counted on a sample with overloads of OLR of 1.56 applied every 150 baseload cycles and compared with the primary crack (Figure 4-30). When including secondary cracks, the total number of cracks

observed on the surface doubled in value and first crack initiation was seen at 30 % as opposed to 42 %. A similar observation was found on the constant amplitude load case, where crack initiation was seen on the first replica (before 10 % fatigue life).

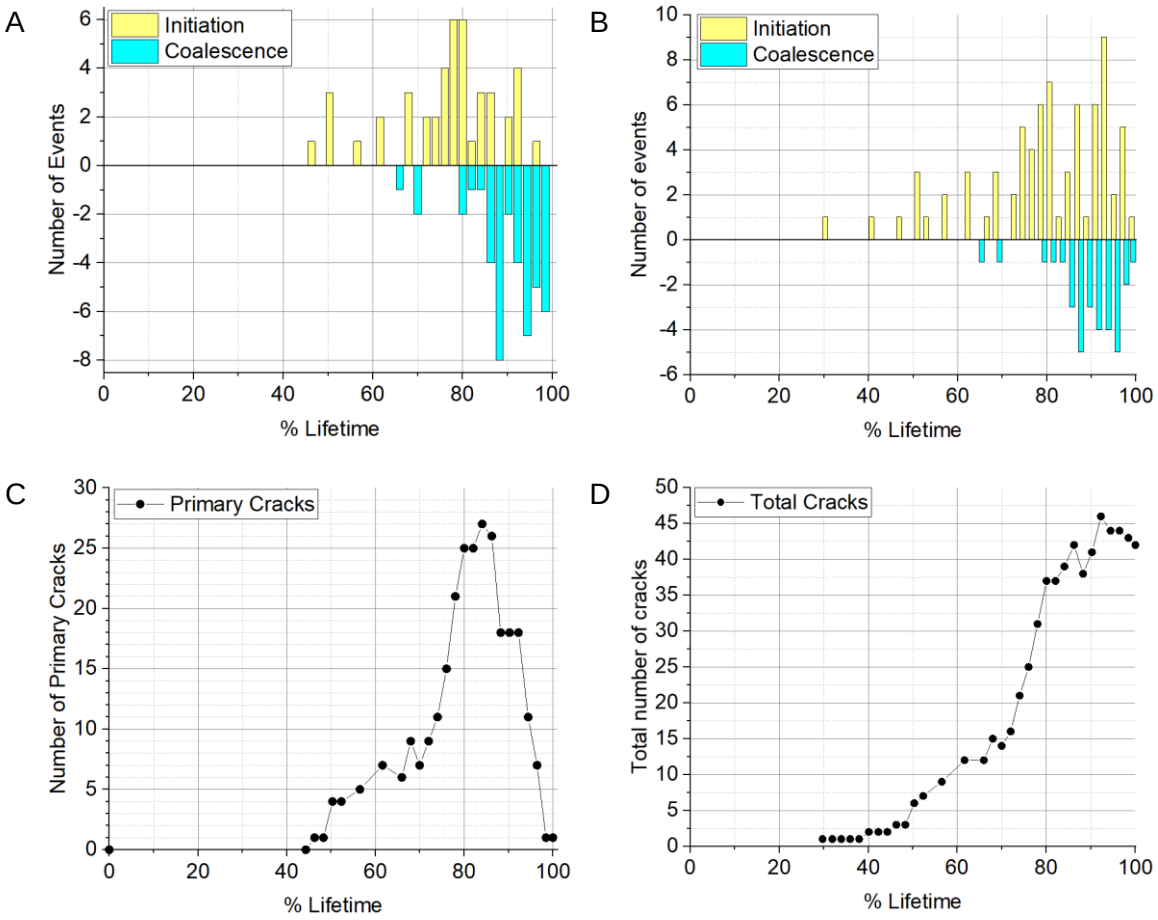

Figure 4-30 A) Number of initiation and coalescence events formed in between each replica for the primary crack only. B) Number of initiation and coalescence events formed in between each replica for the total number of cracks on the notch surface (primary and secondary). C) The cumulative total number of cracks that made up the primary crack with respect to lifetime. D) The cumulative total number of cracks that made up the total number of cracks (primary and secondary cracks) with respect to lifetime.

In this study, cracks were seen to initiate early in the fatigue life at pre-existing corrosion pits since corrosion pits themselves can be considered pre-existing cracks [177]. In this study, only corrosion pits where short crack propagation was observed on the first surface replica record were considered as cracks initiating from 0 cycles (all of which were secondary cracks). Early short crack growth observed on the surface via replicas was notably slow at corrosion pits, with only one crack tip seen initially emanating from the pit and the second opposite crack tip often appearing later. The *a/c* ratios of the corrosion pits are quite shallow (typically 0.16 ± 0.02) which may have led to a higher ΔK initially at the

deepest part of the elliptical crack encouraging crack initiation from the base of the pit rather than crack growth on the surface until an equilibrium *a/c* ratio was achieved.

The methods for counting crack initiation events for the primary crack highlighted a discrepancy. The number of crack initiation events for the primary crack found by counting ratchet marks was twenty-three, while the same sample had forty-four crack initiations for the same primary crack according to the replica record. While counting crack initiations from the replica record is considered a more accurate estimate, ratchet marks were used to be consistent in comparing number of initiation sites across all the samples, more than half of which did not have a replica record.

Higher strain ranges resulted in more crack initiation sites as is expected and was also observed by He et al [50]. Introducing a single overload cycle every 150 cycles increased the number of initiation events compared to constant amplitude loading at the baseload cycles. Polishing the U-notch surface increased the observed number of crack initiations when compared to the as-received surface condition containing corrosion pits. The number of cycles to crack initiation was noticeably reduced for pitted surface conditions as the corrosion pits acted as immediate stress raisers. Early short crack growth led to increased shielding activity and therefore less surface area on the U-notch capable of inducing crack initiation. Polishing the U-notch surface greatly increased the number of cycles to first observed crack initiation (from slip bands) and local stress raisers such as corrosion pits were greatly reduced. The lack of early short crack growth both reduced shielded notch surface area and increased the number of cycles to initiation, providing suitable conditions for a higher number of PSB to form and a greater number of crack initiation events.

4.4.4 Short crack behaviour and growth

Some non-uniform fatigue regions were observed, typically biased towards one side of the notch where crack initiation and short crack growth activity was much more intense on one side than the other. In some cases, crack initiation began at one edge of the notch and grew from one side to the other. The data from samples that displayed non-symmetrical fatigue regions were excluded where possible from the short crack growth rate data for consistency.

Previous analysis of short crack growth rate versus $\Delta K_{Surface}$ values have typically included only cracks that have grown since previous replicas since one limitation of a Log-Log axis is that zero values cannot be included. A typical observation in this study was that cracks could stop growing temporarily in between replicas and start to grow again in subsequent replicas. A grouping strategy was therefore adopted to include cracks that had zero growth since the previous replica (known as arrested cracks). The data was grouped into suitable $\Delta K_{Surface}$ ranges, the growth rate and $\Delta K_{Surface}$ values within each data set averaged and plotted. The maximum and minimum values within each data set were used to define the

error range within the data. The effect of including temporary crack arrests can be seen below. Primary cracks that formed part of the main crack excluding and including arrested periods is shown in Figure 4-31 A). Including arrested periods results in a slight reduction in the crack growth rates as expected. A larger reduction in crack growth rates was seen for secondary cracks that did not form part of the main crack (Figure 4-31), due to the larger shielding effects from the dominant primary crack. When arrested periods are excluded from the results, the primary cracks and secondary cracks show similar crack growth rates (Figure 4-31 C). However, when arrested cracks are included, the larger shielding effect from the primary crack becomes evident (Figure 4-31 D). No cracks with a $\Delta K_{Surface}$ > 30 MPam$^{0.5}$ were observed to arrest and therefore no reduction in crack growth rate can be seen by including arrested cracks at higher $\Delta K_{Surface}$ values. Fatigue lifing predictions should include crack arrest estimates within the primary crack since this is a significant controlling factor influencing the fatigue behaviour and life of U-notched samples at these strain levels.

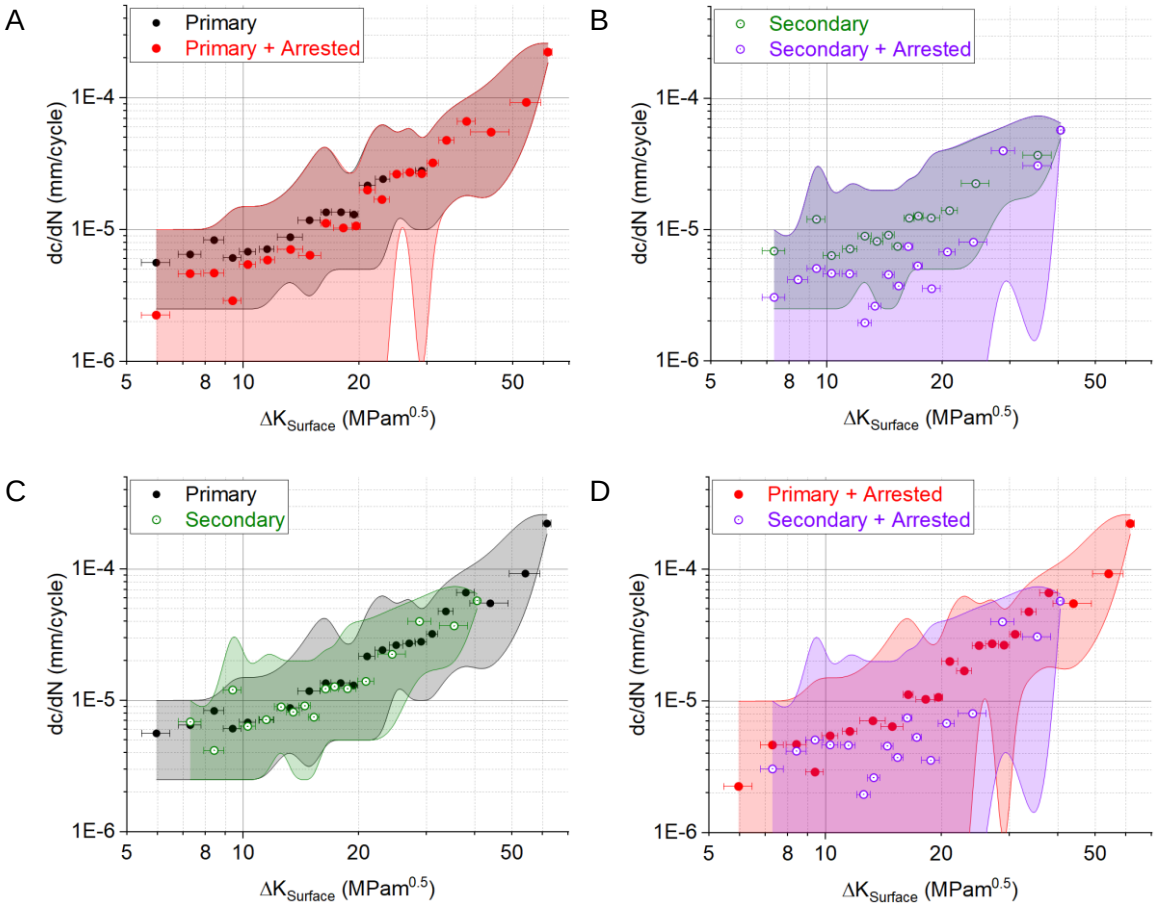

Figure 4-31 Short crack *dc/dN* versus $\Delta K_{surface}$ for constant amplitude loading conditions for, A) cracks that made up the primary crack for growing cracks only, compared with growth and arrested periods. B) Secondary crack growth only compared with secondary growth and arrested periods. C) Primary cracks compared with secondary cracks for growth only. D) Primary cracks compared with secondary cracks both including arrested periods.

Overloads with OLR of 1.56 applied every 150 baseload cycles appeared to have a crack growth rate reducing effect. Many possible reasons for this effect have been explored by numerous authors with plastic closure effects and compressive residual stress ahead of the crack tip being the most widely accepted and most likely reason for this behaviour (Chapter 2.2.4) [91, 110].

A 2-D FE model using monotonic true stress and true strain material properties from M01-03 tensile data (Chapter 3.3.4) was used in a loading and unloading step process to explore the effect of an overload cycle on residual stress within the notch stress field (Figure 4-32). Second order plane elements (CPE8R) were used, and a mesh convergence study carried out to ensure an adequate mesh. The presence of an overload with OLR 1.11 (10 % overload) increased compressive residual stress by 28 % when compared to the baseload cycle. An overload with OLR of 1.56 (50 % overload) increased the compressive residual stress at the notch surface by 110 % and produced a much higher counterbalancing tensile residual stress deeper into the notch stress field. The smaller extent of the residual stress field from an OLR of 1.11 every 150 baseload cycles is likely to be relaxed by the subsequent baseload cycles than that of the OLR of 1.56 applied every 150 cycles. This, together with the lower compressive residual stress levels produced, may explain why a small overload such as OLR of 1.11 has little effect on fatigue lifetime whereas the larger overload has a clear lifetime extending effect. This is due to the compressive residual stress that would be present within the notch leading to delayed crack initiation and retarded short crack growth [62, 90, 93, 103, 105, 107, 108, 171].

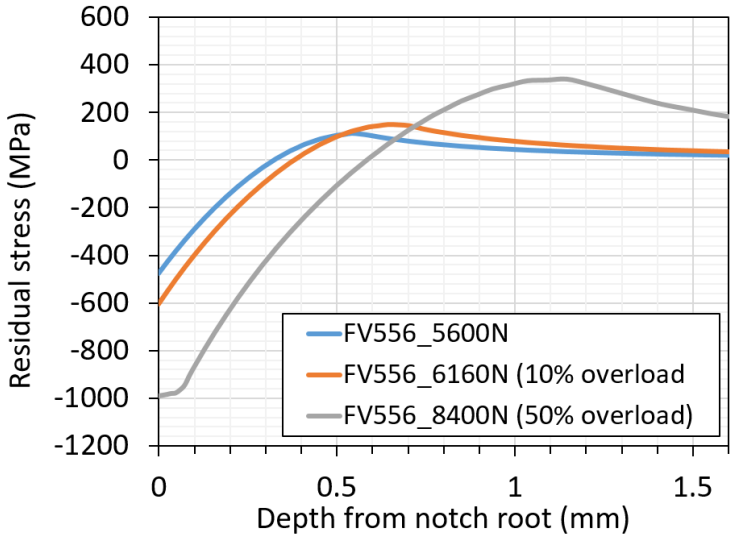

Figure 4-32 The residual stress with notch depth from the centre of the notch surface following a baseload, an overload with OLR of 1.11 (10 %) and an overload with OLR of 1.56 (50 %).

The presence of an overload with OLR of 1.56 appeared to increase the scatter of the crack growth data. It is likely that the increase in the total number of cracks and crack interactions

(coalescence and shielding) increased the variability in short crack growth rates [74]. Secondly, crack coalescence events were observed at lower $\Delta K_{Surface}$ values, also suggesting an increase in the number of cracks and therefore typically reduced crack lengths at coalescence. Despite the large amount of scatter and error in measuring short cracks on the replica surface, a reduction in short crack growth rate (by a factor of approximately 2.5) can clearly be observed.

The crack growth of microstructurally small cracks comparable to grain size on a polished U-notch was found to be heavily dependent upon microstructure, preferring to grow along prior-austenite grain boundaries and martensitic laths in FV448 [5]. A similar behaviour was observed in FV566 material with microstructurally small cracks revealing prior-austenite grain boundary shapes as the crack tip grew in multiple directions. Physically short cracks tended to be less dependent upon microstructure and exhibited transgranular growth perpendicular to the tensile axis. In the as-received notch surface condition, physically short cracks were also somewhat influenced by the surface conditions. Cracks were observed to grow along machining marks and seemingly preferred to grow through successive corrosion pits (Figure 4-33).

Figure 4-33 Surface replica of as-received surface condition at 74 % lifetime. The central crack can be seen growing through corrosion pits, following machining marks and coalescing with cracks almost parallel with the tensile axis. Crack growth behaviour is less dictated by microstructure and more by surface features than a polished surface condition where these features were removed.

4.4.5 Coalescence behaviour

Crack coalescence behaviour tended to be typical of that seen in other materials. In one example (Figure 4-20 C and D), cracks grew past each other and then shielded each other whereby crack deflection occurred, and the cracks coalesced. In polished surface conditions, initial short crack growth and crack coalescence was seen to be influenced by microstructure. This was also observed by other authors [5, 74]. However, in the as-received surface condition, crack coalescence was observed to be also somewhat affected by machining marks and corrosion pits.

4.4.6 Long crack growth

Beachmarking at the final stages of fatigue life indicated that the overload cycle was causing increasingly larger bursts of accelerated monotonic crack growth. As ΔK increased, the crack growth rate tended towards constant amplitude loading conditions due to the higher m value in the Paris-law regime. Increasing magnitude of bursts of crack growth from the overload cycle may help explain this behaviour. The ΔK versus crack growth rate for the stage III regime is often not accurately captured using the DCPD method. The beachmarks were used to define stage III crack growth using the method described in Appendix A. The results show agreement with the grow-out data and begin to suggest a typical stage III crack growth behaviour [26] at ΔK values above 35 MPam$^{0.5}$ (Figure 4-34 A).

The long crack data (of which only grow-out results are shown) and short crack growth rates for OLR of 1.56 applied every 150 baseload cycles are compared in Figure 4-34 B). Short cracks appear to grow faster initially than long cracks at small ΔK values. This phenomenon is well known in the literature and is attributed to LEFM limitations in describing short crack stress states, together with a lack of closure. However, the short crack data does not then match the long crack data at higher ΔK values as expected. The calculated a/c ratio from 4-2 is based upon an equilibrium ΔK around the perimeter of single semi-elliptical cracks, accounting for smaller a/c ratios as the crack grows towards the neutral axis due to bending conditions. However, this does not account for the sudden large reduction in a/c ratios that may arise from coalescence events, thus affecting the validity of ΔK values calculated for the longer “short” cracks.

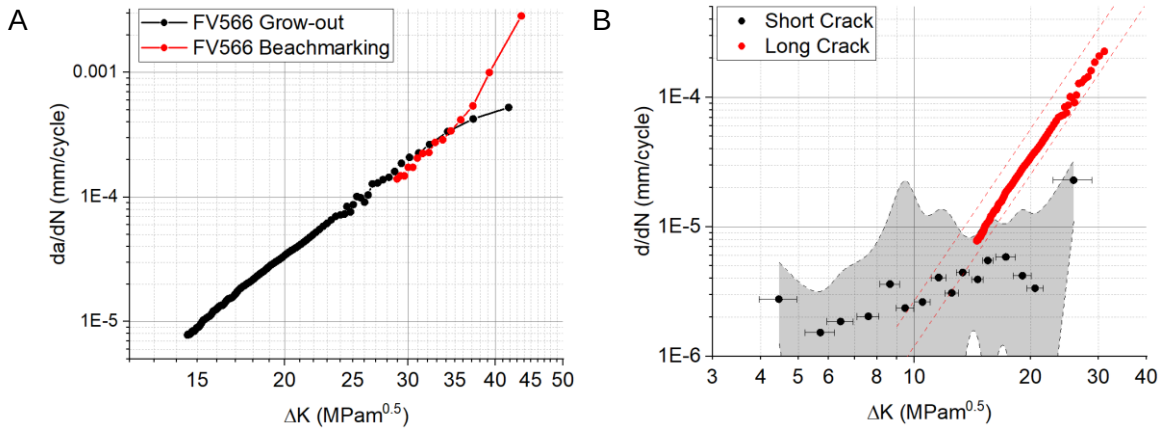

Figure 4-34 A) da/dN versus ΔK measured using DCPD from the grow-out stage of a long crack test of FV566 sample with OLR of 1.56 applied every 150 baseload cycles, compared with da/dN versus ΔK where crack growth rate was calculated by measuring distance between subsequent beachmarks. B) Short and long crack growth rate versus ΔK for OLR of 1.56 applied every 150 baseload cycles loading conditions.

4.5 Summary and conclusions

Microhardness indentation measurements were taken at locations of interest at fir-tree-root-fillets of in-service FV566 blades roots (identified from FE modelling by FNC) to investigate strain hardening with notch depth. The results were inconclusive and did not identify strain hardening or residual stress effects.

Specimens extracted from the blade roots of ex-service low pressure steam turbine blades made from FV566 were notched and subjected to both long and short crack testing. Overloads with OLRs of 1.07, 1.11 and 1.56 were applied every 150 baseload cycles and compared with constant amplitude loading.

The source of crack initiation was surface condition dependent with corrosion pits dominating the as-received surface condition and slip bands dominating the polished surface condition. Polishing the surface increased the number of cycles to crack initiation. Additionally, introducing an overload of OLR 1.56 every 150 base load cycles further increased the number of cycles to crack initiation.

A higher strain range and polished surface condition resulted in higher number of crack initiation events observed on the notch surface. A higher number of crack initiations resulted in a shorter average crack length before consistent crack coalescence activity. However, the presence of an overload cycle induced a compressive residual stress within the notch stress field that consequently reduced the crack growth rate of short cracks. Characteristic ‘in-plane’ and ‘out-of-plane’ crack coalescence behaviour was seen throughout all tests regardless of load or surface conditions.

The long crack growth rate versus ΔK between constant amplitude loading and with small OLRs of 1.07 and 1.11 every 150 base load cycles were similar. However, the crack growth rate for both long and short cracks was retarded when an overload of 1.56 was applied every 150 base load cycles. This was attributed to the compressive residual stress induced in the notch stress field and ahead of the crack tip from each overload cycle (in line with expected behaviour from the literature).

Visible beachmarks due to bursts of monotonic failure from overloads with OLR of 1.56 were observed every 150 baseload cycles within 1000 cycles of final failure and were used to define the stage III crack growth regime for FV566.

Chapter 5: Notch geometry and shot peening effect on fatigue behaviour

5.1 Introduction

Cracks were observed via NDT methods during routine inspection of in-service turbine blades (personal communication, EDF, 5th January 2018). A lifetime extension strategy, such as grinding out the existing cracks followed by a surface modification process such as shot peening, could be incorporated into maintenance routines to extend the service-life of turbine blades [5]. Grinding out existing cracks will consequently increase the depth and alter the radius of the notch (Figure 5-1) which may then be detrimental to fatigue life. In contrast, the fatigue process is temporarily reversed, requiring crack initiation and short crack growth to reoccur. Additionally, shot peening the notch surface will introduce beneficial residual compressive stress and work-hardening in the notch surface region, offering additional resistance to fatigue. This chapter explores how the application of a lifetime extension strategy involving changing the notch geometry followed by shot peening the notch surface may affect fatigue behaviour at each fatigue stage including crack initiation, coalescence, and propagation within steam turbine blade materials, taking into account the variation in the notch fatigue stress field and its interaction with the shot peening process.

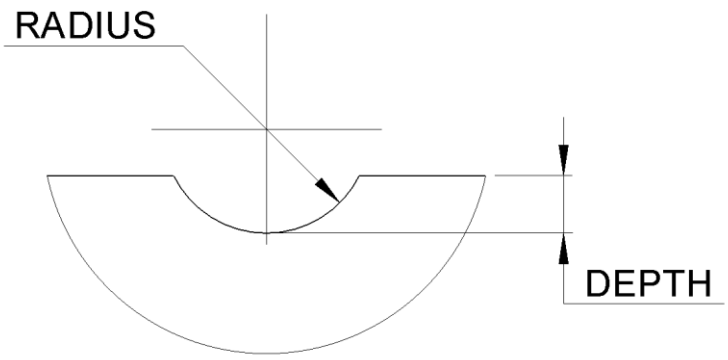

Figure 5-1 A schematic identifying the depth and radius of a typical U-notch geometry representative of in-service turbine blade fir-tree-root-fillets.

It is well known that introducing a notch redistributes stress within a sample, creating an area of localised stress (above nominal stress) on and beneath the notch centre surface known as the notch field (Figure 5-2). Many studies have been carried out to understand how notch geometry affects the maximum stress experienced on the notch surface based upon elastic material assumptions (Peterson's being the most widely known) [178]. While changing the radius of the notch can alter the magnitude of the maximum stress at the notch surface by changing notch geometry, the depth of the notch can additionally impact the

nominal stress by changing sample geometry such as reducing cross sectional area of the sample. Therefore, the influence of notch depth on stress concentration factor is sample geometry dependent.

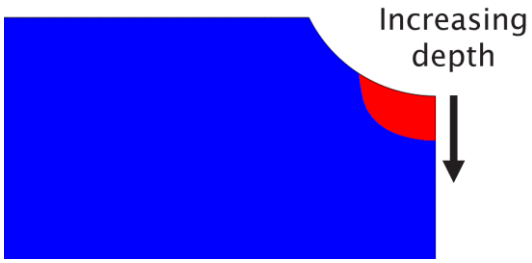

Figure 5-2 A 2D half model of a typical U-notch sample, the area of material shaded red indicates the notch field where material experiences a stress above the nominal stress due to the presence of the notch.

Elastic material behaviour assumptions may be reasonable in the high cycle fatigue regime, where the maximum stress typically occurs on the notch surface. In the low cycle fatigue regime, loading typically surpasses the yield strength of the material. Material plasticity behaviour affects the distribution of stress and strain within the notch field as seen in Figure 5-3 and also in Liao et al [86] (Chapter 2.1.7.1). After unloading, permanent plastic deformation in the material results in residual stress within the notch field [153] which has an effect on fatigue behaviour as seen in Figure 4-32 . Changing the notch geometry changes the distribution of stress range and strain range within the notch field during cyclic loading. This in turn may affect the distribution of residual stress in the LCF regime and therefore the short crack fatigue behaviour and ultimately the fatigue life of the specimen.

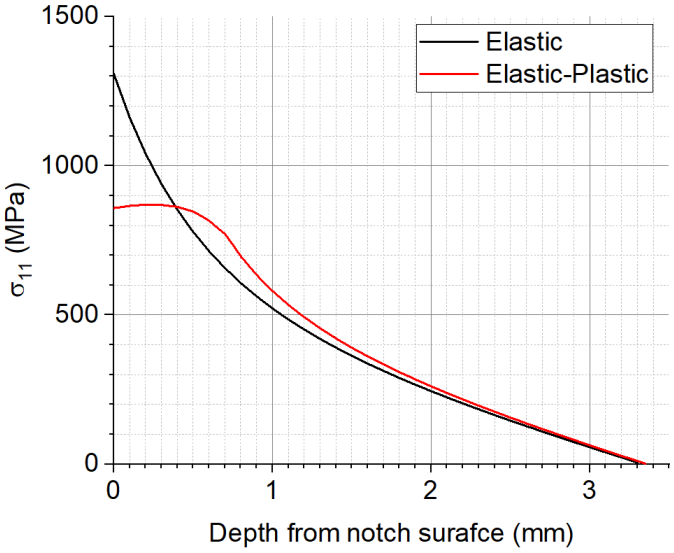

Figure 5-3 Stress versus notch field depth (depth beneath the notch surface) for an elastic material model and an elastic-plastic material model using the FE model (developed in Chapter 3.2.6) for a typical U-notch geometry as seen in Chapter 4 (notch depth of 1.25 mm and notch radius of 2.25 mm).

Samples made from FV448 material with a typical U-notch geometry of notch depth 1.25 mm and notch radius of 2.25 mm, representative of in-service fir-tree-root-fillets, (as in Chapter 4) were analysed with an FE model that accounts for material plasticity and material hardening behaviour [10]. Increasing the radius of the notch geometry from 2.25 mm to 5.25 mm while maintaining the same maximum tensile stress at the notch surface resulted in a slightly reduced maximum stress and a notch field that penetrated deeper beneath the notch surface [10] (Figure 5-4). Decreasing the notch radius and increasing the notch depth is a conservative and therefore practical approach to investigating the effects of grinding out existing cracks from fir-tree-root-fillets of in-service turbine blades. Additionally, it is useful to consider the stress range and strain range applied to a sample during cyclic loading fatigue. There has not been an extensive focus on the stress and strain range distribution within the notch field in the literature. The FE quarter-model based upon elastic-plastic material behaviour developed in Chapter 3.2.6 can be used to investigate stress range and strain range distributions with R-ratio of 0.1 within the notch field. The strain range applied at the notch surface can be kept constant (by changing the load accordingly) to isolate effects of notch geometry.

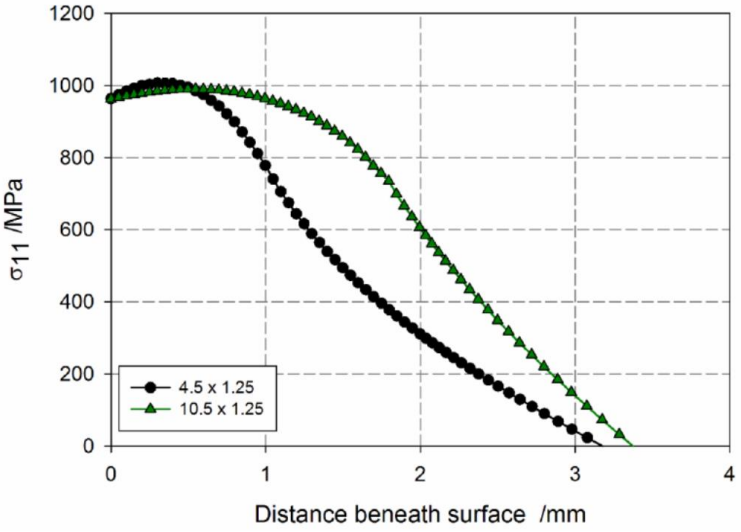

Figure 5-4 Tensile stress versus depth beneath the notch surface for typical U-notch geometry of radius 2.25 mm and 1.25 mm depth compared with a wider notch radius of 5.25 mm and 1.25 mm depth which experience the same maximum tensile residual stress at the notch surface from [10].

Shot peening is a frequently used surface modification method for localised areas such as the fir-tree-root-fillets of low-pressure turbine blades [22, 72, 151]. It is known that shot peening can extend the fatigue life of notched components by inducing surface strain hardening up to 150 µm and compressive residual stress field up to 500 µm beneath the notch surface. Increased dislocation density may limit the movement of PSBs inhibiting crack initiation, while the compressive residual stress produced by the constrained plastic deformation at the surface reduces the effective mean stress, increasing resistance to

fatigue crack propagation [5, 10, 22, 50, 51, 72, 126, 151]. Conversely, shot peening also increases surface roughness which is considered detrimental to fatigue due to the presence of local stress concentration features which induce earlier crack initiation behaviour [179].

Additionally, for extreme LCF conditions (< 10 000 cycles), the application of relatively high strain ranges (> 1 %) can relax the compressive residual stress produced from shot peening within the first 1 % of fatigue life for FV448 material [10, 125-128]. With a diminished compressive residual stress field, the retardation effect from shot peening on short crack propagation is no longer apparent. Studies have shown that the benefits of shot peening outweigh the drawbacks for the majority of fatigue situations resulting in an improved resistance to fatigue overall, including for in-service turbine blade in low cycle fatigue conditions [5, 10, 125].

This chapter will investigate the effect of changing the notch radius and depth with constant applied strain range at the notch surface on the distribution of stress range and strain range within the notch field using elastic-plastic FE modelling. Experimental testing on polished and shot penned samples has been carried out to investigate the effect of changing notch radius and depth on fatigue behaviour in terms of initiation, short crack growth and coalescence events.

5.2 Experimental Methodology

5.2.1 Notch stress field characterisation

5.2.1.1 FE Modelling

Preliminary FE modelling was carried out using the FE model developed in Chapter 3.2.6 to identify the loads P_{max} and P_{min} required to produce total strain ranges of 0.75 %, 1.15 % and 1.65 % at the notch surface based upon an R-ratio of 0.1 for all notch geometries (Figure 5-5). The longitudinal stress range (σ_{max} - σ_{min}) and longitudinal total strain range (ε_{max} - ε_{min}) along the notch field depth, notch profile and notch width highlighted by yellow lines in Figure 5-6 were obtained for each notch geometry. A linear unloading step from P_{max} to 0 N was introduced where the residual stress in the longitudinal direction along the notch field was obtained for all notch geometries.

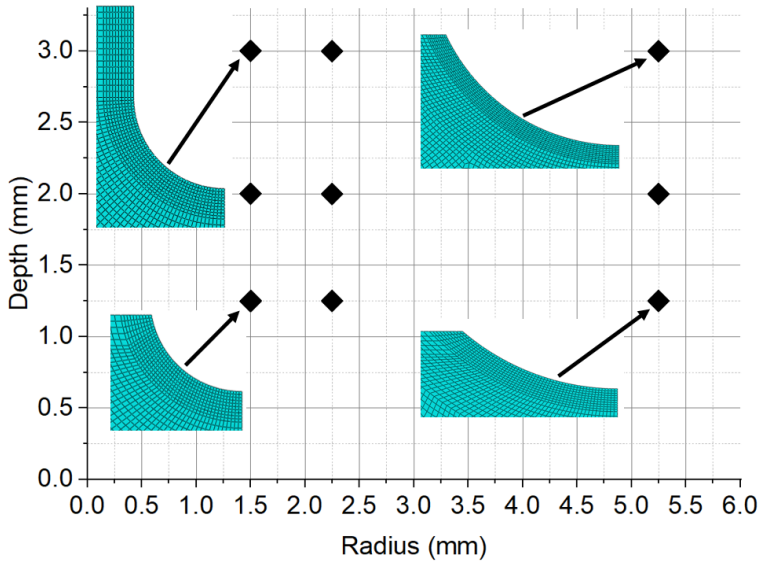

Figure 5-5 Notch depth in mm versus the notch radius in mm for various notch geometries that were modelled and analysed using FE modelling software (ABAQUS).

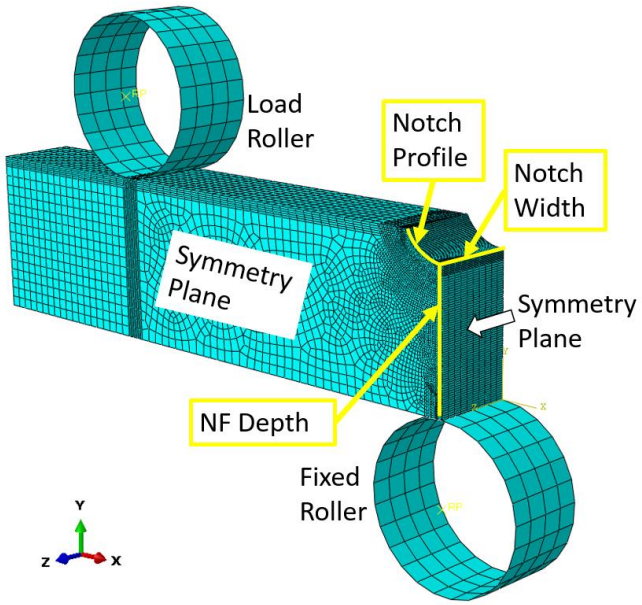

Figure 5-6 A typical U-notch geometry quarter-model created using FE modelling software (ABAQUS). The longitudinal stress and longitudinal total strain were obtained along the notch field depth (NF Depth), notch profile and notch width locations outlined by yellow lines.

The notch field depth was normalised using Equation 5-1 to allow similitude and direct comparison of the notch field with notch geometries of various notch depths. The neutral axis is therefore expected to be located at a normalised depth of approximately 0.5 regardless of the notch geometry (Figure 5-7).

$$NF\ Depth = \frac{x}{W - d} \qquad \text{Equation 5-1}$$

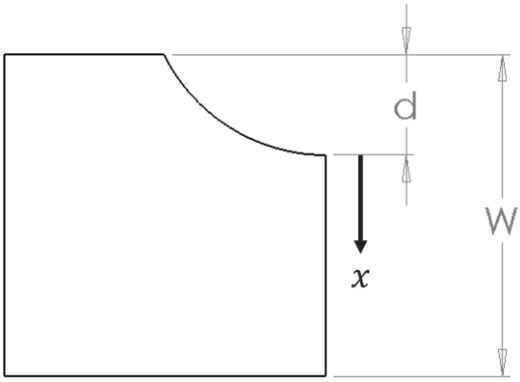

Figure 5-7 A schematic depiction of the variables for calculating the normalized notch stress field depth. *W* is the sample depth, *d* is the notch depth and x is the depth from the beginning of the notch surface.

5.2.1.2 Residual stress from shot peening

X-ray Diffraction (XRD) using a Stresstech Xstress Robot was carried out on a shot peened U-notch sample with notch radius of 2.25 mm and notch depth of 1.5 mm from blade M08 to obtain residual stress profiles at Coventry University, courtesy of Mitchell Leering. XRD was carried out in the longitudinal direction and transverse direction at three locations on a U-notched surface and flat surface totalling six tests (Figure 5-8). The XRD equipment was calibrated and validated on stress free Fe powder. A collimator diameter of 0.5 mm with exposure time of 20 seconds over 12 tilts from -45° to 45°. The peak diffraction angle was found to be 156.4°. A daily zero reading was taken which was used to determine measurement error. An exposure time of 50 seconds with tilt oscillation of 0° was used when testing the shot peened sample. Layers of material from the notched surface and flat surface were removed incrementally from the sample, XRD was carried out after each layer removed to obtain residual stress versus depth from surface profiles. Each layer was removed using an electro-polishing method (Struers LectroPol) with A2 electrolyte, a mask of 0.5 mm^2, 20 V flow rate of 14 for 12 seconds. XRD was carried out for each layer until a reading of 0 MPa residual stress was sustained for at least 100 µm.

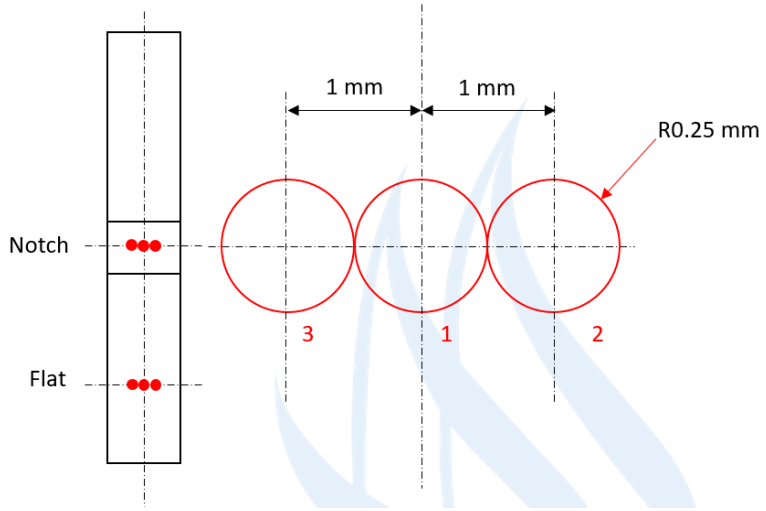

Figure 5-8 XRD measurements were taken at three locations on the flat surface and on the notch centre surface totalling six tests.

5.2.2 Short crack testing

5.2.2.1 Sample preparation

Plain bend bars made from FV566 were extracted from ex-service turbine blades (M08 and M09) and U-notched with varying depths and radii machined in the centre of the sample. The notch surfaces of all U-notch samples were 'fully' polished with a rotary tool using 9 µm polishing suspension until all corrosion pits were completely removed. The U-notch surface and corresponding top surface of some of the U-notch samples were shot peened with a T0 industrial standard shot peen (MI230R 200% 13A) by Sandwell UK Ltd. The shot diameter was 0.58 mm, shot hardness (Hardness Rockwell C) 45 – 52 HRC and shot velocity was 57 ms^{-1}.

The depth and radius of the notch geometries were measured (Figure 5-9) using optical microscopy and image post-processing software (Image J). The final notch geometries are presented in Figure 5-10 with notch geometries from Soady [10] included for comparison.

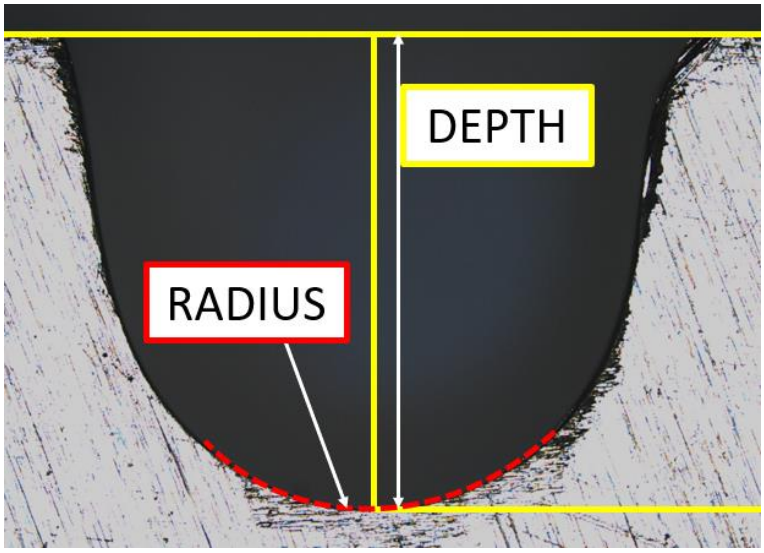

Figure 5-9 The depth of the notch was measured from the top surface of the sample to the centre of the U-notch. The radius of the notch was approximated by overlaying the radius of an arc (defined by three points) on the image to fit the centre of the U notch as closely as possible.

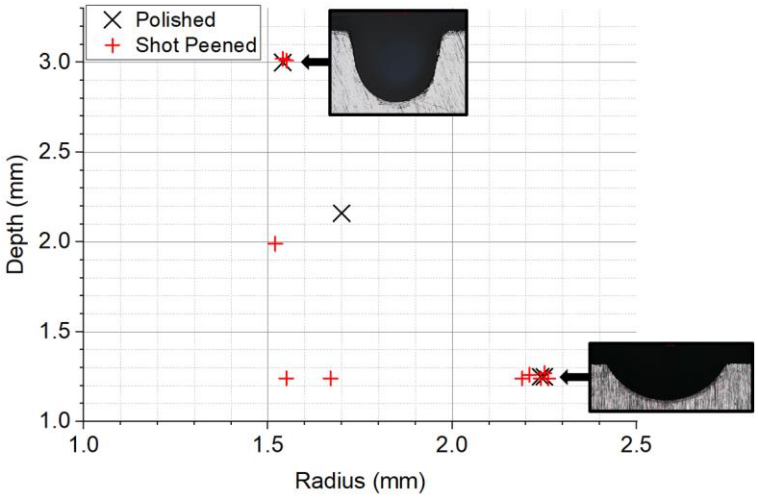

Figure 5-10 Notch depth in mm versus the notch radius in mm for various notch geometries introduced into plain bend bar samples from M08 and M09 blades.

5.2.2.2 Notch surface characterisation

Surface roughness R_a measurements were taken using a profilometer (Infratouch) in accordance with *BS EN 4288: 1998* [175] to compare the roughness of the 'fully' polished and shot peened surface condition (Figure 5-11). A measurement length of 5 mm and *Lc* value of 0.8 was used to measure the surface roughness in the traverse direction (perpendicular to the tensile axis) for all notch surfaces.

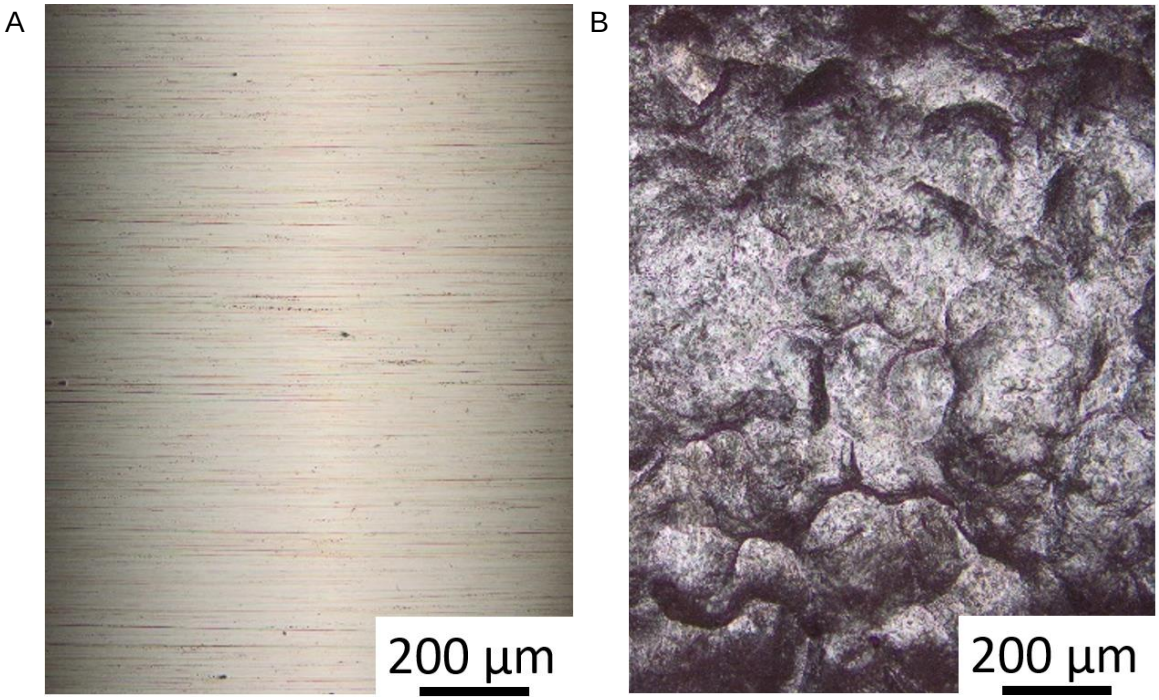

Figure 5-11 Optical microscopy images of A)The 'fully' polished notch surface condition for M08 and M09 blade surfaces where no residual corrosion pits were present. B) The T0 shot peened surface condition.

5.2.2.3 Continuous and interrupted fatigue testing of U-notch samples

Fatigue testing was carried out under 3-point bend constant amplitude cyclic loading conditions on U-notched samples using an Instron TM ElectroPulse E10000 Electromechanical fatigue testing machine. All testing was carried out at room temperature using a sinusoidal waveform at a frequency of 10 Hz and with an R-ratio of 0.1.

Continuous fatigue testing was carried out on U-notch samples to obtain representative lifetimes for various notch geometries, surface conditions and strain ranges (0.75 %, 1.15 % and 1.65 %). Interrupted fatigue testing was carried out on U-notch samples involving regular surface replication of the notch root. The continuous and interrupted short crack testing method is discussed in more detail in Chapters 4.2.2.4 and 4.2.2.5.

5.2.2.4 Determination of the *a/c* ratio

Partial-lifetime interrupted fatigue testing was carried out on samples with polished and shot peened notch surfaces to obtain crack aspect *a/c* ratios. Tests were cyclically loaded at a constant amplitude with relatively high strain range of approximately 1.5 % based upon FE modelling to induce a high number of initiation events. Constant amplitude cyclic loading was carried out and surface replication of the notch surface recorded until approximately 50 % - 60 % of expected fatigue life when multiple cracks of lengths 200 µm – 300 µm were observed. A heat-tinting process was carried out after cyclic loading; the samples were

oxidized in a furnace at 600 °C for 2 hours and air cooled for at least 6 hours. The sample was immersed in liquid nitrogen for approximately 10 minutes to allow the sample to cool below the ductile to brittle transition temperature. The cold samples were manually broken in half with a hammer. The broken samples were left to heat naturally to ambient temperature and placed in a desiccator. A JSM 6500F field emission gun scanning electron microscope (FEG-SEM) was used to observe and identify semi-elliptical fatigue regions on the fracture surfaces.

The *a/c* ratios were calculated by measuring the length of the crack ($2c_{project}$) and the area (*A*) from the semi-elliptical fatigue region produced by short crack growth on the fracture surface using image analysis software (Image J). Equation 5-2 was used to calculate the corresponding '*a'* value and the subsequent *a/c* ratio (Figure 4-10).

$$a = \frac{2A}{\pi c} \qquad \text{Equation 5-2}$$

5.2.2.5 Post-test analysis

An optometry surface profiling microscope (Alicona) was used to observe and analyse the fracture surfaces of samples failed by fatigue testing. The surface topology of the fracture surface close to the notch surface was recorded as height (a distance parallel to the tensile axis) from a reference plane using optometry surface profiling (Figure 5-12 A). Twenty locations were chosen at random along the width of the sample to represent initiation events. The projected distance parallel to the tensile axis for each successive initiation location (known as out-of-plane distance) were found (Figure 5-12 B and C). The average out-of-plane distance was calculated ($\bar{d}$) using Equation 5-3 for notch geometries with various notch radii.

$$\bar{d} = \frac{1}{n}\sum_{1}^{n} d_n \qquad \text{Equation 5-3}$$

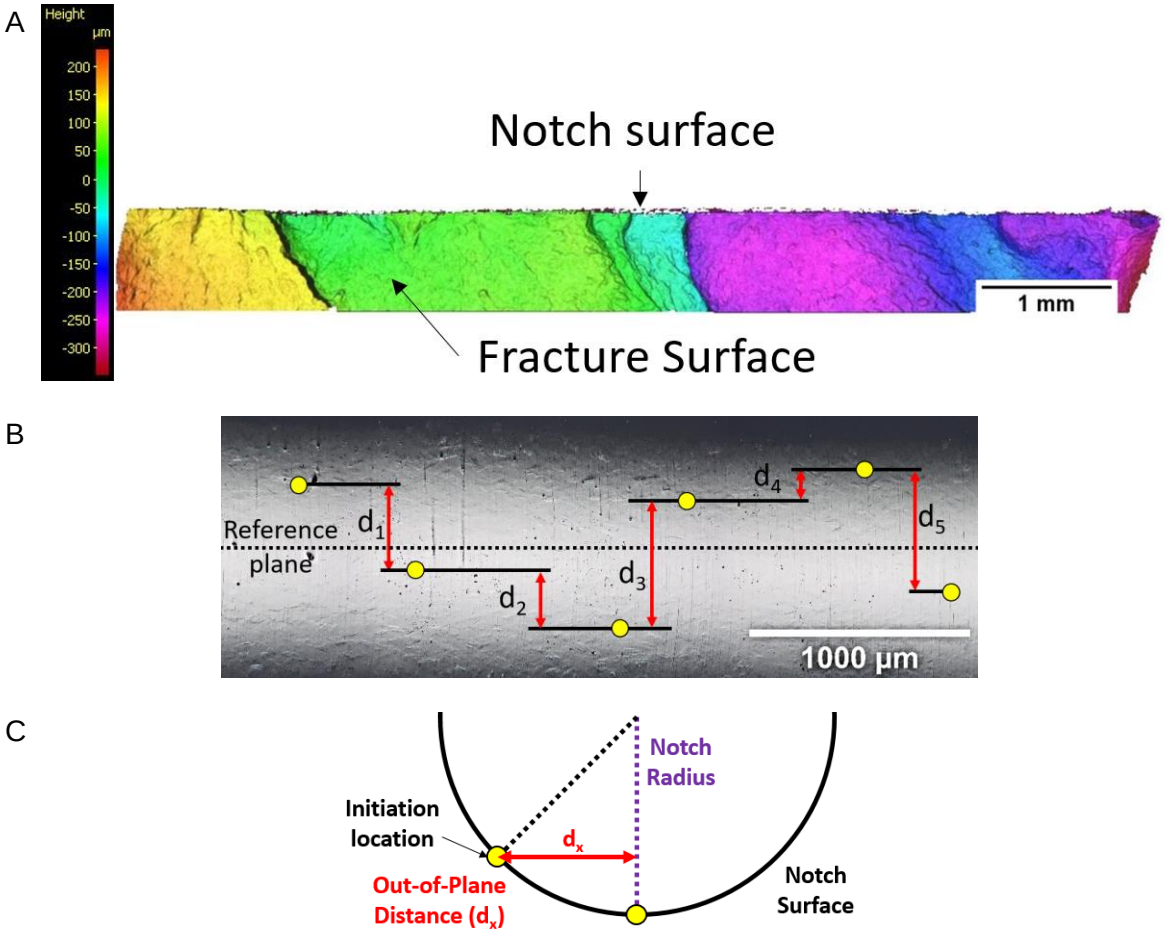

Figure 5-12 A) The colour coded topology of the fracture surface (close to the notch surface) showing the height as distance from a reference plane (parallel to the tensile axis). B) Typical notch surface section with random initiation locations (as yellow dots). The out-of-plane distance d_x is calculated by measuring the projected distance parallel to the tensile axis between two neighbouring initiation locations. C) Schematic side view of a typical U-notch sample.

5.3 Results

5.3.1 Surface roughness

The polished notch surfaces from blades M08 and M09 had an average R_a surface roughness of 0.039 µm ± 0.015 µm (one standard deviation). The shot peened notch surfaces have a surface roughness R_a of 2.7 µm ± 0.4 µm (one standard deviation) (Figure 5-13).

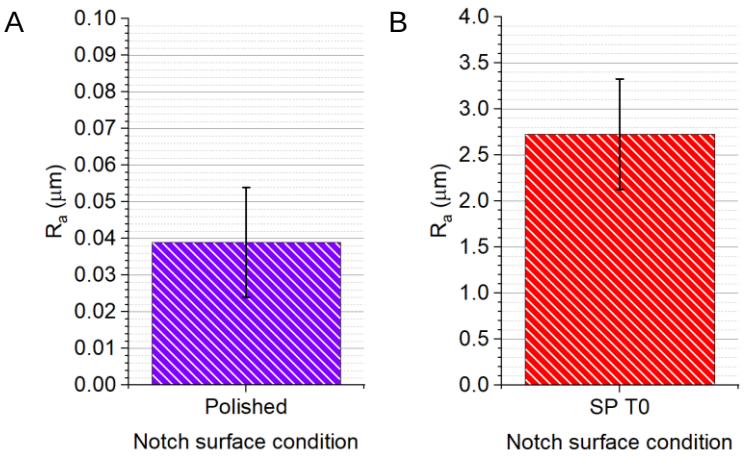

Figure 5-13 Surface roughness R_a of A) 'fully' polished notch surface and B) T0 shot peened notch surface conditions for blades M08 and M09.

5.3.2 Notch geometry on the notch field

The stress range and strain range distribution versus notch field depth for various notch geometries was found using the FE model discussed in Chapter 5.2.1.1. The stress range distribution within the notch field subjected to an applied strain range of 0.75 % on the notch surface can be seen in Figure 5-14 A). At the notch surface the stress range was approximately 850 MPa, the stress range increased to a maximum of approximately 900 MPa at a normalised notch field depth of 0.05. The strain range then decreased rapidly until normalised depth of 0.1. The rate at which the strain range decreased with notch field depth decreased gradually until approximately 0.3 normalised notch field depth. The stress range decreased linearly until a strain range of zero was observed at the neutral axis at 0.47 normalised depth.

An equivalent strain range distribution within the notch field for an identical geometry and applied strain range can be seen in Figure 5-14 B). At the notch surface the strain range was 0.75 % which then decreased rapidly and somewhat linearly until a strain range of 0.4 % at 0.06 normalised depth. The rate at which the strain range decreased with notch field depth decreased gradually until 0.15 % strain range at normalised depth of 0.2. The strain range then decreased linearly until a zero strain range was observed at the neutral axis.

Figure 5-14 A) and B) show the stress range and strain range distributions within the notch field for notch geometries of increasing depth while keeping applied strain range at the notch surface and radius constant at 0.75 %. The stress and strain range near the notch surface was identical. The magnitude of the maximum stress range slightly increased while the location of the maximum stress range shifted deeper into the notch field. At normalised

depth of 0.1, changing the notch depth from 1.25 to 3 mm resulted in the largest stress range difference of 125 MPa and strain range difference of 0.075 %.

Figure 5-14 C) and D) show the effect of changing notch radius on stress range and strain range distributions within the notch field at a constant strain range of 0.75 % at the notch surface. The shaded region for each notch radius shows the range of notch field distributions between notch depths of 1.25 mm and 3 mm. Increasing the notch radius from 1.5 mm to 5.25 mm decreased the stress range at the surface of the notch from 850 MPa to 820 MPa. The maximum stress range decreased from approximately 900 MPa to 850 MPa while the normalised distance of the maximum stress from the notch surface increased from 0.05 to 0.08. The stress range and strain range were almost doubled between a notch field depth of 0.15 and 0.2 from the notch surface. The strain range distribution shifted towards a linear relationship with increasing notch radius. Altering the notch radius has a more profound effect on the distributions of stress range and strain range within the notch field than changing depth for the notch geometries tested. Figure 5-14 E) and F) show the effect of increasing the strain range at the notch surface on the distribution of stress range and strain range within the notch field for a constant notch radius of 2.25 mm. Increasing the applied strain range from 0.75 % to 1.65 % only slightly increases the stress range at the notch surface by 20 MPa due to material plasticity but increased the stress range and strain range and overall size of the notch field.

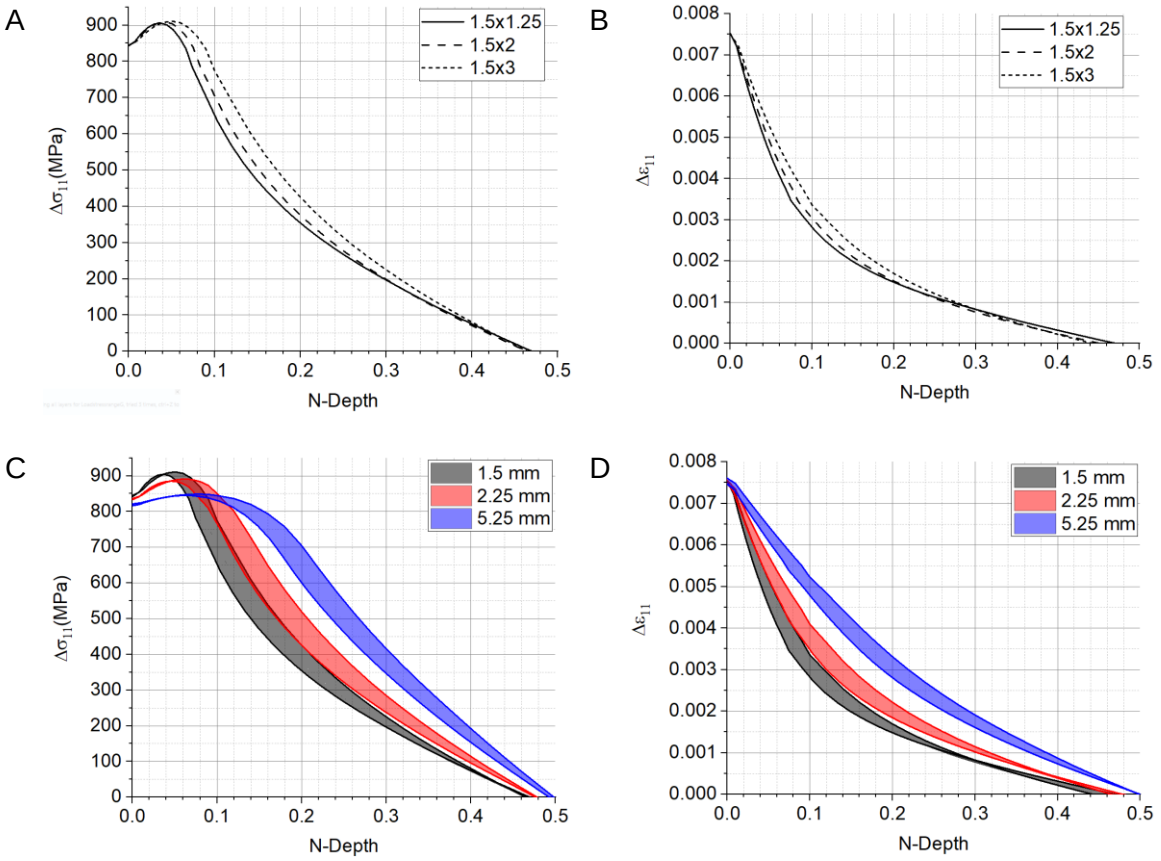

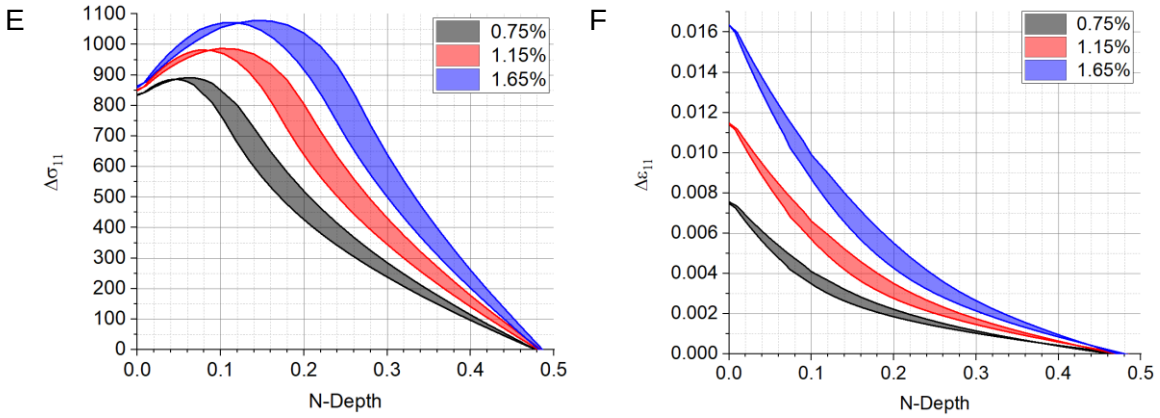

Figure 5-14 FEA results of the distribution of stress and strain range with increasing normalised depth from the notch surface (N-Depth) for A) Stress range distribution within the notch field with notch radius of 1.5 mm and increasing notch depths of 1.25 mm, 2 mm and 3 mm. B) Strain range distribution within the notch field with notch radius of 1.5 mm and increasing notch depth. C) Effect of increasing notch radius on stress range distribution within the notch field for applied strain range of 0.75 %. D) Effect of increasing notch radius on strain range distribution within the notch field for applied strain range of 0.75 %. (The shaded regions show the range of notch field distributions between notch depths of 1.25 mm and 3 mm). E) Effect of increasing strain range at the notch centre on the stress range distribution within the notch field with a constant notch depth of 2.25 mm. F) Effect of increasing strain range at the notch centre on the strain range distribution within the notch field with a constant notch depth of 2.25 mm. (The shaded regions show the range of notch field distributions between notch radii of 1.5 mm and 5.25 mm).

The longitudinal residual stress versus normalised notch field depth from the surface of the notch for various notch geometries was found by fully unloading the FE model after P_{max} was applied. The residual stress profile for a 1.5 mm notch radius with notch depths between 1.25 mm and 3 mm with an applied strain range of 0.75 % (P_{max} = 0.81 %) can be seen in Figure 5-15 A). A compressive residual stress of 440 MPa was observed at the notch surface which decreases rapidly at a near linear rate until 0.04 normalised depth when zero residual stress was seen, subsequently followed by a counterbalancing tensile residual stress. A maximum tensile residual stress of 100 MPa was seen at 0.07 normalised depth. Which then decreases with a steadily decreasing rate until no residual stress is observed at the neutral axis at normalised depth of approximately 0.5. This residual stress distribution is typically expected for all notch geometries loaded in the LCF regime. Increasing notch depth slightly increased the maximum residual compressive residual stress on the notch surface by 10 MPa. The maximum tensile residual stress was slightly increased by 10 MPa and occurred deeper in the notch field at 0.09 normalised depth from the notch surface.

Increasing the applied strain range at the notch surface from 0.75 % to 1.65 % increased the maximum compressive residual stress from 440 MPa to 950 MPa. The compressive to tensile residual stress transition occurs deeper in the notch field from 0.04 to 0.065 normalised depth. The maximum tensile stress was increased from 100 MPa to 300 MPa and occurred deeper in the notch field from 0.07 to 0.14 normalised depth (Figure 5-15 B).

Increasing the notch radius from 1.5 mm to 5.25 mm (Figure 5-15 C) while maintaining constant applied strain range at the notch surface of 0.75 % decreased the compressive residual stress on the notch surface from 440 MPa to 385 MPa. The compressive to tensile residual stress transition occurred deeper in the notch field from 0.04 to 0.08. Increasing the applied strain range to 1.65 % (Figure 5-15 D) produced a similar but more profound effect to the distribution of residual stress within the notch field when notch radius was increased.

Figure 5-15 E) and F) show how increasing the applied strain at the notch surface influences the residual stress distribution within the notch field. Increasing the notch surface strain range from 0.75 % to 1.65 % greatly increases the maximum compressive residual stress at the notch surface increased by around 100 %. The compressive to tensile residual stress transition occurs deeper in the notch field. The counterbalancing tensile residual stress is greatly increased by around 300 %. Increasing the notch radius from 1.5 mm to 2.25 mm has a marginal impact on the residual stress distribution when compared with increasing strain range for the geometries and strain ranges applied.

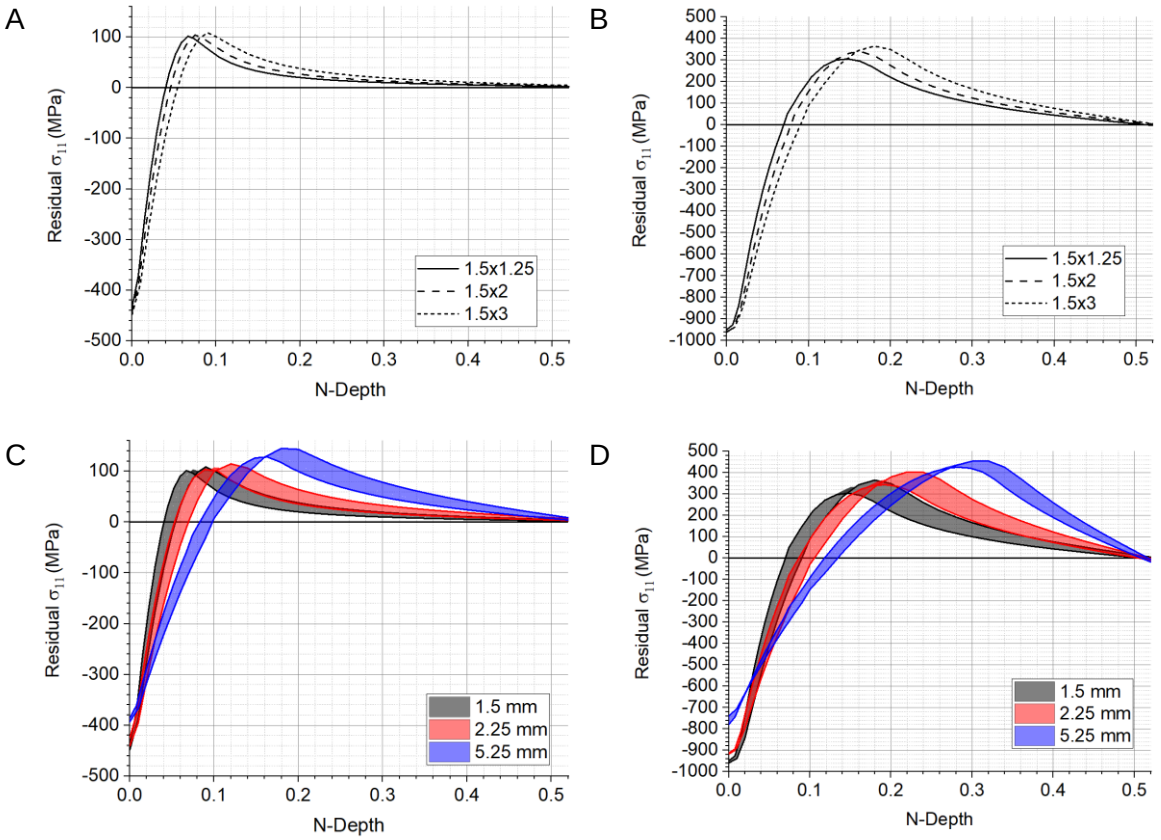

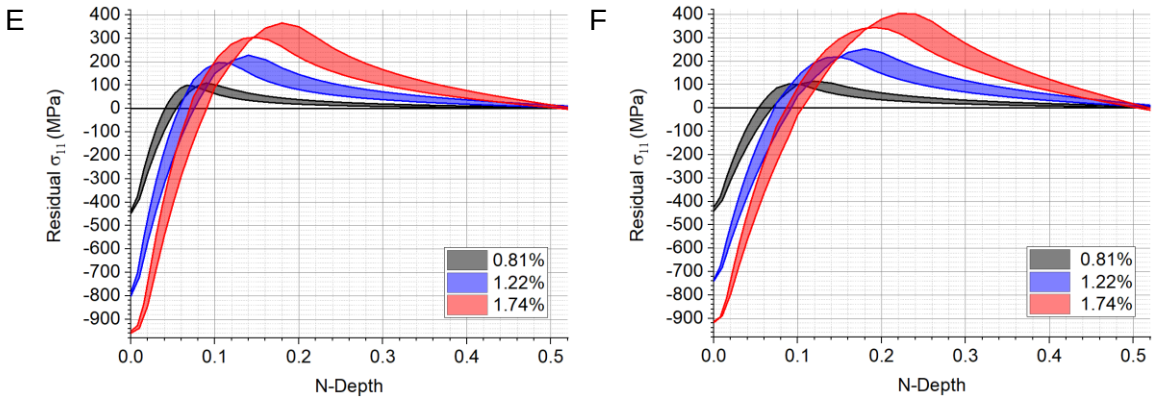

Figure 5-15 FEA results of the distribution of residual stress in the longitudinal direction after unloading from P_{max} with increasing normalised depth from the notch surface (N-Depth) for A) Notch radius of 1.5 mm and increasing notch depths of 1.25 mm, 2 mm and 3 mm with total longitudinal strain range of 0.81 % applied at the notch centre. B) Notch radius of 1.5 mm and increasing notch depths of 1.25 mm, 2 mm and 3 mm with a strain range of 1.74 % at the notch centre. C) Effect of increasing notch radius on residual stress distribution within the notch field for strain range of 0.81 % applied at the notch centre D) Effect of increasing notch radius on residual stress distribution within the notch field with strain range of 1.74 %. (The shaded regions shows the range of notch field distributions between notch depths of 1.25 mm and 3 mm). E) Effect of increasing strain range at the notch centre on the residual stress distribution within the notch field for notch radius 1.5 mm. F) Effect of increasing strain range at the notch centre on the residual stress distribution within the notch stress field for notch radius of 2.25 mm. (The shaded regions shows the range of notch field distributions between notch radii of 1.5 mm and 5.25 mm).

5.3.3 XRD results from shot peening

Coventry University performed XRD using an incremental layer removal technique on a T0 shot peened FV566 sample to obtain residual stress versus depth profiles. The average residual stress in the longitudinal and transverse directions after each layer removed from three locations were averaged for both the flat surface and the U-notched surface (Figure 5-16). The results from the flat surface suggest that there is little difference in the residual stress with depth between the longitudinal and transverse direction as expected (Figure 5-16 A). The residual stress profiles measured from the notch surface show slightly less residual stress in the longitudinal direction. Little difference in the residual stress distribution was found between the flat surface and notch surface in the transverse direction. The residual stress in the longitudinal direction measured within the notch is also slightly less than the flat surface suggesting the results for the notch longitudinal may be too small.

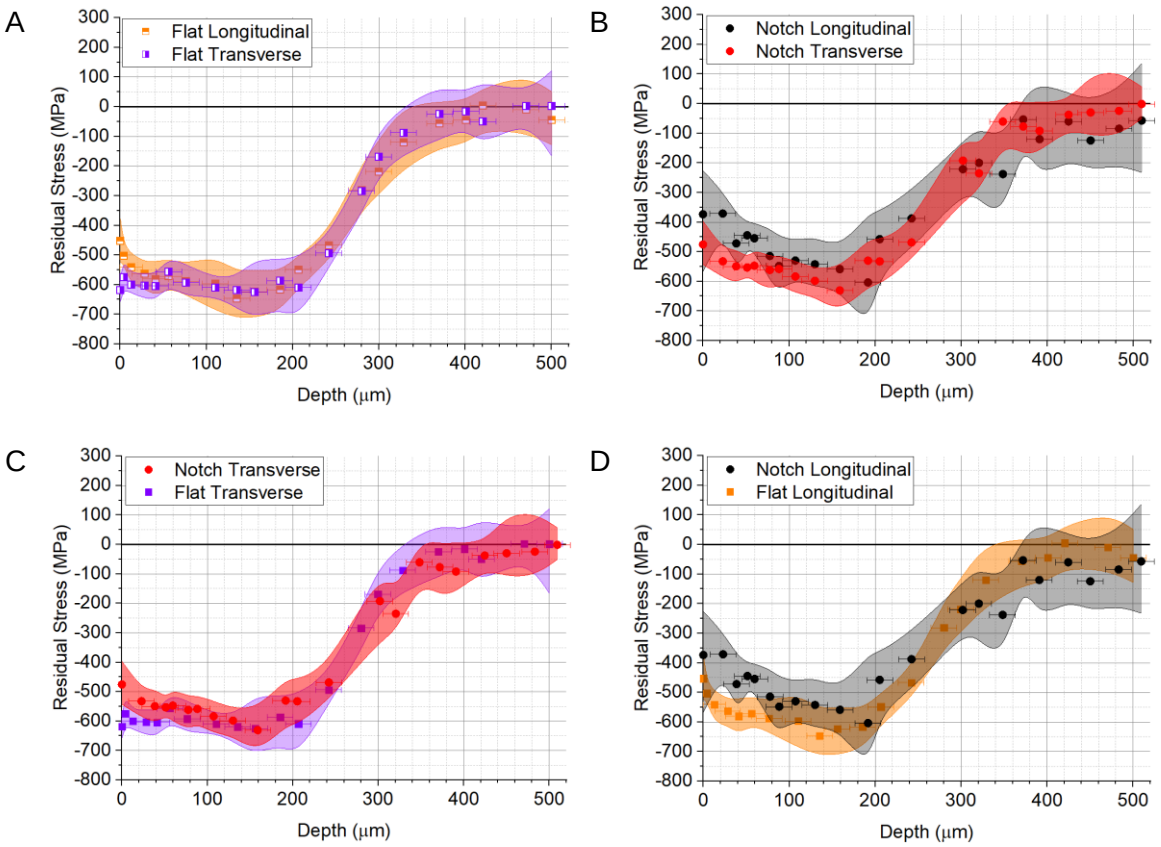

Figure 5-16 Residual stress from T0 shot peening versus depth from the surface in FV566 for A) the longitudinal and transverse direction on a flat surface, B) the longitudinal and transverse direction in the centre of a notch with radius of 2.25 mm and depth of 1.25 mm, C) the transverse direction for a flat and notched surface, D) the longitudinal direction for a flat and notched surface. The shaded regions show the expected error range based upon testing at three locations and additional measurement error from daily zero readings.

5.3.4 U-notch fatigue behaviour

5.3.4.1 Crack initiation behaviour

The number of crack initiation events forming the primary crack in various notch geometries and plain bend bars were plotted against applied strain range for FV448 [10], FV566 blades M06 from Chapter 4, M08 and M09 (Figure 5-17). Increasing the strain range tended to increase the number of crack initiation events on all notch geometries including plain bend bars as expected. Changing both the notch radius and depth did not appear to have a clear impact on the number of crack initiation events. Plain bend bars (from FV448) tended to have a lower number of crack initiation events than notched samples especially with increasing strain ranges (Figure 5-17 A and B). Surface condition appeared to have the largest influence on the number of crack initiation events (Figure 5-17 C) and is explored in more detail.

Total longitudinal strain range between 0.45 % and 0.6 %;

- The total number of crack initiation events was less than 5 for as-received (containing corrosion pits) and shot peened (FV448) surface conditions.

Total longitudinal strain range between 0.6 % and 0.9 %;

- The as-received, polished and shot peened (FV448) notch surface conditions all had a similar number of crack initiation events at these strain ranges with an average of 8 crack initiation events.
- The average number of crack initiation events for the shot peened (FV566) surface condition is 27 which was much higher than the other surface conditions.

Total longitudinal strain range between 1.15 % and 1.2 %;

- No data exists for the as-received surface condition for these strain ranges although an estimate of 10 crack initiation events could be considered a reasonable approximation based upon a linear extrapolation.
- The average number of crack initiation events for the shot peened samples slightly increased from 26 to 33.
- The average number of crack initiation events on the polished surface increased significantly from 8 to 31 crack initiation events.
- The number of crack initiation events were similar for both polished and shot peened samples at this strain range.

Total longitudinal strain range between 1.6 % and 1.65 %;

- Crack initiation events only slightly increased for the as-received surface condition from 7 at 0.75 % strain range to 12 for the 1.65 % strain range.
- Crack initiations events slightly increased for the shot peened surface condition from 33 to 37.

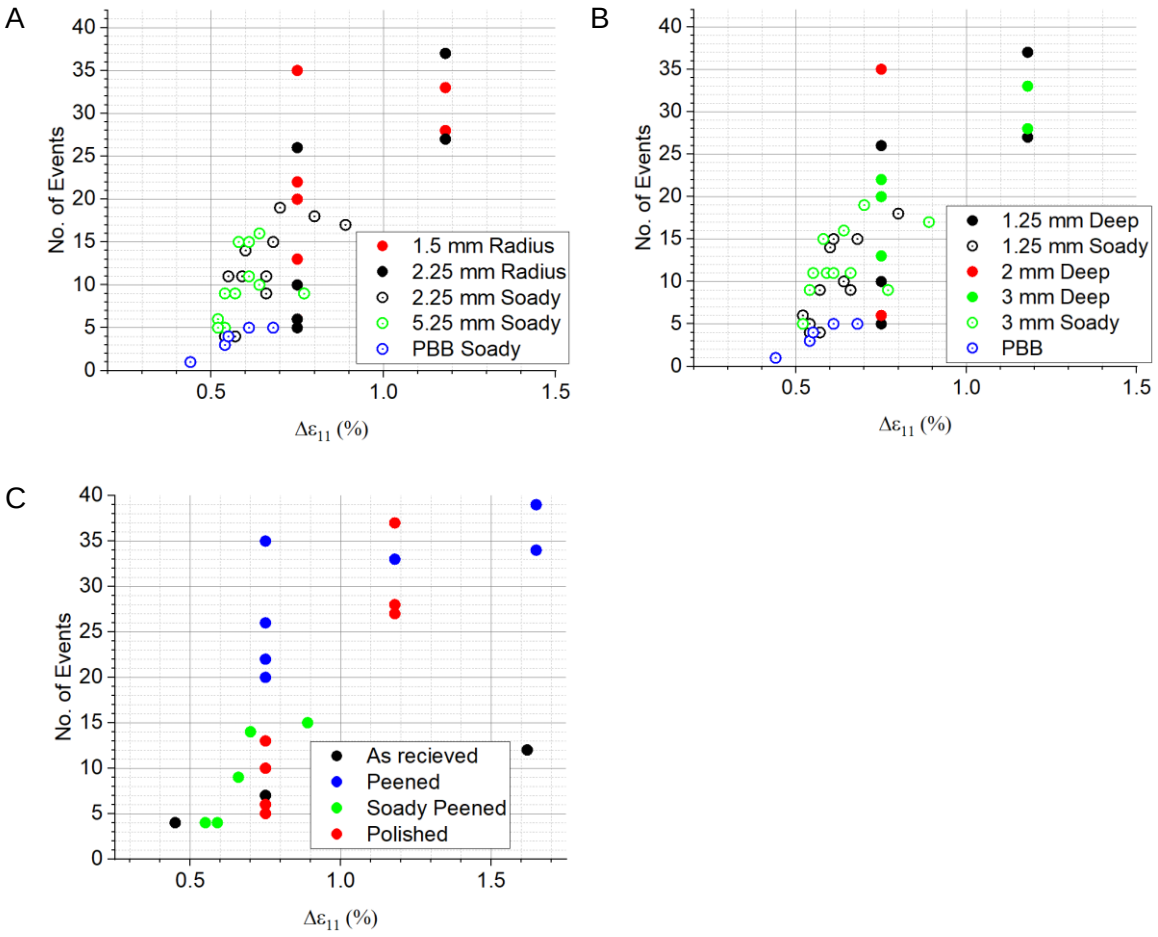

Figure 5-17 The number of initiation events versus total longitudinal strain range for A) varying notch radius, B) varying notch depth and C) notch surface condition. The results include FV448 produced by Soady [10].

5.3.4.2 Short crack behaviour and growth

The short crack growth rate versus $\Delta K_{Surface}$ for two samples with typical notch geometry (2.25 mm radius and 1.25 mm depth) and a sharper and deeper notch geometry (1.5 mm radius and 3 mm depth) were compared. Both samples were subjected to interrupted lifetime testing with total longitudinal strain range of 0.75 % at the polished notch surface. The results in Figure 5-18 A) suggest that the short crack growth rate versus $\Delta K_{Surface}$ behaviour is minimally affected by a relatively small change in notch geometry under linear elastic fracture mechanics assumptions.

The short crack growth rate versus $\Delta K_{Surface}$ for two samples with a polished notch surface and with a T0 shot peened notch surface condition were compared. Both samples were subjected to interrupted lifetime testing with total longitudinal strain range of 0.75 % at the polished notch surface with a typical notch geometry (2.25 mm radius and 1.25 mm depth). The crack growth rate between the two notch surface conditions was similar at low $\Delta K_{Surface}$ values between 5 and 6 $MPam^{0.5}$. The residual stress from the shot peening process

resulted in a slight decrease with increasing $\Delta K_{Surface}$ values until 20 MPam$^{0.5}$ where crack growth rate was ten times slower than the polished notch surface condition. The crack growth rate then rapidly increased towards polished surface condition levels until 30 MPam$^{0.5}$ where short crack growth rate was 5 times slower than the polished notch surface condition and coalescence events took over short crack growth behaviour.

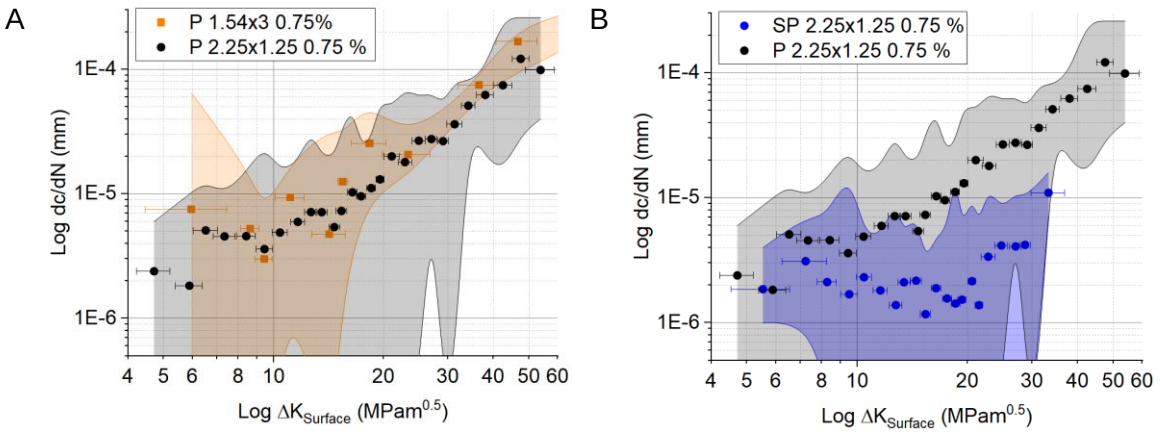

Figure 5-18 Short crack growth rate versus $\Delta K_{Surface}$ for A) two polished notch surfaces with different notch radius and depth B) polished and shot peened notch surface conditions with a typical notch geometry.

5.3.4.3 Coalescence behaviour

Optometry surface profiling was carried out on the fracture surfaces of all samples and the out-of-plane variance obtained based upon twenty random initiation locations. The effect of notch radius, surface condition and strain range on the out-of-plane variance can be seen in Figure 5-19). The notch surface condition was not found to affect out-of-plane variance significantly (Figure 5-19 A), while increasing the strain range tended to increase the out-of-plane variance (Figure 5-19 B). The out-of-plane variance for notch radius of approximately 2.25 mm was 64.5 µm ± 20.8 (one standard deviation) while for a 1.5 mm notch radius the out-of-plane variance was 60.9 µm ± 15.1 (one standard deviation). Overall, the notch radius did not decrease the out-of-plane variance significantly as expected. At isolated strain ranges of 1.65 % and 1.18 %, the out-of-plane variance slightly decreased with a sharper notch radius.

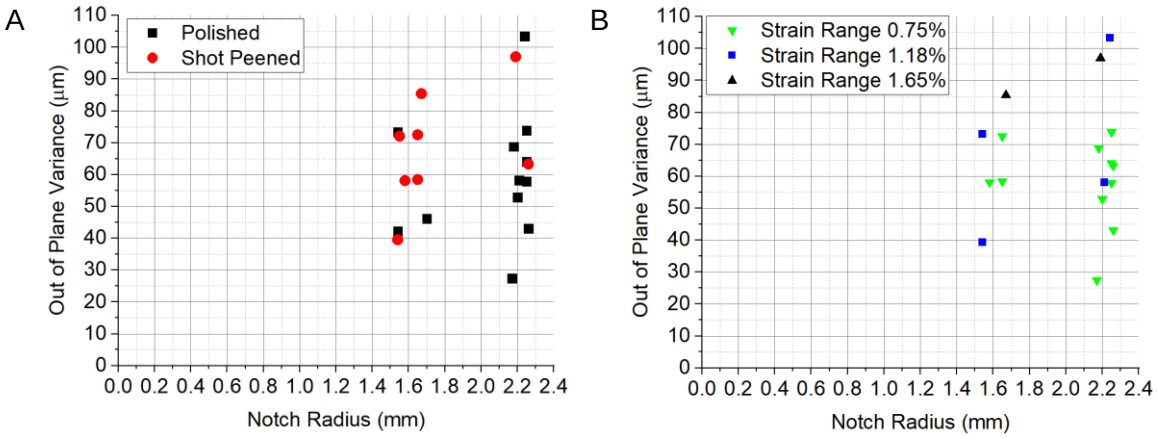

Figure 5-19 A) Out-of-plane variance versus notch radius for polished samples and shot peened samples. B) Out-of-plane variance versus notch radius for three strain ranges of 0.75 %, 1.18 % and 1.65 %.

Crack coalescence behaviour was observed to display characteristic in-plane and out-of-plane crack coalescence behaviours as discussed in Chapter 4.3.2.4 and was seemingly independent of notch geometry.

5.3.4.4 Short crack initiation and coalescence interaction

The number of crack initiation events (adding to the total number of cracks that made up the primary crack) and coalescence events (subtracting from the total number of cracks that made up the primary crack) for several samples are presented in Figure 5-20. A visual schematic representation to scale of the short crack initiation, growth and coalescence interaction can be seen in the crack evolution diagrams available on YouTube. A detailed description of initiation, short crack growth and coalescence activity for three samples based upon Figure 5-20 and Figure 5-21 is presented below.

Polished notch surface with sharper and deeper notch geometry of radius of 1.54 mm and depth of 3 mm at a constant amplitude strain range of 0.75 % (crack evolution diagram available at https://www.youtube.com/watch?v=uyD2Pd4gs5E);

- Crack initiation began around 20 % lifetime.
- No activity was seen between 20 % and 60 % lifetime where a second crack initiation event took place. One crack grew during this period.
- Two crack initiation events took place between 75 % to 80 % lifetime.
- Crack coalescence was first observed around 83 % lifetime.
- The lack of initiation activity resulted in one dominant primary crack. The primary crack produced a large area of crack shielding and relatively large plastic zone of heightened strain ahead of the crack tips, inducing crack initiations to form in the path of the primary crack.

- The propagation mechanism of the dominant primary crack predominantly featured encompassing smaller cracks that initiated ahead of the primary crack tips in the form of in-plane coalescence. The growth rate of the primary crack continued to increase until a full width crack was achieved.

Polished notch surface with notch radius of 2.25 mm and notch depth of 1.25 mm at a higher constant amplitude strain range of 1.18 % (crack evolution diagram available at https://www.youtube.com/watch?v=kE3UmSUmPzk);

- Crack initiation was first observed around 17 % lifetime.
- Crack initiation activity was most intense between 17 % and 32 % lifetime.
- Crack coalescence was first observed around 58 % lifetime.
- The most number of cracks that made up the primary crack (19) were observed at 55 % lifetime which was sustained until 65 % lifetime.
- Crack initiation activity decreased around 65 % lifetime.
- No initiation or coalescence activity was seen between 70 % and 80 % lifetime.
- The last initiation event was observed around 81 % where coalescence activity defined the remainder of short crack growth behaviour until a full width crack was achieved.

Shot peened notch surface with notch radius of 2.25 mm and notch depth of 1.25 mm at a constant amplitude strain range of 0.75 % (crack evolution diagram available at https://www.youtube.com/watch?v=2MS0NIYdje8);

- Crack coalescence was seen at 7 % lifetime.
- Crack initiation activity increased in intensity and was most intense at 14 % lifetime.
- The first coalescence event was observed at 21 % lifetime.
- The crack initiation activity intensity decreased until 40 % lifetime where initiation activity reduced. Two crack coalescence events were also seen at 40 % lifetime.
- Low initiation and coalescence activity was seen between 40 % and 80 % lifetime with two initiation and coalescence events. Short crack growth was particularly slow during this period
- Crack initiation activity increased between 81 % and 88 % lifetime when the last initiation event was observed; the maximum total number of cracks that made up the primary crack was 22 at approximately 86 % lifetime.
- Crack coalescence activity rapidly increased in intensity and took over short crack growth behaviour until a full width crack was achieved.

Initiation activity was typically observed earlier in lifetime and with a higher intensity for the shot peened surface condition. Subsequently, crack coalescence was also observed earlier. A period of inactivity was observed in shot peened samples lasting 40 % of lifetime where short crack growth was particularly slow. Whereas for the polished surface condition,

initiation and coalescence activity tended to be sustained throughout life once regular crack initiation activity began. A relatively atypical short crack growth propagation behaviour was seen for the sharper and deeper polished notch featuring a highly dominant main crack.

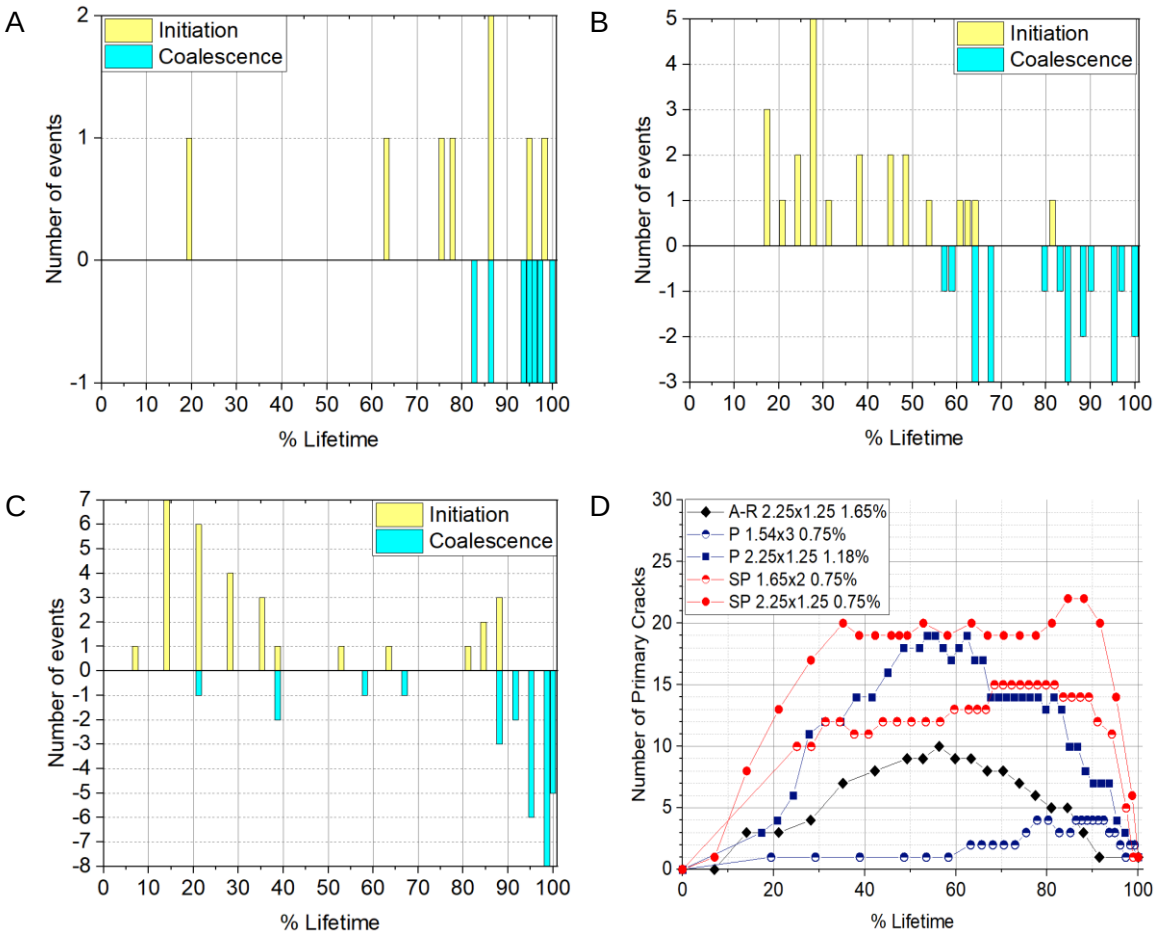

Figure 5-20 The number of initiation events in yellow (adding to the number of primary cracks) and coalescence events in blue (subtracting from the number of primary cracks) formed in between each replica for A) polished notch surface with notch radius of 1.54 mm and notch depth of 3 mm at a constant amplitude strain range of 0.75 %, B) polished notch surface with notch radius of 2.25 mm and notch depth of 1.25 mm at a constant amplitude strain range of 1.18 %, C) shot peened notch surface with notch radius of 2.25 mm and notch depth of 1.25 mm at a constant amplitude strain range of 0.75 %, D) the total number of cracks that made up the primary crack versus percentage lifetime for samples under constant amplitude loading conditions with different surface conditions, notch geometries and strain ranges.

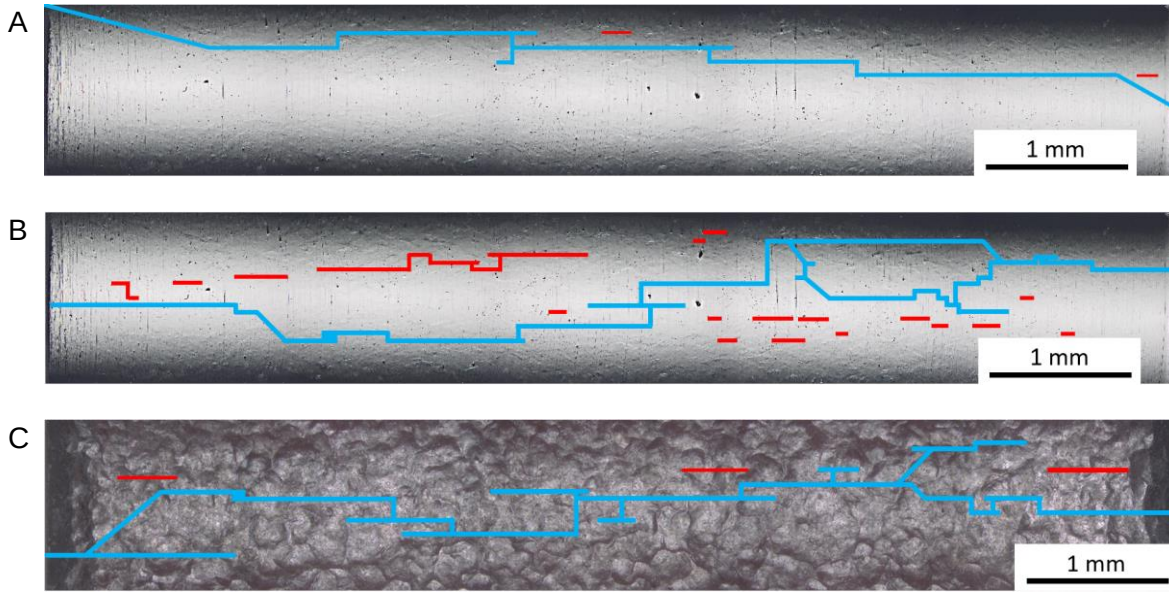

Figure 5-21 The final notch surface replica record from the crack evolution diagrams for A) polished notch surface with notch radius of 1.54 mm and notch depth of 3 mm at a constant amplitude strain range of 0.75 %, B) polished notch surface with notch radius of 2.25 mm and notch depth of 1.25 mm at a constant amplitude strain range of 1.18 %, C) shot peened notch surface with notch radius of 2.25 mm and notch depth of 1.25 mm at a constant amplitude strain range of 0.75 %.

5.3.4.5 Determination of the *a/c* ratio

Interrupted partial lifetime testing followed by a heat-tinting process was carried out on samples with polished and shot peened notch surface conditions. Semi-elliptical fatigue regions indicating short crack growth were identified on the fracture surfaces of the sample and the *a/c* ratio determined. The *a/c* ratios are presented in Figure 5-22 along with results from He et al [50] and *a/c* ratios based upon theoretical equilibrium ΔK values around the perimeter of the semi-ellipse [50, 51].

The *a/c* ratios for a polished notch surface were between 0.7 and 0.8. Longer crack lengths tended to have a slightly higher *a/c* ratio than theoretical equilibrium. The results from He et al [50] for a polished sample tended to be higher with *a/c* ratios of 0.95 or 1.15. The shot peened sample showed much more variation in *a/c* ratios than the polished surface condition. Four main clusters were observed with *a/c* ratios of 1.2, 0.8 - 0.9, 0.6 and 0.25 - 0.4. A similar clustering of *a/c* ratios was seen in He et al [50].

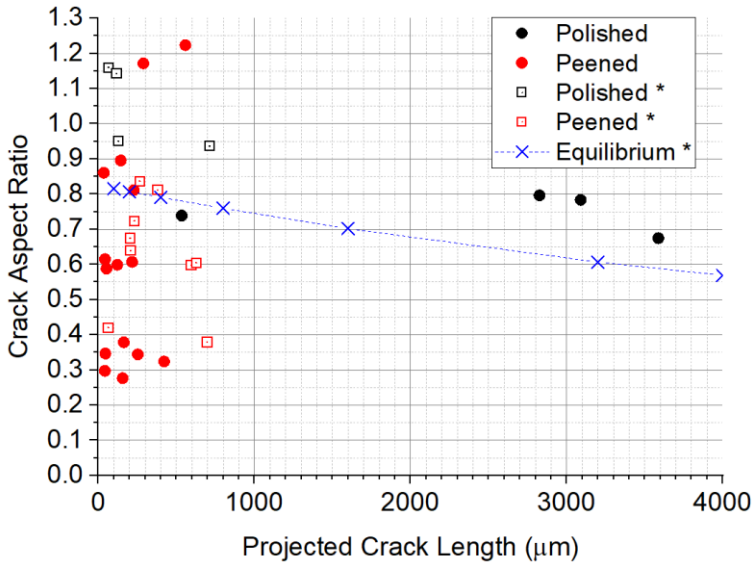

Figure 5-22 Crack aspect ratio (*a/c*) versus projected length of surface crack measured from semi-elliptical fatigue regions on the fracture surface. * Hollow symbols and the theoretical equilibrium aspect ratios (in blue) are taken from He et al [50] and [51].

5.4 Discussion

5.4.1 Notch surface characterisation

The surface roughness of U-notched samples from blade M08 and M09 were measured and compared with polished U-notch samples from blade M06 (from Chapter 4). The polished samples from blade M08 and M09 had a smoother surface and less variation in the surface roughness due to the extended polishing time which removed all corrosion pitting from the notch surfaces (Figure 5-23 A).

The shot peened U-notch sample made from FV566 had a lower surface roughness R_a when compared with FV448 [22, 50]. The difference in surface roughness is attributed to differences in the shot peening process such as small variations in shot size or velocity [180]. It was shown in Chapter 3.4.2 that FV566 has a higher hardness and larger yield strength than FV448, the heightened resistance to deformation could be a minor contributing factor to the lower R_a values observed.

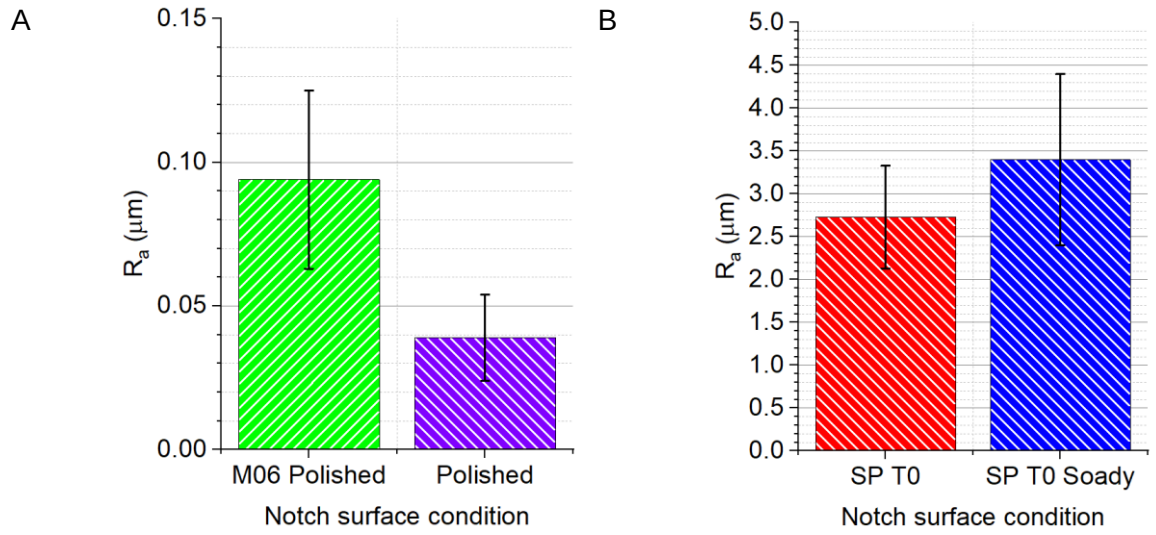

Figure 5-23 A) Surface roughness R_a for the polished notch surface condition from M06 blade material with residual corrosion pits (Chapter 4.3.2.1) compared with the 'fully' polished notch surface condition from blades M08 and M09. B) Surface roughness R_a for T0 shot peened notch surface condition from blades M08 and M09, compared with FV448 [22, 50].

5.4.2 Changing notch geometry on the notch field

The effect of changing the notch depth and radius on the distribution of stress range and strain range within the notch field was investigated using 3D FE modelling with elastic-plastic material behaviour. The typical distribution of stress within the notch field found in this study was similar to other research [86]. A 3D FE model was considered more accurate since a 2D model using plane stress or plane strain elements resulted in an overestimation of the distribution of stress and strain within the notch field (Figure 5-24) due to the assumption of an infinite width geometry. While the 3D model accounts for the finite width of the test samples, a 2D model would have resulted in similar conclusions with less computational effort and may be more representative of turbine blade geometry in industry.

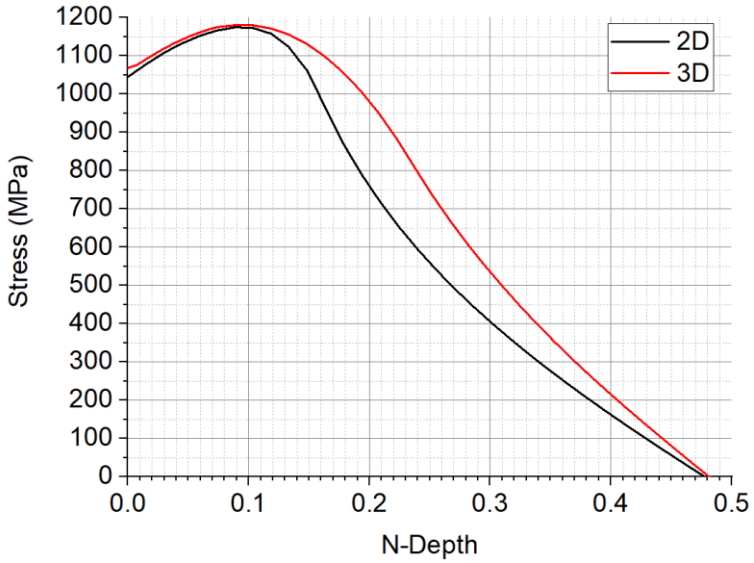

Figure 5-24 Stress versus normalised depth from the notch surface of a U-notched sample with notch radius of 2.25 mm and notch depth of 1.25 mm using 2D (with plane stress mesh elements) and 3D FE modelling methods.

Altering the notch geometry will also affect the stress and strain range at the notch surface for the majority of industrial components are likely subjected to constant load conditions. The strain range at the notch surface was kept constant (by adjusting the load accordingly) to isolate and better understand the effects of changing notch radius and depth on stress and strain range distribution within the notch field.

Altering the notch geometry changed the distribution of longitudinal stress, longitudinal strain and residual stress especially near the notch surface. Increasing the notch depth increased the stress range, strain range and residual stress within the notch field at all depths, especially at 0.15 – 0.2 normalised notch depth. Increasing the notch radius reduced the concentration of stress near the surface of the notch but increased the normalised depth range of the notch stress field. Increasing the strain range increased the magnitude and normalised depth range of the notch field. For the notch geometries chosen, changing notch depth is considered to be the least likely variable to affect fatigue behaviour, followed by changing notch radius. Depending on the sample/component geometry, changing the notch depth could have a more significant impact on the applied strain range experienced at the notch surface due to constant loading conditions which has the largest influence on the notch field and fatigue life.

5.4.3 Shot peening and residual stress

The XRD results from T0 shot peening on the U-notch surface suggested a higher compressive residual stress was achieved in the longitudinal measurement direction than in the transverse direction. The measurement angle of ± 45°, applied to the transverse direction, was limited to ± 30° in the longitudinal direction due to shadowing effects from the

notch geometry. The limited angle range also reduced the d-spacing range (Figure 5-25 A and B), that may have resulted in a seemingly reduced compressive residual stress. XRD was carried out on the same sample on a flat shot peened surface allowed a full 45° measurement range in both directions. The residual stress profiles in both the longitudinal and transverse direction were similar, suggesting that material anisotropy of the material has a minimal impact on compressive residual stress from shot peening.

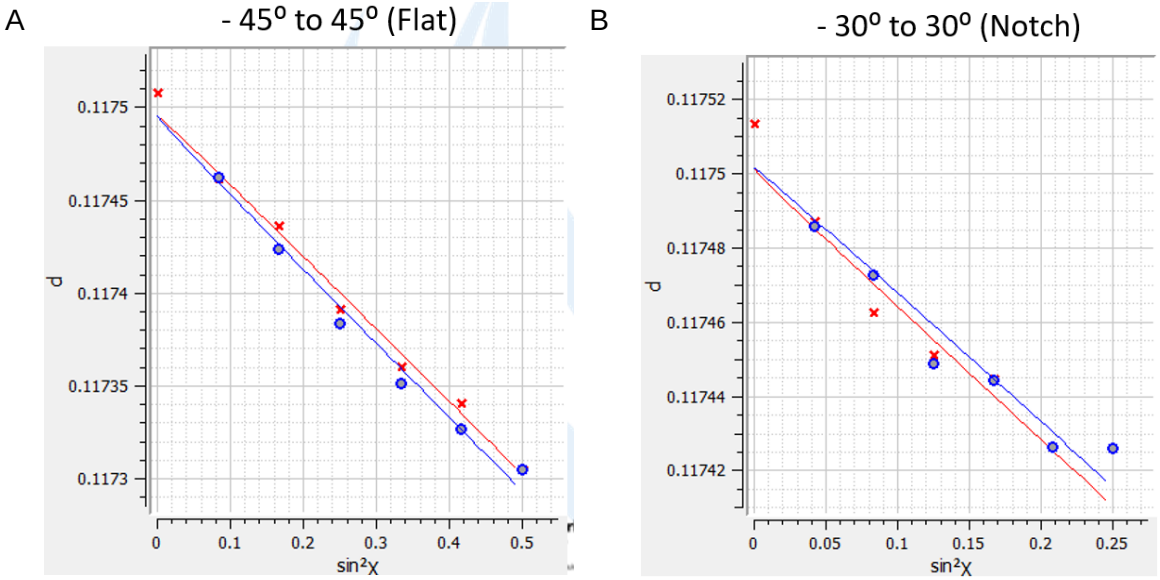

Figure 5-25 A) d-spacing versus $\sin^2\chi$ on the surface of a T0 shot peened U-notch in the transverse direction with a detectable range of ± 45°, B)) d-spacing versus $\sin^2\chi$ on the surface of a T0 shot peened U-notch in the longitudinal direction with a detectable range of ± 30° due to notch geometry shadowing effects.

The compressive residual stress from a similar T0 shot peened U-notch surface with identical dimensions was obtained via XRD in FV448 material [126]. Accounting for the presumed conservative residual stress result in the longitudinal direction for FV566, comparing FV566 with FV448 suggests a larger compressive residual stress in FV448 despite the reduced material strength properties observed in Chapter 3.4.2. Surface roughness testing showed that a harsher T0 shot peening process may have been applied to the U-notch surface of the FV448 material which may result in a larger compressive residual stress observed overall [181, 182].

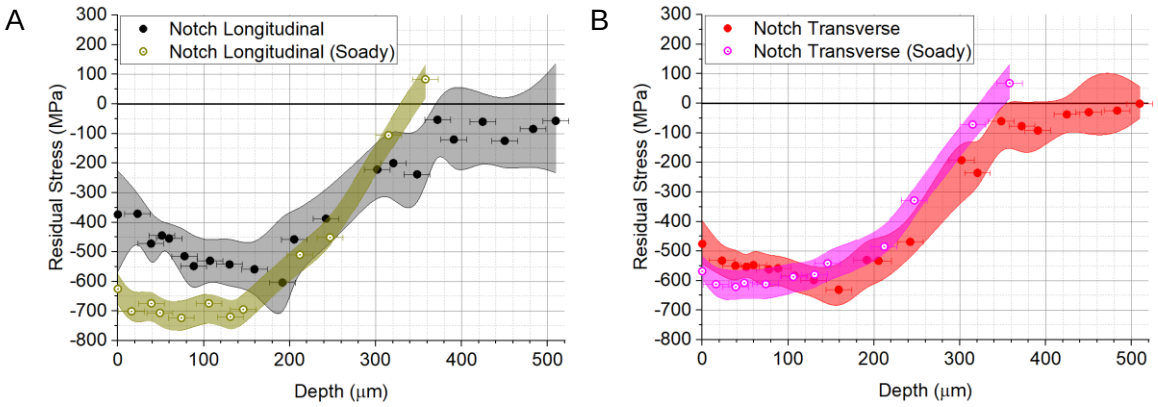

Figure 5-26 Longitudinal residual stress versus depth from the notch surface after T0 shot peening for FV566 compared with FV448 [126] in the A) longitudinal direction and B) transverse direction.

5.4.4 Shot peening and notch geometry on crack initiation behaviour

Increasing the strain range at the notch surface increased the number of crack initiation events regardless of surface condition or notch geometry. The effect of changing the notch radius or depth on number of crack initiation events could not be determined due to intervening variables such as differences in material, notch geometry and surface conditions. An as-received notch surface typically had a low number of crack initiation events, as discussed in Chapter 4.3.2.2. The shot peened notch surface typically had more crack initiation events than a polished or as-received notch surface, especially at lower strain ranges.

The number of crack initiation events observed on a shot peened U-notch surface for FV448 with applied strain ranges between 0.6 % and 0.9 % was similar to polished samples made from FV566. However, the number of initiation events in shot peened samples made from FV566 almost doubled for the same strain range. The number of crack initiation events was found for FV448 by backtracking replica records. By contrast, an optometry surface profiling microscope was used (described in Chapter 4.2.3) to identify ratchet marks on the fracture surface and estimate the number of initiation events in all samples for consistency. The shot peening process induced the formation of pre-existing cracks and laps on the notch surface before cyclic testing was carried out (Figure 5-27), a feature seen in similar shot peened steels [72, 183, 184] leading to more tortuous short crack growth [5]. Estimating number of crack initiations by identifying ratchet marks is therefore likely to be overestimated due to the more tortuous characteristic of short crack growth in a shot peened sample.

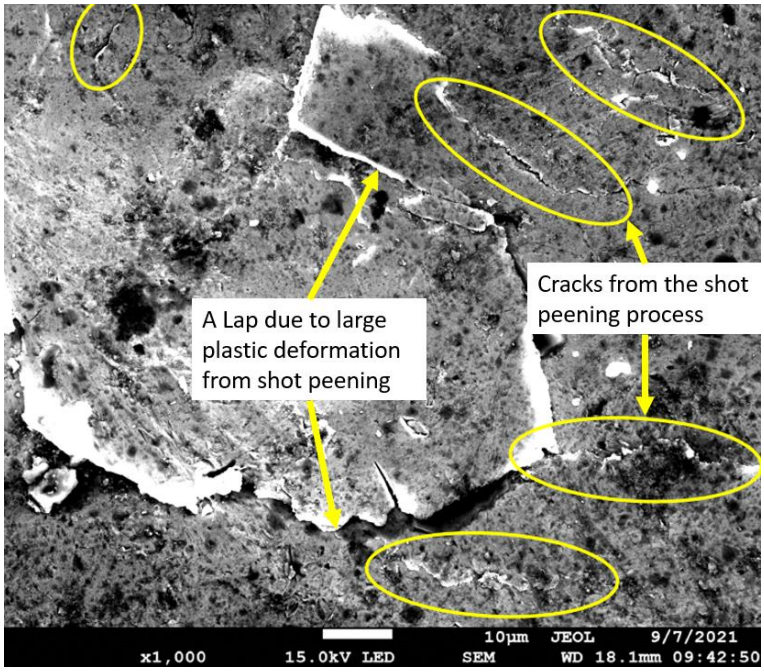

Figure 5-27 SEI image of pre-existing cracks of length 20 – 50 µm and a lap (material that has folded over itself due to large plastic deformation) on the T0 shot peened surface prior to cyclic testing.

5.4.5 Shot peening and notch geometry on short crack growth behaviour

Increasing notch depth and decreasing notch radius at the notch surface with constant applied strain range was found to slightly impact the distribution of stress range, strain range and residual stress within the notch field. Despite this, interrupted lifetime testing revealed that changing notch geometry (from 2.25 mm radius and 1.25 mm depth to 1.5 mm radius and 3 mm depth) did not significantly affect the short crack growth rate versus $\Delta K_{Surface}$ relationship based upon LEFM assumptions. For the notch geometries and applied strain ranges tested, changing the notch geometry has a minimal effect on short crack growth behaviour.

T0 shot peening produced a compressive residual stress field up to 350 µm beneath the notch surface. In Chapter 4 it was found that the compressive residual stress induced from a periodic tensile overload results in a retardation of the short crack growth rate. Similarly, the compressive residual stress from shot peening alters the mean stress via superposition of internal and external stresses resulting in retardation of short crack growth. This effect from cold working surface modification is well documented [5, 49-51, 72, 185, 186]. Initially, the crack growth rate was slower with increasing $\Delta K_{Surface}$ values until 20 MPam$^{0.5}$. Early crack coalescence behaviour led to several cracks with low *a/c* ratios. These cracks will display a preference to grow deeper until an equilibrium *a/c* ratio is achieved. Furthermore, the presence of the compressive residual stress retards short crack growth, making surface cracks appear to grow relatively slowly. This apparent period of slow crack growth was

observed as suppressed crack initiation and coalescence activity lasting approximately 40 % - 80 % lifetime was observed on shot peened U-notch samples that was not typically observed on polished U-notch samples (Figure 5-20 C and D). As the *a/c* ratio approaches equilibrium and grows past the compressive residual stress field, the short crack growth rate increased rapidly, approaching non-peened short crack growth rates at large ΔK values.

The out-of-plane distance between twenty random initiation locations on all samples were chosen. Decreasing the notch radius did not affect the out-of-plane variance observed as expected only marginally decreasing the out-of-plane variance by less than 6 %. This result was surprising since an independent study using FE modelling to extract the strain range across the central 'Notch Profile' (Figure 5-6) showed that reducing notch radius from 2.25 mm to 1.5 mm was estimated to result in a 45 % reduction in the out-of-plane variance (Figure 5-28). It may be anticipated that a smaller out-of-plane variance due to a sharper notch may lead to a reduction in crack shielding effects and reduce the number of cycles necessary to complete the crack coalescence phase of fatigue life and consequently possible overall fatigue life. The surface of a notch with 2.25 mm radius can be uniformly polished with standard equipment. However, a smaller notch radius introduced equipment limitations which hindered polishing quality. The increased surface roughness likely induced crack initiation further from the centre of the notch surface, increasing the out-of-plane distance.

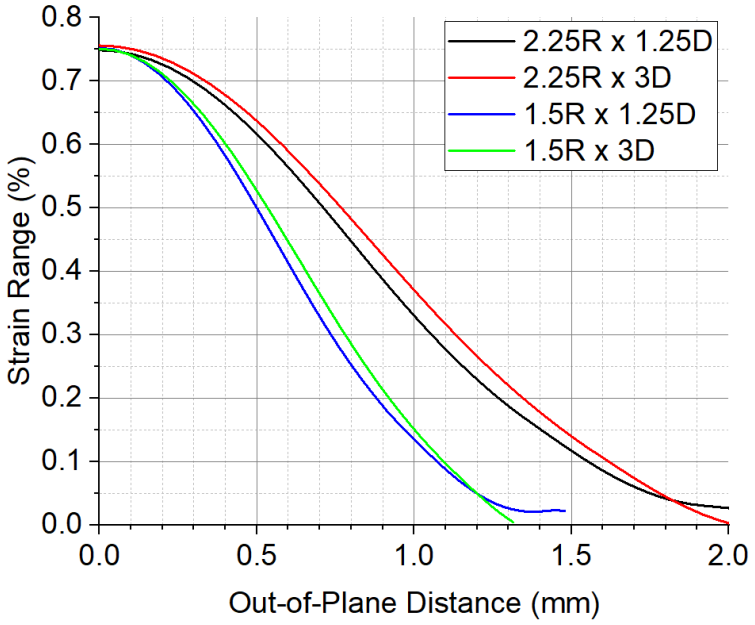

Figure 5-28 Strain range versus out-of-plane distance obtained from FE modelling for various notch geometries where R is the notch radius in mm and D is the notch depth in mm.

5.4.6 Short crack fatigue behaviour

In Chapter 4.3.2.4, a compressive residual stress from an overload cycle was found to increase the number of cycles to crack initiation, it may then be expected that a compressive residual stress from shot peening would hinder crack initiation. Figure 5-17 C) appears to show a relatively high number of initiations initially occurring at 25 % lifetime for a shot peened U-notch sample. However, the earliest replica record available was taken at 25 % lifetime when crack initiation activity was already somewhat developed. Crack initiation activity was typically observed within the first 15 % lifetime of shot peened U-notched samples, earlier than polished U-notch surface conditions. Shot peening increased the roughness of the notch surface resulting in a high density of localised stress concentrations which promoted the growth of pre-existing cracks (induced by the shot peening process, Figure 5-27) early in the fatigue lifetime.

It was observed in Figure 5-22 that low *a/c* ratios were typical of shot peened surface conditions for small crack lengths below 500 µm projected surface length. This was due to many crack initiation events and particularly early crack initiation activity between densely packed pre-existing cracks.

The fracture surfaces of polished U-notch samples made from FV448 contained semi-elliptical crack shapes with higher than expected *a/c* ratios based upon a theoretical equilibrium shape predicted under bending conditions. This higher *a/c* ratio is attributed to the presence of elongated stringers running into the specimen depth, initiating a deeper crack [50]. Such stringers did not appear to impact *a/c* ratios in a similar way for U-notch samples made from FV566, partly linked to a lower occurrence of stringers and less alignment of any stringers that were present compared to the FV448. The *a/c* ratios for both polished and shot peened samples without the influence of coalescence were found to be in agreement with theoretical equilibrium predicted values (Figure 5-29 A).

Crack coalescence immediately increases the surface length of the crack. However, the depth calculated by the area of the semi-ellipse does not experience such an immediate transformation, typically leading to a reduction in *a/c* ratio. In some instances, a coalesced crack that is allowed to develop unhindered will regain an a/c ratio based upon theoretical equilibrium such as in Figure 5-29 B). In this instance, the *a/c* ratio can be approximated for both initial cracks since they can be individually isolated but tended to be overestimated based upon the expected theoretical equilibrium ratios. The shot peening process induced early crack coalescence events, leading to long surface cracks with particularly low *a/c* ratios (Figure 5-29 C). Typically, multiple crack coalescence events occurred and formed atypical semi-elliptical fatigue region shapes that did not allow isolation of single cracks.

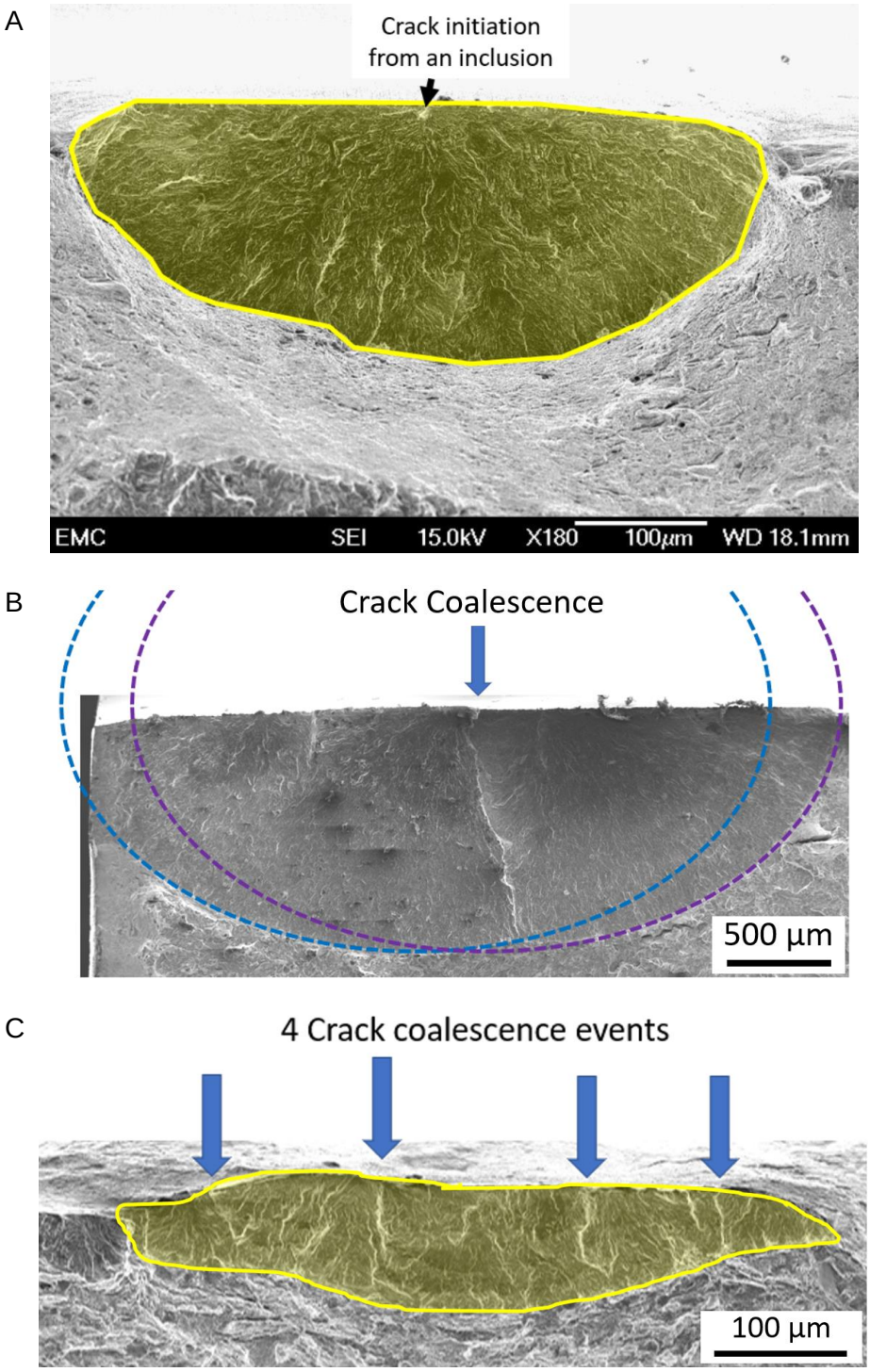

Figure 5-29 A) A semi-elliptical fatigue region (in yellow) on the fracture surface with *a/c* ratio of 0.74 that has initiated from an inclusion likely composed of MnS from a polished notch sample. B) Two semi-elliptical cracks that have coalesced and allowed to develop. Both cracks that comprise the coalesced crack can be isolated. C) Four semi-elliptical cracks that have coalesced on a shot peened U-notch sample, forming a non-equilibrium prediction shaped, very shallow semi-elliptical fatigue region. The *a/c* ratio is approximately 0.3, due to multiple early crack coalescence events from closely packed pre-existing cracks induced by the shot peening process.

5.5 Summary and Conclusions

XRD was carried out to measure compressive residual stress profiles induced by the T0 shot peening process which were typical of T0 shot peened samples made from FV448. The residual stress measured in the longitudinal direction on the notched surface was underestimated due to limitations in measurement angle range due to the notch geometry. Such measurement limitations were eliminated on a flat surface which showed similarity between the longitudinal and transverse directions.

The number of initiation events for the primary crack increased with increasing strain range regardless of surface condition or notch geometry. The effect of changing notch radius or depth on number of crack initiations could not be isolated due to additional intervening variables. Shot peening the notch surface tended to induce more crack initiation events especially for lower strain ranges tested. Shot peening also increased the tortuosity of the surface crack leading to a potential overestimation of the number of initiation events from ratchet marks identified using optometry surface profiling of the fracture surface.

FE modelling was used to investigate the effect of changing notch radius and notch depth on the distribution of stress range, strain range and residual stress after unloading within the notch field. It was found that changing the notch depth and notch radius for the geometries tested did not significantly impact the distribution of stress, strain or residual stress within the notch field and did not affect short crack growth behaviour. Depending upon sample geometry and loading conditions, changing the notch depth may influence the applied strain range, which had the largest effect on stress, strain and residual stress within the notch field.

Changing the notch geometry had a minimal effect on the short crack growth rate dc/dN versus $\Delta K_{Surface}$ based upon LEFM assumptions. On the other hand, the compressive residual stress induced by shot peening considerably retarded the surface crack growth rate by up to 10 times compared to a polished sample. The crack growth rate rapidly increased towards non-peened levels once the short crack had grown through the region of compressive residual stress. This retardation in short crack growth resulted in a characteristically long period of relatively low initiation and coalescence activity between 40 % and 80 % lifetime in shot peened samples.

The out-of-plane variance for twenty random locations representing initiation events along the fracture surface near the notch surface was calculated for all samples. A 6 % reduction in out-of-plane variance was found when a notch radius of 2.25 mm was compared with a sharper notch radius of 1.5 mm, which was less than the expected 45 % reduction in out-of-plane variance based upon a preliminary FE modelling study. Limitations in sample

preparation procedures leading to non-uniform roughness on the notch surface may account for this unexpected result.

The *a/c* ratios were determined from semi-elliptical short crack fatigue regions on the fracture surfaces of polished and shot peened samples. Semi-elliptical fatigue regions on polished U-notch samples typically suggested *a/c* ratios in agreement with theoretical equilibrium predictions. The equilibrium shape predictions are based on K-calculations for semi-elliptic cracks of different sizes at the maximum depth and surface positions under bending conditions being equivalent. Shot peening altered the condition of the notch surface and induced a compressive residual stress that had a clear impact on *a/c* ratios. A high number of crack initiation events initiating from pre-existing cracks led to early multiple crack coalescence events. Additionally, the compressive residual stress induced from shot peening retarded crack growth in the depth direction resulting in atypical shallow semi-elliptical shapes with relatively low *a/c* ratios as was also observed in FV448 material [50].

Chapter 6: Adopting a mitigation strategy for fatigue life extension and lifetime prediction

6.1 Introduction

In Chapter 1.3.1, it was discussed that cracks were observed via non-destructive testing in the fir-tree-root-fillets of in-service low-pressure turbine blades during routine inspection. The current recommendation to industry includes replacement of damaged turbine blades that contain cracks at considerable cost due to the serious safety risk in the event of catastrophic failure. An alternative repair approach has been proposed known in this study as the 'lifetime extension strategy', that involves grinding out existing cracks from fir-tree-root-fillets followed by shot peening, in an attempt to extend the operational service life of low-pressure steam turbine blades. This repair strategy effectively regresses the fatigue process resulting in additional cycles to progress the fatigue process to the pre-repaired stage. Furthermore, shot peening the notched surface induces further resistance to fatigue [50]. However, changing the notch geometry will likely increase the strain range applied at the notch surface which is considered detrimental to fatigue. This complex interaction of counterbalancing factors has been investigated experimentally.

A similar lifetime extension strategy, known as the 'blend-polish-peen repair' strategy was carried out on FV448 material by He [5]. A shot peened U-notch sample was cyclically loaded with R-ratio of 0.1 under constant amplitude loading conditions with a strain range of 0.68 % at the notch surface until surface cracks of 1.2 – 1.5 mm were observed. The cracks were ground away using industry representative methods. Although the aim was to remove all cracks, residual cracks with low *a/c* ratios were observed on the notch surface after the grinding process was carried out. The notch surface with pre-existing cracks was re-peened and subjected to constant amplitude cyclic loading with the same strain range of 0.68 % at the notch surface. The number of cycles to fatigue indicated that the blend-polish-peen repair strategy offered no improvement in the fatigue life. Residual cracks after a grinding process may be representative of a possible outcome in an industrial environment. However, complete removal of residual cracks could be consistently achieved in industry via a surface replication examination approach and may result in a further increase in operational service life of in-service turbine blades.

The longitudinal tensile strain range at the notch surface was kept constant throughout testing which is not considered representative of real-life conditions. It is necessary to consider an expected increase in the strain range at the notch surface for appropriate

industrial application of the lifetime extension strategy. The Coffin-Manson [133-135] relation adequately represents the relationship between strain range and total lifetime in the LCF regime [187]. However, this total life approach is unable to predict the number of cycles to a specific period during the fatigue lifecycle, such as when a short crack has grown a specific length. To predict this, damage tolerant lifing approaches must be utilized.

The fatigue lifecycle process in U-notch samples can be split into four phases [26]:

1. The number of cycles to crack initiation
2. The number of cycles for short crack growth
3. The number of cycles for crack coalescence of short cracks until the crack has grown the full width of the sample
4. The number of cycles for long crack growth to failure.

Surface replication from interrupted fatigue tests of U-notched samples have been obtained for various geometries, surface and loading conditions. This data can be used to estimate number of cycles to crack initiation (Chapter 6.4.4.1), and the Paris–law [150] constants can be determined from crack growth rate versus $\Delta K_{Surface}$ data (Chapter 6.4.4.2) which can be used to estimate the number of cycles to complete the short crack phase. Similarly, the Paris-law can also be used to estimate the number of cycles for the final long crack phase (Chapter 6.4.4.4).

Separating the fatigue lifecycle into four distinct phases allows an investigation into how the notch geometry, surface conditions and loading conditions impact each phase of the lifecycle. Additionally, a partial-life prediction can be made such as the number of cycles to 1 mm short crack growth, necessary for the lifetime prediction of U-notched samples subjected to the proposed lifetime extension strategy. So far, the effect of various surface and loading conditions on the fatigue behaviour of U-notched sample has been investigated. In this chapter the effect of the various surface and loading conditions on the total fatigue life and number of cycles for each lifecycle phase will be investigated, along with their contribution towards a prediction model for U-notch samples subjected to a lifetime extension strategy.

It was discussed in Chapter 1.3.1 that in-service turbine blades were subjected to a 10 % over-speed test per year (equivalent to single periodic overloads with OLR of 1.11 applied every 150 baseload cycles). Single periodic overload cycles are known to increase the fatigue life in stainless steel materials, where the increase in fatigue life is generally attributed to compressive residual stress ahead of the crack tip and closure effects (Chapter 2.2.4). In Chapter 4.4.4, it was argued that a compressive residual stress was induced by the overload cycles within the notch field that hindered crack initiation, possibly due to

increased resistance to persistent slip band formation, a result also found by Zheng et al [188]. It was also found that overloads with OLR of 1.11 were below a threshold value of OLR between 1.44 and 1.55 [90, 105], and subsequently no retardation effect was seen in the short crack growth rate (compared to constant amplitude loading conditions at the baseload strain range). A small overload with OLR of 1.11 (equivalent to a 10 % over-speed test) is therefore not expected to significantly impact fatigue behaviour or life after shot peening.

The Palmgren-Miner rule is commonly used to predict the total fatigue lifetime of components subjected to variable amplitude loading conditions such as single periodic tensile overloads. The Palmgren-Miner rule is a damage accumulation model which predicts that each cycle inflicts fatigue damage that is linearly proportional to the magnitude of the applied load. It then follows that the Palmgren-Miner rule predicts a reduction in the fatigue life of components subjected to overload cycles greater than the baseload cycles [142]. This has been shown to be an over-conservative approach to lifetime prediction, especially in the low cycle fatigue regime, in some cases by a factor of twenty [143]. The Palmgren-Miner rule does not consider strain hardening and residual stresses induced from the overload cycles that are known to increase fatigue life. Despite this, the Palmgren-Miner rule is the preferred lifetime prediction method for components with variable amplitude loading conditions in industry, due to the lack of an equally simple and practical alternative [143].

The characteristic fatigue lifetime extension from shot peening has been investigated in detail by numerous authors. The compressive residual stress and strain hardening induced by the shot peening process acts as a significant barrier to short crack initiation and growth [50], which outweighs the increase in surface roughness that is known to reduce fatigue life [179]. The lifetime extension from shot peening is known to diminish with increasing strain range, especially in the low cycle fatigue regime, where large plastic deformation causes residual stress relaxation effects.

A single periodic fully reversed overload with a magnitude of 0.6 % maximum tensile strain and -0.6 % maximum compressive strain was applied at N = 1000 cycles followed by constant amplitude to failure (of ± 0.3 % maximum and minimum strain) to a T1 shot peened cylindrical specimen made from normalized steel material. The results suggested significant relaxation the compressive residual stress from T1 shot peening and reduced the lifetime of samples by up to 60 % compared with constant amplitude loading [130]. The compressive loading from the fully reversed loading condition is expected to increase the effects of residual stress relaxation. It is anticipated then that some residual stress relaxation may be expected from single periodic tensile overloads with OLR of 1.56 every 150 cycles that may affect the total life.

B.M.D. Cunningham

The work in this chapter aims to investigate the effects of notch geometry, surface conditions and loading conditions on the total fatigue lifetime and the number of cycles for each phase of the fatigue lifecycle for U-notch samples made from FV566. The development of a lifetime prediction model capable of accounting for a lifetime extension strategy utilizing both total life and damage tolerant approaches, will be compared with experimental testing of U-notch samples subjected to a lifetime extension strategy. The lifetime prediction model will be used to explore the efficacy of the lifetime extension strategy as a maintenance procedure for in-service turbine blades with minor overloads.

Some of the work presented in this chapter has been published in the following paper [153] and is presented here with additional analysis of published data:

B. M. D. Cunningham, A. Evangelou, C. You, A. Morris, J. Wise P. A. S. Reed, A. Hamilton *'Fatigue crack initiation and growth behaviour in a notch with periodic overloads in the low-cycle fatigue regime of FV566 ex-service steam turbine blade material'*. Fatigue Fract Eng Mater Struct. 2021. https://doi.org/10.1111/ffe.13617

6.2 Experimental Methodology

Details regarding material extraction in the form of plain bend bars of FV566 from ex-service low pressure turbine blade root fixings (LD 66) is available in Chapter 3.2.1.

6.2.1 Sample preparation

Plain bend bars from blade M08 made from FV566 had a typical U-notch with industry relevant dimensions (2.25 mm radius and 1.25 mm deep) machined into the centre of the samples for short crack testing as previously described in Chapter 4.2.2.1. The notch surfaces of all U-notch samples were 'fully' polished to an approximate R_a of 0.039 µm with a rotary tool using 9 µm polishing suspension until all corrosion pits were completely removed (Figure 5-11 A).

6.2.2 Interrupted partial lifetime testing

Interrupted partial lifetime fatigue testing was carried out under 3-point bend constant amplitude cyclic loading conditions on all U-notched samples using an Instron TM ElectroPulse E10000 electromechanical fatigue testing machine. All tests were carried out at room temperature using a sinusoidal waveform at a frequency of 10 Hz and with R-ratio of 0.1. Single tensile periodic overloads with OLR of 1.56 (Equation 4-1) were applied every 150 baseload cycles with a slower frequency of 1 Hz for one test. The surface replication

Chapter 6: Adopting a mitigation strategy for fatigue life extension and lifetime prediction method discussed in Chapter 4.2.2.4 was used to monitor the short crack growth. The test was finished once a short crack with a projected surface length of 1 mm was observed.

6.2.3 Application of the lifetime extension strategy

The cracks formed during interrupted partial lifetime testing were ground away using a rotary power tool and carbide mounted tip with a diameter of 3 mm (available from PTEFD) and lubricant (WD 40). A second notch was formed inside the original notch with total notch depth of 2 mm (Figure 6-1 A) or 3 mm (Figure 6-1 B). The top surface including the notch surface was subjected to a T0 industrial standard shot peen (MI230R 200% 13A) by Sandwell UK Ltd as in Chapter 5.2.2.1 with an approximate R_a of 2.7 µm (Figure 5-11 B). The depth and radius of the notch geometries were measured and displayed in Figure 5-10 using optical microscopy and image processing software (Image J).

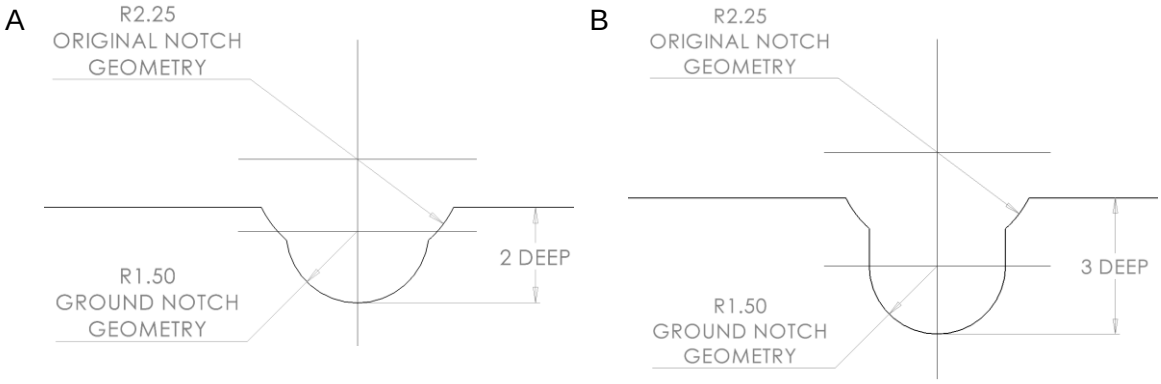

Figure 6-1 Schematic showing the profile of a notch after the lifetime extension strategy has been applied to a typical notch geometry at a total depth of A) 2 mm and B) 3 mm.

The ‘repaired’ samples were subjected to interrupted lifetime testing under the same conditions as in Chapter 6.2.2 until failure and the number of cycles recorded. The nominal local strain range condition in the notch was kept the same for both the first round of fatigue testing (before the lifetime extension strategy) and the second round of fatigue testing (after the lifetime extension strategy) by reducing the load range (calculated using FE modelling).

6.3 Results

6.3.1 Short crack growth behaviour

The short crack growth rate versus $\Delta K_{Surface}$ for two U-notched samples with and without a tensile periodic overload with OLR of 1.56 applied every 150 baseload cycles were compared. Both notch surfaces were T0 shot peened and were subjected to a constant amplitude strain range of 0.75% at the notch surface (Figure 6-2 A) but had different notch geometries. The overload appears to initially retard the growth rate of cracks below $\Delta K_{Surface}$ of 10 MPam$^{0.5}$. Under constant amplitude loading, the compressive residual stress from shot peening appears to decrease the crack growth rate of cracks below $\Delta K_{Surface}$ of 20 MPam$^{0.5}$ as previously discussed in Chapter 5.3.4.2. Conversely, the application of single periodic overload cycles increased the crack growth rate of cracks below $\Delta K_{Surface}$ of 20 MPam$^{0.5}$ at a much slower rate than a non-shot-peened notch surface condition. The crack growth rate of cracks above a $\Delta K_{Surface}$ of 20 MPam$^{0.5}$ increased significantly for both constant amplitude and overload loading conditions. A greater range in the crack growth rate of cracks between $\Delta K_{Surface}$ of 10 and 25 MPam$^{0.5}$ (represented as the shaded green area) was observed. The average crack growth rate for cracks above a $\Delta K_{Surface}$ of 25 MPam$^{0.5}$ was consistently slower when the single tensile periodic overload cycles were applied. Despite these observations, the retarded crack growth rate of shot peened samples due to the compressive residual stress is minimally impacted by the overload cycles. In Figure 6-2 B, samples with single periodic overloads with OLR of 1.56 every 150 baseload cycles with polished and shot peened notch surface conditions are compared with constant amplitude loading. The average crack growth rate for a shot peened sample with (and without) single periodic overloads considerably retards the short crack growth rate more than single periodic overload cycles alone, especially for higher $\Delta K_{Surface}$ values.

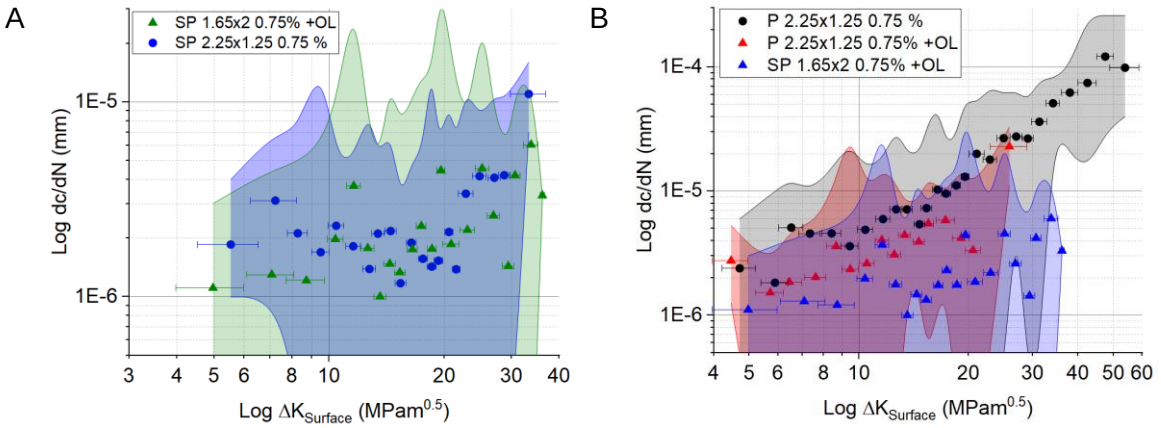

Figure 6-2 Short crack growth rate versus $\Delta K_{Surface}$ for U-notch samples under a baseload strain range of 0.75 % for A) shot peened (SP) notch surface of different notch geometries under constant amplitude and with single periodic overloads (OL) with OLR of 1.56 every 150 baseload cycles, B) polished (P) notch surface under constant amplitude loading, polished notch surface with single periodic overloads every 150 baseload cycles and shot peened notch surface with a different notch geometry and single periodic overloads every 150 baseload cycles.

6.3.2 Short crack initiation and coalescence interaction

The number of crack initiation events and coalescence events (for the primary crack only) for two samples that were subjected to the lifetime extension strategy are presented in Figure 6-3. A visual schematic representation of crack initiation, short crack growth and crack coalescence interaction can be seen in the crack evolution diagrams available on YouTube, as detailed below. A detailed description of the crack initiation, short crack growth and crack coalescence activity for the two U-notched samples subjected to a lifetime extension strategy are presented below (Figure 6-3 and Figure 6-4).

A polished typical notch geometry (notch radius of 2.25 mm and a notch depth of 1.25 mm) was subjected to constant amplitude cyclic loading with a strain range of 0.75 % on the notch surface. Once a surface crack with a projected length of 1 mm crack was observed the lifetime extension strategy was applied. The second phase of fatigue testing was carried out on a shot peened notch surface with notch radius of 1.65 mm and a notch depth of 2 mm with identical loading conditions. The crack evolution diagram is available at https://www.youtube.com/watch?v=W1DT7y4YVPA. The following landmark events are described below:

- Crack initiation on the polished notch surface began around 20 % lifetime.

- Crack initiation activity was low with 1 or 2 cracks initiating in between each replica; a surface crack with a projected length of approximately 1 mm was observed at 35 % lifetime.
- A lifetime extension strategy was applied, removing all surface cracks, followed by T0 shot peening on the notch surface and corresponding top surface of the sample.
- Crack initiation activity on the shot peened notch surface was first observed around 50 % lifetime (the first replica record available).
- The first crack coalescence event was observed around 55 % lifetime.
- Crack initiation activity reduced in intensity followed by three crack coalescence events until 60 % lifetime.
- Low initiation activity was seen with 4 initiation events occurring between 60 % and 90 % lifetime. Short crack growth was particularly slow during this period.
- The maximum number of cracks that made up the primary crack was 15 between 68 % and 82 % lifetime.
- Crack coalescence activity increased at 82 % lifetime and took over short crack behaviour until a full width crack was observed.

A polished typical notch geometry (notch radius of 2.25 mm and a notch depth of 1.25 mm) was subjected to single tensile periodic overloads with OLR of 1.56 every 150 baseload cycles with a strain range of 0.75 % at the notch surface. Once a surface crack with a projected length of 1 mm crack was observed the lifetime extension strategy was applied. The second phase of testing was carried out on a shot peened notch surface with notch radius of 1.65 mm and notch depth of 2 mm with identical loading conditions. The crack evolution diagram is available at https://www.youtube.com/watch?v=71VQmezhdHg. The following landmark events are described below:

- Six crack initiations on the polished notch surface were observed around 13 % lifetime (first available replica).
- Crack coalescence was first seen relatively early around 22 % lifetime.
- Crack initiation activity increased substantially around 30 % lifetime.
- Crack coalescence activity subsequently increased from 35 % to 38 % lifetime. A surface crack with projected length of 1 mm was observed around 38 % lifetime.
- A lifetime extension strategy was applied, removing all surface cracks, followed by T0 shot peening on the notch surface and corresponding top surface of the sample.
- Crack initiation activity on the shot peened notch surface was first observed around 49 % lifetime.
- Crack initiation activity increased with a similar intensity observed on the polished notch surface between 55 % and 60 % lifetime.

- Crack initiation activity reduced in intensity from 60 % to 75 % lifetime.
- Crack coalescence activity was high between 70 % and 75 % lifetime.
- A period of low activity dominated by coalescence behaviour was seen between 75 % and 85 % lifetime.
- Low initiation activity with increased coalescence activity was seen between 85 % and 95 % lifetime.
- Coalescence activity substantially increased around 95 % to 98 % where the primary crack grew the full width of the sample.

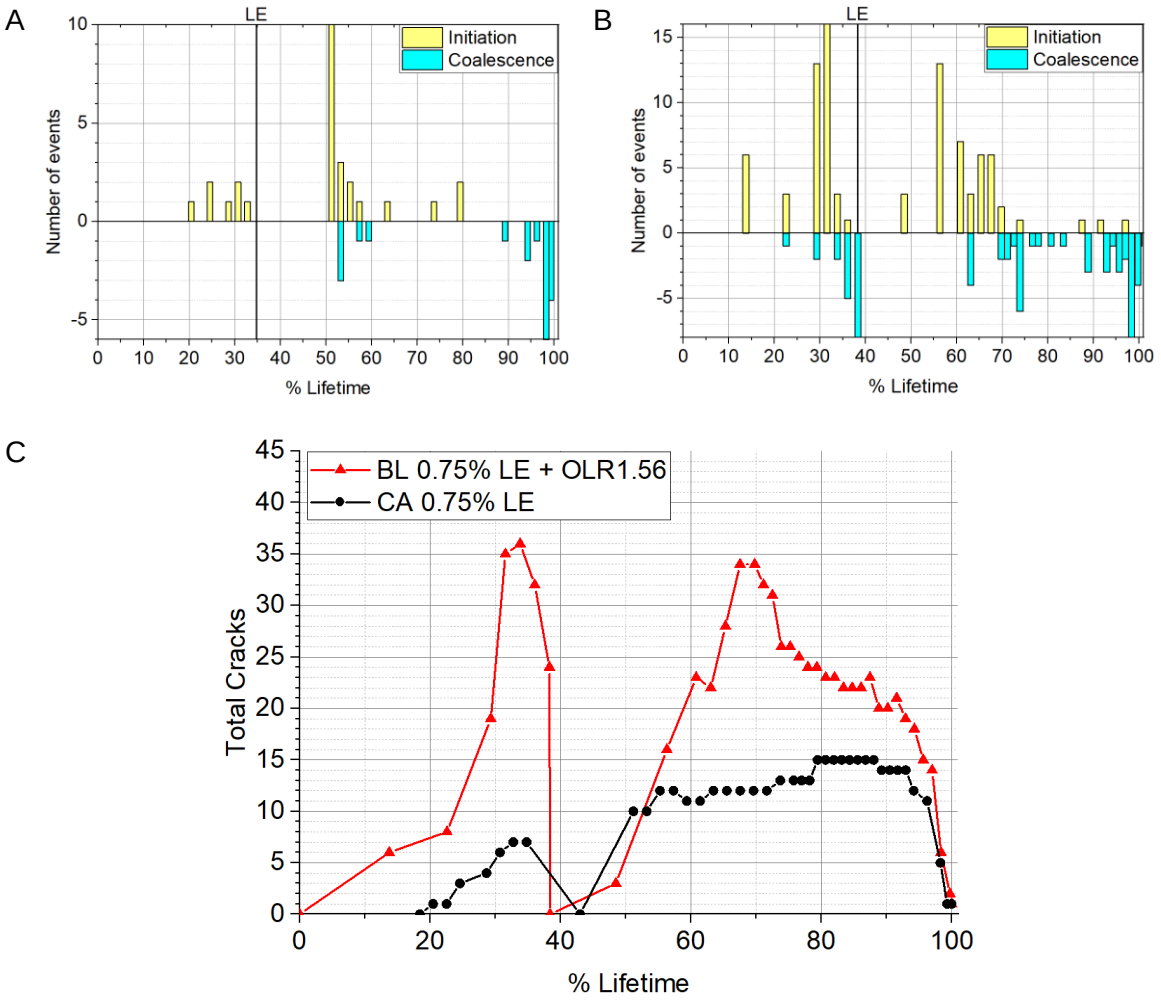

Figure 6-3 The number of initiation events in yellow (adding to the number of primary cracks) and coalescence events in blue (subtracting from the number of primary cracks) formed in between each replica for A) a sample subjected to the lifetime extension strategy (LE) under constant amplitude loading and B) a sample subjected to the same lifetime extension strategy with single periodic tensile overloads (OL) with OLR of 1.56 applied every 150 baseload (BL) cycles. C) The total number of cracks that made up the primary crack versus percentage lifetime for both samples subjected to the lifetime extension strategy.

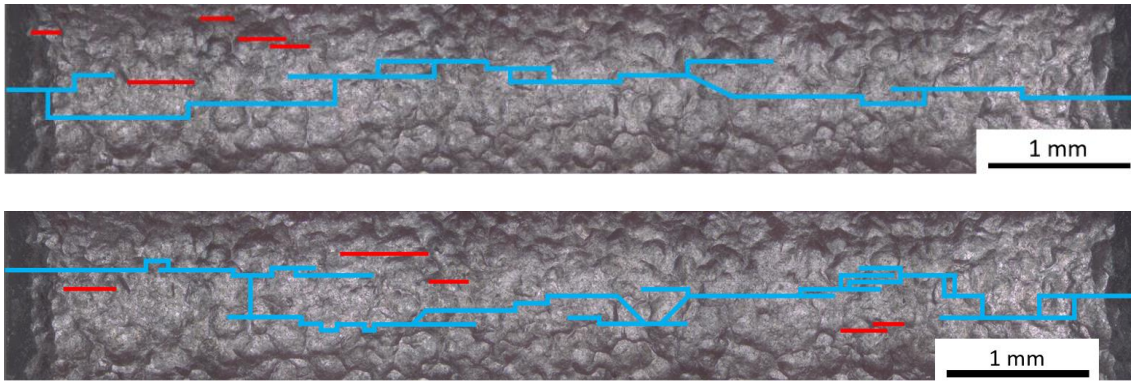

Figure 6-4 The final notch surface replica record from the crack evolution diagrams for A) a sample subjected to the lifetime extension strategy under constant amplitude loading at a constant amplitude strain range of 0.75 %. B) A sample subjected to the same lifetime extension strategy with single periodic tensile overloads with OLR of 1.56 applied every 150 baseload cycles with a constant amplitude strain range of 0.75 %.

6.3.3 Experimental lifetime of U-notch samples

The fatigue lifetimes of all short crack tests presented in Chapters 4, 5 and 6 are displayed as longitudinal tensile strain range versus cycles to failure (S-N) graphs in Figure 6-5. U-notch samples made of FV566 from blade M06 were compared with previous results from FV448 material [50, 126] (Figure 6-5 A). The notch geometry of all samples was 2.25 mm radius and 1.25 mm depth and were cyclically loaded with an R-ratio of 0.1. FV566 material appeared to be more resistant to cyclic loading compared to FV448 material. An as-received notch surface condition (containing corrosion pits) tended to result in slightly lower lifetimes than polished samples (in both materials) despite the presence of residual pits after polishing. A small overload with OLR of 1.11 had a very small (almost negligible and within scatter) effect on fatigue lifetime, whereas a larger OLR of 1.56 has a more pronounced lifetime extending effect. The overload also appears more effective at extending the lifetime of the sample when the U-notch surface was polished. Frazer-Nash Consultancy carried out fully reversed (R-ratio of -1) fatigue lifetime testing on FV566 samples from blades M11 to M15. These samples tended to have lower lifetimes especially at high strain ranges.

Varying the notch radius and notch depth of U-notched samples made from both FV566 across multiple blades (M06, M08 and M09) and FV448 [126], minimally impacted their fatigue lifetimes (Figure 6-5 B). No observable relationship between notch radius and notch depth and fatigue lifetime can be made from the data provided. A 1.54R x 3D (notch radius of 1.54 mm and notch depth of 3 mm) U-notch sample had the highest lifetime of other notch geometries tested at the same longitudinal strain range of 0.68 %. However, a sample

with the same notch geometry failed with fewer cycles than other notch geometries when subjected to a strain range of 1 %. The U-notch samples had similar lifetimes which were within expected scatter. A notch geometry of 5.25 mm radius was fatigue tested in FV448 material. The lifetimes of these samples showed less resistance to cyclic fatigue compared with FV566, but this is attributed to the difference in material performance and not to the increased radius of the notch geometry.

The effect of shot peening the U-notch surface and the application of the lifetime extension strategy on subsequent fatigue lifetimes was investigated on FV566 U-notched samples (Figure 1-5 C). At relatively low strain ranges (0.8 % or less) a T0 shot peen to the notch surface tends to increase fatigue lifetime over polished samples. A polished sample and shot peened sample were subjected to constant amplitude loading at a strain range of approximately 0.4 %. The polished sample failed at approximately 137 400 cycles whereas no cracks were observed on the shot peened sample at 2 240 000 cycles, where the test was subsequently stopped and not run to failure. The lifetime extending effect of shot peening diminished as strain range increased. At strain ranges above 1.2 %, the fatigue lifetime of shot peened samples were equivalent to polished counterparts. The lifetime extension strategy extended the lifetimes of U-notched samples when the strain range applied at the notch surface was kept constant throughout testing. The lifetime extension (of approximately 93 % for polished samples and 57 % for shot peened samples) was observed for both constant amplitude loading conditions and with periodic tensile overloads with OLR of 1.56 applied every 150 baseload cycles. The overload cycles did not provide any additional lifetime extension to the samples as was observed with polished surface condition.

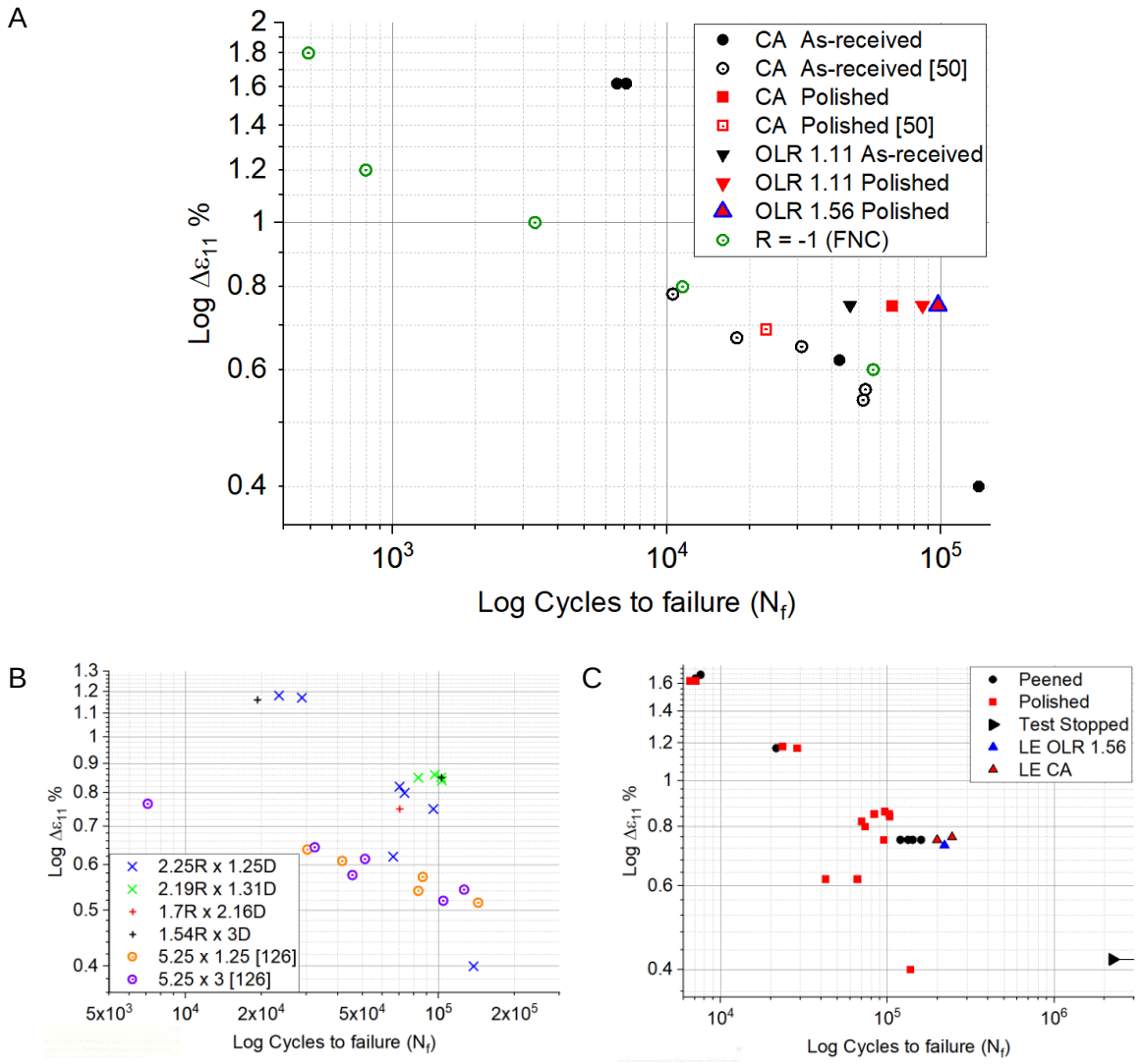

Figure 6-5 Longitudinal strain range at the notch surface versus number of cycles to failure for A) U-notched samples both in the as received and polished notch surface conditions under constant amplitude (CA) and single periodic overloads with OLRs of 1.11 and 1.56 at R-ratio of 0.1. The results are compared with FV448 material from He et al [50] and Soady et al [126]. The hollow green results show R-ratio = -1 carried out by Frazer-Nash Consultancy (FNC) for comparative purposes. B) U-notched samples with various notch radii (R) and notch depths (D). Hollow results include a notch radius of 5.25 mm made from FV448 from Soady et al [126] for comparison. C) U-notched samples with polished and shot peened (Peened) notch surface conditions. The results include three samples subjected to the lifetime extension strategy (LE), two samples under constant amplitude loading and one sample subjected to the LE strategy with single periodic overloads with OLR of 1.56 every 150 baseload cycles throughout the test. Note that one shot peened U-notch fatigue test was stopped (not run to failure) as no cracks were found to have initiated within 2 250 000 cycles.

6.4 Discussion

6.4.1 The combined effects of shot peening and overloads on short crack initiation and propagation behaviour

Shot peening was found to have a more profound retardation effect on short crack growth than single periodic overload cycles with an OLR of 1.56 applied every 150 baseload cycles, especially between $\Delta K_{Surface}$ values of 15 and 20 $MPam^{0.5}$. It was also found that the compressive residual stress from shot peening diminished considerably at high strain ranges, such as 1.69 %. It may be expected that single periodic overloads applied to a shot peened sample contribute to relaxation of the compressive residual stress from shot peening and increase short crack growth rates. While possible residual stress relaxation effects could be seen between $\Delta K_{Surface}$ values of 15 and 20 $MPam^{0.5}$, the crack growth rates were still considerably slower than observed for single periodic overload cycles on a polished sample. Another factor not yet considered is that of strain hardening on the short crack growth properties, which may potentially contribute towards the retention of short crack growth resistance. Overall, shot peening retains its retarding properties on short crack growth rates despite additional overload cycles.

A significant delay in the number of cycles to crack initiation was found for a polished sample with single periodic overloads of 1.56 applied every 150 baseload cycles. The delay to crack initiation was attributed to compressive residual stress in the notch field from the overload cycles. A shot peened sample under similar loading conditions was tested whereby the delay to crack initiation was not seen. The increased surface roughness and presence of pre-existing cracks induced crack initiation early in lifetime regardless of the presence of overload cycles (Figure 6-6). It was also found in Chapter 4.3.2.2 that single periodic overloads with OLR of 1.56 increased the total number of cracks that ultimately formed the primary crack. A similar increase in the total number of cracks was also observed in a shot peened sample with similar loading conditions. The increase in the total number of cracks led to increased coalescence seen during the characteristic period of inactivity typically seen in shot peened samples in Chapter 5.3.4.4.

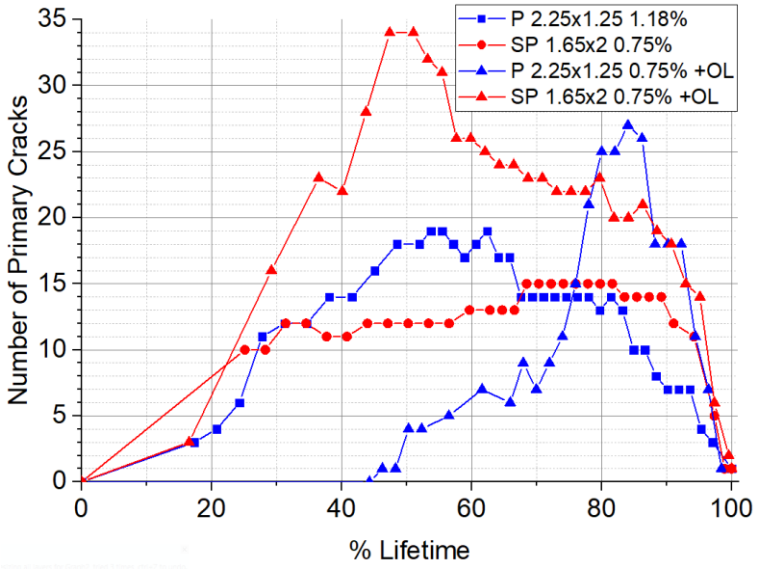

Figure 6-6 The total number of cracks that formed the primary crack versus lifetime percentage for polished and shot peened notch surface conditions under constant amplitude loading and single periodic tensile overloads with OLR of 1.56 every 150 baseload cycles loading conditions.

6.4.2 Application of the lifetime extension strategy

All cracks were fully ground away and no residual cracks on the notch surface were observed in all three FV566 samples tested to offer the greatest lifetime extension possible from the strategy. It is possible that residual cracks may be present after a grinding out process in an industrial situation. A similar lifetime extension strategy involving grinding out existing cracks followed by shot peening was carried out on FV448 material. After the grinding out stage of the lifetime extension strategy was completed, residual cracks with low *a/c* ratios were observed on the notch surface using microscopy. The presence of the residual cracks resulted in early crack initiation and no effective lifetime extension effect was seen (the total lifetimes were similar between samples with or without the lifetime extension strategy applied) [5].

It took over 2 hours to grind a 0.75 mm deep layer of material from the notch surface with a width of 8 mm using very careful metallographic techniques. The application of this strategy in an industrial application such as the fir-tree-root of turbine blades with additional constraints is therefore potentially time consuming and could increase cost. A machining on site approach may be a more appropriate application of the lifetime extension strategy. This approach may increase surface roughness, induce residual stresses on the notch surface and produce a high temperature that may cause changes to the material properties

considered deleterious to fatigue resistance and needs further investigation before implementation.

6.4.3 Lifetime prediction based upon a total life approach

6.4.3.1 Predicted lifetime of U-notched samples

The Coffin-Manson law (Equation 6-1) was used to characterise the relationship between strain range at the notch surface versus the number of cycles to total failure for U-notched samples made from FV566. The Coffin-Manson equation was re-written into a simpler form shown in Equation 6-2.

$$\frac{\Delta\varepsilon}{2} = \frac{\sigma'_f}{E}\left(2N_f\right)^b + \epsilon'_f\left(2N_f\right)^c \qquad \text{Equation 6-1}$$

$$\Delta\varepsilon = A\left(N_f\right)^b + \epsilon'_f\left(N_f\right)^c \qquad \text{Equation 6-2}$$

The Coffin-Manson constants for both polished and shot peened U-notch surfaces were found (Table 6-1) by empirically fitting the elastic strain range component (green data points) and the plastic strain range component (red data points) using regression analysis. The resulting Coffin-Manson curves for the polished and shot peened U-notch surface conditions are presented in Figure 6-7. Results below a strain range of 0.6 % were omitted from the fitting process as the fatigue test with the shot peened sample was stopped and not run to failure. The average number of cycles for a polished U-notch surface at 0.75 % longitudinal strain range was 89 300 while the Coffin-Manson lifetime prediction is 115 245 cycles. This difference indicates the importance of a large dataset at various strain ranges to improve the accuracy of the prediction.

Surface Condition	**Coffin-Manson Constants**			
	A	***b***	ϵ'_f	***c***
Polished	0.00365	0	0.539	-0.424
Shot Peened	0.00365	0	0.501	-0.411

Table 6-1 Coffin-Manson constants obtained by empirical fitting to experimental data for polished and shot peened U-notch surface conditions.

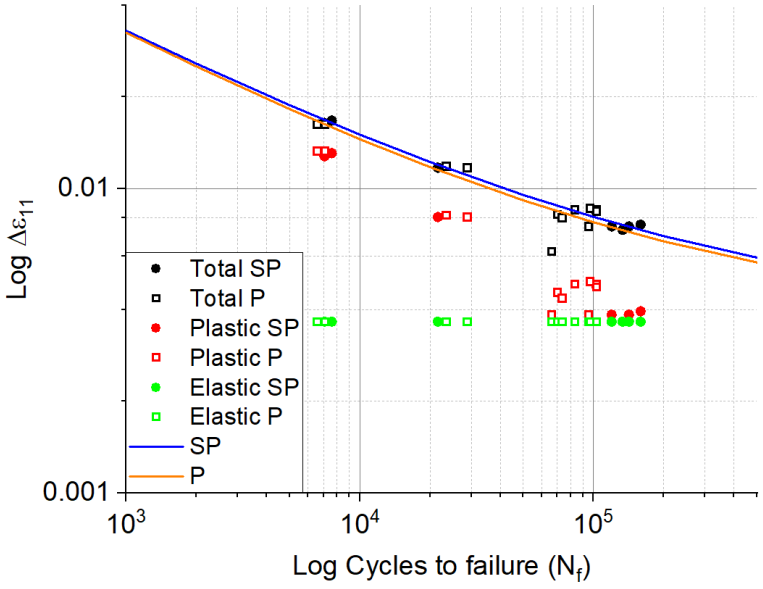

Figure 6-7 Longitudinal strain at the notch surface versus lifetime for polished (hollow squares) and shot peened (filled circles) U-notch samples. The total strain applied to the notch surface during testing (black data points) are split into their plastic strain (red data points) and elastic strain (green data points) counterparts. The resulting Coffin-Manson curves for the polished notch surface condition (orange line) and the shot peened notch surface condition (blue line) are presented.

The lifetime extension obtained in U-notch samples from the shot peening process can be predicted from the difference between the Coffin-Manson curves for the shot peened and polished U-notch surface conditions (Figure 6-8 A). As the strain range at the notch surface increases, the lifetime extension from shot peening decreases with a near power-law relationship. The benefit from shot peening (taken as the percentage increase in lifetime from a polished sample) also decreases with a near power-law relationship (Figure 6-8 B), showing the fatigue resisting properties of shot peening diminish with increasing strain range. At high strain ranges (> 1.2 %), the lifetime extension effect from shot peening is considered minimal. The diminishing benefit of shot peening, especially at high strain ranges, was also observed in [126, 130] and is attributed to compressive residual stress relaxation due to high plastic deformation during cyclic loading in the low cycle fatigue regime.

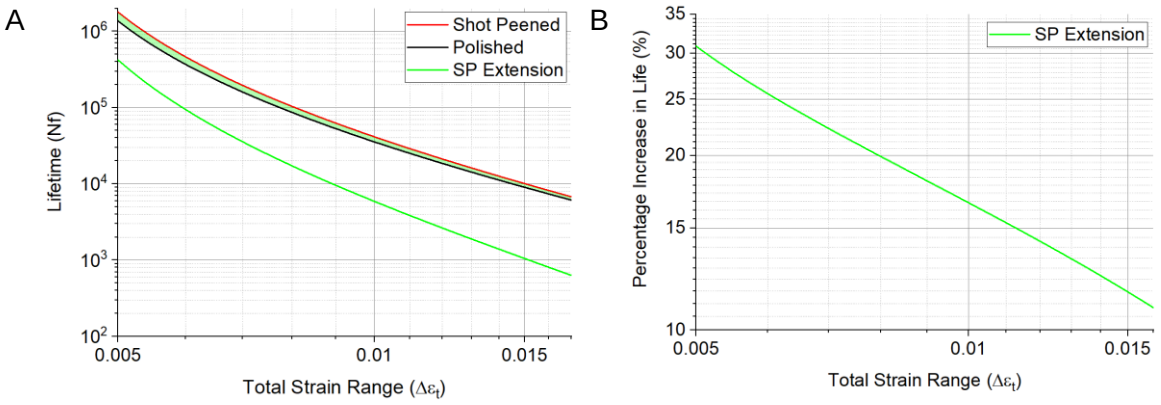

Figure 6-8 Predicted total lifetimes (using the Coffin-Manson relationship) with increasing total longitudinal strain range for shot peened (red line) and polished (black line) notch surface conditions. The difference between the Coffin-Manson relationships for shot peened and polished surface condition is indicative of the expected lifetime extension from the application of shot peening (green shaded area and green line 'SP Extension'). B) The lifetime extension from shot peening presented as a percentage increase in life compared with a polished surface condition. Note the lifetime here is plotted against the strain range (N-S curve).

6.4.3.2 Accounting for overloads

The Palmgren-Miner rule cumulative damage approach (Equation 6-3) was used to predict the lifetime of fatigue samples with single periodic tensile overloads with OLR of 1.56 every 150 base load cycles.

$$N_{fOL} = \frac{n_{BL}}{n_{BL} + n_{OL}} N_{f\Delta\varepsilon BL} + \frac{n_{OL}}{n_{BL} + n_{OL}} N_{f\Delta\varepsilon OL} \qquad \text{Equation 6-3}$$

A polished U-notch sample with notch radius of 2.25 mm and notch depth of 1.25 mm was subjected to constant amplitude loading at the baseload level with a longitudinal strain range of 0.75 % at the notch surface, which failed at 46 654 cycles. A second polished U-notch sample was subjected to constant amplitude loading at the overload level strain range of 1.69 % at the notch surface which failed at 6576 cycles. A lifetime prediction of 46 389 cycles for a polished U-notch sample and with periodic tensile overloads with OLR of 1.56 was made using the Palmgren-Miner rule (Equation 6-3). A third polished U-notch sample was subjected to single periodic tensile overloads with OLR of 1.56 (strain range of 1.69 % at the notch centre) applied every 150 baseload cycles (0.75 % strain range at the notch centre) to test the prediction which failed at 57 228 cycles. The Palmgren Miner rule was found to be over-conservative by 23 % (Table 6-2).

Cyclic loading	**Miners rule prediction**	**Number of cycles to failure**	**Miners rule error**
CA $\Delta\varepsilon$ = 0.75 %	N/A	46 654	N/A
CA $\Delta\varepsilon$ = 1.69 %	N/A	6 576	N/A
OLR of 1.56 applied every 150 baseload ($\Delta\varepsilon$ = 0.75 %) cycles	46 389	57 228	23 %

Table 6-2 The lifetime of two constant amplitude tests at the base load level (0.75 %) and overload level (1.69 %) were used to predict the lifetime for a sample with single tensile periodic overloads with OLR of 1.56 applied every 150 baseload cycles using the Palmgren-Miner rule.

The Palmgren-Miner rule is a damage accumulation rule that always predicts a lower fatigue lifetime for occasional overloads when compared with constant amplitude loading conditions. The Palmgren-Miner rule does not take into account the effects of plasticity and therefore residual stress and strain hardening effects of localised material during low cycle fatigue [142, 143]. Therefore, the Palmgren-Miner rule is typically considered to be a conservative prediction.

6.4.4 Lifetime Prediction based upon damage tolerant approaches

Lifetime prediction using total life approaches allow lifetime prediction of samples subjected to similar surface and loading conditions. Quantification of a representative error range is loosely based upon existing experimental data that tends to be relatively scarce. While total life approaches may be adequate prediction methods, they cannot be used to estimate the fatigue life at some arbitrary point during the fatigue life (such as when a short crack of 1 mm is observed). Lifetime prediction using damage tolerant methods were therefore used to investigate the impact of surface and loading conditions on the number of cycles for each of the four fatigue lifecycle phases (initiation, short crack growth, crack coalescence and long crack growth).

6.4.4.1 Number of cycles to crack initiation fatigue phase

Several interrupted fatigue tests have been carried out throughout Chapters 4, 5 and 6 on U-notch samples with various surface and loading conditions, the information obtained from replica records regarding the initiation phase of the fatigue lifecycle is presented in Table 6-3. Crack initiation was recorded as a percentage of lifetime so that samples with various

strain ranges could be compared. The number of cycles to crack initiation for a strain range of 0.75 % are known directly from replica records obtained during testing. The number of cycles to crack initiation for various strain ranges can be predicted using the Coffin-Manson relationship and the percentage lifetime to crack initiation from replica records. This prediction method assumes that strain range has no effect on lifetime percentage to crack initiation. When more than one replica record exists for a given surface and loading condition, the average lifetime percentage and total life are used. The error is given by the maximum and minimum experimental values. When one replica record exists, the percentage life to initiation error is based upon the percentage lifetime of the previous and succeeding replica records.

Surface/Loading condition	**Lifetime (%)**	**Number of cycles to Initiation**	**Error (Cycles)**
As-Received	7 < 14.1 < 21.1 [a]	9 333 [a]	+ 4 633 [a] - 4 633 [a]
Polished	11.2 < 29.1 < 56 [b]	26 000 [b]	+ 24 000 [b] -16 000 [b]
Polished + OL	31.3 < 38.7 < 46.1 [b]	37 800 [b]	+ 7 200 [c] - 7 200 [c]
Shot Peened	7.2 < 17.3 < 36 [b]	24 000 [b]	+ 26 000 [c] - 14 000 [c]
Shot Peened + OL	0 < 16.5 < 29.2 [d]	22 650 [d]	+ 17 400 [e] - 22 650 [e]

Table 6-3 The lifetime percentage and the number of cycles when crack initiation was first observed on U-notch samples for various surface and loading conditions. [a] The percentage lifetime was found for a sample with constant amplitude loading at a strain range of 1.69 %, the number of cycles to crack initiation was estimated based upon the total lifetime of a sample with a strain range of 0.75 % with similar surface conditions. [b] The number of cycles was estimated based upon an average percentage lifetime and averaged total lifetime. [c] The error was based upon the maximum and minimum percentage lifetime observed from experimentation. [d] The results are based upon a single test. [e] The error is based upon the number of cycles to the nearest previous and succeeding replica records.

The higher surface roughness and presence of corrosion pits caused early onset of crack initiation and therefore a lower lifetime percentage to crack initiation (Figure 6-9). The typically lower lifetimes for as-received surface condition samples also contributed towards the lower number of cycles to crack initiation. The percentage lifetime was obtained from a sample subjected to a higher strain range of 1.69 %, it is therefore assumed that strain range is independent of percentage lifetime.

It was observed that a smoother surface finish of the U-notch on the polished sample changed the mechanism of crack initiation from initiation at stress raisers (corrosion pits) to persistent slip bands Chapter 4.3.2.2, which increased the number of cycles to crack initiation (Figure 6-9). When single periodic tensile overloads with OLR of 1.56 were applied to the sample, the number of cycles to crack initiation increased further due to the compressive residual stress within the notch field Chapter 4.4.4.

Shot peening the U-notch surface resulted in crack initiation occurring earlier in lifetime by over 10 % compared to a polished notch surface, regardless of loading conditions (Table 6-3). However, shot peened U-notch samples typically failed after a greater number of cycles. Despite a lower percentage life to crack initiation, the number of cycles to crack initiation was similar to a polished notch surface (Figure 6-9). The increased surface roughness and pre-existing cracks on the shot peened U-notch surface, considered detrimental to fatigue [26, 179], counteracted the crack initiation inhibiting quality of the compressive residual stress from shot peening and appeared to offer no additional resistance to fatigue during the crack initiation phase. Similarly, the addition of single periodic tensile overloads with OLR of 1.56 applied to the shot peened U-notch sample did not result in enhanced fatigue resistance in the crack initiation phase as was seen in the polished surface condition (Figure 6-9). It is likely that the compressive residual stress due to shot peening was partially relaxed in the initial stages of cyclic loading in the LCF regime, resulting in decreased resistance to crack initiation.

The larger sample size accounts for the larger amount of error seen for the polished and shot peened surface conditions. One sample was available for the shot peened U-notch surface with overloads; the error for this surface condition is high due to the large number of cycles to the nearest previous and succeeding replica record. The polished surface condition with overload cycles has a relatively small error range based upon two tests, which is too small a sample size to be considered an accurate representation of the error. One sample was available for the as-received surface condition from which replicas were taken with reduced number of cycles per interval resulting in a relatively small error range.

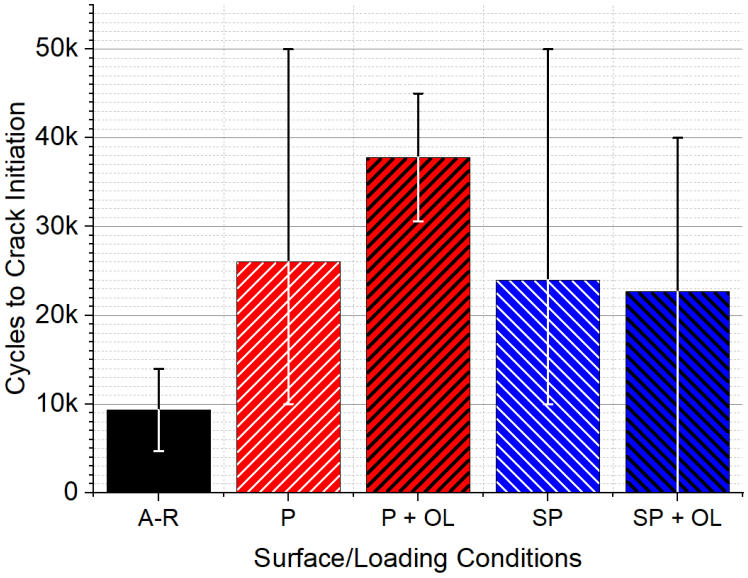

Figure 6-9 The number of cycles to crack initiation for U-notched samples with various surface and loading conditions. As-Received (A-R), Polished (P), Polished with single periodic overloads with OLR of 1.56 every 150 baseload cycles (P+OL), Shot Peened (SP) and Shot Peened with single periodic overloads with OLR of 1.56 every 150 baseload cycles (SP+OL).

6.4.4.2 Number of cycles for short crack propagation phase

Short crack growth rate versus $\Delta K_{Surface}$ information was obtained from interrupted testing of multiple U-notch samples with various surface and loading conditions presented throughout Chapters 4, 5 and 6. The Paris-law constants *C* and *m* (Equation 6-4) were found by empirical regression fitting existing data from replica records (including arrested cracks). The $\Delta K_{Surface}$ value was calculated using the approach detailed in Appendix C.

$$\frac{da}{dN} = C\Delta K_{Surface}{}^{m} \qquad \text{Equation 6-4}$$

The number of cycles for the short crack phase can be found using an iterative feedback loop process (Figure 6-10) based upon the Paris-law relationship found for each surface and loading condition.

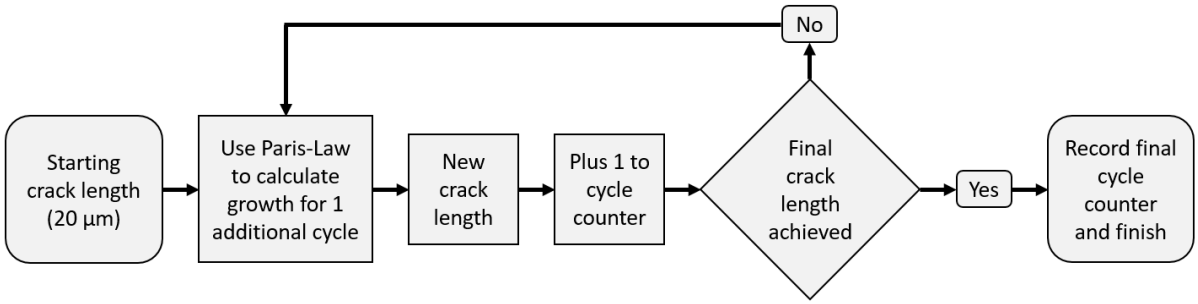

Figure 6-10 A schematic flow diagram showing the iterative feedback loop process used to calculate the number of cycles to grow a crack from a pre-defined initial crack length to a target crack length.

An initial starting projected surface short crack length of 20 µm was chosen to represent the crack length immediately following initiation typically observed on replica records. An initial crack length error of ± 5 µm was chosen to represent measurement error and small variations in crack length immediately following initiation. The final (or target) crack length was calculated based upon the average number of initiations events that form the main primary crack for each surface and loading condition and the width of the sample (Equation 6-5).

$$Target\ final\ crack\ length = \frac{Number\ of\ initiation\ events}{Width\ of\ sample} \qquad \text{Equation 6-5}$$

A final crack length error was found from the range of crack initiation events observed over multiple samples for each surface and loading condition. Where only one sample is available, an error range of ± 20 % in the number of crack initiation events that formed the main crack were used. The number of initiation events forming the main crack were found using the method described in Chapter 4.2.3 and not from replica records and therefore may be subject to data processing error. The method of calculating the final crack length assumes the cracks initiate at the same time, the location of all crack initiation events are equidistant and in plane of one another. The assumptions applied may typically result in a conservative estimate of the number of cracks for the short crack phase. The error in the number of cycles does not include a possible increase or decrease in the Paris-law constants due to variations in material properties between blades. The Paris-law constants, number of cycles for the short crack phase and associated error was calculated for various surface and loading conditions (Table 6-4). Due to non-linear crack growth rate versus $\Delta K_{Surface}$ relationship due to the compressive residual stress field for shot peened surface conditions two Paris-law constants were found for $\Delta K_{Surface}$ below and above 20 MPam$^{0.5}$

Surface/Loading condition	Paris-law Constants		Final Crack Length (µm)	Number of cycles for short crack phase	Error (Cycles)
	C	***m***			
Polished	3.6×10^{-8}	2.05	1000	43 800	+ 9 100 - 5 200
Overload	1.2×10^{-8}	2.3	350	54 300	+ 8 900 - 7 100
Shot Peened	1.6×10^{-6} 2.2×10^{-12}	0 4.5[a]	315	92 200	± 28 900
Shot Peened + Overload	3.5×10^{-7} 1.4×10^{-11}	0.65 4.04[a]	229	64 500	+ 12 000 - 9 500

Table 6-4 The Paris-law constants by empirical fitting of experimental short crack growth rate versus $\Delta K_{Surface}$ data for various surface conditions (polished and shot peened) and loading conditions (constant amplitude and overloads with OLR of 1.56 every 150 baseload cycles). The estimated number of cycles for the short crack phase is calculated based upon the Paris-law constants and initial starting crack (20 µm) to the final crack length and associated error for each surface and loading condition. [a] The Paris-law constants for $\Delta K_{Surface}$ values greater than 20 $MPam^{0.5}$.

The source of the most significant proportion of error, either from the starting crack length or the final crack length, was surface condition dependent. The total difference in the number of cycles due to an error of ± 5 µm in the initial starting crack length of 20 µm was 5775 cycles for the polished U-notch condition. The total difference in the number of cycles due to error in the final crack length was altered due to two variables, resulting in an error of 8500 cycles:

- The number of crack initiation events for the polished surface condition was smaller than the shot peened surface condition, ranging from 5 to 10 cracks. Despite the relatively small range, the low number of total cracks resulted in a large final crack length range of 800 µm.
- The Paris-law constant *m* was high and therefore the crack growth rate increased significantly with increasing $\Delta K_{Surface}$ values.

The total difference in the number of cycles due to an error of ± 5 µm in the initial starting crack length of 20 µm was 6250 cycles for the shot peened U-notch surface condition. The

total difference in the number of cycles due to the error in the final crack length was significantly altered by both variables, resulting in a much more substantial error of 54 700 cycles.

- A higher total number of crack initiation events and a higher range of crack initiation events between 20 and 35, resulted in a final crack length range that was significantly reduced to 175 µm compared with the polished notch surface.
- However, the Paris-law constant *m* value was zero due to the compressive residual stress and strain hardening from shot peening. Additionally, the final crack length did not surpass a $\Delta K_{Surface}$ of 20 MPam$^{0.5}$. Therefore, the crack growth rate did not increase with increasing $\Delta K_{Surface}$ values, making the final crack length a much more significant source of error.

The error from the expected variation in the final crack length was the most significant source of error for both surface conditions. It was more significant for a shot peened notch surface (90 % of total error) than for the polished notch surface (60 %) due to the substantial retardation of the short crack growth rate especially between $\Delta K_{Surface}$ values between 15 and 20 MPam$^{0.5}$.

The polished U-notch surface (also equivalent to the As-Received U-notch surface) required the least number of cycles for the short crack phase. A greater number of cracks due to single periodic tensile overloads with OLR of 1.56 every 150 baseload cycles sample reduced the average final crack length immediately before crack coalescence. However, the short crack growth rate was retarded sufficiently due to compressive residual stress in the notch field to increase the number of cycles during the short crack growth stage compared with constant amplitude loading. Introducing a single periodic tensile overload with OLR of 1.56 every 150 baseload cycles on a shot peened notch surface further increased the total number of initiation events resulting in the shortest final crack length of all surface and loading conditions. The compressive residual stress from the shot peening process appeared to be slightly relaxed especially between $\Delta K_{Surface}$ values between 15 and 20 MPam$^{0.5}$ resulting in a reduced number of cycles for the short crack phase (Figure 6-11).

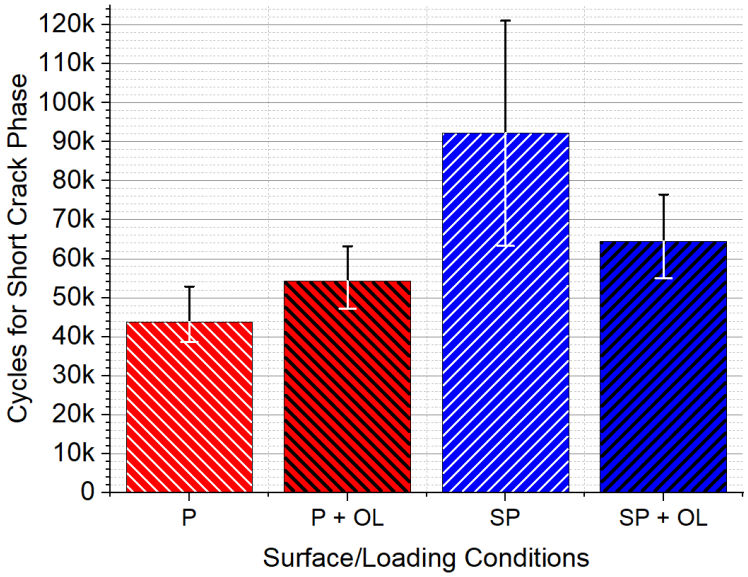

Figure 6-11 The number of cycles for the short crack phase for U-notched samples with Polished (P), Polished with single periodic overloads with OLR of 1.56 every 150 baseload cycles (P+OL), Shot Peened (SP) and Shot Peened with single periodic overloads with OLR of 1.56 every 150 baseload cycles (SP+OL) surface and loading conditions.

6.4.4.3 Coalescence Phase

The crack coalescence phase was defined as the number of cycles during dominant coalescence behaviour of short cracks until the primary crack had grown the full width of the sample. The number of cycles for the crack coalescence phase was found by subtracting the total number of cycles found from the other three phases (initiation, short crack and long crack) from the average total number of cycles to failure for each surface and loading condition from experimentation. The error range for the coalescence phase was found by totalling the suggested error from the other three phases.

The polished notch surface condition required an additional 25 000 to 30 000 cycles for the coalescence phase to match with experimentally obtained total lifetimes. The number of cycles for the crack coalescence phase for the polished notch surface with overload with OLR of 1.56 every 150 baseload cycles was negative. This result suggests that the methods chosen to predict the number of cycles for one or more of the other three phases may produce over-conservative estimates. The required number of cycles for the crack coalescence phase for a shot peened the notch surface with constant amplitude loading conditions was between 15 000 and 20 000 cycles. When overloads with OLR of 1.56 every 150 baseload cycles were introduced, the number of cycles for the crack coalescence phase increased to between 40 000 and 45 000 cycles. The approximated error for the

coalescence phase is based upon an accumulation of the error from the other three phases and therefore is not included in any forthcoming total life error ranges (Figure 6-12).

The methodology used to predict the number of cycles for the crack coalescence phase does not adequately indicate how the surface and loading conditions affect the crack coalescence phase. Instead, the results are reflective of the methods used for determining the number of cycles and the accumulation of approximate error across the other three phases. The number of cycles to crack coalescence may depend on out-of-plane variance, the number of cracks that form the primary crack, the strain range and surface conditions which has not been fully explored in this project.

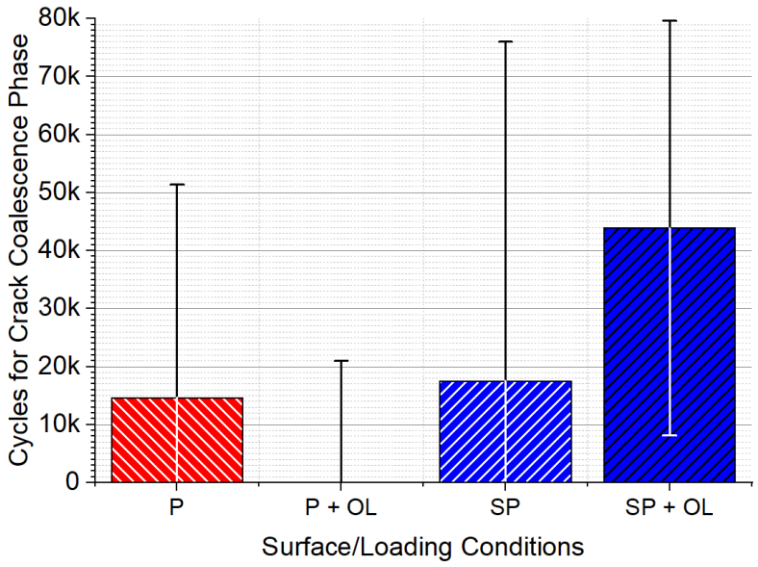

Figure 6-12 The number of cycles for the crack coalescence phase for U-notched samples with Polished (P), Polished with single periodic tensile overloads with OLR of 1.56 every 150 baseload cycles (P+OL), Shot Peened (SP) and Shot Peened with single periodic tensile overloads with OLR of 1.56 every 150 baseload cycles (SP+OL) surface and loading conditions.

6.4.4.4 Long crack growth to failure phase

Long crack growth rate versus ΔK relationships were found from long crack testing SEN bend samples with constant amplitude loading conditions and with overloads with OLR of 1.56 every 150 baseload cycles (Chapter 4.3.3). The Paris-law constants C and m (Equation 2-24) were found (Table 6-5) by empirical regression fitting existing data (Figure 4-23). The ΔK value was calculated using the method described in Appendix A. An estimated error of ± 50 % in the crack growth rate versus ΔK relationship was used (found in Chapter 4.4.4) to account for measurement and calibration error and possible variations in baseline mechanical and fatigue material properties between blades. An initial starting

long crack length of 1 mm was chosen to represent the depth of the long crack after the main crack had grown the entire width of the sample. An error of ± 0.2 mm was chosen to represent variation in long crack depth after the crack coalescence phase. The final crack length of 6.42 mm for constant amplitude loading and 6.14 mm from single periodic tensile overloads with OLR 1.56 every 150 baseload cycles loading conditions was measured directly from the fracture surfaces of failed long crack samples (Figure 4-27 A and B) to *BS ISO 12108:2012* [157]. The number of cycles for the long crack phase to final failure was found using the iterative feedback loop seen in Figure 6-10 and the results shown in Table 6-5 and Figure 6-13.

An error of ± 0.2 mm in the initial starting length resulted in an approximated error range of 2200 cycles (35 % of the total error) for constant amplitude and 4000 cycles (45 % of the total error) for the overload loading conditions. The estimated percentage lifetime for the long crack phase for both loading condition is less than 6 %, or 12 % considering a worst case scenario based upon the total approximated error. The long crack phase is therefore the least significant phase during the fatigue lifecycle of U-notched components. The Paris-law constant '*C*' was considered a more significant contributing factor in the number of cycles for the long crack phase. The crack growth rate was significantly reduced for relatively small ΔK values between 15 and 20 MPam$^{0.5}$ by a factor of three. The number of cycles during the long crack growth stage for the OLR sample was increased by 25 %, despite a shorter critical crack length, due to the compressive residual stress ahead of the crack tip despite visible bursts of plastic deformation at the very end of fatigue life.

Loading condition	**Paris-law Constants**		**Lifetime (%)**	**Number of cycles for long crack phase**	**Error (Cycles)**
	C	***m***			
Constant Amplitude	7.3 x 10^{-9}	3.1	5.4 %	4800	+ 3650 - 2550
OLR of 1.56 / 150 BL cycles	5.8 x 10^{-11}	4.4	6 %	6000	+5400 -3600

Table 6-5 The Paris-law constants by empirical fitting of experimental long crack growth rate versus ΔK data for constant amplitude loading and with a tensile periodic overload with OLR of 1.56 applied every 150 baseload cycles. The duration of the long crack phase is displayed both as percentage lifetime and as the number of cycles with associated error in number of cycles for both loading conditions.

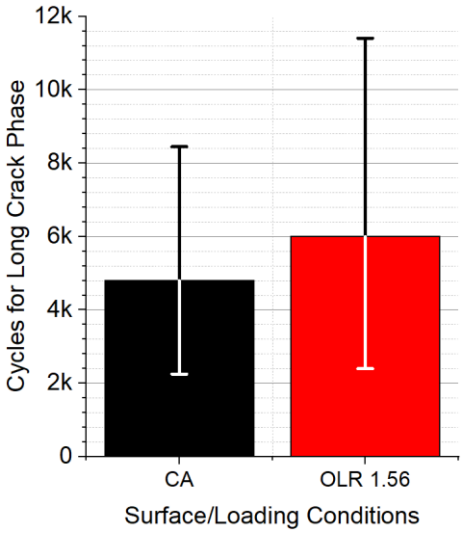

Figure 6-13 The number of cycles for the long crack phase for U-notched samples under constant amplitude loading conditions and with single periodic overloads with OLR of 1.56 every 150 baseload cycles.

6.4.4.5 Total lifetime by phase

The four characteristic fatigue lifecycle phases of U-notched samples (crack initiation, short crack, crack coalescence and long crack) with various surface and loading conditions were stacked and compared (Figure 6-14). The fatigue life and approximate error for the As-Received surface condition is the lowest of all surface and loading conditions. The number of cycles to initiation is particularly reduced due to corrosion pits acting as stress concentration features resulting in early crack initiation behaviour. Polishing the notch surface resulted in an increase in the number of cycles to crack initiation, subsequently leading to an increase in the average fatigue life of the U-notched samples. Overload cycles with OLR less than or equal to 1.11 were not found to make a significant difference to the number of cycles for each lifecycle phase or to the total fatigue life and is comparable to constant amplitude loading conditions.

However, the addition of larger overloads with OLR of 1.56 applied every 150 baseload cycles were found to increase the total life of U-notched samples overall. The number of cycles for crack initiation were significantly increased due to the compressive residual stress in the notch field. Additionally, the number of cycles for the short crack phase were slightly increased due to compressive residual stress ahead of the crack tip induced by the overload cycles. This result is expected for stainless steel material and is in agreement with several authors [60, 62, 90-93, 95-97, 110, 189]. It is important to note that no cycles were predicted during the coalescence phase, indicating that the number of cycles during the initiation phase may not be accurate and requires further investigation.

Shot peening increased the lifetime of U-notched samples regardless of loading conditions. The lifetime extension is attributed to residual compressive stress and strain hardening beneath the notch surface due to shot peening, hindering short crack growth and increasing the number of cycles for the short crack phase. The significantly retarded short crack growth rate is responsible for the relatively large approximated error in the total life.

While an attempt to visually approximate the contribution of each phase for each surface and loading condition was carried out (Figure 6-14). Stacking phases on top of each other incorrectly assumes that phases happen one after another, in reality, phases can occur simultaneously over a transitional period. Nonetheless, the results highlight the short crack phase is the most significant proportion of the fatigue life in all samples (for a strain range of 0.75 % at the notch surface) followed by the crack initiation phase (the significance of which increases with reducing strain range at the notch surface). On the other hand, the long crack phase is the least influential and therefore a lifetime extension strategy in this area is less likely to result in significant improvements in fatigue life. The contribution of each phase of the fatigue lifecycle can be considered when improving lifetime predictions for these set of testing conditions that has service relevance to improved lifetime extension estimates in ageing last stage low-pressure steam turbine blades.

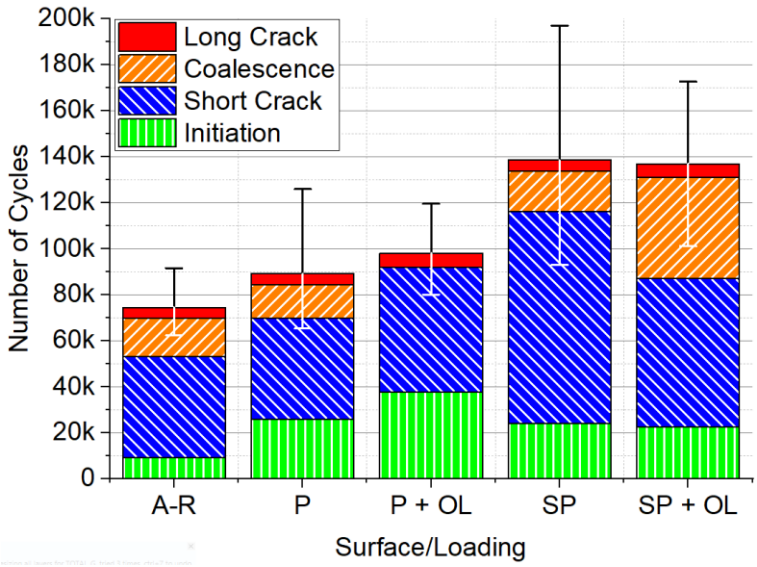

Figure 6-14 The average total lifetime in cycles for U-notched samples with As-Received (A-R), Polished (P), Polished with single periodic tensile overloads with OLR of 1.56 every 150 baseload cycles (P+OL), Shot Peened (SP) and Shot Peened with single periodic tensile overloads with OLR of 1.56 every 150 baseload cycles (SP+OL) surface and loading conditions. The lifecycle for each U-notch surface and loading condition are split into their four respective phases namely initiation, short crack, crack coalescence and long crack phases with total accumulated error.

6.4.5 Lifetime extension strategy prediction and limitations

The lifetime for the samples subjected to the lifetime extension strategy were predicted using both total life and damage tolerant approaches with the following method (Table 6-6).

- The maximum longitudinal strain range at the notch surface was found using FE modelling.
- The Coffin-Manson strain range versus total lifetime relationship for polished U-notch surface conditions was used to predict the number of cycles to failure for the polished sample.
- The average percentage life to crack initiation for a polished U-notch surface was used with the Coffin-Manson prediction to estimate the number of cycles to crack initiation.
- The Paris-law relationship for either the constant amplitude or with single periodic tensile overloads with OLR of 1.56 every 150 baseload cycles was used to estimate the number of cycles required for a short crack to grow a projected distance of 1 mm from an initial projected crack length of 20 μm.
- The lifetime extension strategy (LE) was applied where existing cracks were ground away followed by shot peening on the entire top surface of the U-notch sample.
- The maximum predicted longitudinal strain range at the notch surface was found using FE modelling for the modified notch geometry (for tested samples, the strain range was kept constant to optimise data output since the Coffin-Manson relation can be used to account for strain range increase after modifying the notch geometry).
- The Coffin-Manson relationship for shot peened U-notch surface conditions was used to predict the number of cycles to failure for the shot peened sample.
- The estimated lifetimes for pre and post lifetime extension strategy are combined to find the total estimated lifetime of the sample.

Sample	**LE CA**	**LE CA**	**LE + OL**
Pre-LE longitudinal strain range	0.0075	0.0075	0.0075
Coffin-Manson for polished U-notch (prediction)	115 245	115 245	115 245
Percentage life for crack initiation (polished sample)	29.1	29.1	38.7
Predicted cycles to crack initiation	33 536	33 536	44 599
Predicted cycles to 1 mm crack growth (Paris-law)	43 800	43 800	54 300
Pre-LE strategy prediction	77 336	77 336	98 899
Actual pre-LE cycles from experimentation	85 000	79 000	83 000
Lifetime extension strategy (LE) applied	-	-	-
Modified notch geometry (radius x depth mm)	1.65 x 2.2	1.58 x 3	1.65 x 2
Post-LE strain range from FE modelling	0.0076	0.0075	0.0074
Coffin-Manson for shot peened U-notch (prediction)	131 030	139 466	148 688
Actual cycles for shot peened experimentation	159 189	119 670	136 960
Total predicted number of cycles (subjected to LE)	208 366	216 802	247 587
Actual total cycles from experiments	244 189	198 670	219 960

Table 6-6 The lifetime prediction for three samples subjected to the lifetime extension strategy (LE). The Coffin-Manson relationship for the polished notch surface condition was used to estimate the number of cycles to crack initiation. The number of cycles during the short crack growth phase to 1 mm projected surface crack length is estimated assuming a starting crack of 20 µm. After the lifetime extension strategy was applied, the Coffin-Manson relationship for the shot peened surface condition was used to estimate the number of cycles to final failure. The total number of cycles for samples subjected to the lifetime extension strategy was predicted and compared to the actual lifetimes obtained from experimental testing.

U-notched samples subjected to the lifetime extension strategy have six fatigue lifecycle phases. The first two phases include a preinitiation phase and short crack growth phase to 1 mm crack growth based upon a polished U-notch surface. The four remaining phases comprise of the post lifetime extension strategy initiation and short crack phases, followed by the crack coalescence and long crack phase extracted from the averaged shot peened U-notch surface condition. The contribution of each phases that account for the total lifetime

of an average U-notch sample subjected to the lifetime extension strategy with constant strain range of 0.75% was compared with polished and U-notch surface conditions for constant amplitude loading (Figure 6-15 A) and with single periodic tensile overloads of 1.56 every 150 baseload cycles (Figure 6-15 B). The total error range was found by accumulating the error from each phase (except for the crack coalescence phase).

The fatigue lifetime prediction method based upon the total life (Coffin-Manson) and damage tolerant (Paris-law) approaches (described and shown in Table 6-6) was used to predict the lifetime for a U-notched sample subjected to the lifetime extension strategy at a strain range of 0.75 % throughout the test. The total error accumulated from each phase was used to represent the approximated prediction error (Figure 6-15 A). The same method was used to estimate the number of cycles for samples subjected to overloads with single periodic tensile overloads with OLR of 1.56.

The total fatigue life found from experimentation of two samples subjected to the lifetime extension strategy with constant amplitude loading were averaged and compared with the prediction approach. The error for the actual lifetime is the range of the two lifetime results obtained. The total fatigue life from an experiment of a sample subjected to the lifetime extension strategy with overloads with OLR of 1.56 every 150 baseload cycles was compared with the prediction approach and the error based on the range of values from the two constant amplitude tests.

The lifetime prediction closely represents the average lifetime of experimentally tested U-notch samples. The predicted lifetime of the sample with additional overloads was higher than experimental results, it appears that the number of cracks to initiation may have been initially overestimated, further suggesting that the number of cycles to crack initiation for a polished sample with overload cycles may require more investigation.

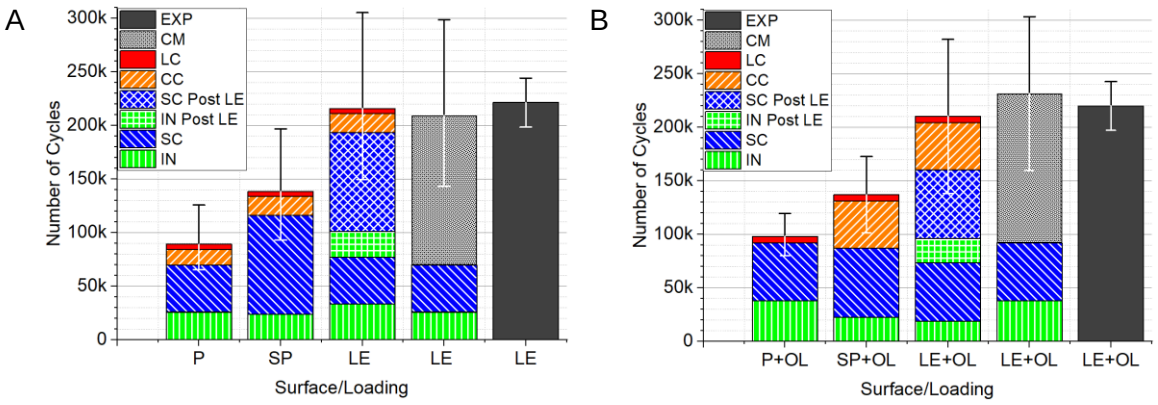

Figure 6-15 A) The total average lifetime for Polished (P) and Shot Peened (SP) U-notched samples under constant amplitude loading at a strain range of 0.75 % and B) with single periodic overloads with OLR of 1.56 every 150 baseload cycles. The individual phases were used to estimate the number of cycles for samples subjected to the lifetime extension strategy (LE) and compared with a method which uses the Coffin-Manson (CM) relationship for shot peened notch surface conditions to predict total life. Both prediction methods are compared with the average lifetime found experimentally (EXP) for the two samples subjected to the lifetime extension strategy.

The predicted lifetimes using the Coffin-Manson relationship for polished and shot peened samples and using the prediction method described above for samples subjected to the lifetime extension strategy are shown in Figure 6-16. Results that fall in the red shaded area represent under-conservative predictions, while the blue shaded area represents over-conservative predictions (within a factor of two). It is not surprising that predictions are both over-conservative and under-conservative due to regression fitting of the experimental lifetime data to obtain the Coffin-Manson constants.

The prediction methods for the lifetime extension strategy appear to be relatively accurate and within 15 % of lifetime found experimentally. However, it is more useful from an industrial perspective to offer a conservative approach based upon worst case scenarios. A conservative lifetime prediction for samples subjected to the lifetime extension strategy was made that accounted for a possible worst-case scenario based upon the accumulated error from each lifecycle phase. The predictions were consistently over-conservative, with one prediction less than half the number of cycles found experimentally.

The Palmgren-Miner rule is typically an over-conservative prediction method and is considered an industrially appropriate for lifetime prediction of samples with single periodic tensile overloads. The Palmgren-Miner rule always predicts a lower lifetime than constant amplitude cyclic loading conditions at the baseload strain range. U-notch samples with

overload cycles with OLR of 1.56 every 150 baseload cycles are expected to increase the total number of cycles to fatigue failure. Therefore, it may be more appropriate to use a lifetime prediction method based upon constant amplitude loading at the baseload strain range, where over-conservative lifetime predictions would typically be expected.

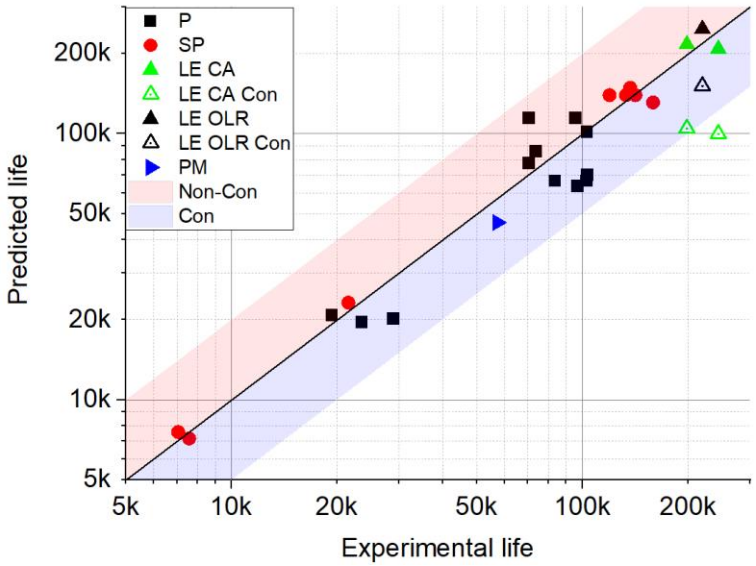

Figure 6-16 Predicted lifetime versus actual lifetime in number of cycles for the polished (P) and shot peened (SP) notch surface conditions as well as samples subjected to the lifetime extension strategy (LE) using conservative (Con) and non-conservative lifetime predictions methods, and using the Palmgren-Miner rule (PM) for a sample with single tensile periodic overloads with OLR of 1.56 every 150 baseload cycles. Results within the red area indicate under-conservative predictions and results within the blue area indicate over-conservative prediction within a factor of two.

The lifetime extension strategy prediction has only been applied to samples that maintain a constant strain range of 0.75 % during the test. In reality, changing the notch geometry will also change the strain range at the notch surface which is expected to have a significant effect on the fatigue life. The Coffin-Manson strain versus lifetime relationship can therefore be used to account for strain range changes after U-notch geometry modification.

The prediction method described previously can be used to estimate the number of cycles to 1 mm short crack growth. The minimum number of cycles remaining that still offers an improvement in lifetime, and therefore the maximum longitudinal strain range at the notch surface that still provides a lifetime extension can be predicted using the Coffin-Manson relationship (Table 6-7).

Sample	**LE CA**
Pre-LE longitudinal strain range	0.0075
Coffin-Manson for polished U-notch (prediction)	115 245
Percentage life for crack initiation	29.1
Cycles to crack initiation (prediction)	33 536
Cycles to 1 mm crack growth (Paris-law)	43 800
Cycles for pre-LE strategy (prediction)	77 336
Lifetime extension strategy (LE) applied	-
Minimum cycles needed for lifetime extension effect	(115 245 – 77 336) = 37 909
Therefore maximum strain range using Coffin-Manson	0.0102

Table 6-7 The lifetime prediction method was modified to find a maximum strain range where the lifetime extension strategy will still produce a lifetime extension. The Coffin-Manson relationship for polished surface conditions was used to estimate the number of cycles to grow a short crack a projected length of 1 mm. After application of the lifetime extension strategy, the minimum number of cycles required to offer a benefit in total fatigue life is calculated. The Coffin-Manson relationship for the shot peened surface condition was used to estimate the maximum strain range at the notch surface that would still offer a benefit to fatigue life.

A more conservative (and therefore industrially relevant) maximum strain range prediction was carried out by considering the worst-case accumulated error found from each lifecycle phase (expect the coalescence phase). It was found that the Coffin-Manson lifetime prediction could itself be under-conservative. The average total lifetimes for polished U-notch surface conditions at a strain range of 0.75 % at the notch surface was lower at 89-300 cycles than the Coffin-Manson total life prediction of 115 245 cycles. Therefore, the maximum strain range considering average lifetimes from experimentation was also predicted for comparison (Table 6-8).

Lifetime prediction method	**Maximum strain range after LE (%)**
Non-conservative lifetime prediction using Coffin-Manson	< 1.02
Conservative lifetime prediction using Coffin-Manson	< 0.86
Non-conservative averaged lifetime from experiments	< 1.23
Conservative averaged lifetime from experiments	< 0.96

Table 6-8 The maximum predicted strain ranges after application of the lifetime extension strategy (LE) that still offers an extension to total fatigue life (after a pre-lifetime extension strategy strain range of 0.75 % at the notch surface). The Coffin-Manson relationship for polished U-notch samples at 0.75 % of 115 245 cycles and the average number of cycles from experimentation of 89 300 cycles were used as the target lifetime for calculating maximum strain ranges. The conservative prediction (worst case) accounts for maximum approximated error in the lifetime prediction.

In Chapter 5, it was deduced that changes in the notch radius and notch depth was not as important as the longitudinal strain range when considering the lifetimes of U-notched samples. Therefore, the notch geometry has not been considered when producing lifetime predictions.

Ultimately, FE modelling can be used to apply this prediction method to complex geometries that include fillets with a notch radius between 1.5 and 2.25 mm, such as the fir-tree-root-fillets of low-pressure turbine blades. Therefore, the prediction method described in this chapter can be used to determine the feasibility of a lifetime extension strategy including grinding out existing cracks followed by shot peening as a maintenance procedure for in-service turbine blades.

6.5 Summary and Conclusions

The short crack growth rate versus $\Delta K_{Surface}$ of U-notched samples with both single periodic tensile overloads with OLR of 1.56 applied every 150 baseload cycles and shot peening surface conditions were investigated. While minimal residual stress relaxation was seen between $\Delta K_{Surface}$ values between 15 and 25 MPam$^{0.5}$, the additional strain hardening effect from shot peening is considered to be unaffected by the presence of overload cycles and significant short crack growth retardation was maintained.

The additional overload cycles with OLR of 1.56 applied every 150 baseload cycles increased the number of crack initiation events that were observed on shot peened U-notch surface conditions. This increase in the number of crack initiation events increased crack coalescence activity during the characteristic period of inactivity that was observed in shot peened samples with constant amplitude loading conditions.

The total number of cycles to fatigue failure found from experimentation of U-notch samples with various notch geometries, loading conditions and surface conditions were compared. The number of cycles for each of the four fatigue lifecycle phases (initiation, short crack, crack coalescence and long crack) were estimated using damage tolerant approaches such as Paris-law. The lifetimes of U-notch samples were dependent upon the cyclic strain range that was applied to the notch surface. U-notch samples with various notch geometries were cyclically loaded with identical strain ranges at the notch surface, the total fatigue life did not appear to be significantly influenced by notch radius or notch depth.

U-notch samples made from FV566 tended to be more resistant to fatigue than U-notch samples made from FV448 with identical notch geometries, surface conditions and loading conditions. U-notch samples with a polished notch surface required more cycles for the crack initiation phase than the as-received U-notch surface due to corrosion pitting causing early crack initiation.

U-notch samples subjected to overload cycles with OLR of 1.11 every 150 baseload cycles resulted in fatigue lifetimes (including number of cycles for each lifecycle phase) that were very similar to constant amplitude loading conditions. On the other hand, overload cycles with OLR of 1.56 every 150 baseload cycles increased the overall life of U-notch samples. The compressive residual stress induced by the larger overload cycle in the notch field and localised compressive residual stress ahead of the crack tip resulted in an increase in the number of cycles during the crack initiation, short crack growth and long crack growth phases.

The total fatigue life of U-notch samples with a T0 shot peened surface was typically extended compared to all other loading and surface conditions, despite the increased surface roughness and presence of pre-existing cracks on the U-notch surface. The lifetime extension was attributed to the compressive residual stress and strain hardening beneath the notch surface from the shot peening process. The substantial retardation in the short crack growth rate significantly increased the number of cycles for the short crack growth phase and was the main contributing factor in the lifetime extension. Additionally, the number of cycles to crack initiation was slightly increased.

The magnitude of the lifetime extension diminished with increasing strain range at the notch surface. At strain ranges above 1.2 % at the notch surface, the lifetime extension from shot peening was no longer observed due to residual stress relaxation. The application of overload cycles with OLR of 1.56 applied every 150 baseload cycles did not significantly affect the total life of one U-notched sample under constant amplitude loading conditions. However, the increased number of total cracks and slight compressive residual stress relaxation may cause a minimal reduction in total lifetime.

A lifetime extension strategy involving grinding out existing cracks followed by shot peening on the entire top surface of U-notch samples was investigated. The overall fatigue life of U-notch samples subjected to the lifetime extension strategy was increased over polished samples or shot peened samples when a constant longitudinal strain range (0.75 %) was maintained during the entire test.

A method involving both total life (Coffin-Manson) and damage tolerant (Paris-law) approaches was used to predict the lifetime of U-notched samples subjected to the lifetime extension strategy. Application of the lifetime extension strategy is expected to change the notch radius and depth that will consequently affect the applied strain range and total fatigue life. Therefore, the method was additionally used to predict the maximum longitudinal strain range at the notch surface that would still offer an increase in total life after the lifetime extension strategy was applied. The prediction method can be used alongside FE modelling techniques to investigate the efficacy of the lifetime extension strategy as a maintenance procedure for in-service turbine blades.

Chapter 7: Summary and Conclusions

The aim of this thesis was to further the understanding of the fatigue behaviour in notches subjected to low cycle fatigue conditions, such as the fir-tree-root-fillets of turbine blades in martensitic stainless steel. This was achieved through experimental testing and finite element modelling and led to the development of a fatigue lifetime prediction model. The efficacy of a lifetime extension strategy involving grinding out existing cracks followed by shot peening along with service relevant loading conditions was investigated using this prediction model. It may be possible to apply the lifetime extension strategy to the fir-tree-root-fillets of turbine blades to extend their service life.

7.1 Material characterisation

Plain bend bars were extracted from the fir-tree-root of ex-service low pressure turbine blades made from FV566 martensitic stainless steel. It is understood from the sponsors that the FV566 material has been austenitised at 1050 °C and oil quenched, followed by tempering at 650 °C. The chemical composition of the FV566 material was found using spectrographic analysis by Southdown Material Testing Ltd. The results suggests that FV566 is similar to other martensitic stainless steels used in the manufacture of turbine blades such as FV448 and FV520B.

The microstructure of FV566 along three perpendicular planes was revealed using Vilella's reagent and found to be typical of tempered martensitic stainless steel. A 3D reconstruction of the material microstructure from images obtained via optical microscopy showed little variation between the three perpendicular planes. Inclusions were observed within the microstructure identified as Aluminium Oxide (Al_2O_3), Manganese Sulphide (MnS) and Silicon Oxide (SiO), which have also been observed in FV448. Stringers composed of Alumina particles were observed, possibly indicative of the rolling direction of the material. An undesirable region of δ-ferrite was observed, likely formed during manufacture of the material prior to heat treatment.

Hardness testing of FV566 and FV520B was carried out on three perpendicular planes. The hardness of FV566 was found to be 354 ± 15 HV 0.2, which was softer than FV520B (377 ± 17 HV 0.2) but harder than FV488 (301 ± 5 HV 0.2). One relatively hard plane was observed in both FV566 and FV520B, possibly indicative of the rolling direction. Tensile testing was carried out on cylindrical dog-bone samples made from FV566 on blades M01, M02 and M03 by Frazer-Nash Consultancy. FV566 material had an average Young's Modulus of 211 GPa, yield strength of 830 MPa and ultimate tensile strength of 976 MPa.

The mechanical properties of FV566 were found to be in between FV448 and FV520B material (FV520B being the strongest material). An attempt was made to estimate the yield strength and ultimate tensile strength from hardness data with varying degrees of success.

A finite element model was developed for a plain bend bar and U-notched bend bars made from FV566. An elastic-plastic material model was used to define the material behaviour based upon the monotonic stress-strain relationship obtained for blade M02 by FNC. A mesh convergence analysis was carried out, which validated the mesh used for collection of data via FE computer simulation. The model was further validated via experimental testing by loading a plain bend bar in 4-point bending and comparing the data collected from a strain gauge with an identical finite element simulation of the experimental test.

Strain controlled fully reversed (R-ratio of -1) cyclic fatigue testing was carried out by FNC on cylindrical dog-bone samples made from FV566. Cyclic softening behaviour was observed at strain ranges of 0.8 % and higher, a typical behaviour seen in similar tempered martensitic steels such as FV448.

Long crack testing of FV566 and FV520B was carried out with SEN bend bars in 3-point bending, under constant amplitude loading conditions. The long crack growth rate versus ΔK relationships were obtained for each material along with ΔK_{th} (threshold) and corresponding Paris-law constants. The long crack growth behaviour of FV566 was found to be similar to FV520B, while FV448 was found to be more resistant to long crack fatigue.

7.2 Baseline U-notch fatigue behaviour

The majority of fatigue tests were carried out on U-notched bend bar samples with notch geometry representative of the fir-tree-root-fillets of in-service turbine blades. The surface roughness of various U-notch surface conditions were measured. An as-received surface representative of possible in-service conditions contained corrosion pitting through exposure to ambient atmospheric conditions and had an average surface roughness of 0.14 ± 0.087 µm. Some notch surfaces were polished but still retained minor residual cracks with an average R_a surface roughness of 0.094 ± 0.031 µm. A ‘fully’ polished U-notch surface condition had an average R_a surface roughness of 0.039 ± 0.015 µm.

The fatigue lifecycle of a typical U-notch bend bar experienced four phases: crack initiation, short crack, crack coalescence and the long crack phase. Experimental testing of U-notch samples with various U-notch surface and loading conditions experienced these four lifecycle phases at similar percentage lifetimes. The number of cycles to crack initiation phase (when crack initiation activity started becoming consistent) for the main/primary crack was seen between 15 % and 35 % lifetime on average. The short crack growth phase

typically consisted of the most number of cycles. Typically, a decrease in initiation activity was followed by an increase in crack coalescence activity and the short crack growth behaviour was dominated by coalescence events rather than by propagation, which defined the crack coalescence phase. Once the crack had grown the full width of the sample, the fatigue behaviour was defined by long crack propagation until failure occurred between the last 5 % and 10 % lifetime. Defining the beginning and end of each phase was subjective since the phases transitioned into one another. For example, crack initiation events were typically observed until the crack grew the entire width of the sample at around 90 % to 95 % lifetime. The corrosion pits in the as-received surface condition acted as stress concentration features and as such were the source for 80 % of crack initiation events that made up the primary crack. The presence of corrosion pits reduced the number of cycles to crack initiation which resulted in the shortest average lifetime of all surface and loading conditions applied with 75 000 cycles to failure under constant amplitude loading conditions with a strain range of 0.75 %.

Polishing the surface and removing the corrosion pits resulted in persistent slip bands becoming the dominant cause of crack initiation. The number of cycles to crack initiation and total number of crack initiation events was increased. Consequently, the average fatigue life of the U-notch samples increased to 89 300 cycles under constant amplitude loading conditions with a strain range of 0.75 %.

Increasing the strain range at the notch surface decreased the fatigue life and increased the total number of crack initiation events on the U-notch surface. The relationship between strain range and total lifetime was captured using the Coffin-Manson total life approach to lifetime prediction.

7.3 Effects of single periodic tensile overloads on fatigue behaviour and life

Industry representative single periodic tensile overloads with OLR of 1.11 applied every 150 baseload cycles did not appear to affect fatigue behaviour in terms of lifetime when compared to constant amplitude loading conditions, as predicted by the literature. These minimal overload cycles are therefore not expected to affect lifetimes of in-service turbine blades.

Single periodic tensile overloads with OLR of 1.56 applied every 150 baseload cycles increased the number of crack initiation events. However, the number of cycles to crack initiation were substantially increased, attributed to a compressive residual stress within the notch field induced by the overload cycles. Secondly, the short crack growth rate and long

crack growth rate were retarded, attributed to compressive residual stress ahead of the crack tip. The lifetime of polished U-notch samples was increased to 98 000 cycles under constant amplitude loading conditions with a baseload strain range of 0.75 %. The relationship between strain range and total lifetime for shot peened surface conditions was also captured using the Coffin-Manson total life approach.

An unsuccessful attempt was made to measure possible strain hardening beneath the notch surface of a fir-tree-root cross section using microhardness indentation subjected to overload cycles with OLR of 1.11. FE modelling was used to measure the predicted compressive residual stress in the notch field for overloads with an OLR of 1.11 and 1.56 using elastic-plastic material modelling behaviour. FE modelling showed that overloads with an OLR of 1.11 induced a minimal residual stress in the notch field, whereas an OLR of 1.56 induced a more substantial compressive residual stress in the notch field, capable of retarding short crack growth.

7.4 Effects of a T0 shot peen on fatigue behaviour and life

The T0 industrial standard shot peening process caused significant plastic deformation on the surface of the U-notch sample, which increased the surface roughness considerably with an average R_a surface roughness of 2.7 ± 0.4 µm. However, a T0 shot peened FV448 sample had a rougher surface, which was attributed to variations in application of shot peening and possible material property effects. Pre-existing cracks were observed on the U-notch surface which were responsible for crack initiation occurring early in the fatigue lifetime. Despite this, the compressive residual stress and strain hardening induced by shot peening beneath the U-notch surface, resulted in a considerable retardation in the short crack growth rates of short cracks (up to ten times slower between $\Delta K_{Surface}$ of 15 and 20 $MPam^{0.5}$). The short crack phase of shot peened samples was significantly increased, consequently increasing the fatigue life of shot peened samples to 139 000 cycles under constant amplitude loading with a strain range of 0.75 %. The fatigue resisting properties from shot peening diminished with increasing strain range due to residual stress relaxation.

Single periodic tensile overloads with OLR 1.56 applied every 150 baseload cycles to a shot peened sample did not affect the number of cycles to crack initiation compared to constant amplitude loading. The total number of crack initiation events that made up the primary crack was increased. This in turn reduced the average length of the short crack assumed to be required for a transition to the crack coalescence phase and therefore decreased the number of cycles for the short crack phase. Possible residual stress relaxation between $\Delta K_{Surface}$ of 15 and 20 $MPam^{0.5}$ may have slightly contributed towards the reduction in the number of cycles. The number of cycles for the crack coalescence phase was increased

(and generally varied considerably between surface and loading conditions) possibly suggesting high error in the assumptions used to define the beginning and end of lifetime phases. Overall, additional overload cycles on a shot peened sample slightly reduced the number of cycles to failure compared with constant amplitude loading.

7.5 U-Notch geometry on fatigue behaviour and life

The U-notch radius was decreased, and the notch depth increased to test how changing notch geometry (from grinding out existing cracks) affects the fatigue life. FE modelling showed that decreasing the radius or increasing the depth while maintaining a constant strain range at the notch surface minimally altered the stress and strain distribution within the notch field. Experimental testing of U-notch samples with constant strain amplitude of 0.75 % on the notch surface also suggested that changing the notch radius and depth did not significantly alter the lifetime of the samples. It is much more likely that increasing the notch depth inadvertently increases the strain range at the notch surface (dependent upon sample or component geometry) which has a more significant factor on fatigue life.

7.6 Application of the lifetime extension strategy and life prediction

U-notch samples were subjected to the proposed lifetime extension strategy whereby a polished U-notch was cyclically loaded with strain range of 0.75 % until a surface crack 1 mm in length was observed. The cracks were ground away followed by shot peening and cyclically loaded until with the same strain range of 0.75 % until failure. The combination of effectively reversing the fatigue process, followed by lifetime extension from shot peening, was responsible for the extension in fatigue life compared to the fatigue life of samples with a polished U-notch.

A lifetime prediction model was developed based upon a total life approach (Coffin-Manson) and a damage tolerant approach (Paris-law) to predict the lifetime of samples subjected to the lifetime extension strategy with both conservative and non-conservative approaches. Additionally, the model was also used to predict the maximum increase in strain range at the notch surface after the lifetime extension strategy was applied that still results in a lifetime extension. The model can be used alongside FE modelling of in-service turbine blade root-fillets to determine the efficacy of the lifetime extension strategy as a maintenance procedure for in-service life extension.

Chapter 8: Recommendations for industry and future work

This chapter aims to provide comments and recommendations for industry based upon the outcome of the research work presented in this thesis. The current work section briefly discusses 'parallel' research work being carried out at the University of Southampton, to develop the understanding of fatigue behaviour across various materials and enhance the appropriability of an industrially relevant prediction model. The future work section explores avenues for further development that was only briefly explored or not considered as part of this PhD.

8.1 Recommendations for industry

8.1.1 General comments

U-notched samples made from FV448 contained stringers that were oriented parallel to the short crack growth depth direction. Crack initiation occurred preferentially at stringers, which caused abnormally high *a/c* ratios and affected early short crack growth. However, stringers were observed as spherical depressions on the fracture surface of some U-notch samples made from ex-service FV566 blade material, indicating that the stringer orientation was parallel to the tensile axis (perpendicular to the axis of centripetal acceleration). The *a/c* ratios of early short cracks tended to be similar to theoretical values (approximately 0.8) and short crack growth behaviour was not affected by stringers. As U-notch samples made from ex-service FV566 material were notched to represent in-service conditions, it may be reasonable to assume that initiation and early short crack growth behaviour of in-service turbine blades will not be influenced by stringers, as observed in FV448 bar stock material studied previously.

One of the aims of this thesis was to understand and quantify possible effects of 10 % over-speeds on the fatigue life of in-service turbine blades. The effects of single periodic tensile overloads with OLR of 1.11 applied every 150 baseload cycles on the fatigue behaviour and lifetimes of U-notched samples were investigated. It was found in the literature that overloads with OLR greater than 1.44 were required to induce changes in fatigue behaviour. Furthermore, no effects of single periodic tensile overloads with OLR of 1.11 every 150 baseload cycles were observed on fatigue behaviour or fatigue lifetimes of representative U-notch samples. Therefore 10 % over-speeds every 150 start-stop cycles are not expected to alter the fatigue behaviour or fatigue life of in-service turbine blades, compared to constant amplitude cycling alone. Minimum over-speeds of 40 % to 50 % applied every 150

start-stop cycles, may induce a compressive residual stress in the fir-tree-root-fillets of in-service turbine blades, shown to increase the number of cycles to crack initiation and retard short crack growth. However, the application of such relatively large over-speeds is ill-advised as a service life extension strategy, due to the high risk of failure to interconnecting components of the turbine assembly.

Non-destructive testing methods are currently adopted by energy companies during inspection of components. Fatigue flaws of 1 mm in size have been identified in the fir-tree-root-fillets of turbine blades (personal communication, EDF, January, 2018). Analysis of surface replicas during fatigue testing of U-notched samples, suggests that flaws of 1 mm in size were first observed to occur on the surface of the U-notch between 78 % and 85 % of total lifetime (for samples with a width of 8 mm and depth of 8 mm). A 1 mm sized short crack in the fir-tree-root-fillet of a turbine blade may not indicate such an advanced stage of fatigue (defined as lifetime percentage). The increased width and depth of the turbine fir-tree-root geometry may result in longer lifetimes than the U-notch sample geometry, but this assumption is yet to be conclusively shown. As such, the results from experimentation suggests that identification of a 1 mm sized flaw in the fir-tree-root-fillets poses a serious risk to safe operation and requires remedial action. It is possible that a lifetime extension strategy, involving grinding/machining out existing cracks followed by shot peening on the fir-tree-root-fillets of in-service turbine blades, may provide some service life extension.

8.1.2 Efficacy and application of the lifetime extension strategy

It is anticipated that the lifetime extension strategy developed in this thesis may be adapted for application during inspection/maintenance procedures to in-service turbine fir-tree-root-fillets with existing short cracks. The following general comments are recommendations for the lifetime extension strategy adaptation to application as a maintenance strategy for extending service life.

So far, the efficacy of the lifetime extension strategy has been based upon tests that have had no initial exposure to fatigue loading. Additionally, the fatigue lives of U-notch samples were defined as when final failure had occurred. However, the question of whether the lifetime extension strategy can be used for industrial purposes must meet separate criteria. The end of fatigue life for in-service turbine blades is reasonably defined by the non-destructive detection of a short crack with surface length of at least 1 mm within the fir-tree-root-fillet. Secondly, the application of the lifetime extension strategy should only be considered on turbine blades that have effectively come to the end of their fatigue lives (or will come to the end of their fatigue lives before the next inspection). As such, the application of the lifetime extension strategy will always provide some extension to the service life of

otherwise condemned turbine blades, by effectively reversing the fatigue process. Safe application of a lifetime extension strategy would therefore depend upon the prediction of the number of start-stop cycles to grow a short crack with surface length of 1 mm, and the number of cycles to the next inspection (accounting for appropriate error). Some additional considerations need to be addressed before the efficacy of the lifetime extension strategy as a maintenance procedure can be fully determined. These will be discussed in turn:

- Can all the surface cracks be 'fully' ground away so as to leave no residual cracks in the in-service turbine fir-tree-root-fillets, as was achieved in experimental tests?
- Is a T0 shot peen suitable for industrial application to in-service blade fir-tree-root-fillets?
- Grinding or machining out existing cracks, thereby changing the notch geometry, will subsequently increase the strain range at the notch surface, which will decrease the fatigue life.
- The U-notch samples are not of representative geometry in terms of actual width and depth of the sample.
- No experimental testing has been carried out to test the applicability of the prediction model for actual turbine blade geometry.

All existing short cracks must be 'fully' removed during the grinding/machining process, leaving no residual cracks on the fir-tree-root-fillet surface. Failure to fully remove all cracks are expected to shorten the total lifetimes of modified components by effectively removing the crack initiation phase [5], and may invalidate the prediction model developed in this thesis. Satisfactory removal of existing cracks by grinding or machining methods, will subsequently increase the depth of the fir-tree-root-fillet notch by at least 75 % of the surface length of the longest crack. This method reasonably assumes that short cracks with at least 1 mm surface length, will have a semi-elliptical *a/c* ratio less than 1.5. The surface should be inspected for the presence of residual cracks immediately after grinding/machining of the fir-tree-root-fillet. This can be carried out by examining silicone surface replica or mobile optical microscopy equipment on the modified fir-tree-root-fillet surface.

Selected U-notch samples received an industrially recognised shot peening process by an independent specialist (Sandwell UK Ltd). This shot peening process is applied to components used in industrial applications. Previous research by He and Soady [5, 10], explored various industrial shot peening procedures and concluded that 'T0' shot peening potentially offered the most benefit to service life extension in a turbine blade representative FV448 material. The suitability of the application of a T0 shot peening process, as well as optimisation processes and quality assurance procedures for industrial application, have been suitably explored in depth by Soady [10].

The last three considerations can be answered with further development of FE modelling combined with additional testing of the root-block of ex-service turbine blades. This proposed future work is discussed in more detail in Chapter 8.2.2.1.

8.2 Current and future work

8.2.1 Current work

Parallel research work that is partially following on from this thesis, is currently being carried out at the University of Southampton by Ara Khodavirdi. Ex-service turbine blades made from FV520B martensitic stainless steel are being used to investigate crack initiation and early short crack growth behaviour. The work is also partially funded by the sponsor of this thesis (EDF Energy). The aim of this collaborative effort is to further the understanding of fatigue behaviour in U-notched martensitic stainless steels, and to progress the development of a prediction model for industrial application.

In Chapter 3.4.2, the yield strengths of FV566, FV448 and FV520B martensitic stainless steels using hardness measurements were found to be estimated with good accuracy. However, the ultimate tensile strength of the materials were typically overestimated. A proposed reason for the lack of accuracy is the method for calculating the ultimate tensile strength was based upon steels with a higher ductility. Work is currently being carried out to include ductility as a variable when estimating ultimate tensile strength. Charpy impact testing could be applied to test specimens that may otherwise not be large enough for tensile testing, and provide ductility information that may increase reliability of ultimate tensile strength estimations.

It has been shown that crack initiation behaviour is affected by surface conditions, therefore the U-notch surface is being characterised using 2D areal profile S_a measurements rather than less informative tactile profile R_a measurements. Areal measurements are considered more informative since they provide topographical information that is more representative of the surface and capture maximum peaks and troughs with high probability.

There is evidence that suggests that the primary initiation mechanism for a polished U-notch surface made from FV566 was from persistent slip band formation. In FV520B, it is suspected that these slip bands prefer to form within retained or reverted austenite phases. Characterising the distribution of these austenite phases via EBSD may provide some probabilistic indication as to where initiations are likely to occur on the U-notch surface. Predicting the location of crack initiations may contribute towards the understanding of the relationship between out-of-plane variance (average out-of-plane distance between crack

initiation locations) and U-notch radius. EBSD will also be applied to the U-notch surface of partially tested samples to understand the role of microstructure on the crack initiation to short crack transition.

After T0 shot peening has been applied to the U-notch surface of FV520B material, pre-existing cracks were observed due to large plastic deformation, a typical observation encountered on FV448 and FV566 material. Cracks preferentially initiated at these pre-existing cracks on the U-notch surface for all three materials tested. Further work is being carried out to investigate how T0 shot peening influences the distribution of crack initiation locations and the transition towards early short crack growth behaviour. The $\Delta K_{Surface}$ of short cracks on shot peened notch surface conditions were calculated assuming theoretical *a/c* ratios. However, a common observation in all three materials, is that the compressive residual stress induced by shot peening process reduces the *a/c* ratio of short cracks. Therefore, work is being carried out to account for the effects of shot peening on *a/c* ratios in $\Delta K_{Surface}$ calculations.

The lifetime prediction model is being further developed to account for the effects of surface conditions and microstructure on the number of cycles to crack initiation. Additionally, the effect of material mechanical properties such as Young's modulus, yield strength, ultimate tensile strength and hardness with lifetime are currently being explored.

8.2.2 Future work

The literature review highlights areas of research that are of relevance to the thesis but were not completed due to software, equipment or time constraints. In addition, the experimental work, analysis of results and overall findings, raised further questions and areas for exploration. These areas will be briefly discussed along with their relevance to the progression of the development of an industrial solution.

8.2.2.1 Development of the FE model

An elastic-plastic material model was used in FE modelling to describe the material behaviour of FV566 during both loading and unloading steps. However, the applied FE model does not account for material hardening effects during loading or the Bauschinger effect during unloading. The isotropic-kinematic hardening model developed by Chaboche [190] is commonly used to describe such material behaviours in steel [6, 187] and has been used successfully in FV448 turbine blade material [10, 125].

The model can be further developed by accounting for residual stress and strain hardening profiles from shot peening. A thermal coefficient is applied to the material and a subroutine

created to assign a temperature to selected mesh nodes. An initial equilibrium step is introduced to allow the nodes with hypothetically inflated temperature to resolve into a residual stress field. The magnitude of the residual stress field can be pre-calculated using an eigenstrain approach to match residual stress profiles obtained experimentally. Combined with the Chaboche isotropic-kinematic hardening material model, residual stress relaxation after a loading cycle can be modelled with accuracy [125]. The residual stress and strain profiles from various shot peening processes could be modelled and adopted to various notch geometries. This can lead to a further understanding of how changing the U-notch geometry after shot peening affects fatigue behaviour and may indicate an optimum notch geometry of relevance to industry.

8.2.2.2 Development of the lifetime prediction model

The Coffin-Manson total life prediction approach was used for both polished and shot peened U-notch surface conditions. This method requires large amounts of experimental testing to obtain the constants and coefficients required for each surface condition. It is well known that the compressive residual stress from the process of shot peening, reduces the cyclic mean stress, which results in a fatigue life extension. Therefore, the Smith-Watson-Topper (SWT) total lifetime prediction approach can be used to account for mean stress effects in the low cycle fatigue regime [126]. The application of the SWT approach requires less experimental testing since only one set of coefficients are required, given the residual stress profiles of each shot peening process can be obtained and incorporated into an FE model. An adequately developed FE model (discussed in the previous chapter) can be used alongside the SWT approach, which may allow for a more extensive and flexible application to lifetime prediction [126].

8.2.2.3 Crack initiation modelling

The number of cycles to crack initiation for various surface conditions was found by retracing replica records and observing directly when initiation was first observed. This approach is not flexible enough to be extended to other surface conditions without further experimental testing. Prediction models developed by Tanaka and Mura [148], based upon the accumulation of irreversible dislocation pile-up, and a critical energy value, can be used to estimate the number of cycles to crack initiation (Chapter 2.4.3.1). A crack initiation prediction model based on Tanaka and Mura may be extended for a variety of surface and loading conditions [191, 192]. The model may therefore be adapted to allow a prediction for crack initiation with various similar industrial shot peening procedures such as T1 [126].

8.2.2.4 Crack coalescence modelling

The number of cycles for the crack coalescence phase was based on the dubious assumption that each of the four fatigue life-cycle phases were mutually exclusive of each other. In reality, the crack initiation, short crack and crack coalescence phases occur simultaneously, where each phase may affect the other over a slow transitional period until a full width crack is achieved. While some observational work was carried out to understand crack coalescence behaviour, more work is needed to incorporate crack coalescence behaviour into a prediction model. The out-of-plane distance between crack initiation locations and the resulting effect on crack coalescence behaviour still needs to be fully understood. The out-of-plane distance between two near coalescing cracks, may impact the short crack growth rate of cracks in the final cycles prior to coalescence. The out-of-plane distance versus crack growth rate during coalescence could be investigated both experimentally and through XFEM modelling. While this work has been attempted on flat surfaces under bending conditions (plain bend bars), such an investigation has not been carried out on the surface of U-notch geometry to the author's knowledge. Understanding the relationship between out-of-plane distance and short crack growth rates may lead to the discovery of a possible relationship between the out-of-plane variance and extension to total fatigue life (It is assumed that an out-of-plane variance of zero will result in the shortest total life). The out-of-plane variance for two U-notches geometries of varying radius was briefly investigated in this thesis. Surprisingly, reducing the U-notch radius has a smaller than expected reduction in the out-of-plane variance of samples under 3-point bending. Further experimentation to discover how out-of-plane variance changes with U-notch radius could provide a prediction of lifetime extension with out-of-plane variance after grinding out existing cracks.

8.2.2.5 Lifetime extension strategy application to industry

The difference between U-notch sample and fir-tree-root-fillet geometry is a notable limitation of the work carried out in this thesis. Understanding these differences is vital to incorporating the lifetime extension strategy as a maintenance procedure with appropriate confidence. One major difference is the width of the fir-tree-root-fillet, which is much wider than the 8 mm width of the U-notch samples. The extra width of the fir-tree-root-fillet geometry may influence initiation location distribution, which may affect early crack growth and coalescence behaviour. A much longer crack is required to achieve a full width crack in fir-tree-root-fillets and therefore the crack coalescence phase may provide an additional lifetime benefit. Furthermore, the loading conditions at the fir-tree-root-fillets are a combination of tensile loading and bending, rather than the pure bending experienced in

experimental testing. A variation in loading conditions could result in a variation in the relationship between crack growth rate and ΔK for both long and short cracks.

A scan of in-service turbine blade geometry can be carried out and imported into FE modelling software, and in-service representative loading conditions applied. Similar FE models of turbine blade geometry has been carried out by Frazer-Nash Consultancy [193] and by E.ON [194] cited in [10] for analysis purposes. FE modelling combined with experimental testing of a turbine root-block assembled with its corresponding rotor disc, could address some of the questions surrounding the differences in geometry, and provide additional confidence in the lifetime extension strategy. In addition, the FE model can be used to estimate the increase in strain range from grinding out existing cracks in the fir-tree-root-fillet geometry. For reasonable application of the lifetime extension strategy, the service life extension should be at least a factor of two times the number of start-stop cycles until the next routine inspection.

The shot peening process caused significant surface damage from high levels of plastic deformation and induced pre-existing cracks. The surface damage ultimately reduced the resistance to crack initiation since pre-existing cracks were observed to be preferred initiation sites. On the other hand, laser shock peening was found to improve the maximum level and depth of beneficial compressive residual stress, and reduce the amount of damage observed on the surface of high strength aluminium material AA7075-T651 [186]. The applicability of laser shock peening as an alternative to shot peening could be explored. A possible increased level of resistance to crack initiation could be investigated on U-notched martensitic stainless steels, which may offer an additional improvement in service-life after turbine blades have been subjected to the lifetime extension strategy.

Appendix A: Long crack testing procedure

A.1 SEN bend test setup

All long crack testing was carried out to British Standards *BS ISO 12108:2012* [157]. The SENB3 (single edge notch 3-point bend) sample was placed in an INSTRON 8502 hydraulic cyclic test machine in 3-point bending test configuration with a top roller span of 40 mm. Conductive wires were spot welded onto the surfaces of the sample and connected to a DCM-2 DCPD (Direct Current Potential Difference) crack growth monitoring machine using the configuration shown in Figure A-1. The surfaces of the sample were polished using progressively finer grinding and polishing stages to 1 µm suspension to increase the spot-welding contact strength. Ten Amps were applied through the sample. The time and the potential difference reading across the crack were recorded. The potential difference across a section of the sample with no crack was measured as a reference reading to account for variables such as temperature and humidity that may affect the baseline reading.

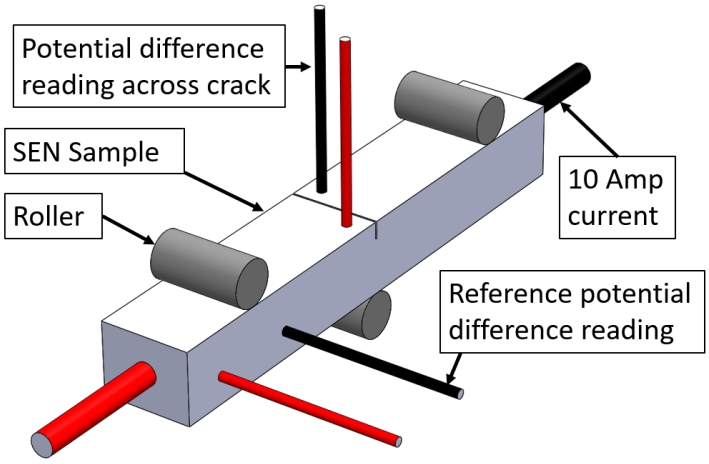

Figure A-1: Schematic model of the SEN bend sample showing the configuration of the wires spot welded to the sample and the roller locations for 3-point bending.

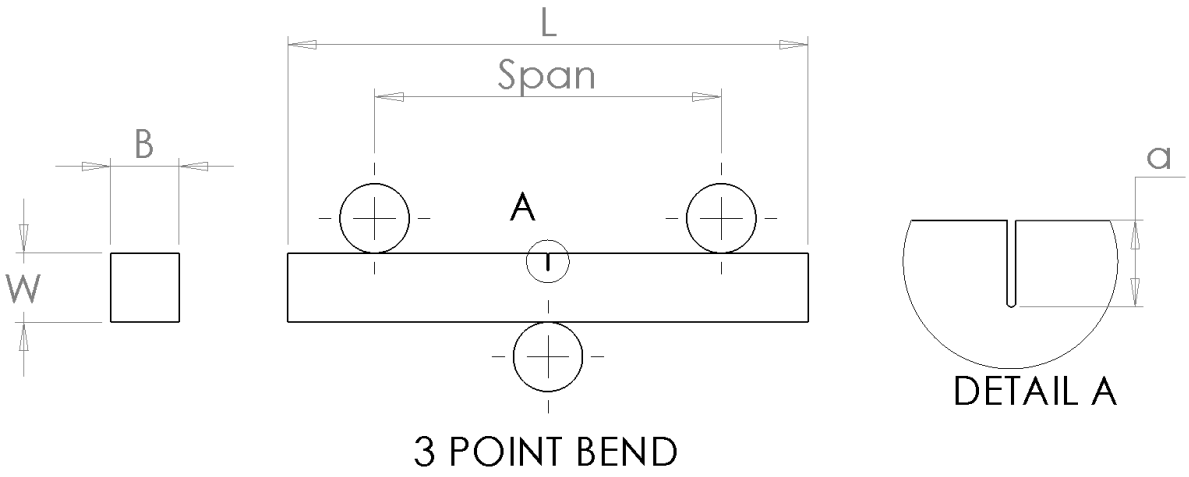

Figure A-2: SENB3 sample drawing showing the dimensions of a (crack length), *W* (sample width) and *B* sample breadth.

As the crack grows, the potential difference across the crack increases. A calibrated empirical relationship found from a previous calibration test (private communication, University of Southampton, April 2018) was used to relate the potential difference across the crack in mV with crack length. The relationship was expressed as a 3rd degree polynomial that can be scaled appropriately for individual test samples.

A.1.1 Calculation of load range for target *ΔK* value

The following procedure was carried out to calculate the load input data required to achieve a target *ΔK* value that is typically found from literature for pre-cracking purposes. Equation A-1 is used to find the X_0 value that is the expected potential difference reading in mV from calibration testing and was found using an iterative solver tool in Microsoft Excel.

$$\left(\frac{a}{W}\right)_i = AX_0{}^3 + BX_0{}^2 + CX_0 + D \qquad \text{Equation A-1}$$

Where $\left(\frac{a}{W}\right)_i$ was calculated by measuring the width of the sample W and the initial crack length a prior to testing (Figure A-2). The cubic constants *A, B, C* and *D* were found from calibration testing.

The potential difference across the crack (X) to reference potential difference ratio (R) is recorded by the DCM2 machine. This is multiplied by the reference potential difference (R) to initial potential difference across crack from calibration tests (X_0). Since the reference potential difference did not change throughout the test, the resulting calculation is a $\frac{X}{X_0}$ ratio. Testing in variable environmental conditions such as high temperature testing, the reference

potential difference will change throughout the test. Hence a $\frac{V}{V_0}$ ratio was used to account for this possibility (Equation A-2).

$$\frac{V}{V_0} = \frac{X}{R} \times \frac{R}{X_0} \qquad \text{Equation A-2}$$

The $\frac{V}{V_0}$ ratio will increase during the test as the crack grows and therefore as $\frac{a}{W}$ ratio increases. The relationship between crack length and potential difference from calibration tests (scaled for this particular test) can be used to calculate the $\frac{a}{W}$ ratio at any given $\frac{V}{V_0}$ reading (Equation A-3) and therefore at any given $\frac{X}{R}$ reading (typically displayed on DCM2 machines).

$$\frac{a}{W} = A\left(\frac{V}{V_0}\right)^3 + B\left(\frac{V}{V_0}\right)^2 + C\left(\frac{V}{V_0}\right) + D \qquad \text{Equation A-3}$$

The geometry correction factor (Y) from Equation A-4 extracted from British Standards *BS ISO 12108:2012* [157] was used to account for the change in sample compliance as the crack grows, necessary when calculating the load range ΔP.

$$\mathrm{Y} = \frac{6\left(\frac{\mathrm{a}}{\mathrm{W}}\right)^{\frac{1}{2}}}{\left[\left(1+2\frac{\mathrm{a}}{\mathrm{W}}\right)\left(1-\frac{\mathrm{a}}{\mathrm{W}}\right)^{\frac{3}{2}}\right]}\left[1.99 - \frac{\mathrm{a}}{\mathrm{W}}\left(1-\frac{\mathrm{a}}{\mathrm{W}}\right)\left(2.15 - 3.93\frac{\mathrm{a}}{\mathrm{W}} + 2.7\left(\frac{\mathrm{a}}{\mathrm{W}}\right)^2\right)\right] \qquad \text{Equation A-4}$$

Equation A-5 can be used to find the cyclic load range *(*ΔP) and therefore the mean load (P_{mean}) and amplitude (P_{amp}) values to achieve a specific *ΔK* value as the crack grows.

$$\Delta P = \frac{\Delta K \times B\sqrt{W}}{Y \times 10^{1.5}} \qquad \text{Equation A-5}$$

Where B is the breadth of the sample (Figure A-2). As the crack grows, the $\frac{X}{R}$ ratio increases and thus the *ΔK* value increases if *(*ΔP*)* remains constant. A target $\frac{X}{R}$ ratio is found by calculating the change in the $\frac{X}{R}$ ratio that results in an increase of the *ΔK* value by approximately 1 %. The load values are decreased accordingly when the target $\frac{X}{R}$ ratios have been achieved during testing to maintain a constant *ΔK* value ± 1 %.

A.1.2 Calculating adjusted *ΔK* value during post-test analysis

The $\frac{a}{W}$ ratio at the beginning of the grow-out stage and at final failure was estimated during testing based upon the relationship found during calibration. The actual $\frac{a}{W}$ ratio at final failure was found by measuring the final crack length of the fracture surface after testing to British Standards *BS ISO 12108:2012* [157] using image processing software. It is likely, that the $\frac{a}{W}$ ratio estimation from calibration testing does not match the measured $\frac{a}{W}$ ratio, and therefore a linear adjustment process is required to fine tune the estimation using Equation A-6:

$$\left(\frac{a}{W}\right)_{adj} = \left(\frac{a}{W}\right)_g + \frac{\frac{a}{W} - \left(\frac{a}{W}\right)_g}{\left(\frac{a}{W}\right)_f - \left(\frac{a}{W}\right)_g} \times \frac{(a_f - a_g)}{W} \qquad \text{Equation A-6}$$

where $\left(\frac{a}{W}\right)_{adj}$ is the adjusted $\frac{a}{W}$ ratio, $\left(\frac{a}{W}\right)_g$ is the $\frac{a}{W}$ ratio at the beginning of the grow-out stage, $\left(\frac{a}{W}\right)_f$ is the $\frac{a}{W}$ ratio at final failure, a_f is the measured crack length at failure and a_g is the measured crack length at the beginning of the grow-out stage.

The adjusted $\frac{a}{W}$ ratios were used to calculate the adjusted geometry factor Y_{adj} in Equation A-7.

$$\mathrm{Y}_{adj} = \frac{6\left(\frac{\mathrm{a}}{\mathrm{W}}\right)_{adj}^{\frac{1}{2}}}{\left[\left(1 + 2\left(\frac{\mathrm{a}}{\mathrm{W}}\right)_{adj}\right)\left(1 - \left(\frac{\mathrm{a}}{\mathrm{W}}\right)_{adj}\right)^{\frac{3}{2}}\right]} \times \qquad \text{Equation A-7}$$

$$\left[1.99 - \left(\frac{\mathrm{a}}{\mathrm{W}}\right)_{adj}\left(1 - \left(\frac{\mathrm{a}}{\mathrm{W}}\right)_{adj}\right)\left(2.15 - 3.93\left(\frac{\mathrm{a}}{\mathrm{W}}\right)_{adj} + 2.7\left(\frac{\mathrm{a}}{\mathrm{W}}\right)_{adj}^{2}\right)\right]$$

Equation A-5 was rearranged to find the final *ΔK* values in Equation A-8.

$$\Delta K_{adj} = \frac{\Delta P \times Y_{adj} \times 10^{1.5}}{B\sqrt{W}} \qquad \text{Equation A-8}$$

The number of cycles was found from time stamp recording and the frequency of the test.

A.1.3 Noise reduction

The potential difference reading across the crack fluctuated during the test which produced noise. The raw data was smoothed using the LOESS function with a 4th degree polynomial and sampling size of 0.1 [10].

Appendix B: Mesh convergence analysis

A mesh convergence analysis was carried out using ABAQUS finite element modelling software to determine and validate an efficient and adequate mesh for experimentation purposes. A quarter-model of a plain bend bar was modelled in a 4-point bending test configuration. An elastic-plastic material model based upon monotonic tensile testing was applied to the model. A global mesh with a course initial mesh size was assigned to the entire model. C8D20 elements were used throughout convergence analysis testing. A load of sufficient magnitude to induce plastic deformation and representative of experimental testing was chosen. The analysis was run and the stress and strain of a node located at a region of interest was recorded (top surface centre of the PBB). The global size of the mesh was decreased with subsequent analysis runs, consequently increasing the total number of mesh elements (Figure B-1).

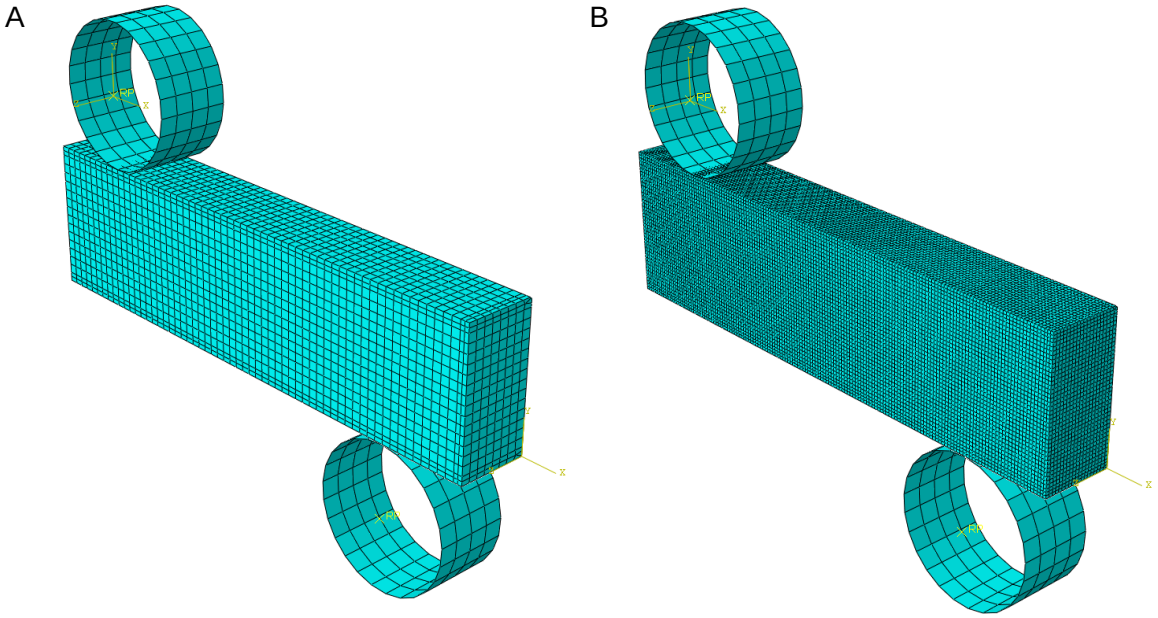

Figure B-1: A) An example of a coarse mesh and B) an example of a higher density mesh.

Tensile stress versus number of elements were plotted for both stress and strain values (Figure B-3). As mesh density increases, the stress and strain values reaches an asymptotic value, at which the mesh is considered adequate. For this particular model, a mesh was considered adequate when a tensile stress of 1400 MPa or 0.008 tensile strain was recorded (at a global mesh size resulting in 60 000 mesh elements).

An optimised mesh was developed (Figure B-2) by decreasing the mesh density only in regions unlikely to affect the tensile stress or strain at the location of interest. The tensile stress and strain obtained by using the optimised mesh model is compared with converged

tensile stress and strain values (Figure B-3). While this mesh configuration model contains fewer mesh elements, it is not expected to reduce the accuracy of the results obtained at the region of interest and is considered adequate for testing purposes.

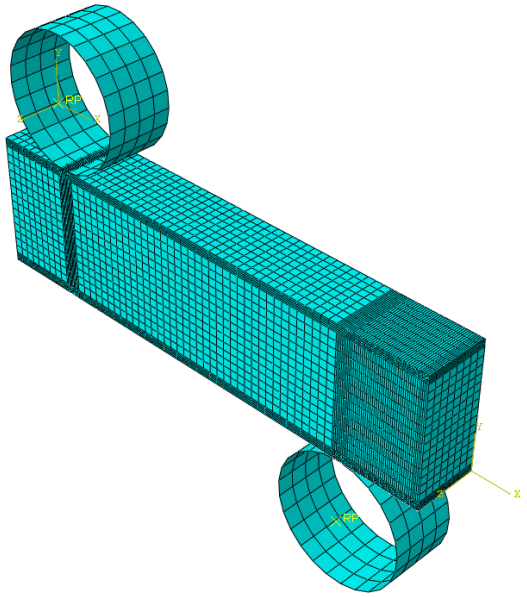

Figure B-2: An example of an optimised mesh with a coarse overall mesh and higher density mesh in areas of interest.

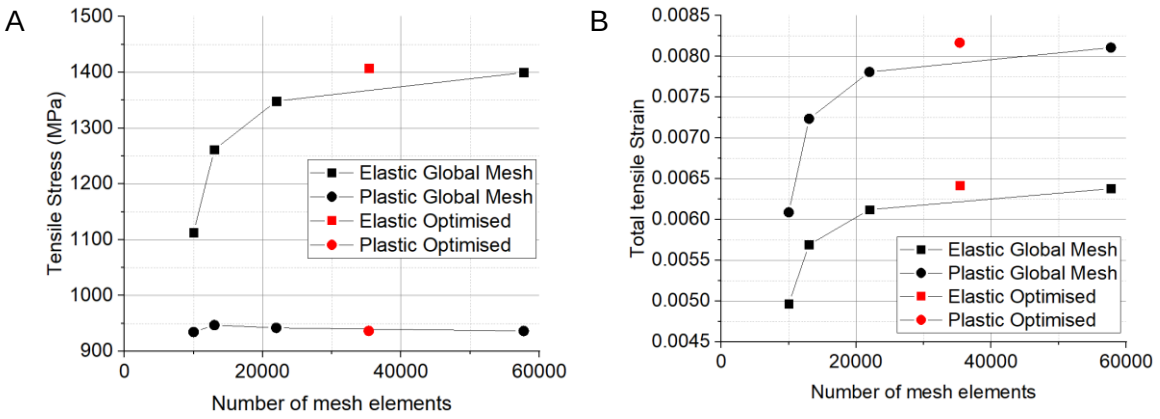

Figure B-3 Mesh convergence analysis results for A) Tensile stress and B) Tensile strain measurements using both linear-elastic and elastic-plastic material models. The results marked in red shows the tensile stress and strain values using the optimised mesh configuration. Only results from models up to 60 000 mesh elements are shown for clarity.

Appendix C: Determination of short crack $\Delta K_{Surface}$

The calculation of $\Delta K_{Surface}$ of short crack surfaces is based upon the work of Scott and Thorpe [52] and Holdbrook and Dover [53].

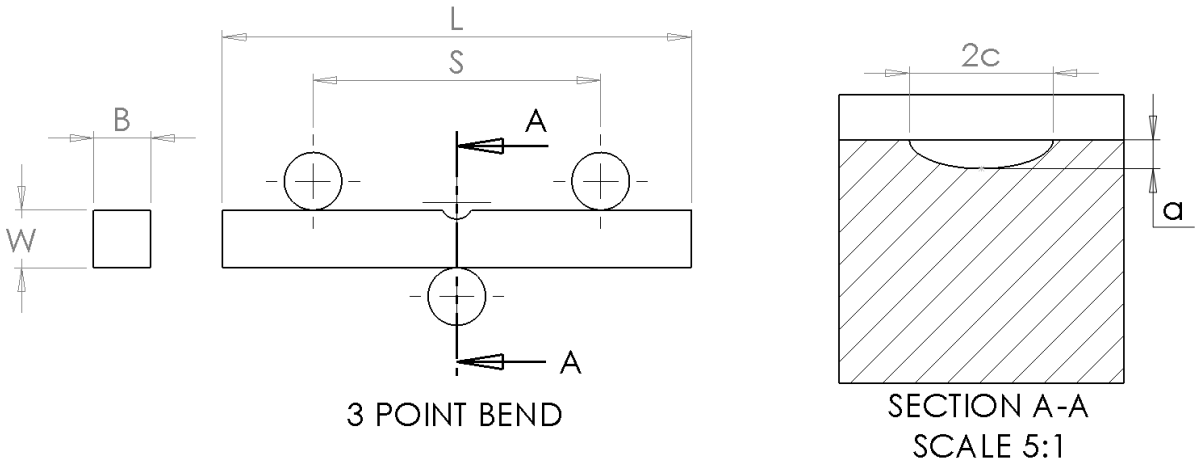

Figure C-1: Drawing of U-notch sample with dimensions labelled. Cross section of U-notched sample through notch centre containing semi-elliptical crack with dimensions labelled.

The theoretical $\frac{a}{c}$ ratio of a semi-elliptical short crack depends upon its projected surface crack length (*2c*) and can be calculated using Equation C-1 [50]. Therefore, the theoretical $\frac{a}{c}$ ratio is calculated for each surface crack measurement and the calculation of $\Delta K_{Surface}$ assumes a perfect semi-ellipse shape.

$$\frac{a}{c} = 0.8238 - 8.4487 \times 10^{-5}(2c) + 5.1931 \times 10^{-9}(2c)^2 \qquad \text{Equation C-1}$$

Where c is half the projected surface crack length and a is the semi-elliptical crack depth (Figure C-1).

A 'crack tip stress intensity factor' (ΔK_1) for semi-elliptical cracks in a semi-finite plate and under pure bending conditions is proposed by Scott and Thorpe [52] in Equation C-2:

$$\Delta \mathrm{K}_1 = \left[\left[M_{f(0)}\left(1 - 0.3\left(\frac{a}{W}\right)\right)\left(1 - \left(\frac{a}{W}\right)^{12}\right)\right] + \left[0.394\, E(k)\left(\frac{a}{W}\right)^{12}\sqrt{\frac{c}{a}}\right]\right]\frac{\sigma_b}{E(k)}\sqrt{\pi a} \qquad \text{C-2}$$

where *W* is the depth of the sample (Figure C-1) and σ_b is the pure bending stress at the notch surface calculated using Equation C-3 or via FE modelling.

$$\sigma_b = \frac{3k_t F(S_t - S_b)}{2BW^2}$$ Equation C-3

Where F is the total maximum force, S_t is the top roller span, S_b is the bottom roller span (for 3-point bending this value is 0), B is the sample breadth (Figure C-1) and k_t is the notch stress concentration factor (Equation C-4).

$$k_t = \frac{\begin{matrix}Maximum\ tensile\ stress\ on\ U-notch\ surface \\ based\ upon\ elastic\ FE\ modelling\ material\ behaviour\end{matrix}}{\begin{matrix}Maximum\ tensile\ stress\ calculated\ from \\ beam\ theory\ with\ equaivalent\ CSA\end{matrix}}$$ Equation C-4

A ‘front face correction factor’ $M_{f(0)}$ (Equation C-5) and an ‘elliptic integral of the second kind’ $E(k)$ (Equation C-6) were found via ‘empirical observation of crack shape during fatigue’ to account for finite plate thickness and surface dimension effects [52].

$$M_{f(0)} = \left[1.21 - 0.1\left(\frac{a}{c}\right) + 0.1\left(\frac{a}{c}\right)^4\right]\sqrt{\frac{a}{c}}$$ Equation C-5

$$\mathrm{E(k)} = \sqrt{1 + 1.47\left(\frac{a}{c}\right)^{1.64}}$$ Equation C-6

A ‘finite width correction factor’ (Equation C-7 to Equation C-10) found by empirical fitting and interpolation of experimental data by Holdbrook and Dover [53] can be used to calculate the final $\Delta K_{Surface}$ for semi-elliptical short cracks.

$$B_w = 1 + \frac{F\left(\frac{a}{c}\right)G\left(\frac{c}{B}\right)H\left(\frac{a}{W}\right)}{(0.2745)^2}$$ Equation C-7

Where:

$$F\left(\frac{a}{c}\right) = 0.381 - 0.141\left(\frac{a}{c}\right) - 0.366\left(\frac{a}{c}\right)^2 + 0.569\left(\frac{a}{c}\right)^3 - 0.248\left(\frac{a}{c}\right)^4$$ Equation C-8

$$G\left(\frac{c}{B}\right) = -0.0239 + 1.434\left(\frac{c}{B}\right) - 2.984\left(\frac{c}{B}\right)^2 + 7.822\left(\frac{c}{B}\right)^3$$ Equation C-9

$$H\left(\frac{a}{W}\right) = -0.0113 + 0.323\left(\frac{a}{W}\right) + 0.749\left(\frac{a}{W}\right)^2 - 0.535\left(\frac{a}{W}\right)^3$$ Equation C-10

Appendix C: Determination of short crack ΔKSurface

The final $\Delta K_{Surface}$ for each crack is found by multiplying the finite width correction factor by the crack tip stress intensity factor ΔK_1 (Equation C-11).

$$\Delta K_{Surface} = B_w \times \Delta K_1 \qquad \text{Equation C-11}$$

References

[1] M. Power. "CCGT technology." http://www.marchwoodpower.com/ccgt/ (accessed 24/10/2018, 2018).

[2] T. Kern, K. Mayer, B. Donth, G. Zeiler, and A. Di Gianfrancesco, "The European efforts in development of new high temperature rotor materials-COST536," 2010.

[3] C. Charlesworth, "Ultrasonic phased array testing in the power generation industry; Novel wedge development for the inspection of steam turbine blades roots," EngD, School of Engineering, University of Warwick, 2011.

[4] A. Morris, "Last stage steam tubine blades," ed. EDF Energy, 2018.

[5] B. He, "Fatigue crack growth behaviour in a shot preened low pressure steam turbine blade material," Thesis (Ph D) - University of Southampton, Faculty of Engineering and the Environment, 2015, Original typescript,, 2015. [Online]. Available: http://eprints.soton.ac.uk/388077/

[6] F. Biglari, P. Lombardi, S. Budano, C. Davies, and K. Nikbin, "Predicting damage and failure under low cycle fatigue in a 9Cr steel," *Fatigue & Fracture of Engineering Materials & Structures,* vol. 35, no. 12, pp. 1079-1087, 2012.

[7] Y. Rae, A. Benaarbia, J. Hughes, and W. Sun, "Experimental characterisation and computational modelling of cyclic viscoplastic behaviour of turbine steel," *International Journal of Fatigue,* 2019.

[8] J. W. Morris, C. S. Lee, and Z. Guo, "The nature and consequences of coherent transformations in steel," *ISIJ international,* vol. 43, no. 3, pp. 410-419, 2003.

[9] M. Kimura, K. Yamaguchi, M. Hayakawa, K. Kobayashi, and K. Kanazawa, "Microstructures of creep-fatigued 9–12% Cr ferritic heat-resisting steels," *International Journal of Fatigue,* vol. 28, no. 3, pp. 300-308, 2006/03/01/ 2006, doi: https://doi.org/10.1016/j.ijfatigue.2005.04.013.

[10] K. A. Soady, "Reducing conservatism in life assessment approaches : industrial steam turbine blade to disc interfaces and the shot peening process," Thesis (Eng D) - University of Southampton, Faculty of Engineering and the Environment, 2013, Original typescript,, 2013. [Online]. Available: http://eprints.soton.ac.uk/355952/

[11] A. Handbook, *Heat treating, vol. 4* (ASM International, Materials Park, OH). 1991.

[12] M. Maalekian, "The effects of alloying elements on steels (I)," Institut für Werkstoffkunde, Schweißtechnik und Spanlose Formgebungsverfahren, 2007. [Online]. Available: https://online.tugraz.at/tug_online/voe_main2.getvolltext?pCurrPk=32837

[13] Y. Liu, D. Ye, Q. Yong, J. Su, K. Zhao, and W. Jiang, "Effect of Heat Treatment on Microstructure and Property of Cr13 Super Martensitic Stainless Steel," *Journal of Iron and Steel Research International,* journal article vol. 18, no. 11, pp. 60-66, November 01 2011, doi: 10.1016/s1006-706x(11)60118-0.

[14] Y. J. Zhao, X. P. Ren, Z. L. Hu, Z. P. Xiong, J. M. Zeng, and B. Y. Hou, "Effect of tempering on microstructure and mechanical properties of 3Mn-Si-Ni martensitic steel," *Materials Science and Engineering: A,* vol. 711, pp. 397-404, 2018/01/10/ 2018, doi: https://doi.org/10.1016/j.msea.2017.11.037.

[15] R. C. Thomson and H. K. D. H. Bhadeshia, "Carbide precipitation in 12Cr1MoV power plant steel," *Metallurgical Transactions A,* journal article vol. 23, no. 4, pp. 1171-1179, April 01 1992, doi: 10.1007/bf02665048.

[16] D.-N. Zou, Y. Han, W. Zhang, and X.-D. Fang, "Influence of Tempering Process on Mechanical Properties of 00Cr13Ni4Mo Supermartensitic Stainless Steel," *Journal of Iron and Steel Research, International,* vol. 17, no. 8, pp. 50-54, 2010/08/01/ 2010, doi: https://doi.org/10.1016/S1006-706X(10)60128-8.

[17] N. Seumangal, "Influence of the heat treatment procedure on the stress corrosion cracking behaviour of low pressure turbine blade material FV566," M.S. Thesis, University of Cape Town, 2017.

[18] J. Fan, X. Guo, C. Wu, V. Crupi, and E. Guglielmino, "Influence of heat treatments on mechanical behavior of FV520B steel," *Experimental Techniques,* journal article vol. 39, no. 2, pp. 55-64, March 01 2015, doi: 10.1111/ext.12019.

[19] Q. Guo and X. Guo, "Research on high-cycle fatigue behavior of FV520B stainless steel based on intrinsic dissipation," *Materials & Design,* vol. 90, pp. 248-255, 2016/01/15/ 2016, doi: https://doi.org/10.1016/j.matdes.2015.10.103.

[20] A. Clark, "Fatigue mechanisms in FV520B, a turbine blade steel," Thesis (Ph D) - Sheffield Hallam University, 1999.

[21] G. Kang and Y. Liu, "Uniaxial ratchetting and low-cycle fatigue failure of the steel with cyclic stabilizing or softening feature," *Materials Science and Engineering: A,* vol. 472, no. 1-2, pp. 258-268, 2008.

[22] K. A. Soady, B. G. Mellor, G. D. West, G. Harrison, A. Morris, and P. A. S. Reed, "Evaluating surface deformation and near surface strain hardening resulting from shot peening a tempered martensitic steel and application to low cycle fatigue," *International Journal of Fatigue,* vol. 54, pp. 106-117, 2013/09/01/ 2013, doi: https://doi.org/10.1016/j.ijfatigue.2013.03.019.

[23] M. Pérez, "Impact of annealing treatments on the softening and work hardening behaviour of Jethete M152 alloy for subsequent cold forming processes," *Materials Science and Engineering: A,* vol. 690, pp. 303-312, 2017/04/06/ 2017, doi: https://doi.org/10.1016/j.msea.2017.03.012.

[24] R. Hales, S. R. Holdsworth, M. P. O'Donnell, I. J. Perrin, and R. P. Skelton, "A Code of Practice for the determination of cyclic stress-strain data," *Materials at High Temperatures,* vol. 19, no. 4, pp. 165-185, 2002/12/01 2002, doi: 10.1179/mht.2002.022.

[25] N. Espinoza, B. Carson, and R. Roberts. "Managing the changing profile of a combined cycle plant." Power. https://www.powermag.com/managing-the-changing-profile-of-a-combined-cycle-plant/ (accessed 24/10/2018.

[26] S. Suresh, *Fatigue of Materials*, 2nd ed. Cambridge: Cambridge University Press, 1998.

[27] S. Barella, M. Boniardi, S. Cincera, P. Pellin, X. Degive, and S. Gijbels, "Failure analysis of a third stage gas turbine blade," *Engineering Failure Analysis,* vol. 18, no. 1, pp. 386-393, 2011/01/01/ 2011, doi: https://doi.org/10.1016/j.engfailanal.2010.09.017.

[28] W. Cui, "A state-of-the-art review on fatigue life prediction methods for metal structures," *Journal of marine science and technology,* vol. 7, no. 1, pp. 43-56, 2002.

References

[29] Y. Zhang, J. Wang, Q. Sun, H. Zhang, and P. Jiang, "Fatigue life prediction of FV520B with internal inclusions," *Materials & Design,* vol. 69, pp. 241-246, 2015/03/15/ 2015, doi: https://doi.org/10.1016/j.matdes.2014.12.022.

[30] J. Man, K. Obrtlik, and J. Polak, "Extrusions and intrusions in fatigued metals. Part 1. State of the art and history," *Philosophical Magazine,* vol. 89, no. 16, pp. 1295-1336, 2009.

[31] P. Mu and V. Aubin, "Microcrack initiation in low-cycle fatigue of an austenitic stainless steel," *Procedia Engineering,* vol. 2, no. 1, pp. 1951-1960, 2010.

[32] J. Polák, "On the role of point defects in fatigue crack initiation," *Materials Science and Engineering,* vol. 92, pp. 71-80, 1987/08/01/ 1987, doi: https://doi.org/10.1016/0025-5416(87)90157-1.

[33] J. Polák, J. Man, T. Vystavěl, and M. Petrenec, "The shape of extrusions and intrusions and initiation of stage I fatigue cracks," *Materials Science and Engineering: A,* vol. 517, no. 1, pp. 204-211, 2009/08/20/ 2009, doi: https://doi.org/10.1016/j.msea.2009.03.070.

[34] J. Man, K. Obrtlík, C. Blochwitz, and J. Polák, "Atomic force microscopy of surface relief in individual grains of fatigued 316L austenitic stainless steel," *Acta Materialia,* vol. 50, no. 15, pp. 3767-3780, 2002/09/03/ 2002, doi: https://doi.org/10.1016/S1359-6454(02)00167-2.

[35] J. Man, P. Klapetek, O. Man, A. Weidner†, K. Obrtlík, and J. Polák, "Extrusions and intrusions in fatigued metals. Part 2. AFM and EBSD study of the early growth of extrusions and intrusions in 316L steel fatigued at room temperature," *Philosophical Magazine,* vol. 89, no. 16, pp. 1337-1372, 2009/06/01 2009, doi: 10.1080/14786430902917624.

[36] A. A. Griffith, "VI. The phenomena of rupture and flow in solids," *Philosophical Transactions of the Royal Society of London. Series A, Containing Papers of a Mathematical or Physical Character,* vol. 221, no. 582-593, pp. 163-198, 1921, doi: 10.1098/rsta.1921.0006.

[37] J. R. Rice, "A path independent integral and the approximate analysis of strain concentration by notches and cracks," *Journal of Applied Mechanics,* vol. 35, no. 2, pp. 379-386, 1968.

[38] D. S. Dugdale, "Yielding of steel sheets containing slits," *Journal of the Mechanics and Physics of Solids,* vol. 8, no. 2, pp. 100-104, 1960.

[39] R. O. Ritchie, "Mechanisms of fatigue-crack propagation in ductile and brittle solids," *International journal of Fracture,* vol. 100, no. 1, pp. 55-83, 1999.

[40] C. Laird and G. Smith, "Crack propagation in high stress fatigue," *Philosophical magazine,* vol. 7, no. 77, pp. 847-857, 1962.

[41] P. J. E. Forsyth, "A two stage process of fatigue crack growth," in *Proceedings of the Crack Propagation Symposium*, Cranfield, UK, 1962, pp. 76-94.

[42] G. E. Totten. (May 2008) Fatigue Crack Propagation. *Advanced Materials and Processes*. 39-41.

[43] K. M. Perkins and M. R. Bache, "Corrosion fatigue of a 12%Cr low pressure turbine blade steel in simulated service environments," *International Journal of Fatigue,* vol. 27, no. 10, pp. 1499-1508, 2005/10/01/ 2005, doi: https://doi.org/10.1016/j.ijfatigue.2005.06.031.

[44] W. Z. Wang, F. Z. Xuan, K. L. Zhu, and S. T. Tu, "Failure analysis of the final stage blade in steam turbine," *Engineering Failure Analysis,* vol. 14, no. 4, pp. 632-641, 2007/06/01/ 2007, doi: https://doi.org/10.1016/j.engfailanal.2006.03.004.

[45] K. Miller, "The behaviour of short fatigue cracks and their initiation part ii-a general summary," *Fatigue & Fracture of Engineering Materials & Structures,* vol. 10, no. 2, pp. 93-113, 1987.

[46] K. Miller, "The short crack problem," *Fatigue & Fracture of Engineering Materials & Structures,* vol. 5, no. 3, pp. 223-232, 1982.

[47] M. H. El Haddad, K. N. Smith, and T. H. Topper, "Fatigue Crack Propagation of Short Cracks," *Journal of Engineering Materials and Technology,* vol. 101, no. 1, pp. 42-46, 1979, doi: 10.1115/1.3443647.

[48] S. Beretta and S. Matteazzi, "Short crack propagation in eutectoid steel wires," *International journal of fatigue,* vol. 18, no. 7, pp. 451-456, 1996.

[49] C. You, M. Achintha, B. Y. He, and P. A. S. Reed, "A numerical study of the effects of shot peening on the short crack growth behaviour in notched geometries under bending fatigue tests," *International Journal of Fatigue,* vol. 103, pp. 99-111, 2017/10/01/ 2017, doi: https://doi.org/10.1016/j.ijfatigue.2017.05.023.

[50] B. Y. He, K. A. Soady, B. G. Mellor, G. Harrison, and P. A. S. Reed, "Fatigue crack growth behaviour in the LCF regime in a shot peened steam turbine blade material," *International Journal of Fatigue,* vol. 82, pp. 280-291, 2016/01/01/ 2016, doi: https://doi.org/10.1016/j.ijfatigue.2015.03.017.

[51] C. You, B. Y. He, M. Achintha, and P. A. S. Reed, "Numerical modelling of the fatigue crack shape evolution in a shot-peened steam turbine material," *International Journal of Fatigue,* vol. 104, pp. 120-135, 2017/11/01/ 2017, doi: https://doi.org/10.1016/j.ijfatigue.2017.07.017.

[52] P. M. Scott and T. W. Thorpe, "A critical review of crack tip stress intensity factors for semi-elliptic cracks," *Fatigue & Fracture of Engineering Materials & Structures,* vol. 4, no. 4, pp. 291-309, 1981, doi: doi:10.1111/j.1460-2695.1981.tb01127.x.

[53] S. J. Holdbrook and W. D. Dover, "The stress intensity factor for a deep surface crack in a finite plate," *Engineering Fracture Mechanics,* vol. 12, no. 3, pp. 347-364, 1979/01/01/ 1979, doi: https://doi.org/10.1016/0013-7944(79)90049-3.

[54] E. Wolf, "Fatigue crack closure under cyclic tension," *Engineering Fracture Mechanics,* vol. 2, no. 1, pp. 37-45, 1970/07/01/ 1970, doi: https://doi.org/10.1016/0013-7944(70)90028-7.

[55] A. K. Vasudeven, K. Sadananda, and N. Louat, "A review of crack closure, fatigue crack threshold and related phenomena," *Materials Science and Engineering: A,* vol. 188, no. 1, pp. 1-22, 1994/11/30/ 1994, doi: https://doi.org/10.1016/0921-5093(94)90351-4.

[56] S. Suresh and R. O. Ritchie, "A geometric model for fatigue crack closure induced by fracture surface roughness," *Metallurgical Transactions A,* journal article vol. 13, no. 9, pp. 1627-1631, September 01 1982, doi: 10.1007/bf02644803.

[57] G. T. Gray, J. C. Williams, and A. W. Thompson, "Roughness-Induced Crack Closure: An Explanation for Microstructurally Sensitive Fatigue Crack Growth," *Metallurgical Transactions A,* journal article vol. 14, no. 2, pp. 421-433, February 01 1983, doi: 10.1007/bf02644220.

[58] J. Maierhofer, D. Simunek, H. P. Gänser, and R. Pippan, "Oxide induced crack closure in the near threshold regime: The effect of oxide debris release,"

International Journal of Fatigue, vol. 117, pp. 21-26, 2018/12/01/ 2018, doi: https://doi.org/10.1016/j.ijfatigue.2018.07.021.

[59] P. Pokorný, T. Vojtek, L. Náhlík, and P. Hutař, "Crack closure in near-threshold fatigue crack propagation in railway axle steel EA4T," *Engineering Fracture Mechanics,* vol. 185, pp. 2-19, 2017.

[60] M. M. I. Hammouda, H. G. Osman, and H. E. M. Sallam, "Mode I notch fatigue crack growth behaviour under constant amplitude loading and due to the application of a single tensile overload," *International Journal of Fatigue,* vol. 26, no. 2, pp. 183-192, 2004/02/01/ 2004, doi: https://doi.org/10.1016/S0142-1123(03)00093-8.

[61] R. C. McClung and H. Sehitoglu, "Closure and Growth of Fatigue Cracks at Notches," *Journal of Engineering Materials and Technology,* vol. 114, no. 1, pp. 1-7, 1992, doi: 10.1115/1.2904135.

[62] C. S. Shin and S. H. Hsu, "On the mechanisms and behaviour of overload retardation in AISI 304 stainless steel," *International Journal of Fatigue,* vol. 15, no. 3, pp. 181-192, 1993/05/01/ 1993, doi: https://doi.org/10.1016/0142-1123(93)90175-P.

[63] C. S. Shin and R. A. Smith, "Fatigue crack growth at stress concentrations—the role of notch plasticity and crack closure," *Engineering Fracture Mechanics,* vol. 29, no. 3, pp. 301-315, 1988/01/01/ 1988, doi: https://doi.org/10.1016/0013-7944(88)90019-7.

[64] S. Dubey, A. B. O. Soboyejo, and W. O. Soboyejo, "An investigation of the effects of stress ratio and crack closure on the micromechanisms of fatigue crack growth in Ti-6Al-4V," *Acta Materialia,* vol. 45, no. 7, pp. 2777-2787, 1997/07/01/ 1997, doi: https://doi.org/10.1016/S1359-6454(96)00380-1.

[65] K. V. Sudhakar and E. S. Dwarakadasa, "A study on fatigue crack growth in dual phase martensitic steel in air environment," *Bulletin of Materials Science,* journal article vol. 23, no. 3, pp. 193-199, June 01 2000, doi: 10.1007/bf02719909.

[66] J. L. Tzou, C. H. Hsueh, A. G. Evans, and R. O. Ritchie, "Fatigue crack propagation in oil environments— II. A model for crack closure induced by viscous fluids," *Acta Metallurgica,* vol. 33, no. 1, pp. 117-127, 1985/01/01/ 1985, doi: https://doi.org/10.1016/0001-6160(85)90225-1.

[67] R. Pippan and A. Hohenwarter, "Fatigue crack closure: a review of the physical phenomena," *Fatigue & fracture of engineering materials & structures,* vol. 40, no. 4, pp. 471-495, 2017.

[68] M. Kamaya, "Influence of the interaction on stress intensity factor of semielliptical surface cracks," *Journal of pressure vessel technology,* vol. 130, no. 1, 2008.

[69] J. Tan and B. Chen, "A new method for modelling the coalescence and growth of two coplanar short cracks of varying lengths in AA7050-T7451 aluminium alloy," *International Journal of fatigue,* vol. 49, pp. 73-80, 2013.

[70] T. Hoshide, M. Miyahara, and T. Inoue, "Life prediction based on analysis of crack coalescence in low cycle fatigue," *Engineering Fracture Mechanics,* vol. 27, no. 1, pp. 91-101, 1987/01/01/ 1987, doi: https://doi.org/10.1016/0013-7944(87)90007-5.

[71] P. Frise and R. Bell, "Modelling fatigue crack growth and coalescence in notches," *International journal of pressure vessels and piping,* vol. 51, no. 1, pp. 107-126, 1992.

[72] B. Y. He, K. A. Soady, B. G. Mellor, A. Morris, and P. A. S. Reed, "Effects of shot peening on short crack growth rate and resulting low cycle fatigue behaviour in low pressure turbine blade material," *Materials Science and Technology,* vol. 29, no. 7, pp. 788-796, 2013/07/01 2013, doi: 10.1179/1743284713Y.0000000230.

[73] Z. Han, C. Qian, and H. Li, "Investigation of the Enhancement Interactions between Double Parallel Cracks on Fatigue Growth Behaviors," *Materials,* vol. 13, no. 13, p. 2952, 2020.

[74] F. Lefebvre and I. Sinclair, "Micromechanical aspects of fatigue in a MIG welded aluminium airframe alloy: Part 2. Short fatigue crack behaviour," *Materials Science and Engineering: A,* vol. 407, no. 1, pp. 265-272, 2005/10/25/ 2005, doi: https://doi.org/10.1016/j.msea.2005.07.014.

[75] Y. Z. Wang, J. Atkinson, R. Akid, and R. Parkins, "Crack interaction, coalescence and mixed mode fracture mechanics," *Fatigue & fracture of engineering materials & structures,* vol. 19, no. 4, pp. 427-439, 1996.

[76] M. Kamaya and N. Totsuka, "Influence of interaction between multiple cracks on stress corrosion crack propagation," *Corrosion science,* vol. 44, no. 10, pp. 2333-2352, 2002.

[77] F. Le Poulain, M. Touzet, M. Puiggali, and I. Aubert, "Mechanical behaviour of a solid with many stress corrosion growing cracks," *Journal of materials science,* vol. 40, no. 7, pp. 1731-1741, 2005.

[78] M. Kamaya and T. Haruna, "Influence of local stress on initiation behavior of stress corrosion cracking for sensitized 304 stainless steel," *Corrosion science,* vol. 49, no. 8, pp. 3303-3324, 2007.

[79] A. Ali, M. W. Brown, and C. A. Rodopoulos, "Modelling of crack coalescence in 2024-T351 Al alloy friction stir welded joints," *International Journal of Fatigue,* vol. 30, no. 10, pp. 2030-2043, 2008/10/01/ 2008, doi: https://doi.org/10.1016/j.ijfatigue.2008.02.014.

[80] M. Kamaya and M. Itakura, "Simulation for intergranular stress corrosion cracking based on a three-dimensional polycrystalline model," *Engineering Fracture Mechanics,* vol. 76, no. 3, pp. 386-401, 2009.

[81] R. E. Peterson, "Notch sensitivity," *Metal fatigue,* pp. 293-306, 1959.

[82] K. Molski and G. Glinka, "A method of elastic-plastic stress and strain calculation at a notch root," *Materials Science and Engineering,* vol. 50, no. 1, pp. 93-100, 1981.

[83] M. M. I. Hammouda, H. E. M. Sallam, and H. G. Osman, "Significance of crack tip plasticity to early notch fatigue crack growth," *International Journal of Fatigue,* vol. 26, no. 2, pp. 173-182, 2004/02/01/ 2004, doi: https://doi.org/10.1016/S0142-1123(03)00094-X.

[84] K. Sadananda and A. K. Vasudevan, "Short crack growth and internal stresses," *International Journal of Fatigue,* vol. 19, no. 93, pp. 99-108, 1997/06/01/ 1997, doi: https://doi.org/10.1016/S0142-1123(97)00057-1.

[85] L. Zhu, Z. Wu, X. Hu, and Y. Song, "Comparative study of small crack growth behavior between specimens with and without machining-induced residual stress of alloy GH4169," *Journal of Mechanical Science and Technology,* vol. 32, no. 11, pp. 5251-5261, 2018.

[86] D. Liao, S. P. Zhu, J. A. Correia, A. M. De Jesus, and F. Berto, "Recent advances on notch effects in metal fatigue: A review," *Fatigue & Fracture of Engineering Materials & Structures,* vol. 43, no. 4, pp. 637-659, 2020.

[87] W. Ramberg and W. R. Osgood, "Description of stress-strain curves by three parameters," 1943.

[88] H. Neuber, "Theory of Stress Concentration for Shear-Strained Prismatical Bodies With Arbitrary Nonlinear Stress-Strain Law," *Journal of Applied Mechanics,* vol. 28, no. 4, pp. 544-550, 1961, doi: 10.1115/1.3641780.

[89] M. Skorupa, "Load interaction effects during fatigue crack growth under variable amplitude loading—A literature review. Part I: Emperical trends," *Fatigue & Fracture of Engineering Materials & Structures,* vol. 21, no. 8, pp. 987-1006, 1998, doi: doi:10.1046/j.1460-2695.1998.00083.x.

[90] P. J. Bernard, L. T.C., and R. C.E., "The effect of single overloads on fatigue-crack propagation in steels," 1977.

[91] D. M. Shuter and W. Geary, "Some aspects of fatigue crack growth retardation behaviour following tensile overloads in a structural steel," *Fatigue & Fracture of Engineering Materials & Structures,* vol. 19, no. 2-3, pp. 185-199, 1996, doi: doi:10.1111/j.1460-2695.1996.tb00958.x.

[92] S. Pommier and M. De Freitas, "Effect on fatigue crack growth of interactions between overloads," *Fatigue & Fracture of Engineering Materials & Structures,* vol. 25, no. 7, pp. 709-722, 2002, doi: doi:10.1046/j.1460-2695.2002.00531.x.

[93] F. Romeiro, M. de Freitas, and M. da Fonte, "Fatigue crack growth with overloads/underloads: Interaction effects and surface roughness," *International Journal of Fatigue,* vol. 31, no. 11, pp. 1889-1894, 2009/11/01/ 2009, doi: https://doi.org/10.1016/j.ijfatigue.2009.01.001.

[94] C. MacDougall and T. H. Topper, "The influence of variable amplitude loading on crack closure and notch fatigue behaviour," *International Journal of Fatigue,* vol. 19, no. 5, pp. 389-400, 1997/05/01/ 1997, doi: https://doi.org/10.1016/S0142-1123(96)00076-X.

[95] S. Suresh, "Micromechanisms of Fatigue Crack Growth Retardation Following Overloads," *Engineering Fracture Mechanics,* vol. 18, no. 3, pp. 577-593, 1983.

[96] C. M. Ward-Close, A. F. Blom, and R. O. Ritchie, "Mechanisms associated with transient fatigue crack growth under variable-amplitude loading: An experimental and numerical study," *Engineering Fracture Mechanics,* vol. 32, no. 4, pp. 613-638, 1989.

[97] D. Damri and J. F. Knott, "Transcient retardations in fatigue crack growth following a single peak overload," *Fatigue & Fracture of Engineering Materials & Structures,* vol. 14, no. 7, pp. 709-719, 1991, doi: doi:10.1111/j.1460-2695.1991.tb00700.x.

[98] X. Zhou, H. P. Gaenser, and R. Pippan, "The effect of single overloads in tension and compression on the fatigue crack propagation behaviour of short cracks," *International Journal of Fatigue,* vol. 89, pp. 77-86, 2016/08/01/ 2016, doi: https://doi.org/10.1016/j.ijfatigue.2016.02.001.

[99] D. Corbly and P. Packman, "On the influence of single and multiple peak overloads on fatigue crack propagation in 7075-T6511 aluminum," *Engineering Fracture Mechanics,* vol. 5, no. 2, pp. 479-497, 1973.

[100] L. Vargas and R. Stephens, "Subcritical crack growth under intermittent overloading in cold-rolled steel," in *Proceedings, Third International Conference on Fracture, Munich, Germany*, 1973, vol. 6.

[101] M. Mlikota, S. Schmauder, Ž. Božić, and M. Hummel, "Modelling of overload effects on fatigue crack initiation in case of carbon steel," *Fatigue & fracture of engineering materials & structures,* vol. 40, no. 8, pp. 1182-1190, 2017.

[102] C. Robin, M. E. Louah, and G. Pluvinage, "Influence of an overload on the fatigue crack growth in steels," *Fatigue & Fracture of Engineering Materials & Structures,* vol. 6, no. 1, pp. 1-13, 1983.

[103] A. Blom, "Overload retardation during fatigue crack propagation in steels of different strengths," *Scand. J. Metall.,* vol. 18, no. 4, pp. 197-202, 1989.

[104] H. Tsukuda, H. Ogiyama, and T. Shiraishi, "Transcient fatigue crack growth behaviour following single overloads at high stress ratios," *Fatigue & Fracture of Engineering Materials & Structures,* vol. 19, no. 7, pp. 879-891, 1996, doi: doi:10.1111/j.1460-2695.1996.tb01023.x.

[105] R. E. Jones, "Fatigue crack growth retardation after single-cycle peak overload in Ti-6Al-4V titanium alloy," *Engineering Fracture Mechanics,* vol. 5, no. 3, pp. 585-604, 1973/09/01/ 1973, doi: https://doi.org/10.1016/0013-7944(73)90042-8.

[106] K. Tokaji, Z. Ando, K. Nagae, and T. Imai, "Effect of sheet thickness on fatigue crack retardation and validity of crack closure concept," in *Proceedings of the second international conference on fatigue and fatigue thresholds*, 1984, vol. 2: Birmingham, pp. 727-737.

[107] K. Sadananda, A. K. Vasudevan, R. L. Holtz, and E. U. Lee, "Analysis of overload effects and related phenomena," *International Journal of Fatigue,* vol. 21, pp. S233-S246, 1999/09/01/ 1999, doi: https://doi.org/10.1016/S0142-1123(99)00094-8.

[108] D. L. DuQuesnay, C. MacDougall, A. Dabayeh, and T. H. Topper, "Notch fatigue behaviour as influenced by periodic overloads," *International Journal of Fatigue,* vol. 17, no. 2, pp. 91-99, 1995/02/01/ 1995, doi: https://doi.org/10.1016/0142-1123(95)95887-M.

[109] C. Robin, M. Busch, M. Chergui, H. Lieurade, and G. Pluvinage, "Influence of Series of Tensile and Compressive Overloads on 316 L Crack Growth," *Fatigue crack growth under variable amplitude loading,* pp. 87-97, 1988.

[110] E. Salvati, H. Zhang, K. S. Fong, X. Song, and A. M. Korsunsky, "Separating plasticity-induced closure and residual stress contributions to fatigue crack retardation following an overload," *Journal of the Mechanics and Physics of Solids,* vol. 98, pp. 222-235, 2017/01/01/ 2017, doi: https://doi.org/10.1016/j.jmps.2016.10.001.

[111] Curtiss-Wright. "Metal Improvement Company - Shot peening applications." https://www.cwst.co.uk/wp-content/uploads/2020/01/new-english-green-book.pdf (accessed.

[112] O. Chopra and W. Shack, "Review of the margins for ASME code fatigue design curve-effects of surface roughness and material variability," Argonne National Lab.(ANL), Argonne, IL (United States), 2003.

[113] N. Alang, N. Razak, and A. Miskam, "Effect of surface roughness on fatigue life of notched carbon steel," *Int. J. Eng. Technol. IJET-IJENS,* vol. 11, no. 01, pp. 160-163, 2011.

[114] P. Maiya and D. Busch, "Effect of surface roughness on low-cycle fatigue behavior of type 304 stainless steel," *Metallurgical Transactions A,* vol. 6, no. 9, pp. 1761-1766, 1975.

[115] H. Itoga, K. Tokaji, M. Nakajima, and H.-N. Ko, "Effect of surface roughness on step-wise S–N characteristics in high strength steel," *International Journal of fatigue,* vol. 25, no. 5, pp. 379-385, 2003.

[116] W. D. Callister Jr and D. G. Rethwisch, *Materials Science and Engineering*, 9th ed. China: John Wiley and Sons, 2015.

[117] D. J. Child, G. D. West, and R. C. Thomson, "Assessment of surface hardening effects from shot peening on a Ni-based alloy using electron backscatter diffraction techniques," *Acta Materialia,* vol. 59, no. 12, pp. 4825-4834, 2011/07/01/ 2011, doi: https://doi.org/10.1016/j.actamat.2011.04.025.

[118] *BS EN ISO 6507-1:2008 Metallic materials - Vickers hardness test*, B. S. Institute, 2018.

[119] G. S. Schajer, "Advances in hole-drilling residual stress measurements," *Experimental mechanics,* vol. 50, no. 2, pp. 159-168, 2010.

[120] M. Olson, A. DeWald, and M. Hill, "Precision of Hole-Drilling Residual Stress Depth Profile Measurements and an Updated Uncertainty Estimator," *Experimental Mechanics,* vol. 61, no. 3, pp. 549-564, 2021.

[121] D. Child, G. West, and R. Thomson, "Assessment of surface hardening effects from shot peening on a Ni-based alloy using electron backscatter diffraction techniques," *Acta Materialia,* vol. 59, no. 12, pp. 4825-4834, 2011.

[122] A. Gariépy, F. Bridier, M. Hoseini, P. Bocher, C. Perron, and M. Lévesque, "Experimental and numerical investigation of material heterogeneity in shot peened aluminium alloy AA2024-T351," *Surface and Coatings Technology,* vol. 219, pp. 15-30, 2013.

[123] A. Fry, "Evaluation of the repeatability of residual stress measurements using x-ray diffraction," 2002.

[124] A. Turnbull, L. Crocker, and S. Zhou, "Do corrosion pits eliminate the benefit of shot-peening?," *International Journal of Fatigue,* vol. 116, pp. 439-447, 2018.

[125] C. You, "Fatigue lifing approaches for shot peened turbine components," University of Southampton, 2017.

[126] K. A. Soady, B. G. Mellor, J. Shackleton, A. Morris, and P. A. S. Reed, "The effect of shot peening on notched low cycle fatigue," *Materials Science and Engineering: A,* vol. 528, no. 29, pp. 8579-8588, 2011/11/15/ 2011, doi: https://doi.org/10.1016/j.msea.2011.08.003.

[127] C. You, M. Achintha, K. A. Soady, N. Smyth, M. E. Fitzpatrick, and P. A. S. Reed, "Low cycle fatigue life prediction in shot-peened components of different geometries—part I: residual stress relaxation," *Fatigue & Fracture of Engineering Materials & Structures,* vol. 40, no. 5, pp. 761-775, 2017, doi: doi:10.1111/ffe.12543.

[128] M. Achintha, C. You, B. Y. He, K. Soady, and P. Reed, "Stress Relaxation in Shot-Peened Geometric Features Subjected to Fatigue: Experiments and Modelling," in *Advanced Materials Research*, 2014, vol. 996: Trans Tech Publ, pp. 729-735.

[129] S. Meguid, G. Shagal, J. Stranart, K. Liew, and L. Ong, "Relaxation of peening residual stresses due to cyclic thermo-mechanical overload," *J. Eng. Mater. Technol.,* vol. 127, no. 2, pp. 170-178, 2005.

[130] K. Dalaei and B. Karlsson, "Influence of overloading on fatigue durability and stability of residual stresses in shot peened normalized steel," *Materials Science and Engineering: A,* vol. 528, no. 24, pp. 7323-7330, 2011.

[131] H. Dianyin and W. Rongqiao, "Combined fatigue experiments on full scale turbine components," *Aircraft Engineering and Aerospace Technology,* vol. 85, no. 1, pp. 4-9, 2013, doi: doi:10.1108/00022661311294085.

[132] Yamamoto. "What is S-N curve?" http://www.yama-kin.co.jp/english/knowledge/knowledge6.html (accessed October, 2018).

[133] O. Basquin, "The exponential law of endurance tests," in *Proc Am Soc Test Mater*, 1910, vol. 10, pp. 625-630.

[134] L. F. Coffin Jr, "A study of the effects of cyclic thermal stresses on a ductile metal," *Transactions of the American Society of Mechanical Engineers, New York,* vol. 76, pp. 931-950, 1954.

[135] S. S. Manson, *Behavior of materials under conditions of thermal stress*. National Advisory Committee for Aeronautics, 1953.

[136] H. Gerber, *Bestimmung der zulässigen spannungen in eisen-constructionen*. Wolf, 1874.

[137] J. Goodman, "Mechanics Applied to Engineering. 1899," ed: London: Longman, Green & Company.

[138] C. R. Soderberg, "Factor of safety and working stress," *Transactions of the American Society of Mechanical Engineers,* vol. 52, pp. 13-28, 1939.

[139] K. N. Smith, "A stress-strain function for the fatigue of metals," *Journal of materials,* vol. 5, pp. 767-778, 1970.

[140] C. You, M. Achintha, K. A. Soady, and P. A. S. Reed, "Low cycle fatigue life prediction in shot-peened components of different geometries – part II: life prediction," *Fatigue & Fracture of Engineering Materials & Structures,* vol. 40, no. 5, pp. 749-760, 2017, doi: 10.1111/ffe.12542.

[141] A. Palmgren, "Durability of ball bearings," *ZVDI,* vol. 68, no. 14, pp. 339-341, 1924.

[142] M. A. Miner, "Cumulative damage in fatigue," *Journal of applied mechanics,* vol. 12, pp. A159-A164, 1945.

[143] Y. S. Sun, "Revised Miner's rule and its application in calculating equivalent loads for components," *Reliability Engineering & System Safety,* vol. 43, no. 3, pp. 319-324, 1994/01/01/ 1994, doi: https://doi.org/10.1016/0951-8320(94)90036-1.

[144] J. Collins, "Fatigue of Materials in Machine Design," ed: John Wiley & Sons, New York, USA, 1981.

[145] Q. Sun, H.-N. Dui, and X.-L. Fan, "A statistically consistent fatigue damage model based on Miner's rule," *International Journal of Fatigue,* vol. 69, pp. 16-21, 2014/12/01/ 2014, doi: https://doi.org/10.1016/j.ijfatigue.2013.04.006.

[146] Z. Birnbaum and S. C. Saunders, "A probabilistic interpretation of Miner's rule," *SIAM Journal on Applied Mathematics,* vol. 16, no. 3, pp. 637-652, 1968.

[147] T. Shimokawa and S. Tanaka, "A statistical consideration of Miner's rule," *International Journal of Fatigue,* vol. 2, no. 4, pp. 165-170, 1980/10/01/ 1980, doi: https://doi.org/10.1016/0142-1123(80)90044-4.

[148] K. Tanaka and T. Mura, "A Dislocation Model for Fatigue Crack Initiation," *Journal of Applied Mechanics,* vol. 48, no. 1, pp. 97-103, 1981, doi: 10.1115/1.3157599.

[149] X. Wu, "On Tanaka-Mura's fatigue crack nucleation model and validation," *Fatigue & Fracture of Engineering Materials & Structures,* vol. 41, no. 4, pp. 894-899, 2018.

[150] P. Paris and F. Erdogan, "A critical analysis of crack propagation laws," *Journal of basic engineering,* vol. 85, no. 4, pp. 528-533, 1963.

[151] Y. Xiang and Y. Liu, "Mechanism modelling of shot peening effect on fatigue life prediction," *Fatigue & Fracture of Engineering Materials & Structures,* vol. 33, no. 2, pp. 116-125, 2010, doi: doi:10.1111/j.1460-2695.2009.01422.x.

[152] N. Pugno, M. Ciavarella, P. Cornetti, and A. Carpinteri, "A generalized Paris' law for fatigue crack growth," *Journal of the Mechanics and Physics of Solids,* vol. 54, no. 7, pp. 1333-1349, 2006.

[153] B. M. D. Cunningham *et al.*, "Fatigue crack initiation and growth behavior in a notch with periodic overloads in the low-cycle fatigue regime of FV566 ex-service steam turbine blade material," *Fatigue & Fracture of Engineering Materials & Structures,* vol. 45, no. 2, pp. 546-564, 2022, doi: https://doi.org/10.1111/ffe.13617.

[154] S. Zhou and A. Turnbull, "Growth rate of short cracks in a steam turbine blade steel," presented at the Parsons, 2011.

[155] *BS EN 6892-1. Metallic materials-Tensile testing-Part 1: Method of test at room temperature*, B. S. Institute, 2016.

[156] *BS ISO 12106: 2017 Metallic materials. Fatigue testing. Axial-strain-controlled method*, B. S. Institute, 2017.

[157] *BS ISO 12108: Metallic Materials - Fatigue Testing - Fatigue Crack Growth Method*, B. S. Institute, 2012.

[158] G. R. Irwin, "Plastic zone near a crack and fracture toughness," in *Proceedings of the 7th Sagamore Ordnance Materials Conference*, New York: Syracuse University, 1960, pp. 63-78.

[159] R. A. Cohen, "An introduction to PROC LOESS for local regression," in *Proceedings of the twenty-fourth annual SAS users group international conference, Paper*, 1999, vol. 273: Citeseer.

[160] C. Liu, S. Liu, S. Gao, Y. Hu, S. Zhang, and H. Zhang, "Fatigue life assessment of the centrifugal compressor impeller with cracks based on the properties of FV520B," *Engineering Failure Analysis,* vol. 66, pp. 177-186, 2016/08/01/ 2016, doi: https://doi.org/10.1016/j.engfailanal.2016.04.028.

[161] B. He, O. Katsamenis, B. Mellor, and P. A. Reed, "3-D analysis of fatigue crack behaviour in a shot peened steam turbine blade material," *Materials Science and Engineering: A,* vol. 642, pp. 91-103, 2015.

[162] K. M. Perkins and M. R. Bache, "The influence of inclusions on the fatigue performance of a low pressure turbine blade steel," *International Journal of Fatigue,* vol. 27, no. 6, pp. 610-616, 2005/06/01/ 2005, doi: https://doi.org/10.1016/j.ijfatigue.2004.12.004.

[163] M. C. d. S. Fernandes, S. Nakamatsu, S. C. d. Rezende, S. C. Maestrelli, L. d. L. Sousa, and N. A. Mariano, "Tempering Temperature Influence on 13Cr4Ni0. 02C Steel Corrosion Resistance," *Materials Research,* vol. 20, pp. 537-542, 2017. [Online]. Available: http://www.scielo.br/scielo.php?script=sci_arttext&pid=S1516-14392017000800537.

[164] G. Farges and D. Degout, "Interpretation of the indentation size effect in vickers microhardness measurements-absolute hardness of materials," *Thin solid films,* vol. 181, no. 1-2, pp. 365-374, 1989.

[165] Y. Xia, M. Bigerelle, J. Marteau, P. E. Mazeran, S. Bouvier, and A. Iost, "Effect of surface roughness in the determination of the mechanical properties of material using nanoindentation test," *Scanning,* vol. 36, no. 1, pp. 134-149, 2015. [Online]. Available: https://hal.archives-ouvertes.fr/hal-01169539/document.

[166] D. Tabor, "The physical meaning of indentation and scratch hardness," *British Journal of Applied Physics,* vol. 7, no. 5, pp. 159-166, 1956/05 1956, doi: 10.1088/0508-3443/7/5/301.

[167] E. J. Pavlina and C. J. Van Tyne, "Correlation of Yield Strength and Tensile Strength with Hardness for Steels," *Journal of Materials Engineering and Performance,* vol. 17, no. 6, pp. 888-893, 2008/12/01 2008, doi: 10.1007/s11665-008-9225-5.

[168] J. T. Busby, M. C. Hash, and G. S. Was, "The relationship between hardness and yield stress in irradiated austenitic and ferritic steels," *Journal of Nuclear Materials,* vol. 336, no. 2, pp. 267-278, 2005/02/01/ 2005, doi: https://doi.org/10.1016/j.jnucmat.2004.09.024.

[169] P. L. Larsson, "Investigation of sharp contact at rigid–plastic conditions," *International Journal of Mechanical Sciences,* vol. 43, no. 4, pp. 895-920, 2001/04/01/ 2001, doi: https://doi.org/10.1016/S0020-7403(00)00056-4.

[170] M. Nakajima, J. W. Jung, Y. Uematsu, and K. Tokaji, "Coaxing effect in stainless steels and high-strength steels," in *Key Engineering Materials*, 2007, vol. 345: Trans Tech Publ, pp. 235-238.

[171] T. H. Topper and M. T. Yu, "The effect of overloads on threshold and crack closure," *International Journal of Fatigue,* vol. 7, no. 3, pp. 159-164, 1985/07/01/ 1985, doi: https://doi.org/10.1016/0142-1123(85)90027-1.

[172] F. Taheri, D. Trask, and N. Pegg, "Experimental and analytical investigation of fatigue characteristics of 350WT steel under constant and variable amplitude loadings," *Marine Structures,* vol. 16, no. 1, pp. 69-91, 2003/01/01/ 2003, doi: https://doi.org/10.1016/S0951-8339(02)00004-7.

[173] M. Skorupa, J. Schijve, A. Skorupa, and T. Machniewicz, "Fatigue crack growth in a structural steel under single and multiple periodic overload cycles," *Fatigue & Fracture of Engineering Materials & Structures,* vol. 22, no. 10, pp. 879-887, 1999, doi: 10.1046/j.1460-2695.1999.00219.x.

[174] N. Fleck, "Fatigue crack growth due to periodic underloads and overloads," *Acta Metallurgica,* vol. 33, no. 7, pp. 1339-1354, 1985.

[175] *BS EN ISO 4288:1998: Geometric Product Specification (GPS) - Surface texture - Profile Method: Rules and procedures for the assessment of surface texture*, B. S. Institute, 1998.

[176] B. T. Moghaddam, A. M. Hamedany, A. Mehmanparast, F. Brennan, K. Nikbin, and C. M. Davies, "Numerical analysis of pitting corrosion fatigue in floating

offshore wind turbine foundations," *Procedia Structural Integrity,* vol. 17, pp. 64-71, 2019.

[177] B. M. Schönbauer *et al.*, "Fatigue life estimation of pitted 12% Cr steam turbine blade steel in different environments and at different stress ratios," *International Journal of Fatigue,* vol. 65, pp. 33-43, 2014/08/01/ 2014, doi: https://doi.org/10.1016/j.ijfatigue.2013.10.003.

[178] W. D. Pilkey, D. F. Pilkey, and Z. Bi, *Peterson's stress concentration factors*. John Wiley & Sons, 2020.

[179] P. S. Maiya and D. E. Busch, "Effect of surface roughness on low-cycle fatigue behavior of type 304 stainless steel," *Metallurgical Transactions A,* journal article vol. 6, no. 9, p. 1761, September 01 1975, doi: 10.1007/bf02642305.

[180] S. Bagherifard, R. Ghelichi, and M. Guagliano, "Numerical and experimental analysis of surface roughness generated by shot peening," *Applied surface science,* vol. 258, no. 18, pp. 6831-6840, 2012.

[181] M. Guagliano and L. Vergani, "An approach for prediction of fatigue strength of shot peened components," *Engineering Fracture Mechanics,* vol. 71, no. 4-6, pp. 501-512, 2004.

[182] W. Zinn and B. Scholtes, "Influence of shot velocity and shot size on Almen intensity and residual stress depth distributions," in *Proceedings of the 9th International Conference on Shot Penning*, Paris, France, 2005, vol. 10.

[183] N. Saklakoglu, A. Bolouri, S. G. Irizalp, F. Baris, and A. Elmas, "Effects of shot peening and artificial surface defects on fatigue properties of 50CrV4 steel," *The International Journal of Advanced Manufacturing Technology,* vol. 112, no. 9, pp. 2961-2970, 2021.

[184] J. Sakamoto, Y. Lee, and S. Cheong, "Effect of surface flaw on fatigue strength of shot-peened medium-carbon steel," *Engineering Fracture Mechanics,* vol. 133, pp. 99-111, 2015.

[185] K. Soady, "Life assessment methodologies incoroporating shot peening process effects: mechanistic consideration of residual stresses and strain hardening Part 1–effect of shot peening on fatigue resistance," *Materials Science and Technology,* vol. 29, no. 6, pp. 637-651, 2013.

[186] A. G. Sanchez *et al.*, "Effects of laser shock peening on the mechanisms of fatigue short crack initiation and propagation of AA7075-T651," *International Journal of Fatigue,* vol. 143, p. 106025, 2021/02/01/ 2021, doi: https://doi.org/10.1016/j.ijfatigue.2020.106025.

[187] K. Nip, L. Gardner, C. Davies, and A. Elghazouli, "Extremely low cycle fatigue tests on structural carbon steel and stainless steel," *Journal of constructional steel research,* vol. 66, no. 1, pp. 96-110, 2010.

[188] X. Zheng and C. Lin, "On the expression of fatigue crack initiation life considering the factor of overloading effect," *Engineering Fracture Mechanics,* vol. 31, no. 6, pp. 959-966, 1988/01/01/ 1988, doi: https://doi.org/10.1016/0013-7944(88)90206-8.

[189] M. Darvish and S. Johansson, "Fatigue crack growth studies under combination of single overload and cyclic condensation environment," *Engineering Fracture Mechanics,* vol. 52, no. 2, pp. 295-319, 1995/09/01/ 1995, doi: https://doi.org/10.1016/0013-7944(94)00217-6.

[190] J. L. Chaboche, "Time-independent constitutive theories for cyclic plasticity," *International Journal of Plasticity,* vol. 2, no. 2, pp. 149-188, 1986/01/01/ 1986, doi: https://doi.org/10.1016/0749-6419(86)90010-0.

[191] N. Jezernik, J. Kramberger, T. Lassen, and S. Glodež, "Numerical modelling of fatigue crack initiation and growth of martensitic steels," *Fatigue & Fracture of Engineering Materials & Structures,* vol. 33, no. 11, pp. 714-723, 2010.

[192] S. Glodež, N. Jezernik, J. Kramberger, and T. Lassen, "Numerical modelling of fatigue crack initiation of martensitic steel," *Advances in Engineering Software,* vol. 41, no. 5, pp. 823-829, 2010.

[193] N. Hill and T. Stuart, "Assessment of Critical Crack Size in an English Electric LP Turbine Stage 5 Blade Firtree - Crack Growth in Stage 5 Firtree of Low Pressure Turbine Report 47723-42760R Issue 2," 2016.

[194] M. Zanjani, "E.ON Engineering Report EEN/09/OSP/SA/1330/R," 2009.